University of South Carolina
Scholar Commons

Theses and Dissertations

1-1-2013

III-V Nitride Micro- and Nano-Scale Cantilevers For Multimodal Sensing Applications

Ehtesham Bin Quddus
University of South Carolina

Follow this and additional works at: http://scholarcommons.sc.edu/etd

Recommended Citation
Quddus, E. B.(2013). *III-V Nitride Micro- and Nano-Scale Cantilevers For Multimodal Sensing Applications.* (Doctoral dissertation). Retrieved from http://scholarcommons.sc.edu/etd/2413

This Open Access Dissertation is brought to you for free and open access by Scholar Commons. It has been accepted for inclusion in Theses and Dissertations by an authorized administrator of Scholar Commons. For more information, please contact SCHOLARC@mailbox.sc.edu.

III-V NITRIDE MICRO- AND NANO-SCALE CANTILEVERS
FOR
MULTIMODAL SENSING APPLICATIONS

by

Ehtesham B. Quddus

Bachelor of Science
Bangladesh University of Engineering and Technology, Dhaka, Bangladesh, 2006

Submitted in Partial Fulfillment of the Requirements

For the Degree of Doctor of Philosophy in

Electrical Engineering

College of Engineering and Computing

University of South Carolina

2013

Accepted by:

Goutam Koley, Major Professor

Tangali S. Sudarshan, Committee Member

Grigory Simin, Committee Member

Richard Webb, Committee Member

Lacy Ford, Vice Provost and Dean of Graduate Studies

© Copyright by Ehtesham B. Quddus, 2013
All Rights Reserved.

DEDICATION

To my parents,

To my lively wife Shakila,

To the loving memory of my grandfathers

ACKNOWLEDGEMENTS

I would like to thank my Supervisor Dr. Goutam Koley for supporting me during these five years. Working with Dr. Koley, in my opinion, is the best thing that a PhD student can wish for. He perfectly translates the character of his students and provides the best conditions for the development of intellectual qualities and creative thinking. I am very grateful to him for his scientific advice and knowledge and many insightful discussions and suggestions he provided me and beyond all his guidance in my tough times.

I owe my gratitude to all of the dissertation defense committee members, Professor Richard Webb, Professor Sudarshan and Professor Simin for their career advice and suggestions in general.

I will forever be thankful to Professor Webb not only to let me use his facility (Low Temperature and Mesoscopic Physics Laboratory aka Dr. Webb's Lab) located at the Nanocenter but also he has been very helpful in providing advice many times during my PhD. In particular, I would like to express my gratitude to Prof. Webb for his support in the nanoscale characterization and device fabrication using his lab facilities. He is one of the smartest people I know; I hope I could be as lively, enthusiastic, and energetic as Dr. Webb.

I also thank to Professor Sudarshan and his Silicon Carbide Lab, particularly in helping me to use the leak detector for my CVD furnace and also letting me use the Cleanroom facility. Part of the NEMS fabrication processes were done at his cleanroom.

The Microfabrication part was done using the class 10/ class 100 cleanroom facilities at the IEN at GaTech. I have been visiting to GaTech since March 2011 and met really nice people and stuff there. They showed me light in the tunnel many times while I was stuck with the complex processes, I owe my gratitude to all of the stuff members of MiRC and IEN who have made this research possible, especially for their personal and technical support.

This work has been done in collaboration with Oakridge National Lab (ORNL) and National Institute of Standards and Technology (NIST). I would like to thank Dr. Karren More at the ShaRE facility at Oak ridge and Prof. Steve Semancik at the NIST for letting me use their state of the art equipments.

I would like to acknowledge the financial support from NSF grant that funded part of the research for this dissertation.

I thank to all the present members of Dr. Koley's group. Special thanks to Amol Singh for guiding me as a senior member, Alina Wilson for helping me last two and half years with Nanowire growth and characterization and also Nick De Roller for providing me the COMSOL simulation results. My research for this dissertation would not have been successful also without the efforts of all the past colleagues in our research group; my salute to the great individuals: Dr. Zhihua Cai, Dr. Razib Shishir, Dr. Muhammad

Qazi, Dr. Jie Lie, Dr. Waliullah Khan Nomani, Mr. Devendra Diwan and Mr. Stephen Orr.

Finally, my long tenure as a graduate student would not have been possible without the support and patience of my family. I wish to express my heartfelt gratitude to my parents and also I am deeply indebted to my beloved wife Shakila Afrin; their love and support have encouraged me to keep moving forward throughout this endeavor.

ABSTRACT

Recent research trends in chemical and biological sensing have been geared toward developing molecular sensor devices that are fast, label free, miniaturized and portable. The performance of these devices can be dramatically improved by utilizing multimodal detection techniques, new materials and micro-/nanofabrication technologies. This is especially true for micro-/nanoscale cantilever sensors, which undergo changes in mechanical or electrical properties upon the specific binding of molecules. To develop the sensor devices with the above attributes, we utilized III-V nitride materials: InN nanowires for realizing nanoscale cantilevers and AlGaN/GaN heterostuctures with or without embedded HFETs, for developing microcantilevers. There are mainly two approaches of fabricating these sensor devices: bottom-up approach for nanocantilevers, and top-down approach for microcantilevers. InN NWs, which exhibit interesting properties such as high carrier density, superior electron mobility, strong surface charge accumulation, and chemical inertness, were synthesized using Chemical Vapor Deposition (CVD) technique by Vapor-Liquid-Solid (VLS) mechanism. The synthesis process was optimized to obtain growth direction modulation and enhanced performance of the devices, largely avoiding the complexity of nanofabrication/ etching typically involved in the realization of nanoscale sensors. With dimensions much smaller than conventional cantilevers, the nanocantilevers are expected to have dramatically improved physical, chemical, and biological sensitivity for sensor applications. The piezoresistive

and piezoelectric properties of AlGaN/GaN heterostructures, their wide bandgap, and chemical inertness make the microcantilevers very attractive for developing highly sensitive sensors suitable for harsh environment applications. The large variation in 2-dimensional electron gas (2DEG) at the interface with mechanical strain makes these microcantilevers much more sensitive than conventional Si based piezoresistive microcantilevers. A process was developed to fabricate free standing AlGaN/GaN microcantilevers on Si(111) substrate using various processing steps involving photolithography, GaN and through wafer Si etching, and dielectric and metal deposition. The detection performance of these cantilevers is largely improved by the utilization of a multimodal detection technique.

TABLE OF CONTENTS

DEDICATION .... **iii**

ACKNOWLEDGEMENTS .... **iv**

ABSTRACT .... **vii**

LIST OF TABLES .... **xiii**

LIST OF FIGURES .... **xiv**

CHAPTER 1 AIM OF DISSERTATION **1**

1.1 Project scope 2

1.2 The research partners 2

1.3 Dissertation Aim 3

1.4 Outline of the dissertation 3

CHAPTER 2 INTRODUCTION & MOTIVATION **6**

2.1 Introduction 7

2.2 Chemical sensor arrays 9

2.3 Classification of sensors 11

2.4 Applications of chemical sensors 15

CHAPTER 3 CANTILEVER SENSORS 24

3.1 Cantilever sensors 25

3.2 Cantilever theory of operation 30

3.3 Modalities of Cantilever Deflection- and Vibration- Based Sensing 39

CHAPTER 4 INDIUM NITRIDE NANOWIRES 59

4.1 Introduction and background 60

4.2 Semiconductor nanowires 60

4.3 Indium Nitride (InN) nanowires 62

4.4 Indium Nitride Nanowire synthesis 70

4.5 Growth optimization: Role of oxygen in the synthesis 77

4.6 Growth direction modulation 84

4.7 Electrical Characterization and Diameter-dependent mobility 86

CHAPTER 5 INDIUM NITRIDE NANOCANTILEVERS 98

5.1 Introduction 99

5.2 InN Suspended nanostructures 102

5.3 Fabrication of InN NEMS resonators 102

5.4 DC characteristics of InN NEMS resonator 107

5.5 Optimization of the release process of suspended Nanostructures 109

5.6 InN Nanoresonators: Focused Ion Beam (FIB) technique 112

5.7 InN Nanowire Based V-shaped Cantilever Sensors 118

5.8 Fabrication steps of InN nanocantilever sensors 136

CHAPTER 6 ALGAN/GAN HETEROSTRUCTURES... 140

6.1 Introduction... 141

6.2 Gallium Nitride crystal structure 144

6.3 Spontaneous and piezoelectric polarization.. 145

6.4 Growth of AlGaN/GaN heterostructures 149

6.5 Formation of 2DEG 152

CHAPTER 7 ALGAN/GAN MICROCANTILVERS 160

7.1 Introduction... 161

7.2 HFET embedded V-shaped AlGaN/GaN microcantilever 162

7.3 V-shaped AlGaN/GaN micro heater cantilever 175

7.4 Fabrication of AlGaN/GaN V-shaped microcantilevers..................................... 184

7.5 Measurements of AlGaN/GaN Microcantilevers.. 199

CHAPTER 8 CONCLUSION AND FUTURE PLAN 225

8.1 Summary.. 226

8.2 Future work.. 227

REFERENCES... 232

APPENDIX A: PROCESS FLOW FOR CANTILEVER FABRICATION 251

APPENDIX B: ELECTRON BEAM LITHOGRAPHY 254

LIST OF TABLES

Table 4.1 Lattice parameters of wurtzite III-V nitrides at 300 K. 65

Table 4.2 Effects of lattice non-ideality on the strength of spontaneous polarization in the III-V nitrides. 67

Table 5.1 Simulated material constants 121

Table 5.2 Simulated Model Properties... 121

Table 6.1 Electronic properties of some common semiconductors, Ref. [241]............. 142

Table 6.2 Structural parameters for AlN, GaN, and InN. 145

Table 6.3 The dependence of spontaneous polarization on the c_0/a_0 ratio, Ref. [243]... 146

Table 6.4 List of elastic and piezoelectric constants used for calculation 148

Table 7.1 Dimension of the AlGaN/GaN HFET embedded microcantilevers and calculated *k* and *f*.. 164

Table 7.2 Dimension of the AlGaN/GaN HFET 164

Table 7.3 Properties of GaN and AlGaN used for COMSOL simulations ([Ref. 253]). 170

Table 7.4 Calculated parameters from the TLM test 201

Table 7.5 Comparison between theoretical and experimental resonant frequency 210

LIST OF FIGURES

Figure 2.1: Various applications of chemical sensors 15

Figure 3.1: Two modes of cantilever-based biomolecule detection: (*a*) deflection mode and (*b*) resonance mode. 31

Figure 3.2: Schematic of a cantilever with length *L* and thickness *H*, with respect to coordinates *X* and *Y*, before being deflected by a point force *F* applied on the tip. 34

Figure 3.3: Schematic diagram of a microcantilever with embedded piezoresistive transduction element embedded at the base of the cantilever. 40

Figure 3.4: Simplified schematic diagram of optical transduction system used in atomic force microscope. 41

Figure 3.5: Simplified schematic diagram of capacitive transduction system of a microcantilever based sensor. Due to adsorption on the functionalizing layer the cantilever bends, changing the capacitance between the two conducting plates 43

Figure 3.6: Schematic of the interaction between probe and target molecules on an embedded-MOSFETcantilever system. The silicon nitride cantilever is a reference, and the gold-coated one is used as a sensing cantilever. Specific biomolecular interactions between receptor and target bend the cantilever. Magnified view of embedded MOSFET in cross section shows stressed gate region when cantilever bends, resulting in change of drain current due to conductivity modulation of the channel underneath the gate.(Figure taken from Ref [137]) 44

Figure 3.7: Resistance of a heated cantilever as a function of power dissipation and illustration of heat transfer by heated cantilevers since they are very sensitive to small thermal agitation (Ref [153]). 46

Figure 3.8: (a) the adsorption and (b) the absorption mechanism of molecules on cantilever surfaces.. 48

Figure 3.9: Nanowire pH sensors. (a) Schematic of an amino-functionalized nanowire device and the protonation/deprotonation equilibria that change the surface charge state with pH. (b) Changes in nanowire conductance as the pH of solutions delivered to the sensor is varied from 2 to 9; inset is a plot of conductance data versus pH. (c) Schematic of an unmodified nanowire sensor containing silanol groups and the

protonation/deprotonation equilibria that change the surface charge state with pH. (d) Conductance of an unmodified Si nanowire device (red) versus pH. The dashed green curve is a plot of the surface charge density for silanol groups on silica as a function of pH (Ref. [157]).. 51

Figure 3.10: (a) Schematic of a single virus binding and unbinding to the surface of a Si nanowire device modified with antibody receptors and the corresponding time-dependent change in conductance. (b) Simultaneous conductance and optical data recorded for a Si nanowire device after the introduction of influenza A solution. The images correspond to the two binding/unbinding events highlighted by time points 1-3 and 4-6 in the conductance data, with the virus appearing as a red dot in the images (Ref. [158]). 52

Figure 3.11: Physics of potentiometric measurement with a cantilever oscillating above substrate. 55

Figure 3.12: Band diagram illustrating Fermi level and vacuum level for Si cantilever probe and semiconductor substrate. 57

Figure 4.1:Density of states in semiconductor structures depending on dimensionality (Ref. [120]). 62

Figure 4.2: Atomic arrangements in In-face and N-face InN crystals. The red arrow pointing from N to In atom shows the direction of the spontaneous polarization (Ref. [184]).. 64

Figure 4.3: The conduction and valence band edges (E_C and E_V, solid lines) and the branch-point energy (E_B, dotted line) with respect to the Fermi level (E_F, dashed line) in the near-surface region of InN(0001). The donor-type surface states (Dss) are also shown, where the unoccupied states above the Fermi level are shown to be positively charged. 69

Figure 4.4: CVD system setup, Pressure and MFC controllers, MFCs, Temperature controllers and heated furnace 71

Figure 4.5: (a) A typical SEM image of InN nanowires as-synthesized on a Si/SiO2 substrate. Inset shows a single NW, scale bar is 20 nm. (b) High resolution TEM image of a single NW growing along [110] direction, the inset shows the hexagonal FFT spectrum. (c) Atomic resolution shows the lattice spacing of the NW............................ 72

Figure 4.6: Energy Dispersive Spectroscopy (EDS) mapping on section of a nanonetwork. (a) STEM Image. (b) In elemental mapping, (c) N elemental mapping and (d) O elemental mapping along the nanonetwork... 74

Figure 4.7: NWs growing on a 40 nm thick SiO2 membrane from catalyst patterns outside the membrane (Si support). 75

Figure 4.8: (a) Raman spectrum of the InN NW junction showing the A1(TO), E2 (high) and A1(LO) phonon peaks at 443, 491 and 594 cm-1. The E1(TO) phonon peak at 475 cm-1 is hidden. (b) Raman spectrum of the SiO2 membrane without InN NW............... 76

Figure 4.9: The morphologies obtained at different oxygen (3% in balance N2) flow rates in sccm: (a) 0 sccm; (b) 2.0 sccm; (c) 4.0 sccm; (d) 8.0 sccm; (e) 10.0 sccm; (f) 14.0 sccm. 80

Figure 4.10: HTREM images of single NWs at different oxygen (3% in balance N2) flow rates in sccm a) 2 sccm; (b) 4.0 sccm; (c) 10.0 sccm; (d) 14.0 sccm. Insets show the hexagonal FFT spectra respectively........ 82

Figure 4.11: Energy Dispersive Spectroscopy (EDS) mapping on section of a nanowire. (a) STEM Image. (b) In elemental mapping, (c) N elemental mapping and (d) O elemental mapping along the nanowire for 4 sccm of O2 concentration. 83

Figure 4.12: Energy Dispersive Spectroscopy (EDS) mapping on section of a nanonetwork. (a) STEM Image. (b) In elemental mapping, (c) N elemental mapping and (d) O elemental mapping along the nanonetwork for 10 sccm of O2 concentration. 84

Figure 4.13: SEM images showing (a) spontaneous bending of InN NW, as well as bending caused by (b) two InN NW guides (c) lithographically deposited 100 nm SiO2 barriers and (d) Lattice resolved TEM images of a NW showing atomic arrangement as the growth direction is changed from [110] to another $[1\bar{1}0]$, inset shows schematic diagram of atomic configurations for 60° (similar to 120°) bend........ 86

Figure 4.14: (a) SEM image of a 3 NW FET in a back-gated configuration. (b) Id-Vd curves for the InN NW FET at gate bias voltages between 0 V to -3.6 V at intervals of -0.4 V. (c) An Id-Vg curve measured at Vd = 0.2 V, with the dId/dVg slope shown by a straight line. (d) I_d-V_d saturation curves measured for gate bias voltages between 0 V and -4.0 V at intervals of -0.5 V. 88

Figure 4.15: Variation of (a) mobility and (b) conductivity of InN NWs as a function of the diameter obtained from single and multi-NW FETs. The respective error bars are also shown. Inset of (b) shows the variation in carrier concentration with NW diameter. 92

Figure 4.16: Variation of (a) mobility and (b) conductivity of InN NWs as a function of NW diameter fitted with diameter-dependant mobility and conductivity obtained from theoretical modeling (solid lines). Inset of (b) shows the variation of mobility with carrier concentration........ 96

Figure 5.1: A typical example of a silicon nanowire based NEMS resonator (Ref. [224]). 99

Figure 5.2: Plots showing the number of yearly peer reviewed publications as obtained from Web of Search with a key “nanocantilever” and “nanocantilever sensor”. 100

Figure 5.3: Wafer information for the processing of InN NEMS resonators 103

Figure 5.4: The fabrication process flow of nanoresonators........ 103

Figure 5.5: (a) Schematic representation and (b) SEM image of alignment mark 104

Figure 5.6: (a) Schematic representation and (b) SEM image of 2 nm thick, 2um diameter catalyst spots 105

Figure 5.7: (a) Schematic representation and (b) SEM image of NWs grown from catalyst spot 105

Figure 5.8: (a) Schematic representation and (b) SEM image of NW and etched trench 106

Figure 5.9: (a) Schematic representation and (b) SEM image of NW, trench and probe contact 107

Figure 5.10: The dc characteristics curves for InN nanoresonators, (a) before trench etching and (b) after trench etching. 108

Figure 5.11: $I_d - V_g$ characteristics of InN NEMS resonator, from this curve we calculated the mobility of the InN NW. 109

Figure 5.12: The schematic representation of the final NEMS resonator, NWs should be going across the trench with no sagging. 110

Figure 5.13: SEM images of InN NWs on the trenches, both cases the NWs fell down inside the trench. 110

Figure 5.14: SEM image of an InN NW across a trench, the trench was etched by Inductively Coupled Plasma (ICP) dry etch recipe. 112

Figure 5.15: (a) Image of a Dual beam FIB, (b) Inside of the dual beam FIB and schematics of different components of a dual beam FIB 113

Figure 5.16: The schematic representation of the final NEMS resonator with FIB; NWs are going across the trench with no sagging and the probe contacts are not solid filled 114

Figure 5.17: (a) SEM image of a pre-growth trench and (b) the SEM image of a pre growth trench and 2nm thick catalyst spots 115

Figure 5.18: SEM image of a pre growth trench and a suspended NW crossing across the trench 116

Figure 5.19: Image of the designing of contact pads via FIB software 116

Figure 5.20: (a) SEM image of a suspended NW and the patterned and deposited FIB traces, (b) SEM image (close view) of another suspended NW, the etched profile can be seen as a measure to disconnect or cut down the NW from conducting through other NWs. 117

Figure 5.21: (a) SEM image of a NEMS resonator by dual beam FIB technique, the traces and pads are seen, (b) optical micrograph image of the wire bonding, (c) SEM image of

the wire bonded contact pads and (d) image of the final 40 pin DIP Chip containing active devices. 118

Figure 5.22: Three-dimensional model used to perform analyses. 121

Figure 5.23: System quality factor (Q_T) as a function of ambient air pressure. After about 200 Pa, damping is predominantly determined by squeeze-film losses. 125

Figure 5.24: Frequency sweep output of the model structure. Displacement is measured at the cantilever tip. 126

Figure 5.25: Sensing configuration for the VNC sensor 128

Figure 5.26: Fundamental resonant frequency change given a mass attachment at the cantilever tip. The inset shows greater detail in the 10^{-23} g decade mass range. 129

Figure 5.27: Capacitance (blue) plotted against the bias applied to the cantilever. Deflection (green) is also present to compare with the device deflection limitation (red) of the dielectric strength of air breakdown point (3×10^6 V/m) 130

Figure 5.28: Resistance change from displacement. The charged cantilever, when subjected to bending (induced or through capacitive force) will exhibit a change in charge, which may be translated into a change in resistance. 131

Figure 5.29: Temperature and current response across a small range of input voltages. 132

Figure 5.30: (a) Scaled (by 190) increase in length of the VNC due to temperature rise caused by an applied bias of 850 mV, and (b) displacement across a range of temperatures given by an applied voltage. 133

Figure 5.31: (a) SEM image of a V-shaped NW deflected back and forth by oxide barriers and (b) SEM image of a suspended NW across the trench. 135

Figure 5.32: The fabrication process flow of V-shaped nanocantilevers. 136

Figure 5.33: SEM image of 200nm thick SiO_2 barriers and (b) SEM image of a V-shaped NW deflected back and forth by SiO_2 barriers 137

Figure 5.34: SEM image of a V-shaped NW device, the etching of the underneath SiO_2 is not performed yet (not V-shaped nanocantilever). The contacts are seen in the SEM image. 138

Figure 6.1: Bandgap of common semiconductors at room temperature plotted against their lattice constant, Ref. [241] 141

Figure 6.2: (a) 2DEG in AlGaN/GaN interface, (b) band diagram and surface states of AlGaN/GaN heterostructure 143

Figure 6.3: Atomic arrangement in Ga-face and N-face GaN crystals. The arrow pointing from N to Ga atom shows the direction of the spontaneous polarization. 144

Figure 6.4: The direction of piezoelectric polarization with (a) compressive, and (b) tensile stress on Al(/Ga/In)N layer. 147

Figure 6.5: Typical layer structures of nitride heterostructures grown by MOCVD. 150

Figure 6.6: Layer structures of Ga-face and N-face nitride heterostructures grown by MBE on sapphire. Note that the N-face structure does not have a nucleation layer (a low temperature GaN nucleation layer can also be used to get N-face polarity). 152

Figure 6.7: Variation of the spontaneous and piezoelectric polarization of $Al_xGa_{1-x}N$ and the bound charge at AlGaN/GaN interface plotted against aluminum mole fraction of $Al_xGa_{1-x}N$ [245]. 155

Figure 6.8: Conduction band diagram, sheet charge densities at the surface and interface of AlGaN/GaN heterostructure. 156

Figure 6.9: Sheet carrier concentration of the 2DEG confined at a Ga-face (GaN/AlGaN/GaN) or N-face (GaN/AlGaN/GaN) interface for different thickness of the AlGaN barrier. The insert shows the maximum sheet carrier concentration of a pseudomorphic grown Ga-face AlGaN/GaN and a N-face GaN/AlGaN heterostructure. 158

Figure 7.1: Schematic diagram of the AlGaN/GaN HFET embedded V-shaped microcantilever. 163

Figure 7.2: (a) Geometrical parameters of a triangular cantilever, (b) Calculation of *moment of cross-sectional area, I* for one rectangular arm of a V-shaped cantilever. ... 166

Figure 7.3: Structure of a general V-shaped microcantilever. 168

Figure 7.4: The model used for COMSOL simulation for the AlGaN/GaN HFET embedded V-shaped microcantilever 169

Figure 7.5: Cross section of a HFET embedded AlGaN/GaN V-shaped microcantilever showing different metal stacks (not drawn to scale). 171

Figure 7.6: (a) The model used for COMSOL simulation for the AlGaN/GaN HFET embedded V-shaped microcantilever, the position of the applied force of 1 nN is shown by arrow and (b) the deflection result with the applied force. 173

Figure 7.7: The *x*-direction strain distribution on the surface of the cantilever. Insets show expanded view of the base area. 174

Figure 7.8: (a) scanning electron microscope (SEM) and (b) infrared (IR) microscope images of the fabricated heated cantilever, indicating heating only near the free end of the cantilever [277]. 176

Figure 7.9: Design of the tapered V-shaped AlGaN/GaN microcantilevers (a) the GaN and AlGaN layer, (b) dimensions of the cantilever and (c) tapered tip dimension from the AutoCad design... 178

Figure 7.10: COMSOL simulated frequency response of the heated microcantilever. .. 179

Figure 7.11: (a) The model used for COMSOL simulation for the tapered V-shaped AlGaN/GaN heated microcantilever, the position of the applied force of 1 nN is shown by arrow and (b) the deflection result with the applied force. 180

Figure 7.12: The *x*-direction strain distribution on the surface of the cantilever. Insets show expanded view of the base area. 181

Figure 7.13: (a) Temperature dependence of the Raman frequency for the active E_2 mode in GaN still attached to the substrates (Δ) and free-standing GaN (O) respectively. (b) Temperature dependence of the Raman frequency for the active A_1(LO) mode in GaN still attached to the substrates (Δ) and free standing GaN (O), respectively. The solid curves give the best fitting using Eq. 7.06. 184

Figure 7.14: Layer information and spec of the AlGaN/GaN wafer. 185

Figure 7.15: (a) View of the complete mask (4" by 4") with various photolithographic layers. (b) View of the all lithography layers of mask superimposed into one single area equal to the sample size of 1.4 cm by 1.4 cm. (c) Partial view of the single V-shaped HFET embedded microcantievers device. (d) Partial view of the single tapered V-shaped heated microcantilevers. 187

Figure 7.16: Schematic diagram and optical images for MESA Etching. 188

Figure 7.17: Schematic diagram and optical images for top cantilever outlining. 190

Figure 7.18: Schematic diagram and optical images for Ohmic contact deposition. 191

Figure 7.19: Schematic diagram and optical image for Schottky Contacts (HFET embedded catilever). 192

Figure 7.20: Schematic diagram and optical image for probe contact. 193

Figure 7.21: Schematic diagram and optical images for back pocket etching............... 194

Figure 7.22: Basics of ICP Bosch process including a passivation and etching step. 195

Figure 7.23: Image of the auto diced cantilever samples after the last step (Bosch process) of dry etching. The samples are still mounted on the carrier wafer by Cool grease....... 196

Figure 7.24: Scanning Electron Microscopy images of fabricated AlGaN/GaN V shaped microcantilevers. (a) shows the tip of HFET embedded cantilever, whereas (b) the tapered shaped tip of the heated cantilever, (c) shows the HFET in one arm of the HFET embedded V cantilever, (d) the base of the heated cantilever and ohmic contact, (e) HFET embedded suspended V shaped cantilever and (f) suspended heated cantilever after through wafer etching. 197

Figure 7.25: TLM contact pads, before annealing and after annealing 200

Figure 7.26: The total resistance between contacts as a function of distance................. 200

Figure 7.27: Current flow of HFET embedded (a) V-shaped and (b) rectangular cantilever 201

Figure 7.28: (a) Optical micrograph image of fabricated AlGaN/GaN HFET embedded V shaped microcantilever, (b) SEM image of fabricated AlGaN/GaN HFET in one arm of the V cantilever. (c) Optical micrograph image of the HFET embedded rectangular microcantilever, and (d) the SEM image of the rectangular cantilever. 2032

Figure 7.29: (a), (c), (d) and (b), (d), (f) SEM images, family of curves and I_d-V_g plots for HFET embedded V-shaped cantilevers and rectangular cantilevers respectively. 203

Figure 7.30: Capacitance voltage profiling, (a) Capacitance per unit area versus applied dc bias on the Schottky contact, (b) Distribution of electron concentration as a function of depth.. 205

Figure 7.31: (a) Schematic diagram of the measurement setup for finding resonant frequency of V-shaped microcantilever using an optical transduction approach and capacitive coupling by a micropositioner needle.. 208

Figure 7.32: Experimental frequency response of the V-shaped AlGaN/GaN microcantilever 209

Figure 7.33: Experimental Setup for microcantilever static bending test....................... 211

Figure 7.34: Microcantilever bending test measurement... 211

Figure 7.35: Top view of a wire bonded chip containing arrays of cantilevers.............. 212

Figure 7.36: SEM image of a HFET embedded suspended cantilever showing source, drain and gate contacts... 213

Figure 7.37: (a) DC drain current transients with 10 µm upward bending applying zero gate bias. (b) DC drain current transients with 10 µm downward bending at V_G = -4 V. 213

Figure 7.38: (a)-(b) Experimental setup of Raman spectroscopy for measuring the temperature of tapered V shaped heated cantilever, (c) SEM image of a heated cantilever 215

Figure 7.39: (a) Typical Raman scattering of AlGaN/GaN free standing film and (b) Raman shift as a function of cantilever temperature.. 216

Figure 7.40: Heated microcantilever temperature as a function of the cantilever power, measured using Raman spectroscopy, where the temperature is based on Stokes peak position... 218

Figure 7.41: (a) Temperatures at three specific locations with the cantilever power of 7 mW based on Stokes peak position. 219

Figure 7.42: (a) SEM image of the tip of the heated micro cantilever and (b) resistance depending upon the voltage level V where square pulses of 2 ms duration are applied to the cantilever. With higher V, the cantilever resistance and generated power increase, reach the maximum, and then decrease until the cantilever reaches steady state.. Heated cantilevers can reach approximately 700˚C within 500µs. 221

Figure 7.43: V-shaped heated cantilever temperature profiling with dissipated power. 222

Figure 7.44: (a) Sensing of different Volatile Organic Compounds (VOCs) at the fixed voltage of 35V and (b) nature of sensing for different VOCs with different voltages (dissipated power). 223

Figure 8.1: V-shaped nanocantilever array and functionalization layer coating. 227

Figure 8.2: Redefined T-gates for the second generation of HFET embedded V-shaped microcantilevers for complete channel turn off, maximum gate modulation. 230

CHAPTER 1

AIM OF DISSERTATION

This first chapter provides the reader a brief introduction to the dissertation "III-V nitride micro- and nano-scale cantilevers for multimodal sensing applications". The aim of the dissertation would be to develop molecular sensors for the detection of various Chemical Warefare Agents and Environment Pollutants. An outline of the dissertation is presented here.

.

1.1 Project scope

Driven by the need for next generation nanoscale technologies for the highly sensititve and multifunctional detection of analyte molecules in atmospheric conditions and investigation of electrical signal propagation in neurons a project was initiated titled “InN nanowire based multifunctional nanocantilever sensors” which was funded by National Science Foundation. This project was combined with another project titled “Remote detection using microcantilever based sensor” which was also funded by National Science Foundation to study the sensing behavior in both micro- and nano-scale. The goal of the project is to develop chip base micro- and nano-scale devices for the detection of various analytes incorporating the multimodal sensing mechanism using III-V nitride materials.

1.2 The research partners

Microelectronics Research Center, Georgia Institute of Technology, Atlanta, GA

- Design and development of AlGaN/GaN V-Shaped microcantilever based sensors by creating deep trench with anisotropic etching (ICP).

University of South Carolina, Columbia, SC

- Growth of InN nanowires using Chemical Vapor Deposition.
- Investigating the structural and electronic properties of InN nanowires using SEM, TEM, EDX, XRD and Scanning Probe Microscopy.
- Study of the electrical properties of InN nanowire based devices.
- Development of InN nanowire based V shaped nanocantilever.

National Institute of Standards and Technology, Gaithersburg, MD

- Development of InN nanowire based nanoheaters, nanoresonators by Focused Ion beam technique.

1.3 Dissertation Aim

1) Synthesis of high quality InN NWs, and the growth optimization for coplanar, small diameter and long NWs suitable for novel nanoscale devices.
2) Development of novel V-shaped nanocantilever devices for sensing applications.
3) Design, development, characterization and sensing of novel V-shaped AlGaN/GaN microcantilevers.

1.4 Outline of the dissertation

While organizing the chapters, attempts have been made to integrate relevant important topics in individual chapters. The dissertation is aimed to the development of micro and nanoscale cantilevers for multifunctional detection of analyte molecules. Thus the dissertation is virtually divided in to two major parts: *the InN NW based nanocantilevers*, presented in Chapter 4 and Chapter 5 and the *AlGaN/GaN based microcantilevers* discussed in Chapter 6 and Chapter 7.

The dissertation starts (Chapter 2) with an introduction to chemical sensors: the definition of chemical sensors, their classifications and state of the art applications. In this dissertation we will primarily emphasize on the development of micro and nano scale chemical sensors for detection of *Chemical Warefare Agents* and *Environmental Pollutants*. Hence, chemical sensors and reagents for environmental monitoring and homeland security are described.

Chapter 3 exclusively focuses on the details of *cantilever sensors and multimodal detection techniques*, covered in both the domains: microcantilevers and nanocantilevers. Current status and review of microcantilever and nanocantilever based detection is presented here. Also the physics of cantilevers, modes of operation, different transduction methods, molecular adsorption mechanism, and techniques for microcantilever functionalization are discussed.

Introduction to semiconductor nanowires (NWs), Indium Nitride and InN NWs are presented at the beginning of Chapter 4. Then the NW synthesis process, structural characterization of the NWs and the growth optimization follows on. The role of oxygen during the growth and the growth direction modulation, two of the most important aspects of this work based on InN NWs, are explained thoroughly. Lastly electrical characterization of the NWs to investigate the material properties is presented where we will demonstrate another important feature of the InN NW based research in our lab, the diameter dependent mobility.

Chapter 5 is dedicated to the development of the InN NW based V-shaped Nanocantilevers (VNCs). This chapter presents a brief introduction to the current status and challenges of nanocantilever fabrication from literature at the beginning. Then the fabrication and characterization of InN NEMS resonators towards the development of VNC is discussed. The challenges and pitfalls have been accounted and the detail fabrication steps for VNCs are explained at the last part. Through theoretical modeling and analysis we have also predicted the mechanical properties and noise sensitivity of the VNCs. The sensing methodologies are discussed as well in this chapter.

Chapter 6 describes the theoretical framework of the GaN material system including crystal structure and polarization effects and the origin of the Two Dimensional Electron Gas (2DEG).

Based on the description of the AlGaN/GaN 2DEG the key topics of microcantilevers are discussed in Chapter 7. In the first part of this chapter design, theoretical calculations and simulations are presented. We fabricated AlGaN/GaN based V-shaped microcantilevers using photolithographic technique. The second part of the chapter briefly discusses the details of the fabrication steps and related issues. Later, we present all the experimental measurements performed on our fabricated microcantilevers. Some sensing characteristics of the microcantilever is presented and analyzed at the last part.

Chapter 8 summarizes all the major contributions of this work to the research community. Also in this chapter we propose future extension of this work and further development.

CHAPTER 2

INTRODUCTION & MOTIVATION

This chapter gives a short introduction to chemical sensors. A brief introduction to currently available chemical sensors and the challenges, their classifications and state of the art applications are presented here. Chemical sensors for the detection of Chemical Warfare Agents and Environmental Pollutants are emphasized in the application part.

2.1 Introduction

Detection of small quantities of molecules is of significant interest for numerous numbers of applications, ranging from gas sensing and environmental monitoring to biological and medical diagnostics. These require the sensors to be inexpensive, power efficient, easily deployable and miniaturized, yet sensitive enough to detect molecules down to the single-molecule level. With the advancement of miniaturization technologies molecular sensors are getting smaller and smaller in dimensions. Miniaturization is also essential for *in vivo* physiological monitoring, sensor portability and minimized sample volumes. Conventional molecular sensors suffer from extensive packaging, complex electronic interfacing and regular maintenance, the use of novel Microlectromechanical systems (MEMS) devices that integrate electronics and micro-mechanical structures on chip could address all those drawbacks.

Microcantilevers are the most simplified MEMS based devices. Diverse applications of microcantilevers in the field of sensors have been explored by many researchers. These sensors have several advantages over the conventional techniques in terms of high sensitivity, low cost, simple procedure, non-hazardous procedures and quick response. Moreover, the technology has been developed in the last few years for the fabrication and use of ***Nanocantilevers*** for sensing applications, thereby giving rise to ***Nanoelectromechanical systems (NEMS).*** This development has increased the sensitivity limit up to the extent that researchers have now started visualizing the counting of molecules.

A molecular sensor is usually evaluated with respect to three major aspects: 1) sensitivity, 2) selectivity, and 3) miniaturization. An ideal sensor should have high sensitivity towards targeting chemicals, excellent selectivity to a specific signal of interest, and a very small dimension.

In this work we are proposing molecular sensors that will be made of novel V-shaped micro- and nano-cantilevers, in the form of arrays in a chip. Due to their reduced dimension, micro and nano scale, many of the individual cantilevers can be integrated together in a chip, thus the final device is ***miniaturized***.

Particles that are smaller than the characteristic lengths associated with the specific phenomena often display new chemistry and new physics that lead to new properties that depend on size. The analyte molecules and the sensing elements are of comparable size for microcantilever based sensing which promotes better sensitivity. Again in the case of nanoscale sensors the size of the structure is reduced further, surface to volume ratio increases considerably and the surface phenomena predominate over the chemistry and physics in the bulk. This enhances the ***sensitivity*** even more since the molecular interaction or sensing occurs at the surface.

The careful selection of superior material quality confirms the fast response. ***InN nanowires***, which have been investigated only in the last few years, exhibit such superior material properties in terms of sensing including high carrier density, high electron mobility, surface charge accumulation and chemical inertness. On the other hand ***AlGaN/GaN heterostructures*** contain a highly conductive two-dimensional electron gas (2DEG) at the interface, which is sensitive to mechanical load, as well as to chemical modification of the surface, and can be used for novel sensing principles and as

transducers for MEMS applications. The ***selectivity*** of the sensor is improved by the ***multimodal detection*** technique apart from the nature of the gas molecules themselves. In multimodal detection technique independent parameters can be independently measured and while they are combined together a unique signature for any particular molecule is obtained.

2.2 Chemical sensor arrays

A chemical sensor is a device that transforms chemical information, ranging from the concentration of a specific sample component to total composition analysis, into an analytically useful signal. The chemical information, mentioned above, may originate from a chemical reaction of the analyte or from a physical property of the system investigated.

A physical sensor is a device that provides information about a physical property of the system. A chemical sensor is an essential component of an ***analyzer.*** In addition to the sensor, the analyzer may contain devices that perform the following functions: sampling, sample transport, signal processing, data processing. An analyzer may be an essential part of an automated system. The analyzer working according to a sampling plan as a function of time acts as a monitor.

Chemical sensors contain two basic functional units: a receptor part and a transducer part. Some sensors may include a separator which is, for example, a membrane. In the ***recepror*** part of a sensor the chemical information is transformed into a form of energy which may be measured by the transducer.

The ***transducer*** part is a device capable of transforming the energy carrying the chemical information about the sample into a useful analytical signal. The transducer as such does not show selectivity.

The receptor part of chemical sensors may be based upon various principles:

- Physical, where no chemical reaction takes place. Typical examples are those based upon measurement of absorbance, refractive index, conductivity, temperature or mass change.
- Chemical, in which a chemical reaction with participation of the analyte gives rise to the analytical signal.
- Biochemical, in which a biochemical process is the source of the analytical signal. Typical examples are microbial potentiometric sensors or immunosensors. They may be regarded as a subgroup of the chemical ones. Such sensors are called ***biosensors.***

In some cases it is not possible to decide unequivocally whether a sensor operates on a chemical or on a physical principle. This is, for example, the case when the signal is due to an adsorption process.

Sensors are normally designed to operate under well defined conditions for specified analytes in certain sample types. Therefore, it is not always necessary that a sensor responds specifically to a certain analyte. Under carefully controlled operating conditions, the analyte signal may be independent of other sample components, thus allowing the determination of the analyte without any major preliminary treatment of the sample. Otherwise unspecific but satisfactory reproducible sensors can be used in series

for multicomponent analysis using a multivariate calibration software and signal processing. Such systems for multicomponent analysis are called sensor arrays.

2.3 Classification of sensors

The development of instrumentation, microelectronics and computers makes it possible to design sensors utilizing most of the known chemical, physical and biological principles that have been used in chemistry.

Chemical sensors may be classified according to the operating principle of the transducer:

1. ***Optical devices*** transform changes of optical phenomena, which are the result of an interaction of the analyte with the receptor part. This group may be further subdivided according to the type of optical properties which have been applied in chemical sensors:

   a) Absorbance, measured in a transparent medium, caused by the absorptivity of the analyte itself or by a reaction with some suitable indicator.

   b) Reflectance is measured in non-transparent media, usually using an immobilized indicator.

   c) Luminescence, based on the measurement of the intensity of light emitted by a chemical reaction in the receptor system.

   d) Fluorescence, measured as the positive emission effect caused by irradiation. Also, selective quenching of fluorescence may be the basis of such devices.

   e) Refractive index, measured as the result of a change in solution composition. This may include also a surface plasmon resonance effect.

f) Optothermal effect, based on a measurement of the thermal effect caused by light absorption.

g) Light scattering, based on effects caused by particles of definite size present in the sample.

2. ***Electrochemical devices*** transform the effect of the electrochemical interaction analyte – electrode into a useful signal. Such effects may be stimulated electrically or may result in a spontaneous interaction at the zero-current condition. The following subgroups may be distinguished:

a) Voltammetric sensors, including amperometric devices, in which current is measured in the d.c. or a.c. mode. This subgroup may include sensors based on chemically inert electrodes, chemically active electrodes and modified electrodes. In this group are included sensors with and without (galvanic sensors) external current source.

b) Potentiometric sensors, in which the potential of the indicator electrode (ion-selective electrode, redox electrode, metaVmeta1 oxide electrode) is measured against a reference electrode.

c) Chemically sensitized field effect transistor (CHEMFET) in which the effect of the interaction between the analyte and the active coating is transformed into a change of the source-drain current. The interactions between the analyte and the coating are, from the chemical point of view, similar to those found in potentiometric ion-selective sensors.

d) Potentiometric solid electrolyte gas sensors, differing from class 2(b) because they work in high temperature solid electrolytes and are usually applied for gas sensing measurements.

3. *Electrical devices* based on measurements, where no electrochemical processes take place, but the signal arises from the change of electrical properties caused by the interaction of the analyte.

a) Metal oxide semiconductor sensors used principally as gas phase detectors, based on reversible redox processes of analyte gas components.

b) Organic semiconductor sensors, based on the formation of charge transfer complexes, which modify the charge carrier density.

c) Electrolytic conductivity sensors.

d) Electric permittivity sensors.

4. ***Mass sensitive devices*** transform the mass change at a specially modified surface into a change of a property of the support material. The mass change is caused by accumulation of the analyte.

a) Piezoelectric devices used mainly in gaseous phase, but also in solutions, are based on the measurement the frequency change of the quartz oscillator plate caused by adsorption of a mass of the analyte at the oscillator.

b) Surface acoustic wave devices depend on the modification of the propagation velocity of a generated acoustical wave affected by the deposition of a definite mass of the analyte.

5. ***Magnetic devices*** based on the change of paramagnetic properties of a gas being analysed. These are represented by certain types of oxygen monitors.

6. ***Thermometric devices*** based on the measurement of the heat effects of a specific chemical reaction or adsorption which involve the analyte. In this group the heat effects may be measured in various ways, for example in the so called catalytic sensors the heat of a combustion reaction or an enzymatic reaction is measured by use of a thermistor. The devices based on measuring optothermal effects can alternatively be included in this group.

This classification represents one of the possible alternatives. Sensors have, for example, been classified not according to the primary effect but to the method used for measuring the effect. As an example can be given the so-called catalytic devices in which the heat effect evolved in the primary process is measured by the change in the conductivity of a thermistor. Also, the electrical devices are often put into one category together with the electrochemical devices.

Sensors have also been classified according to the application to detect or determine a given analyte. Examples are sensors for pH, for metal ions or for determing oxygen or other gases. Another basis for the classification of chemical sensors may be according to the mode of application, for example sensors intended for use in vivo, or sensors for process monitoring and so on. It is, of course, possible to use various classifications as long as they are based on clearly defined and logically arranged principles.

The biosensors are not presented as a special class because the process on which they are based is, in general, common to chemical sensors. They may be also

differentiated according to the biological elements used in the receptor. Those may be: organisms, tissues, cells, organelles, membranes, enzymes, antibodies, etc. The biosensors may have several enzymatic systems coupled which serve for amplification of the signal.

2.4 Applications of chemical sensors

Figure 2.1 shows various applications of chemical sensors including monitoring automobile emission gasses, medical diagnosis, industrial control, national security, indoor air quality control, and environmental evaluation.

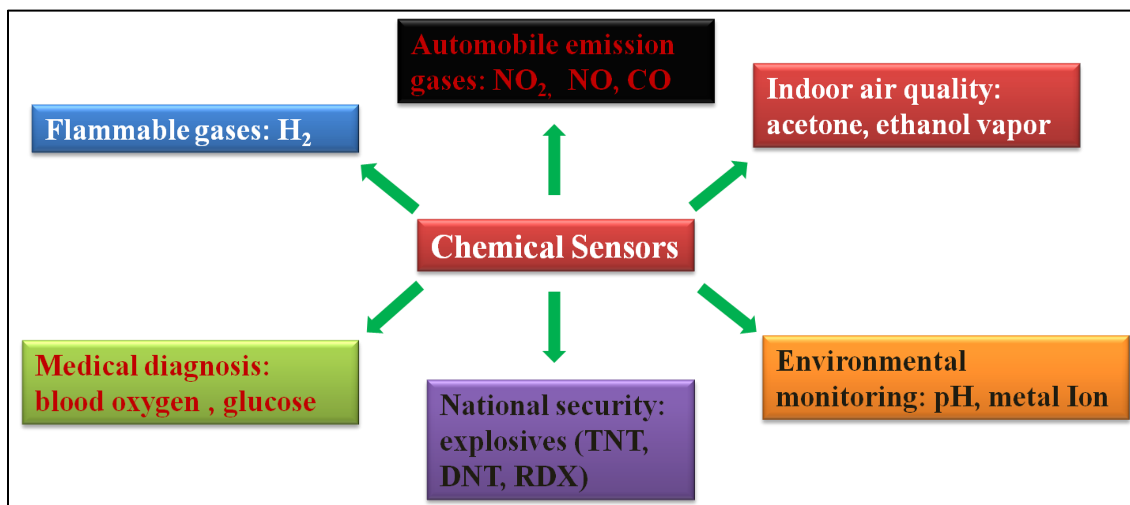

Figure 2.1: Various applications of chemical sensors

The regulation on ***automobile emission*** usually involves toxic gases such as nitrogen oxide (NOx), carbon monoxide (CO), or volatile hydrocarbons.

A ***general medical*** examination requires measuring these substances in human body such as glucose, blood oxygen, and cholesterol, which lead to determine possible disease or disorder of a patient.

In a research lab or industrial factory, it is extremely important to prevent accidents from leakage of ***flammable gases such as H_2***, thus the concentration of H_2 on working sites needs to be monitored in real-time.

There are ***indoor air pollutants*** such as ***volatile organic compounds*** (VOCs) including acetone, ethanol and isopropanol. These organic compounds are widely used as ingredients in household products and extensive exposure to these VOCs can lead to disorder, sickness or even death [1].

Particularly, there have been significant increasing technical demands on indentifying ***explosive chemicals*** due to challenges of anti-terrorism worldwide. Sensors are required to be deployed at public transport station, plaza, schools, and commercial buildings to detect trace amount of explosive molecule such as TNT, DNT, and RDX [2]. Apart from explosive chemicals, recently in last few decades there have been several incidents of the use of ***CWAs*** (mustard gas, sarin, etc.) around the world that killed thousands of lives and threatened the whole civilization [3]. These incidents worldwide highlight the importance of having a continuous detection and monitoring of these kinds of chemical agents and explosives for both defense and homeland security.

2.4.1 Chemical Sensors for Environmental Monitoring

Chemical sensors are expected to play a critical role in environmental monitoring (both indoor and outdoor) and environmental control (air, water), facilitating a better

quality of life. The projected increase in global energy usage and unwanted release of pollutants has led to a serious focus on advanced monitoring technologies for environmental protection, remediation, and restoration. In a recent study, the World Health Organization (WHO) reported that over 3 million people die each year from the effects of air pollution. Furthermore, reports from World Energy Congress (WEC) suggest that if the world continues to use fuels reserves at the current rate, the environmental pollution in 2025 will create irreversible environmental damage. Long-term exposure to air pollution provokes inflammation, accelerates atherosclerosis, and alters cardiac function. Within the general population, medical studies suggest that inhaling particulate matter (PM) is associated with increased mortality rates which are further magnified for people suffering from diabetes, chronic pulmonary diseases, and inflammatory diseases. Pollution, in general is contamination that renders part of the environment unfit for intended or desired use. Natural processes release toxic chemicals into the environment as a result of ongoing industrialization and urbanization. Major contributors to large-scale pollution crisis are deforestation, polluted rivers, and contaminated soils. Other sources of pollution include emissions from iron and steel mills; zinc, lead, and copper smelters; municipal incinerators; oil refineries; cement plants; and nitric and sulphuric acid producing industries. Of the group of pollutants that contaminate urban air, nitrous oxide (NOx), fine suspended PM, sulphur dioxide (SO2), and ozone pose the most widespread and acute risks. Recent studies on the effects of chronic exposure to air pollution have singled out PM suspended in smog (NOx) and volatile organic compounds (VOCs) as the pollutant most responsible for life-shortening respiratory and associated health disorders. Since the Clean Air Act was adopted in 1970,

great strides have been made in the U.S. in reducing many harmful pollutants from air, such as SO2. Levels of NOx, however, have increased by 20% over the last 30 years. Sources of NOx include passenger vehicles, industrial facilities, construction equipment and railroads, but of the 25 million tons of NOx discharged annually in the U.S., 21% of that amount is generated by power plants alone, resulting in rising threats to the health of the general population. Furthermore, the SCanning Imaging Absorption SpectroMeter for Atmospheric CHartographY (SCIAMACHY) shows rapid increase in NOx columns worldwide, especially during 2003–2006.

Rapid detection of contaminants in the environment by emerging technologies is of paramount significance. Environmental pollution in developing countries has reached an alarming level thus necessitating deployment of real-time pollution monitoring sensors, sensor networks, and real-time monitoring devices and stations to gain a thorough understanding of cause and effect. A tool providing interactive qualitative and quantitative information about pollution is essential for policy makers to protect massive populations, especially in developing countries.

2.4.2 Chemical Sensors for Homeland Security

2.4.2.1 Chemical warfare agents (CWA)

A United Nations report dated 1969 defines chemical warfare agents (CWA) as "... chemical substances, whether gaseous, liquid or solid, which might be employed because of their direct toxic effects on man, animals and plants ...".

The Chemical Weapons Convention defines chemical weapons as including not only toxic chemicals but also ammunition and equipment for their dispersal. Toxic

chemicals are stated to be "... any chemical which, through its chemical effect on living processes, may cause death, temporary loss of performance, or permanent injury to people and animals".

In order to be considered a CWA the following must be satisfied:

- The presumptive agent must not only be highly toxic but also "suitably highly toxic" so that it is not too difficult to handle.
- The substance must be capable of being stored for long periods in containers without degradation and without corroding the packaging material.
- It must be relatively resistant to atmospheric water and oxygen so that it does not lose effect when dispersed.
- It must withstand the heat developed when dispersed.

The first nerve gas was invented by the Germans; it is odorless and colorless and attacks the body muscles, including the involuntary muscles. The gases classified as chemical warfare agents are characterized by poisonous or corrosive nature. These gases can be categorized according to the portal of entry into the body and their physiological effects:

1. Vesicants or blister gases- these produce blisters on all body surfaces. Examples include lewsite and mustard gas. About 10 milligrams of mustard gas in the lungs will kill a person.
2. Lacrimators such as tear gas produce severe eye irritation;
3. Sternutators also called vomiting gases cause nausea;

4. Nerve Gases inhibit proper nerve function;

5. Lung irritants which attack the respiratory tract, causing pulmonary edema.

2.4.2.2 Nerve Agents

Nerve agents affect the transmission of nerve impulses within the nervous system. They belong to the compound group known as organo-phosphorous compounds (OP). OP compounds are stable, easily dispersed, highly toxic and have rapid effect. In their pure state they are colorless liquids with varying volatiles. Nerve agents enter the body through inhalation or through the skin, the port being important for determining the time the agent takes effect. Since nerve agents are fat-soluble they can penetrate the outer layers of the skin so it takes some time before the poison reaches the blood vessels. On the other hand when it enters through the respiratory system the effect is rapid since the lungs contain numerous more blood vessels facilitating rapid assimilation and transportation to the key organs.

Nerve agents include physostigmine (reversible) and organophosphorus (irreversible) cholinesterase inhibitors, which disable enzymes responsible for the transmission of nerve impulses. Initial incapacitating effects of organophosphorus agents occur within 1-10 minutes of exposure, and death occurs within 15 minutes for Tabun, Sarin, and Soman and from 4-42 hours for VX.

Some nerve agents include: Tabun (NATO military designation, GA), Sarin (NATO military designation, GB), Soman (NATO military designation, GD), GF (Cyclohexyl methylphosphonofluoridate), VX (Methylphosphonothioic acid S-(2-(bis(1-methylethyl)amino)ethyl) O-ethyl ester), GE (Phosphonofluoridic acid, ethyl-, isopropyl

ester), VE (Phosphonothioic acid, ethyl-, S-(2-(diethylamino)ethyl) O-ethyl ester), VG (Amiton), VM (Phosphonothioic acid, methyl-, S-(2-(diethylamino)ethyl) O-ethyl ester), etc.

2.4.2.3 Blister/Vesicant Agents

Vesicant agents cause blisters on skin and damage the eyes, mucous membranes, respiratory tract, and internal organs. Through chemical processes, mustard agents destroy different substances within cells of living tissue. Initial effects are somewhat delayed for mustards, occurring 12 to 24 hours after exposure, but are rapid for other agents. Symptoms are variable and acute mortality is low, but death can occur from complications after lung injury.

Some blister agents include: Lewisite (L), Mustard-Lewisite (HL), Nitrogen mustards (HN-1,HN-2, HN-3), Phosgene oxime (CX), Sulfur mustards (H, HD, HT).

2.4.2.4 Blood Agents

Agents are highly volatile, but rapidly acting agents that cause seizures, respiratory failure, and cardiac arrest through interference with absorption of oxygen into the bloodstream.

Some blood agents include: Cyanogen chloride (CK), Hydrogen cyanide (AC)

2.4.2.5 Pulmonary Agents

Such agents are liquids dispersed in a gaseous form that damage the respiratory tract and cause severe pulmonary edema in about four hours, leading to eventual death. Effects are variable, and can be rapid or delayed depending on the specific agent.

Some pulmonary agents include: Chlorine, Chloropicrin (PS), Diphosgene (DP), Phosgene (CG).

Chemical warfare was first used effectively in World War I, when the Germans released chlorine gas against the Allies. Later in the War they used mustard gas. Soon both sides were using chemical warfare extensively leading to the introduction of gas masks. The fear of the detrimental effects of chemical warfare caused many countries to abstain from using it and except for the use of poison gas by the Italians in the war against Ethiopia (1935-36) and by the Japanese against Chinese guerrillas (1937-42), chemical warfare was not employed after World War I. This is not to say however, that the military powers of the world did not continue to develop new gases.

It is well known that chemical warfare was used in the Iran-Iraq War. In fact, Iraq has used poison gas on its own civilians, in particular the Kurds. In the Persian Gulf War, the UN troops were equipped with antidotes for nerve gas, protective clothing, and gas masks in case Iraq used poison gas. Then there was the release of sarin in a Tokyo subway station in 1995.

2.4.2.6 Explosives detection

The Intelligence Reform and Terrorism Prevention Act of 2004 (P.L. 108-458) directed the U.S. Department of Homeland Security (DHS) to place high priority on developing and deploying passenger explosives screening equipment. The illicit use of explosives has become a daily event in the modern world. For terrorist organizations and insurgents, the Improvised Explosive Device (IED) has become a weapon of choice. These devices are being used to kill or harm civilians and military personnel as well as destroy vital infrastructure and assets. Because they can take different forms and be

delivered to their targets in a variety of ways, these devices are proving difficult to overcome.

CHAPTER 3

CANTILEVER SENSORS

Review of microcantilever and nanocantilever based detection, current status and their various aspects including miniaturization, sensitivity, and selectivity, with special emphasis on Multimodal detection mechanism are presented here. The physics of cantilevers, modes of operation, different transduction methods, molecular adsorption mechanism, and techniques for microcantilever functionalization are also discussed.

3.1 Cantilever sensors

A single supported beam, known as a cantilever, is a basic mechanical structure with well described strain and bending characteristics [4]. These two aspects, strain and bending, are the bases of most cantilever applications in static sensing. Moreover, a cantilever can be described as a second-order system with distinct resonance characteristics determined by the cantilever mass and spring constant as well as by the ambient conditions [5]. Therefore, any changes in these parameters will be reflected as a variation in the resonance characteristics. This characteristic makes the cantilever a prominent choice for dynamic sensing applications [6-10]. Extensively used as building blocks in civil and aeronautical structures, cantilevers were first introduced in the sensors realm as strain gauges [11, 12]. Despite earlier applications as microphones [13], pressure sensors [14], and accelerometers [15, 16], it was the invention of the atomic force microscopy (AFM) [17] that gave a robust commercial momentum to cantilever-based sensors. Also, it was upon the development of AFM that the potential of the cantilever as a dynamic sensor was explored [17-20]. Within a very short period of time, atomic resolution was attained [21], and the atomic force microscope is now one of the most important tools in nanoscience [22, 23]. Perhaps equally important is that the advent of AFM has led to the growth of the wider field of cantilever-based sensing, including a wide range of scanning probe microscopies (SPM), and many different forms of static (that is, non-scanned) sensing. Today's SPM can be used to image local forces arising from magnetic and magnetic resonance interactions; forces from local electrostatics, surface potentials, surface temperatures, and chemical bonding; and forces from many other local origins. Similarly, applications for non-scanned microcantilever sensors are equally diverse,

including infrared imaging, nanocalorimetry, vapour- and liquid-phase chemisensing, electrometry, mass detection and many others [24-26]]. At microscale dimensions the practical upper limit to fundamental-mode cantilever resonant frequencies is generally of the order of several megahertz [27]. For SPM this imposes a substantial limitation upon scan rate, which directly determines the speed at which images can be acquired. Moreover, the standard approaches used to make microelectromechanical systems (MEMS) cannot provide access to the nanoscale, where very large improvements in sensitivity can be attained [28]. Recent demonstrations and applications of the unprecedented sensitivity available from nanoelectromechanical (NEMS) devices include milestones such as sub single-charge electrometry [29], singleelectron- spin paramagnetic resonance [30], zeptogram-scale mass sensing [31], zeptonewton-scale force sensing [32] and subfemtometre displacement sensing [33]. In fact, with these continuing advances, NEMS sensors are rapidly converging towards the ultimate, quantum limits of force and displacement detection [34].

The field of microcantilever sensors has been extensively developed in recent years [35-40]. The main topics covered in the recent publications include the following: detection of vapors and volatile compounds (e.g., HF vapor) using individual microcantilevers operated in beam deflection static mode [41-44]; gas-phase sensing applications for solvents using piezo-resistive cantilevers [45-55]; biochemical applications in static mode in liquids [56-58] (e.g., as a glucose sensor); and C-reactive protein detection using dynamic-mode piezo-resistive microcantilevers [59, 60]. Several efforts have investigated the usability of microcantilever sensors as detectors for explosives [61-63] or *Escherichia Coli* bacteria [64, 65]. A pH sensor using hydrogel

coatings [66, 67] has been suggested, as has the observation of electrochemical redox reactions using microcantilevers [68]. The theory of molecule adsorption on cantilevers has been investigated in several publications [69-73], whereas the bending, calibration, and curvature of cantilevers has been studied experimentally [74-76]. A new strategy to grow polymer brushes on the surface of microcantilevers has been proposed [77]. Others have described the production of polymer microcantilevers [78]. Torsional or lateral resonance modes could also be exploited for improved mass sensing in dynamic mode [79, 80]. Nanowire electrodes attached to cantilevers in an array could be used for local multiprobe resistivity measurements [81], and two-dimensional microcantilever arrays have been suggested for multiplexed biomolecular analysis [82]. Chemical sensor applications of resonant cantilevers have included humidity sensors [83, 84] or the detection of mercury vapours [85]. Complementary metal oxide semiconductor (CMOS) cantilevers coated with chemically sensitive polymers have previously been used for the detection of volatile organic compounds [83, 86-90]. A miniaturized system with an array of coated cantilevers for the simultaneous detection of hydrogen and mercury vapours was reported in [91]. Quantitative detection of the components of a binary mixture was demonstrated by ETH group (Switzerland) and by Kim et al. [92]. Cantilevers can be included in application-specific chemical sensor systems [86] along with other types of CMOS-based microtransducers such as capacitors [93, 94] or microcalorimeters [95].

In contrast to microcantilevers, NEMS based naocantilever devices/sensors are still largely pursued only within the province of specialists. A current barrier to their practical development and widespread use is the difficulty of fabricating ultrasmall

mechanical devices and also the successful realization of NEMS achieving sensitive displacement transduction at the nanoscale.

Miniaturization of the cantilever usually acts favorably in increasing the fore and mass sensitivity, since the mass of the cantilever is greatly reduced by the reduction of size. Around 1992, H. Rohrer, N. Garcia, and Vu Thien Binh proposed the use of a metal nanocantilever as a force sensor in AFM [96]. The cantilever was produced by heating a sharp metal tip in a vacuum to induce surface diffusion and formation of a head and a filiform neck. The phenomena was calculated by F. Nicols and W.W. Mullins [97] and demonstrated by Vu Thien Binh and M. Dreschler [98-100]. A feasibility study of using the thermally fabricated nanocantilever was pursued by a number of groups. A mechanical nanosensor in the gigahertz range was proposed in early 1994, which was the 1st realization of ultrahigh frequency NEMS based nanocantilevers [101]. In 1999 Japanese scientists at Institute of Industrial Science, University of Tokyo led by D. Saya, [102] introduced a fabrication method of nanocantilevers by anisotropic etching of silicon by KOH. Well defined single-crystal silicon nanocantilevers were fabricated with lengths of 100 nm to a few mm, with natural frequencies ranging from 1 MHz to 1 GHz [103]. Thundat *et al* from Oak Ridge National Laboratory described micromachined silicon nanocantilevers of 0.5 to 4 microns in length fabricated with the use of a focused ion beam (FIB) at 2002 [104]. Nanocantilevers from nanostructures were first demonstrated by Zhong L. Wang at the Georgia Institute of Technology at 2003 [105]. Their group used long ribbon-like synthesized nanostructures of semiconducting oxides and sulfides, such as, CdO, ZnO, Ga_2O_3 , PbO_2, In_2O_3 , SnO_2 , and ZnS [106-107]. Nanobelts are single crystals with specific oriented surfaces. The rectangular cross section, uniform

thickness, and ribbon (belt) like morphology make nanobelts an ideal candidate for cantilever applications [107]. The development of nanocantilever arrays for the early detection of precancerous and malignant lesions from biological fluids for the fight against cancer was first proposed by Mauro Ferrari at 2005 [108]. Before that large-scale fabrication and characterization of nanocantilever arrays using Cd-doped ZnO were reported by Shao-Min Zhou *et al* [109].

Recently, nanocantilevers of 90 nm thick and made of silicon nitride, have been used by the group of researchers led by Harold Craighead, Cornell University to detect a single piece of DNA 1578 base pairs in length [110]. The group claimed that they can accurately determine a molecule with mass of about 0.23 attograms (1 attogram = 10^{-18} gram) employing these nanocantilevers. The researchers placed nanoscale gold dots at the very ends of the cantilevers, which acted as capture agents for sulfide-modified double-stranded DNA. But in principle, gold nanodots could be used to capture any biomolecule having a free sulfide group. Scanning laser beams were used to measure the vibrational frequency of the cantilevers. The researchers believe that nanodevices based on nanocantilevers would eliminate the need for PCR amplification for the detection of defined DNA sequences, thereby simplifying methods used to screen for specific gene sequences and mutations.

Similarly, N. Nelson-Fitzpatrick *et al*. [111] at the University of Alberta, Canada have made ultra thin resonant nanocantilevers, of the order of 10 nm, in aluminum-molybdenum composites. The group claims that the development of NEMS-based devices in metallic materials would enable new areas of applications for the direct

sensing of various chemical compounds thus obviating the need of intermediate surface derivatization.

Researchers at Purdue University are involved in the creation of nanocantilevers. They employed an array of nanocantilevers of varying length with thickness of about 30 nm and functionalized them with antibodies for viruses [112]. They came up with very interesting results pertaining to the variation in antibody density with respect to the length of nanocantilevers.

Besides the aforementioned groups, the development of nanocantilever-based bio and chemical sensors for has been conducted by various research groups from the University of California at Berkeley, Caltech, Oak Ridge National Laboratory, Cornell University, IBM Zurich Research Laboratory, and others during the past decade. Since these pioneering studies were performed, a growing number of research groups have joined this field, greatly expanding the scope of nanocantilever sensors. Thus, several review articles describing the diverse range of nanocantilever-based sensing applications have been published in major engineering, physics, chemistry, and biology journals.

3.2 Cantilever theory of operation

A cantilever beam is usually subjected to loads laterally or transversely to its axis, and is commonly used in structures and machines. In order to understand the mechanical behavior of the microcantilever as a cantilever beam, we briefly review cantilever beam theory. Bernoulli-Euler beam theory is the most commonly used for scientific and engineering problems because of its reasonable approximations and simplicity. The Bernoulli-Euler beam model has the following basic assumptions: [113]

- One dimension is larger than the other two
- The material is linear elastic
- The Poisson effect is negligible
- The cross-sectional area is symmetric so that the neutral and centroid axes coincide
- Planes perpendicular to the neutral axis remain perpendicular after deformation
- The angle of rotation is small so that the small angle assumption can be used

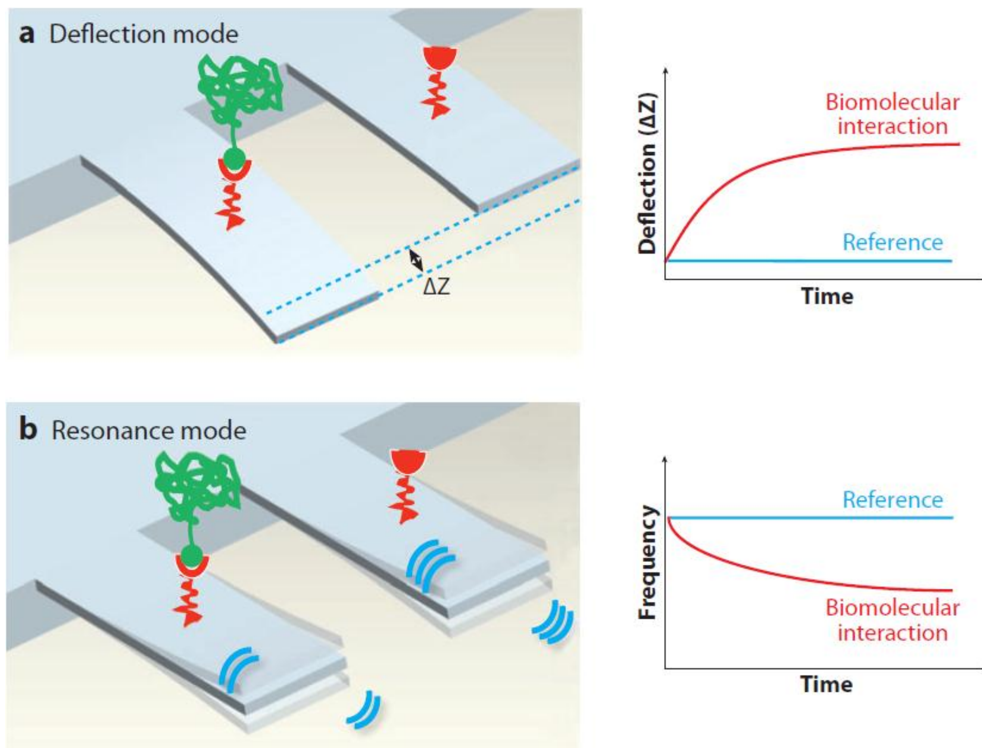

Figure 3.1: Two modes of cantilever-based biomolecule detection: (*a*) deflection mode and (*b*) resonance mode (Ref [113]).

Micro- and nanosized cantilevers are robust devices whose high sensitivity and selectivity allow them to detect physical, chemical, and biological components by measuring changes in cantilever bending or in resonant frequency. In this section, we briefly discuss two operational principles of cantilever-based biosensors: cantilever static bending (deflection mode) and cantilever vibration, i.e. shifts in resonant frequency (resonance or dynamic mode). Before that the characteristics of second-order systems are briefly reviewed.

3.2.1 Second-Order Systems

The motion of a cantilever resonator, as a lumped mass-spring system, can be described by the differential equation of a second-order system with constant coefficients [114]:

$$m\frac{d^2y}{dt^2} + B\frac{dy}{dt} + ky = F(\Omega t) \tag{3.01}$$

where $y(t)$ is the displacement of the lumped mass m, k is the spring constant, B is the velocity-related damping coefficient, and F is the excitation force applied on the lumped mass with an angular velocity of Ω. From the properties of the second-order system, the natural resonance frequency f_0 is calculated:

$$f_0 = \frac{\omega_0}{2\pi} = \frac{1}{2\pi}\sqrt{\frac{k}{m}} \tag{3.02}$$

where ω_o is the natural angular velocity (radial resonance frequency) of the system.

The quality factor (Q or Q-factor) of a damped system is defined as [115]

$$Q = 2\pi\frac{\text{stored vibration energy}}{\text{dissipated energy per cycle}} \tag{3.03}$$

In a second-order electrical system, the definition in Eq. (3.03) can be described in terms of the real and imaginary parts of impedance [116]:

$$Q = \frac{\mathrm{Im}(Z)}{\mathrm{Re}(Z)} \tag{3.04}$$

A second-order mechanical system is analogous to an electrical system by corresponding F and dy/dt to voltage V and current I, respectively. This way, Q is calculated as

$$Q = \frac{m\omega_0}{B} = \frac{k}{B\omega_0} = \frac{\sqrt{km}}{B} \tag{3.05}$$

The free vibration resonance angular velocity ωmax is given by [114]

$$\omega_{\max} = \omega_0 \sqrt{1 - \frac{1}{4Q^2}} \tag{3.06}$$

Excited by a sinusoidal force F, the vibration amplitude will be [114]

$$y(t) = \frac{\beta}{k} |F| \sin(\Omega t - \theta) \tag{3.07}$$

where $|F|$ is the maximum amplitude of the applied force, β is the magnification factor

$$\beta = \frac{1}{\sqrt{\left(1 - \frac{\Omega^2}{\omega_0^2}\right)^2 + \left(\frac{1\Omega}{Q\omega_0}\right)^2}} \tag{3.08}$$

and θ is the phase angle expressed as

$$\theta = \tan^{-1}\left(\frac{\Omega / \omega_0}{Q (1 - \Omega^2) / \omega_0^2} \right) \tag{3.09}$$

The forced vibration resonance angular velocity Ω*o* is given by

$$\Omega_0 = \omega_0 \sqrt{1 - \frac{1}{2Q^2}} \tag{3.10}$$

In the case of weak damping, or alternatively large Q, the resonance frequency can be closely approximated by Eq. (3.10); in other words, $\Omega o = \omega_o$ and $\omega_{max} = \omega_o$. The most common way to measure the Q-factor of a resonator is based on the half-power bandwidth $\Delta f\text{-}3dB$ in the resonance transfer function [117]:

$$Q = \frac{f_0}{\Delta f_{-3dB}} \tag{3.11}$$

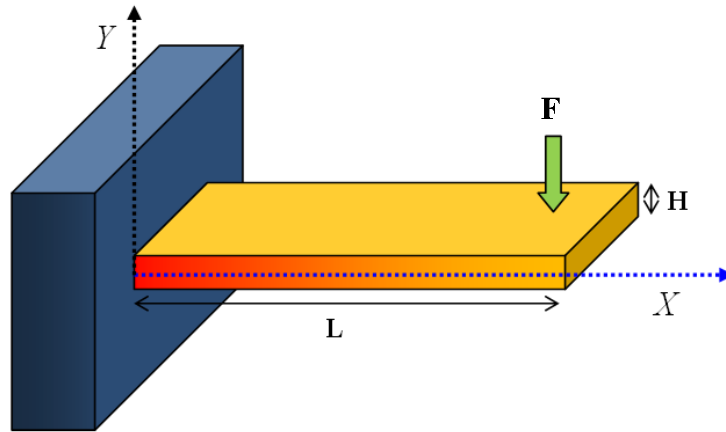

Figure 3.2: Schematic of a cantilever with length L and thickness H, with respect to coordinates X and Y, before being deflected by a point force F applied on the tip.

3.2.2 Cantilever Bending (Static mode)

The cantilever bending y as the result of applying a point force F on the beam free end (i.e., the tip – see Figure 3.2) is described at a point x along the cantilever length as [118]

$$y(x) = \frac{FL}{2EI} x^2 \left(1 - \frac{x}{3L}\right) \tag{3.12}$$

where E is the Young's modulus, I is the moment of inertia, and L is the beam length. Equation (3.12) is valid as long as the beam deflection is negligible compared to its length (i.e., y << L). Regarding Eq. (3.12), the cantilever spring constant, i.e., the ratio of force to deflection on the cantilever tip, can be calculated as

$$k = \frac{F}{y(L)} = \frac{3EI}{L^3} \tag{3.13}$$

In general, if the force is exerted at an arbitrary point *xf* on the cantilever, the bending will be [119]

$$y(x) = \frac{FL}{2EI} \times \begin{cases} \frac{x_f}{L} x^2 \left(1 - \frac{x}{3x_f}\right) & x \le x_f \\ 2\frac{x_f^2}{L}\left(\frac{x_f}{3} + \frac{x - x_f}{2}\right) & x_f \le x \le L \end{cases} \tag{3.14}$$

The moment of inertia for a rectangular cantilever beam is given as [1]

$$I = \frac{1}{12} W h^3 \tag{3.15}$$

where W and h are the width and length of the cantilever. The induced longitudinal stress on the cantilever is calculated as [120]

$$\sigma_x = z \frac{E}{\rho} \tag{3.16}$$

where z is the distance from the beam neutral axis, and ρ is the beam radius of curvature. For a point force F applied at the point x_f on a single-layer rectangular cantilever, the stress is

$$\sigma_x = \begin{cases} \frac{12(x_f - x)}{h^3 W} F \end{cases} \tag{3.17}$$

From Eq. (3.16) it can be seen that the maximum stress occurs on the cantilever surface. Also, from Eq. (3.17), the stress magnitude is the highest at the cantilever clamped end, and linearly decreases toward the tip. When a point force is applied at the tip, the magnitude of the longitudinal stress at point x is

$$\sigma_x = \frac{12(L-x)}{h^3 W} F \tag{3.18}$$

In a single-layer rectangular cantilever, where the neutral axis is located at the center of the beam, the maximum stress at point x is ($z = h/2$)

$$\sigma_x = \frac{6(L-x)}{h^3 W} F \tag{3.19}$$

On the other hand, considering Eqs. (3.13), (3.15), and (3.18), the induced stress resulting from a deflection $\Delta y = y(L)$ at the tip is

$$\sigma_x = \frac{3E(L-x)z}{L^3} \Delta y \tag{3.20}$$

and the maximum stress at point x is ($z = h/2$)

$$\sigma_x = \frac{3}{2} \frac{Eh(L-x)}{L^3} \Delta y \tag{3.21}$$

In assessing the performance of a cantilever in force sensing applications, an important figure is the cantilever's force spectral density $S_{F(f)}$, which is defined as the Fourier transform of the autocorrelation function of the fluctuating (time dependent) effective force on the cantilever tip [121]. The "force noise spectral density" is given by $(S_{F(f)})0.5$ (unit: N/Hz1/2), and the total root mean square force noise is the integral of force noise spectral density over the measurement bandwidth. In some literature the force noise spectral density is also called force sensitivity [121, 122]. Ideally, the noise performance

of the cantilever is limited to the sensor's thermomechanical noise [123, 124]; in this case $S_{F(f)}$ is calculated as (lumped-mass model)

$$S_F = 4k_B TB = 4k_B \, Tk / (2\pi Q f_0) \tag{3.22}$$

where k_B and T are the Boltzmann constant and temperature, respectively. As mentioned in Section 2.2.1, k, f_0, Q, and B are the cantilever's spring constant, resonance frequency, quality factor, and damping coefficient, respectively

3.2.3 Cantilever Vibration (Dynamic mode)

The equation of cantilever motion for flexural vibrations of an undamped system is given by [125]

$$EI \frac{\partial^4 y(x,t)}{\partial x^4} + \rho \mathrm{A} \frac{\partial^2 y(x,t)}{\partial t^2} = 0 \tag{3.23}$$

where ρ is the mass density and A is the cross-sectional area. Equation (2.23) is solved by assuming the possibility of separation of time and space:

$$y(x,t) = y(x) e^{i\omega_n t} \tag{3.24}$$

where ω_n is the angular resonance frequency of the nth overtone (flexural mode). With the above assumption, the differential equation for the spatial coordinates based on Eq. (3.23) can be written as

$$EI \frac{\partial^4 y(x)}{\partial x^4} - \rho \mathrm{A} \omega_n^2 y(x) = 0 \tag{3.25}$$

For a cantilever (clamped-free beam), the boundary conditions are as follows: at the clamped end ($x = 0$):

$$y(0) = 0, \left. \frac{\partial y}{\partial x} \right|_{x=0} = 0 \tag{3.26}$$

and at the free end ($x = L$):

$$\left.\frac{\partial^2 y}{\partial x^2}\right|_{x=L} = 0, \left.\frac{\partial^3 y}{\partial x^3}\right|_{x=L} = 0 \tag{3.27}$$

The deflection y, i.e., the vibration amplitude, along the beam is

$$y(x) = c_1\left(\cos\frac{\lambda_n}{L}x - \cosh\frac{\lambda_n}{L}x\right) + c_2\left(\sin\frac{\lambda_n}{L}x - \sinh\frac{\lambda_n}{L}x\right) \tag{3.28}$$

with

$$\lambda_n^4 = \frac{\rho \mathrm{A} \omega_n^2 L^4}{EI}, \quad \cos\lambda_n x \cosh\lambda_n = -1 \tag{3.29}$$

and

$$c_1 = \frac{y(L)}{2},$$

$$c_2 = -\frac{\cos(\lambda_n) + \cosh(\lambda_n)}{\sin(\lambda_n) + \sinh(\lambda_n)} \times c_1, \tag{3.30}$$

Hence, from Eqs. (3.15) and (3.29), the resonance frequency of a rectangular cantilever beam is calculated as [126]

$$f_n = \frac{\omega_n}{2\pi} = \frac{\lambda_n^2}{2\pi\sqrt{12}}\frac{H}{L^2}\sqrt{\frac{E}{\rho}} \tag{3.31}$$

For a simple rectangular cantilever beam, the values of λ_n are as follows

$$\lambda_1 = 1.875,$$
$$\lambda_2 = 4.694,$$
$$\lambda_3 = 7.855,$$
$$\lambda_4 = 10.996,$$

and for n > 4 $\lambda_n \approx \left(n - \tfrac{1}{2}\right)\pi$

3.3 Modalities of Cantilever Deflection- and Vibration- Based Sensing

3.3.1 The Piezoresistive Deflection Detection Method

The piezoresistive method [127, 128] involves the embedding of a piezoresistive material near the top surface of the cantilever to record the stress change occurring at the surface of the cantilever. As the microcantilever deflects, it undergoes a stress change that will apply strain to the piezoresistor, thereby causing a change in resistance that can be measured by electronic means. The advantage of the piezoresistive method is that the readout system can be integrated on the chip. The disadvantage is that the deflection resolution for the piezoresistive readout system is only one nanometer compared with one Angstrom by optical detection method. Another disadvantage with the method is that a piezoresistor has to be embedded in the cantilever. The fabrication of such a cantilever with a composite structure is more complicated.

The piezoresistor material in the beam must be localized as close to one surface of the cantilever as possible for maximum sensitivity. The type of doping being used for fabrication of the piezoresistive material is an important factor. The piezoresistive coefficient of N-type silicon is greater than that for P-type. The resistance of a piezoresistive material changes when strain is applied to it. The relative change in resistance as function of applied strain can be written as:

$$\frac{\Delta R}{R} = K_l \delta_l K_t \delta_t \tag{3.32}$$

where K denotes the Gage Factor, which is a material parameter. The subscripts l and t refer to the longitudinal and the transversal part of the Gage Factor.

The sensitivity of a piezoresistor varies proportionally to the thickness t and the radius of curvature. The Gage Factor is proportional to Young's Modulus, E, which is the intrinsic characteristic of material. The gage factor can also be calculated directly by straining the cantilevers and measuring the resistance change.

$$GF.\delta = \frac{\Delta R}{R} \tag{3.33}$$

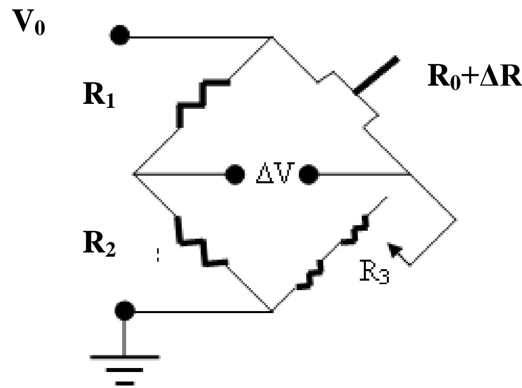

Figure 3.3: Schematic diagram of a microcantilever with embedded piezoresistive transduction element embedded at the base of the cantilever.

where δ is the strain in the material and R is the resistance. For a sensitive device, the gage factor should be of the order of 100.

The piezoresistive cantilever beam can be used as an arm of the Wheatstone Bridge circuit as shown in Fig. 3.3.

The resistance of the variable resistance arm (R_0+ΔR) in the above figure can be determined by using the common Voltage divider formula and is shown as below:

$$\Delta V = V_0 \left\{ \frac{R_3}{R_1 + R_2} - \frac{R_3}{R_0 + \Delta R + R_3} \right\}$$

$$\Rightarrow R_0 + \Delta R = R_3 \left\{ \frac{V_0 (R_1 + R_2)}{R_2 V_0 - \Delta V (R_1 + R_2)} - 1 \right\} \tag{3.34}$$

There would be a resistance change whenever the cantilever is subjected to a deflection.

3.3.2 The Optical Deflection Detection Method

The optical method [129], as shown in Fig. 3.4, employs a laser beam of very low power of the order that does not affect the biomolecules coated on the surface of the microcantilever and a position sensitive detector (PSD). The laser beam falls on the cantilever and gets reflected as the gold layer coated on the surface of the cantilever gives

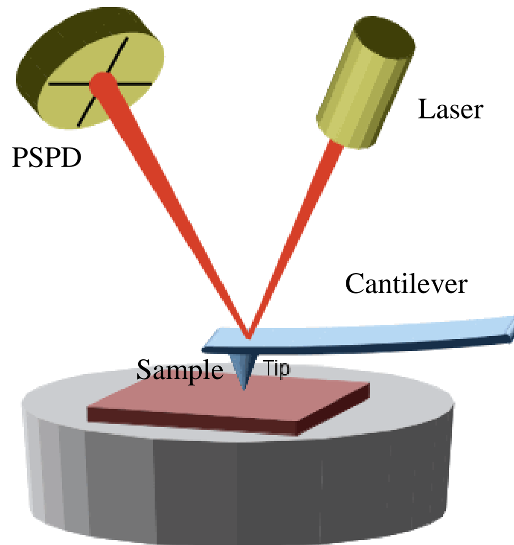

Figure 3.4: Simplified schematic diagram of optical transduction system used in atomic force microscope.

it an almost mirror like finish. The reflected beam falls on the PSD. When the cantilever is undeflected i.e. it is not coated with any molecule, the laser beam would fall on a particular spot on the PSD. As the cantilever deflects, the position of the beam changes, which, in turn, is calculated using appropriate electronics. The advantage of this detection system is that it is capable of detecting deflection in the sub-nanometer range. But this method also has its own disadvantages. The presence of a focused laser beam in a liquid cell environment can result in additional thermal management issues giving rise to extraneous readings. Secondly, the alignment system is expensive and involves great precision, which can ultimately raise the cost of the whole diagnostic kit. In addition, it also reduces the kit's portability.

3.3.3 The Capacitive Deflection Detection Method

Another frequently used technique is the capacitance method. This approach allows one to measure the changes in capacitance that arise from the displacement of a conductor on the cantilever and a fixed conductor on the substrate. Because the cantilever is separated from the fixed conductor by a small gap, deformation of the cantilever can generate a variation in capacitance that is inversely proportional to the separation gap. The capacitance method provides high sensitivity and absolute displacement, and its performance is comparable to that of an integrated microsystem. However, the capacitance method does not work well in an electrolyte solution due to the Faradic current, corresponding to the reduction or oxidation of a chemical species that obscures a desired signal. Furthermore, detection can be adversely affected by variations in the dielectric constant of the medium.

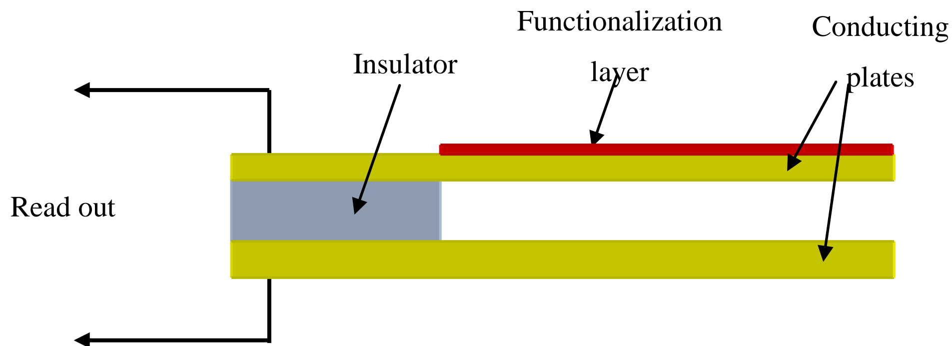

Figure 3.5: Simplified schematic diagram of capacitive transduction system of a microcantilever based sensor. Due to adsorption on the functionalizing layer the cantilever bends, changing the capacitance between the two conducting plates

3.3.4 The Interferometry Deflection Detection Method

The interferometer optical-detection method, which is based on the interference between a reference laser beam and the laser beam reflected off the cantilever, provides a more sensitive technique for measuring the deflection of a cantilever. Interferometry is highly sensitive and can provide direct and absolute displacement. Rugar et al. [130] developed a deflection sensor based on the interference of light between the cleaved end of an optical fiber and the back of a cantilever. Using this technique, the authors achieved subnanometer deflection and successfully used single-spin magnetic resonance microscopy. Although interferometry is highly sensitive up to 0.1 $\overset{\circ}{A}$, it has several disadvantages. For example, it requires tedious positioning of the fiber, it is relatively inefficient in liquids, and it works well for only small displacements.

3.3.5 Field-effect transistor (FET) embedded Microcantilevers

One of the very early studies on FET embedded microcantilevers was done by Beck *et al.*, where strain sensitive cantilevers were fabricated from AlGaAs/GaAs heterostructures [131-132]. The strain induced electrical response in GaAs is believed to be from piezoelectric effect [133] and the deformation potential [134]. Later AlGaAs/GaAs cantilevers were also applied for different applications including surface potential mapping [135] and charge imaging [136]. FET-based stress sensors are widely reported for micromechanical devices such as accelerometers, resonators, and parallel cantilevers for scanning probe microscopy, as well as for residual stress measurements.

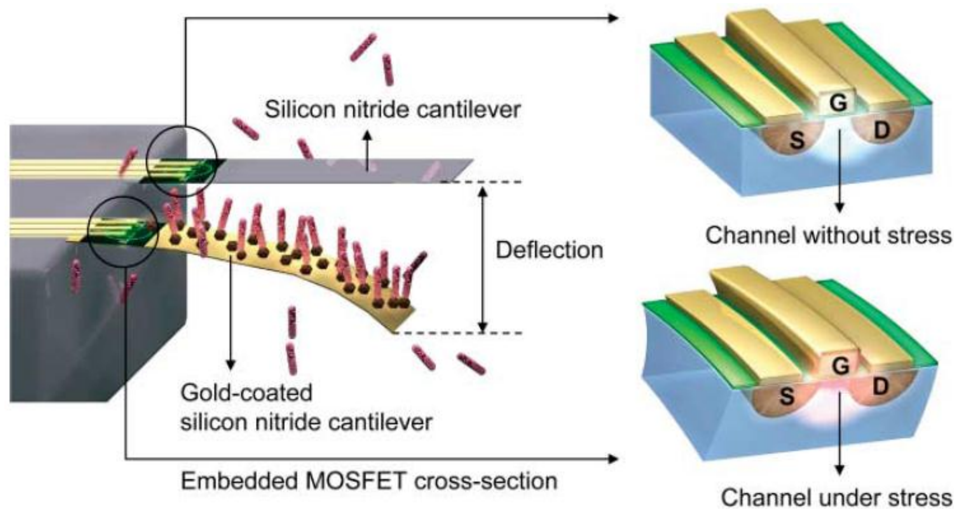

Figure 3.6: Schematic of the interaction between probe and target molecules on an embedded-MOSFETcantilever system. The silicon nitride cantilever is a reference, and the gold-coated one is used as a sensing cantilever. Specific biomolecular interactions between receptor and target bend the cantilever. Magnified view of embedded MOSFET in cross section shows stressed gate region when cantilever bends, resulting in change of drain current due to conductivity modulation of the channel underneath the gate.(Figure taken from Ref [137])

Metal oxide semiconductor field effect transistor (MOSFET) embedded microcantilevers are also ideal candidates for effective electronic detection platform for biological and chemical microsensors, harnessing the engineering benefits of complementary MOS (CMOS) integration [137-141]. When a microcantilever bends as a result of adsorption-induced surface stress, modulation of the channel current underneath the gate region results from altered channel mobility of the transistor due to increased channel resistance. As fixed biased voltages are applied on the gate and source-drain region of the transistor, any change in channel mobility will result in change in the drain current of the transistor. Apart from a decrease in channel conductivity, the channel mobility is also affected by the generation of trap states and band structure alteration.

3.3.6 Piezoelectric deflection detection

Rather than relying on external actuating, researchers have developed self-actuating and sensing cantilevers through the direct integration of piezoelectric material into the cantilever. This technique involves coating the cantilevers with piezoelectric materials, which develop a measurable charge due to cantilever bending. The main advantage of the piezoelectric method is that it can convert a mechanical signal into a direct electrical signal with a high quality factor, thereby providing a sensitive tool for qualifying and quantifying biomolecules [142-145].

Recently there have been demonstrations of converting mechanical energy into electrical energy by nanowires using the coupling effects of semiconducting and piezoelectric properties possessed by wurtzite structured materials, such as ZnO [146-148], Zn [149], CdS [150], GaN [151] and InN [152]. When deformed by an external

force, the nanowires (NWs) would generate a piezoelectric potential (piezopotential), which acts as the driving force to propel the flowing of carriers through an external load. Nanocantilevers of piezoelectric materials might use this deflection induced detection mechanism.

3.3.7 Thermal response

Heated cantilevers can detect changes in power dissipation and cooling capacity of micro/nanojets by heat transfer since heated cantilevers are very sensitive to small thermal agitation. A heated cantilever was demonstrated by King's group to investigate the cooling capacity of the liquid and gaseous microjets and thermal transport between the cantilever heater and the impinging jet environment [153].

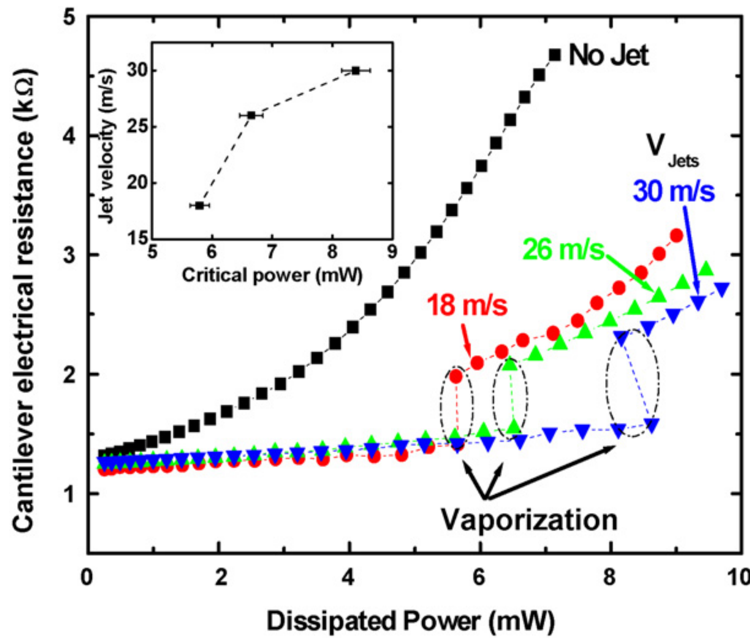

Figure 3.7: Resistance of a heated cantilever as a function of power dissipation and illustration of heat transfer by heated cantilevers since they are very sensitive to small thermal agitation (Ref [153]).

Figure 3.7 shows the resistance of a heated cantilever as a function of dissipated power with and without additional cooling by liquid microjets. Without jet impingement, the results show typical nonlinear electrical properties of the heated cantilever. With jet impingement, the cantilever can dissipate more power without significant temperature rise. There are discontinuities representing local vaporization of liquid butane droplet and each discontinuity is associated with a critical power. The inset shows the critical power increases as the jet velocity increases.

3.3.8 Conductometric response

The use of microcantilevers and NEMS devices for sensor applications requires an in-depth knowledge of adsorption and abosorption mechanisms and functionalization layer, especially for selective detection of different analytes.

3.3.8.1 Adsorption on cantilever surfaces

Adsorption is a process where atoms or molecules from the gas phase or from solution bind in a condensed layer on a solid or liquid surface. The molecules that bind to the surface are called the adsorbates while the substance that holds the adsorbate is called the absorbent or substrate. Removal of the molecules from the surface is called desorption. Kayser, proposed a distinction between adsorption, where the gas binds directly to the surface of a solid, and absorption, where the gas dissolves directly into the bulk of a fluid or solid. Adsorption of a gas onto a solid is quite different from absorption of a gas into a solid or liquid in that in adsorption, the quantity of gas that adsorbs scales with the surface area rather than the volume of the adsorbent.

A classification of adsorption distinguishes two classes, a weak interaction between adsorbate and substrate, the so-called physisorption, where the adsorption energy is typically less than 0.3 eV per adsorbate particle (6.9 Kcal/mol) and there is no covalent bond and secondly chemisorption, where the adsorption energy is larger and

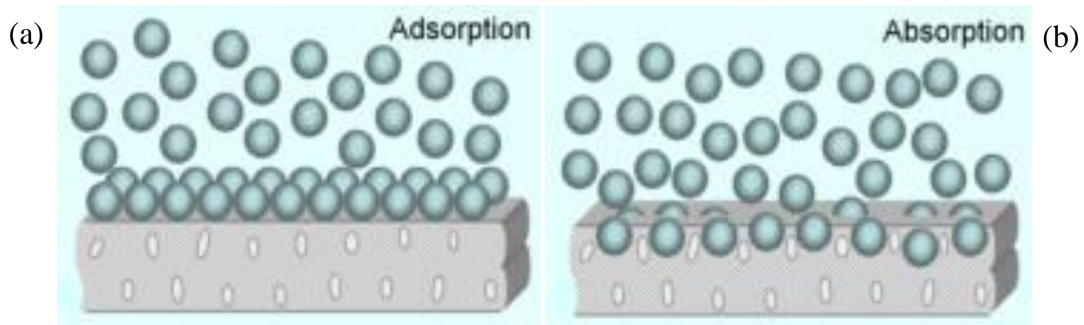

Figure 3.8: (a) the adsorption and (b) the absorption mechanism of molecules on cantilever surfaces

there is a chemical bond between the adsorbate and the surface [154] and the adsorbate's electronic structure is significantly modified. In contrast to chemisorption, physisorption is governed by polarization and dispersion (Van der Waals) forces, and as a result, the electronic structure of the adsorbate is perturbed to a much lesser extent [154]. For chemisorption systems there is a further classification of the nature of bonding, based on electronic, electrical, vibrational and thermal properties. Altogether there are four different types of bonding: 1) Van der Waals, 2) Covalent, 3) Metallic and 4) Ionic.

Adsorption is usually described through isotherms, that is, functions which connect the amount of adsorbate on the adsorbent, with its pressure (if gas) or concentration (if liquid). One can find in literature several models describing process of

adsorption, namely Freundlich isotherm, Langmuir isotherm, BET isotherm, etc where Langmuir isotherm [155] is most widely used.

3.3.8.2 Functionalization layers

Functionalization is the act attaching functional groups to modify the surface of a material by bringing physical, chemical or biological characteristics different from the ones originally found on the surface of a material. Functional groups are specific groups of atoms within molecules that are responsible for the characteristic chemical reactions of those molecules. However, the term ‘functionalization’ loosely applies to coating a sensitive layer to a solid surface in order to facilitate sensing of specific target molecules. For sensor applications, the cantilevers have to be coated with specific sensor layers that reversibly respond to different chemicals in solution or gas phase. There are many materials including metals and organic chemical/biological molecules that can be used for the selective layers, the choice of which affects the selectivity, reproducibility, and sensitivity of the microcantilever sensor system.

Functionalization methods are also important to realize a microcantilever system as a sensor. There are numerous techniques to coat a microcantilever beam with material. First of all, conventional evaporation and sputtering methods are commonly used to deposit metallic or ceramic materials in microfabrication batch processes. These methods are suitable for coating large areas or coating a single side of microcantilever beams, but not individual microcantilevers in an array without complex shadow masking processes. Other simple methods to coat microcantilevers use manual approaches such as pipetting, dropping, and pin-dipping. Disadvantages of these simple methods include scalability to large arrays of microcantilevers, limited reproducibility, and time-consuming. For a

microcantilever array, microfluidic network devices can be used to deliver specific solutions to each microcantilever through separate microfluidic channels [156]. A capillary array is another approach to simultaneously coat multiple microcantilevers. A simple array of glass capillaries designed to accommodate the dimensions and pitch of the microcantilevers in a linear array is filled with a variety of solutions containing materials such as polymers, self-assembled monolayers, protein solutions, and single-stranded DNA oligonucleotides [156]. This method involving insertion of the microcantilever array into the capillary array to functionalize microcantilevers. All of above methods for an array use manual alignment of the microcantilever array and functionalization device, and are limited for a large number of microcantilevers. A micro/nano-inkjet printing technique overcomes the disadvantages since it affords efficient, rapid, and reliable functionalization of only one side of the microcantilevers. By adjusting the size and number of droplets spotted on the microcantilever, the thickness of the selective layer coating can be precisely controlled [156]. The down side is that it is a serial method.

The nanowireFET sensor devices are modified with specific surface receptors as the functionalization layer to represent a powerful detection platform for a broad range of biological and chemical species in solution. The first example demonstrating the ability of nanowire FET devices to detect species in liquid solutions was demonstrated in 2001 for the case of hydrogen ion concentration or pH sensing [157] with a fictionalization layer. A basic p-type Si nanowire device was converted into such a sensor by modifying the silicon oxide surface with 3-aminopropyltriethoxysilane, which yields amino groups at the nanowire surface along with the naturally occuring silanol (Si-OH) groups of the

oxide, as shown in Fig. 3.9 (a). The amino and silanol moieties function as receptors for hydrogen ions, which undergo protonation/deprotonation reactions, thereby changing the net nanowire surface charge.

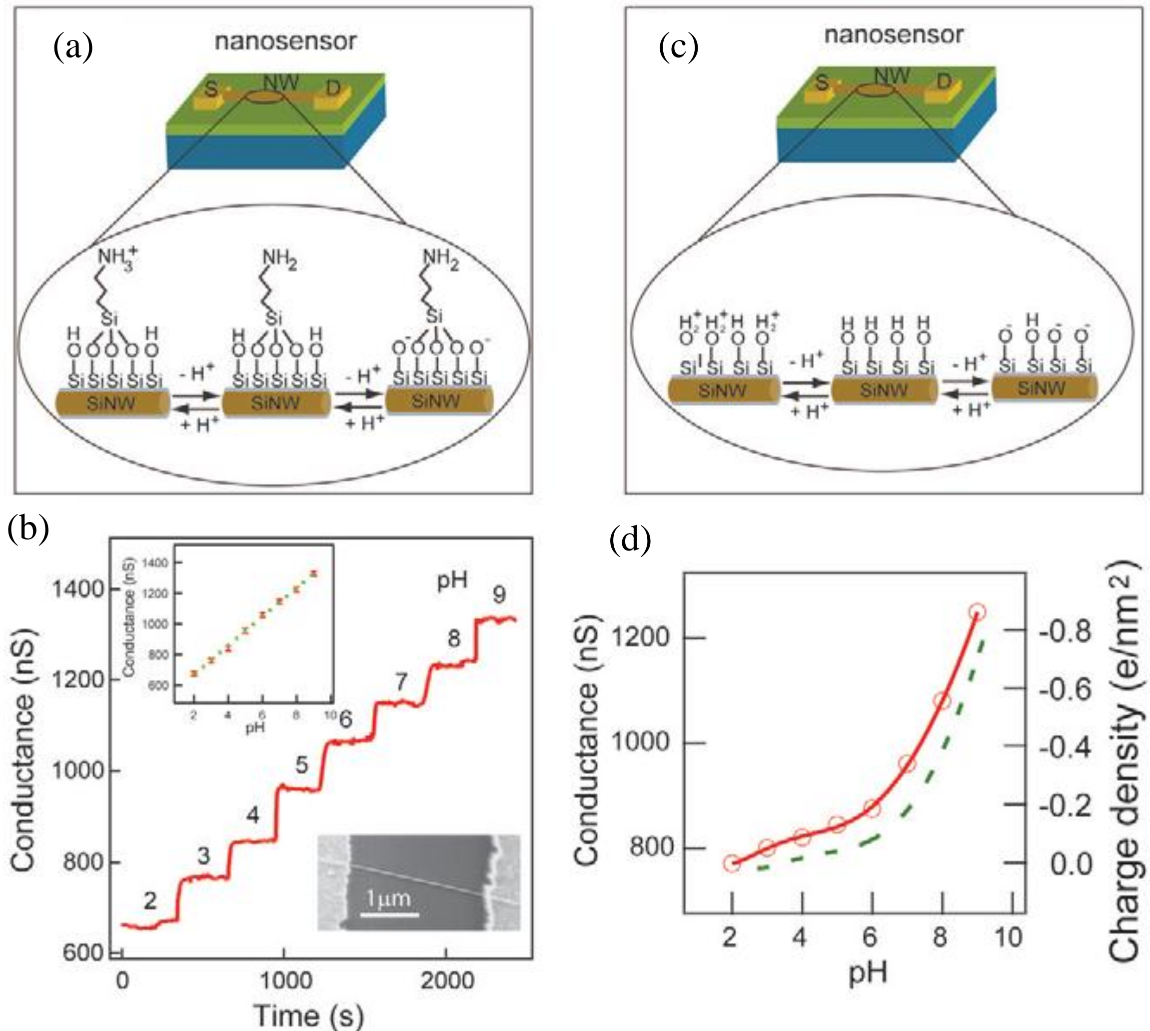

Figure 3.9: Nanowire pH sensors. (a) Schematic of an amino-functionalized nanowire device and the protonation/deprotonation equilibria that change the surface charge state with pH. (b) Changes in nanowire conductance as the pH of solutions delivered to the sensor is varied from 2 to 9; inset is a plot of conductance data versus pH. (c) Schematic of an unmodified nanowire sensor containing silanol groups and the protonation/deprotonation equilibria that change the surface charge state with pH. (d) Conductance of an unmodified Si nanowire device (red) versus pH. The dashed green curve is a plot of the surface charge density for silanol groups on silica as a function of pH (Ref. [157]).

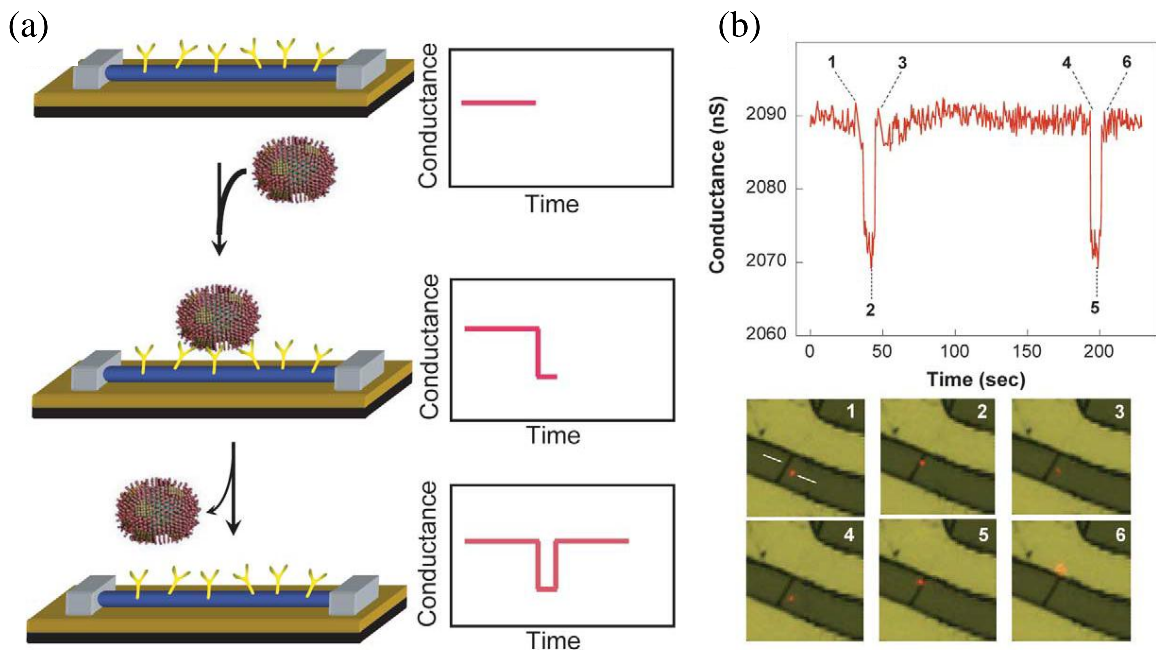

Figure 3.10: (a) Schematic of a single virus binding and unbinding to the surface of a Si nanowire device modified with antibody receptors and the corresponding time-dependent change in conductance. (b) Simultaneous conductance and optical data recorded for a Si nanowire device after the introduction of influenza A solution. The images correspond to the two binding/unbinding events highlighted by time points 1-3 and 4-6 in the conductance data, with the virus appearing as a red dot in the images (Ref. [158]).

For the detection of viruses [158], which are among the most important causes of human disease [159] and an increasing concern as agents for biological warfare and terrorism [160,161] a NW FET device can be functionalized with antibody and when a virus particle binds to an antibody receptor on a nanowire device, the conductance of that device will change from the baseline value, and when the virus unbinds again, the conductance will return to the baseline value. Significantly, delivery of highly dilute influenza A virus solutions, on the order of 80 aM (10-18 M) or 50 viruses/μl, to p-type Si nanowire devices modified with monoclonal antibody for influenza A produces well-

defined, discrete conductance changes (Fig. 3.10 (b)) that are characteristic of binding and unbinding of single negatively charged influenza viruses [158].

3.3.8.3 A model case: Metal oxide based gas sensor systems

Metal oxide semiconductor (MOS) based conductometric sensors are one of the most commonly used sensors for environmental monitoring. With the metal oxide bulk or thin film acting as a receptor material, the detection mechanism is based on the change in material resistivity after exposure to the analyte gas. Chemical (change in surface oxygen concentration) and local carrier concentration change (change in redox state) mechanism is generally accepted as the origin of resistance change [162]. A comprehensive treatment on the conduction mechanism prevalent in metal oxide gas sensors was carried out by Barsan *et al.* [162] Recently, metal oxide nanostructures18 have been used as sensing elements targeting improved sensitivity and selectivity.

The conductance of 1D metal oxide nanomaterials can be expressed as [108]

$$G = \frac{n_0 e \mu \pi (D - 2\omega)^2}{4l} \tag{3.35}$$

where n_0 represents carrier concentration, μ represents mobility, l is the length of the nanostructure, D is the diameter of the nanostructure, and ω is the width of surface charge region that is related to the Debye length of the nanomaterials.

The Debye length of sensing materials, in turn, can be expressed as [108]

$$\omega = (eV_S / kT)^{0.5} L_D \tag{3.36}$$

$$L_D = (\varepsilon\varepsilon_0 \, kT / e^2 n_0)^{0.5} \tag{3.37}$$

where ε_0 is the absolute dielectric constant, ε is the relative dielectric permittivity of the structure, k is the Bolzmann's constant, T is the temperature, and V_S is the adsorbate-induced band bending. The sensor response in these systems can be defined as [108]

$$S = \frac{(G_1 - G_0)}{G_0} = 4\frac{(\omega_0 - \omega_1)}{D} \tag{3.38}$$

where G_0 and G_1 are the conductance before and after exposure to the analyte. As inferred from Eqs 1-4, applying an external gate voltage, doping metal impurities during material growth, modulating operating temperature, and changing the geometry of the nanostructures can improve the sensitivity.

3.3.9 Potentiometric response

Compared to conventional cantilever chemical sensors, which are based on monitoring the static deflection or resonant frequency or amperometric response, the potentiometric cantilever sensors enjoy several advantages: First, the sensor can operate by measuring the surface work function change of the substrate instead of that of the cantilever, because only the relative work function change is critical. This is very suitable for practical sensor designs since this method does not requires to modify the cantilevers using selective coating which can lead to nonuniformity in cantilever sensitivity. Second, this technique provides the great possibility of tuning the sensitivity of the sensor by varying the amplitude of the applied ac voltage or reducing the cantilever-reference electrode distance or increasing Q factor or reducing string constant of cantilever or increasing differential capacitance. Third, since surface work function changes are measured directly for sensing, only the surface electronic properties of the functionalization layers are important.

Mechanism of Potentiometric Microcantilever Sensor

The capacitive force between cantilever and substrate illustrated in Figure 4.1 will be discussed first. In general, any two different materials will have dissimilar electrochemical potentials, thus when two materials are brought to close contact, the electrons will transfer from one to the other. For example, if two metals Pt and Au are brought to close contact, then electron will flow from Au to Pt due to the higher work function of Pt. Thus an electrostatic potential will form between negatively charged Pt and positively charged Au. Since the electrons will continue to flow until the electrochemical potentials of the two materials are the same, the contact potential difference is given by

$$V_{con} = (\phi_{Pt} - \phi_{Au}) / q \quad , \tag{3.39}$$

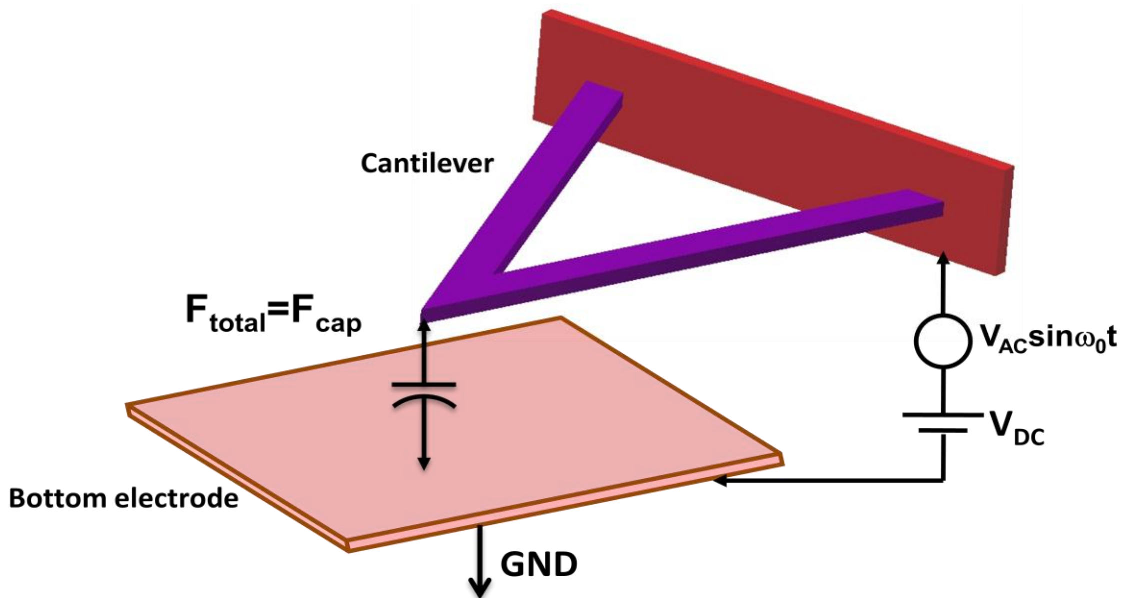

Figure 3.11: Physics of potentiometric measurement with a cantilever oscillating above substrate.

where ϕ_{Pt} and ϕ_{Au} are work function of Pt and Au, respectively. In actual setup of potentiometric sensing, the cantilever probe and substrate are electrically connected. Thus, a contact potential difference forms due to work function difference between cantilever probe and substrate. On the other hand, the charge present on surface of a substrate will also create an image charge on the cantilever probe, giving rise to an electrostatic potential between substrate and cantilever. The case of applying an external bias is similar to these cases discussed. When an external bias is applied between cantilever and substrate, it will intentionally separate charge and create a potential difference on these two.

As shown in Figure 3.11, assuming there are no charges present on the surface of substrate, a microcantilever is oscillating above substrate driven by an AC bias at angular frequency ω and a static DC bias. The total capacitive force between the microcantilever and substrate contributes to a capacitive force F_{cap} given as [163, 164]

$$
\begin{aligned}
F_{total} = F_{cap} &= 1/2\frac{\partial C}{\partial Z}(V_{ac}\sin\omega t + V_{dc} - \Delta\phi/q)^2 \\
&= [1/4\frac{\partial C}{\partial Z}V_{ac}^{2} + 1/2\frac{\partial C}{\partial Z}(V_{dc} - \Delta\phi/q)^2] + [\frac{\partial C}{\partial Z}(V_{dc} - \Delta\phi/q)V_{ac}\sin\omega t] + [1/4\frac{\partial C}{\partial Z}V_{ac}^{2}\cos 2\omega t] \\
&= F_{dc} + F_{\omega} + F_{2\omega}
\end{aligned}
\tag{3.40}
$$

where $\Delta\phi$ is work function difference between cantilever and substrate and Z is distance between cantilever and substrate. The total capacitive force consists of three components: a static force, an alternative force at frequency ω, and an alternative force at frequency

2ω. If the frequency ω of the AC bias is closed to the fundamental resonant frequency of the cantilever, the resonant amplitude will be [165]

$$a_{\omega} = \frac{|F_{\omega}|}{k} Q \tag{3.41}$$

where k is spring constant and Q is Quality factor. The resonant amplitude at frequency ω is amplified by Q times and dominates the motion of oscillating cantilever. Taking Eq. 3.40 and Eq. 3.41, the change in resonant amplitude will be

$$\Delta a_{\omega} = -\frac{Q}{k} \times \frac{\partial C}{\partial Z} \times \frac{\Delta \phi}{q} \times V_{ac} . \tag{3.42}$$

From Eq. 3.42, we can infer that the change in resonant amplitude is directly proportional to work function difference $\Delta\phi$. The resonant amplitude is also affected by

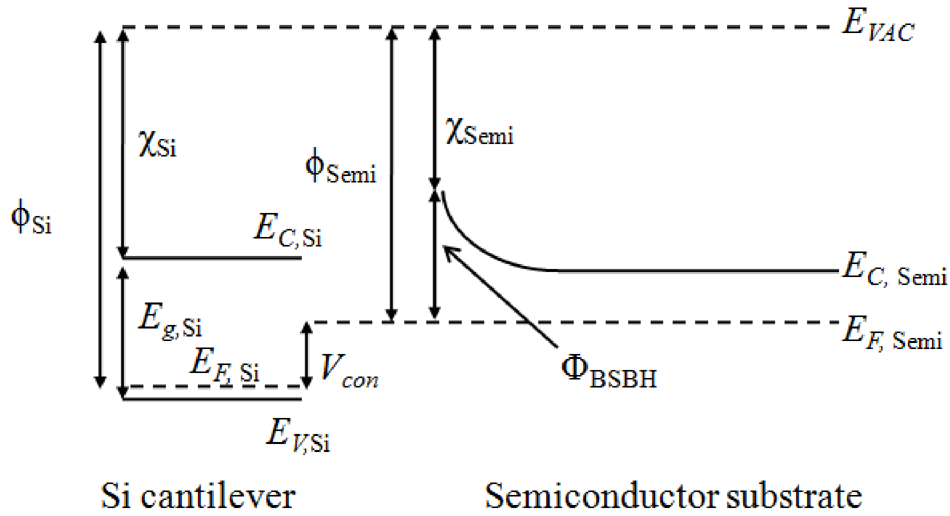

Figure 3.12: Band diagram illustrating Fermi level and vacuum level for Si cantilever probe and semiconductor substrate.

other factors such as Q factor, spring constant, differential capacitance, and amplitude of the AC bias, providing opportunities to tune sensitivity by optimizing these factors. Figure 3.12 shows a band diagram of the microcantilever and substrate, indicating that surface work function of the substrate consists of surface electron affinity and surface barrier height. The process of adsorption/desorption of molecular on substrate can change substrate's surface work function by affecting its surface electron affinity and surface barrier height (Assume a heavily p-type doped Si cantilever is applied in Figure 3.12). If cantilever is made of inert materials to target molecular, the contact difference potential will be a function of surface work function of substrate. Without affecting any of the factors in in Eq. 4.4, the resonant amplitude will be only determined by the surface work function, which can be utilized as an effective signature for chemical detection [164,166,167].

CHAPTER 4

INDIUM NITRIDE NANOWIRES

This chapter contains brief introduction of the InN NW synthesis process, structural characterization of the NWs and the growth optimization process. The role of oxygen during the growth is explained briefly. Lastly electrical characterization of the NWs to investigate the material properties is presented briefly.

4.1 Introduction and background

Nanoscale sensors, in various forms, have been under intense research focus in the past several years due to their high sensitivity toward changes in many physical parameters such as, mass [168], force [169], energy [170], stress [171], temperature [172], charge [173], and spin [174]. Additionally, these systems promise high integration density and low power consumption, two of the most desirable aspects of an integrated system [175]. A combination of all these properties can lead to potential applications of these sensors in a large variety of civilian and military applications. There are currently two approaches for nanoscale sensor fabrication: top-down and bottom-up. In the top-down approach, one uses expensive and complicated fabrication processes to realize the nanostructures, which limits their applications to only very specific and niche areas. In the bottom-up approach, the nanostructures are realized through inexpensive NW synthesis processes that can open up opportunities for widespread applications. In addition, the uniformity and quality of the nanostructures (which seriously impact the device characteristics) that are naturally obtained during the synthesis process cannot be achieved by current state-of-the-art nanofabrication tools. However, controlled positioning of the NWs over a large area has been quite difficult to achieve so far, restricting their applications to individual devices, or to low levels of integration.

4.2 Semiconductor nanowires

One-dimensional nanostructures (1D) such as nanowires and nanotubes have been of great interest for future nanoscale building blocks and substantial promise for integrated nanoscale systems when the current silicon (Si) or other conventional

semiconductor technology reaches their physical limits. To sustain the historical scaling trend beyond CMOS, novel one-dimensional structures, including carbon nanotubes (CNTs) and semiconductor nanowires (NWs), have been proposed as the active components (as well as interconnects) in future nanoscale devices and circuits. In this case, the critical device size is defined during the growth (chemical synthesis) process and can be controlled with atomic scale resolution. To date, great efforts and progress have been made in the field of CNTs, although CNT based applications are still hindered by difficulties to produce uniform, semiconducting nanotubes. On the other hand, semiconductor NWs can be prepared with reproducible electronic properties in high-yield, as required for largescale integrated systems. Furthermore, the well-controlled NW growth process implies that materials with distinct chemical composition, structure, size and morphology can be integrated [176]. Such an ability to build specific functions into the system during growth may in turn lead to bottom-up assembly of integrated circuits [177], which offers the potential of parallel production of massive number of devices with similar material and electrical/optical properties. Drastically different from the 'top-down' paradigm commonly used in today's semiconductor industry, this 'bottom-up' paradigm, analogous to the way that nature works, may prove to be a suitable solution to the technological challenges as devices approach atomic size.

From a fundamental physics point of view, the lowdimensional nanowire structure is an ideal platform to probe properties which may be inaccessible or hard to achieve in larger devices, due to the reduced device size and ideal material properties. This is because electrons in nanowires are quantum confined laterally and thus occupy energy levels that are different from the traditional continuum of energy levels or bands

found in bulk materials. Figure 4.1 shows that density of states in semiconductor structures depends on dimensionality [178]. Peculiar features of this quantum confinement exhibited by certain nanowires manifest themselves in discrete values of the electrical conductance. Such discrete values arise from a quantum mechanical restraint on the number of electrons that can travel through the wire at the nanometer scale. There are many applications where nanowires may become important in electronic, opto-electronic and nanoelectromechanical devices, as additives in advanced composites, for metallic interconnects in nanoscale quantum devices, as field-emitters and as leads for biomolecular nanosensors [179].

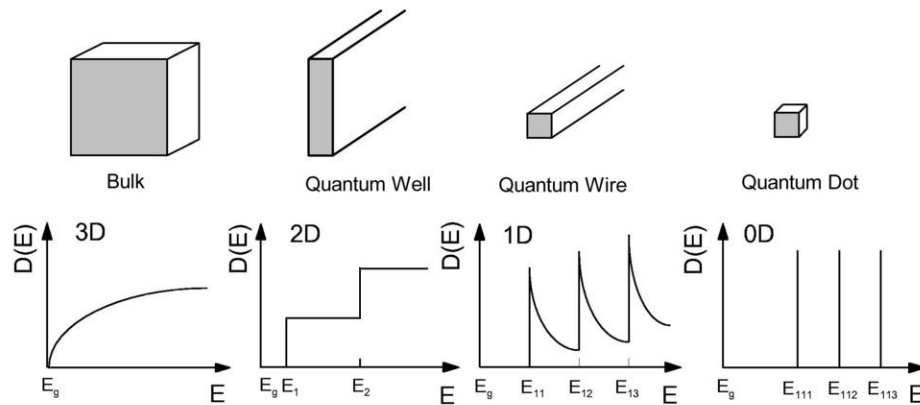

Figure 4.1: Density of states in semiconductor structures depending on dimensionality (Ref. [120]).

4.3 Indium Nitride (InN) nanowires

The major characteristics of a nanoscale sensor are strongly influenced by the properties of the material (usually semiconductor) from which it is made. Usually, for

chem-FET type sensing (based on surface depletion caused by adsorbed molecules) the material should have a high carrier density, high mobility, chemical inertness, and thermal stability. NEMS devices would additionally require smooth and highly crystalline NWs for high quality factor, and large piezoresistivity for efficient transduction of device deflection. Most semiconductors and their NWs display some of the above mentioned properties, but rarely all. InN NWs, which have been investigated only in the last few years, exhibit most of these, in addition to two other special properties that are not generally observed. Firstly, there is a high density of carriers present in the NW (from unintentional doping), a large fraction of which is can be the surface [180]; and secondly, these NWs exhibit spontaneous and barrier induced growth redirections while otherwise growing straight on the substrate surface [181]. The first property, when combined with high mobility of these NWs (our results indicate mobility >1000 cm^2/Vs is possible), can lead to highly sensitive deflection transduction (based on surface depletion change) as will be utilized in our NEMS devices. The second property has been recently observed in our laboratory [182], and can be exploited to synthesize NWs of special shapes and sizes by controlling their growth directions using patterned barriers.

4.3.1 InN wurtzite structure

There are two phase structures, α-phase and β-phase, for Group III-nitride materials. The thermodynamically stable phases are hexagonal wurtzite structure (α-phase), and the metastable phases are zincblende structure (β-phase) for AlN, GaN and InN [183]. The wurtzite nitrides are grown and studied almost exclusively. The wurtzite

structure consists of tetrahedrally coordinated indium and nitrogen atoms that are stacked in an ABABAB pattern (Zincblende is stacked in an ABCABC pattern). In wurtzite structure, each atom is tetrahedrally bonded to four atoms of the other type, and the primitive unit cell is simple hexagonal with a basis of four atoms, two of each kind. There is no inversion symmetry in this lattice along the [001] direction (see Fig. 2.1), resulting in all atoms on the same plane at each side of a bond being same. Hence, an InN crystal has two distinct faces, the In-face and the N-face. The arrangement of atoms for In-face and N-face InN are shown in Fig. 4.2. Note that for In-face the N-atom is stacked directly over the In-atom and vice-versa for the N-face.

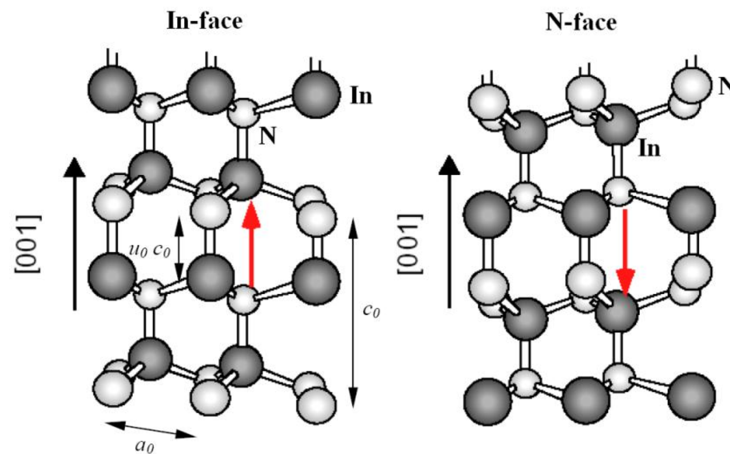

Figure 4.2: Atomic arrangements in In-face and N-face InN crystals. The red arrow pointing from N to In atom shows the direction of the spontaneous polarization (Ref. [184]).

The wurtzite lattice is characterized by three parameters: the edge length of the basal hexagon (a_0), the height of the hexagonal lattice cell (c_0), and the cation-anion bond length ratio (u_0) along the [001] axis in units of c_0. The subscript "0" indicates these values are those of the equilibrium lattice. These dimensions are marked in Fig. 4.2. In an

ideal wurtzite crystal structure, the c_0/a_0 ratio is 1.6330 and u_0 is 0.375. Because of the different metal cations, the bond lengths and the resultant c_0/a_0 ratio of AlN, GaN and InN are different (as listed in Table 4.1). It is obvious from Table 2.1 that among the group-III nitrides, InN is second closest to the ideal structure. This fact is very important because the degree of non-ideality is an important factor in determining the strength of polarization in group-III nitrides.

Table 4.1 Lattice parameters of wurtzite III-V nitrides at 300 K.

Material	*Ideal*	*AlN*	*GaN*	*InN*
a_0 (Å)[b]	-	3.112	3.189	3.54
c_0 (Å)[b]	-	4.982	5.185	5.705
c_0/a_0 (exp.)[b]	-	1.6010	1.6259	1.6116
c_0/a_0 (cal.)[a]	1.6330	1.6190	1.6336	1.6270
u_0[a]	0.375	0.380	0.376	0.377

[a]Ref. [183].

[b]Ref. [185].

4.3.2 Spontaneous and piezoelectric polarizations

In the group-V elements, nitrogen is the smallest and the most electronegative atom, which has a great influence on the properties of the III-nitrides. Because of the $1s^2 2s^2 2p^3$ electronic configuration of the nitrogen atom, the electrons involved in the metal-nitrogen covalent bond will be strongly attracted by the coulomb potential of the nitrogen atomic nucleus. This means that the metal-nitrogen covalent bond will have

stronger ionicity compared to other III-V covalent bonds. This ionicity will result in macroscopic polarization if there is a lack of inversion symmetry in the crystal.

As mentioned before, there is no inversion symmetry in the wurtzitic III-nitrides along the c-axis. Absence of this inversion symmetry, in addition to the strong ionicity of the metal-nitrogen bond, results in a strong macroscopic polarization along the [001] direction in the III-nitrides [183], [185]. This same effect also exists in the [111] direction of zincblende GaAs and InP, though to a much lesser extent because of the relatively smaller ionicity of the III-V covalent bond. Since this polarization effect occurs in the equilibrium lattice of the III-nitrides at zero strain, it is called spontaneous polarization [183], [185].

Apart from the ionicity of the III-V covalent bond, the degree of non-ideality of the crystal lattice also affects the strength of spontaneous polarization. In III- nitrides, although the covalent bond parallel to the c-axis is strongly ionic and is primarily responsible for the spontaneous polarization, the other three covalent bonds in the tetrahedral structure are also equally ionic. The resultant polarization from these other three bonds is actually aligned in the opposite direction and serves to counteract the polarization of the other bond (see Fig. 2.1). As the c_0/a_0 ratio decreases (c_0 decreases and a_0 increases), these three covalent bonds will be at a wider angle from the c-axis, and their resultant compensation polarization will decrease, giving rise to a stronger macroscopic spontaneous polarization. Table 4.2 shows the c_0/a_0 ratio and the spontaneous polarization for GaN, InN and AlN. We can see that as the lattice non-ideality increases (c_0/a_0 ratio decreases away from 1.6330 of the ideal lattice), the value of spontaneous polarization (P_{SP}) increases from GaN to InN to AlN.

Table 4.2 Effects of lattice non-ideality on the strength of spontaneous polarization in the III-V nitrides.

Material	*AlN*	*GaN*	*InN*
c_0/a_0[a]	1.6010	1.6259	1.6116
P_{SP} (C/m^2)[a]	-0.081	-0.029	-0.032

[a]Ref. [183], [184].

Following the previous discussion on lattice non-ideality influencing the strength of spontaneous polarization, one can imagine that if the ideality of the III-nitride lattices is changed externally, then due to the strong ionicity of the metal-nitrogen covalent bond there will be dramatic changes in the polarization of the crystal. One way to change the ideality of the crystal lattice is through strain. If stress is applied to the III-V nitride lattice, the ideal lattice parameters c_0 and a_0 of the crystal structure will change to accommodate the stress. Thus the polarization strength will be changed. This additional polarization in strained III-nitride crystals, in addition to the spontaneous polarization already present, is called piezoelectric polarization [183], [185]. For example, if the nitride crystal is under biaxial compressive stress, the in-plane lattice constant a_0 will decrease and the vertical lattice constant c_0 will increase, making the c_0/a_0 ratio increase towards the ideal lattice value of 1.6330. This will decrease the polarization strength of the crystal, since the piezoelectric polarization and the spontaneous polarization will act in opposite directions. On the other hand, if the nitride crystal is under tensile stress, the in-plane lattice constant will increase and the vertical lattice constant will decrease, lowering the c_0/a_0 ratio further away from 1.6330. This will increase the overall

polarization, since the piezoelectric and the spontaneous polarizations now act in the same direction.

4.3.3 Surface band bending and charge accumulation

Normally, depletion layers occur at III–V semiconductor surfaces, with the surface Fermi level located in the band gap at the G-point. This depletion of conduction electrons allows the ionized acceptor-type surface states to be neutralized, giving overall charge neutrality. Narrow band gap Group III-nitride semiconductors, such as InN, InAs and InSb, usually show an accumulation layer due to pinning of the Fermi level above the conduction band edge at the NW surface, while semiconducting GaN NWs show an depletion region due to pinning of the Fermi level below the conduction band edge at the NW surface [186]. For the wurtzitic InN nanowires, polarization (polar direction [001]) is always directed perpendicularly to the NW growth direction [110], and is also perpendicular to the NW surface. Therefore, the Fermi level is pinned above the conduction band edge at the nanowire surface for InN nanowires due to the sheet charge caused by the polarizations, much like InN film. Therefore, the free electrons move to the surface and form a charge accumulation layer, combining with the accumulation charge caused by the spontaneous and piezoelectric polarizations in InN nanowires [183] [see schematic bandgap diagram of Fig. 4.3 (a)]. In addition, the pinning of the surface Fermi level at the same energy for a-plane (i.e. [110]) and both polarities of c-plane (i.e. [001] and $[00\bar{1}]$) InN means that the band bending close to the surface is very similar, resulting in similar near-surface charge profiles [187].

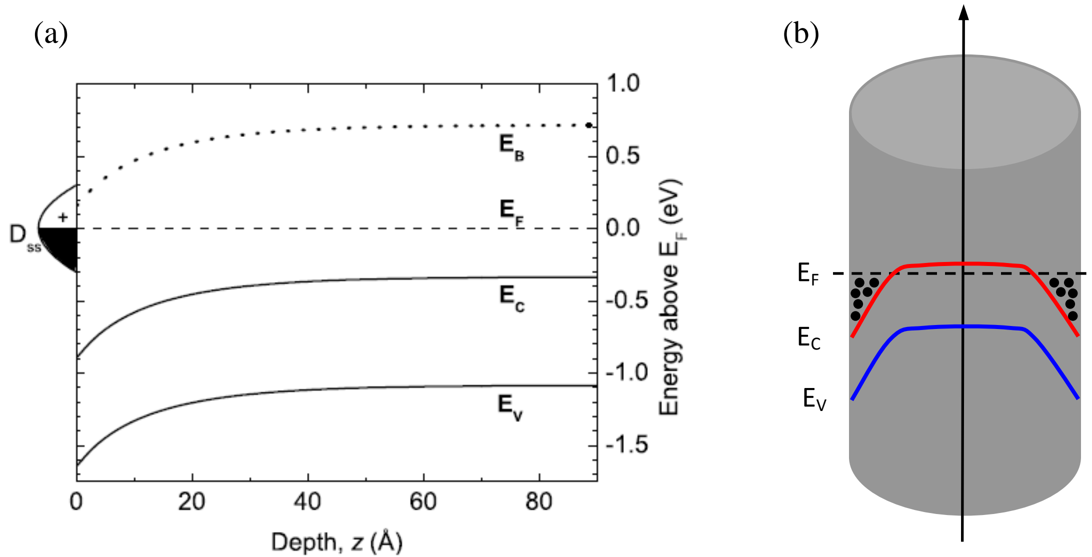

Figure 4.3: The conduction and valence band edges (E_C and E_V, solid lines) and the branch-point energy (E_B, dotted line) with respect to the Fermi level (E_F, dashed line) in the near-surface region of InN(0001). The donor-type surface states (Dss) are also shown, where the unoccupied states above the Fermi level are shown to be positively charged.

The observed electron accumulation at the surface of *n*-type InN is due to the presence of positively charged donor-type surface states. The existence of such surface states requires that the following conditions are satisfied. First, in order to have predominantly donor-type character, the surface states must lie below the branch-point energy E_B. This is the crossover point from states higher in the gap that are mainly of conduction band character (acceptor-type) to states lower in energy that are mainly of valence band character (donor-type) [187,188]. This branch-point energy falls close to the center of the band gap (in one dimension) in the complex band structure [188]. Second, the surface states must be at least partly above the Fermi level, since valence band (donor-type) states are positively charged when unoccupied and neutral when occupied. The surface Fermi level can be pinned above the Γ--point conduction band

minimum (CBM) by unoccupied, positively charged donor-type surface states. These donors acquire a positive surface charge by emitting electrons into the conduction band. This results in downward band bending and electron accumulation. This combined requirement that the surface states are ionized donors and lie above the Fermi level can be achieved only in *n*-type semiconductors when the Γ-point CBM lies significantly below E_B.

4.4 Indium Nitride Nanowire synthesis

High quality InN NWs synthesis was carried out by VLS mechanism in a high temperature horizontal quartz-tube furnace (used as the CVD system) at a controlled temperature range through the direct reaction between metallic In and NH_3 using Au as catalyst particle (Fig. 4.4). 20 A° thick lithographically patterned catalyst spots were deposited by E-beam evaporation on n^+ (100) Si/ SiO_2 (100-nm-thick) substrate. The thickness and size of the patterned Au catalyst significantly vary the quality of the NWs which has been reported previously [182]. A Boron Nitride boat holding both the catalyst patterned substrate and Indium wire (99.999% purity, Aldrich) was placed inside the quartz tube. The substrate was placed around 3-4mm downstream from the In wire along the gas flow direction. The growth was performed at a nominal temperature between 650^0C to 730 ^{0}C keeping the system pressure constant at 150 Torr for ~30 min. A mixture of 17 sccm N_2 (99.999% purity, National Welders) and 0-20 sccm O_2 (3% in National Welders UHP balanced N_2) was flown over molten In, while the NH_3 (99.9995% purity, Matheson Tri-gas) flow rate was maintained at 100 sccm for the optimum growth condition.

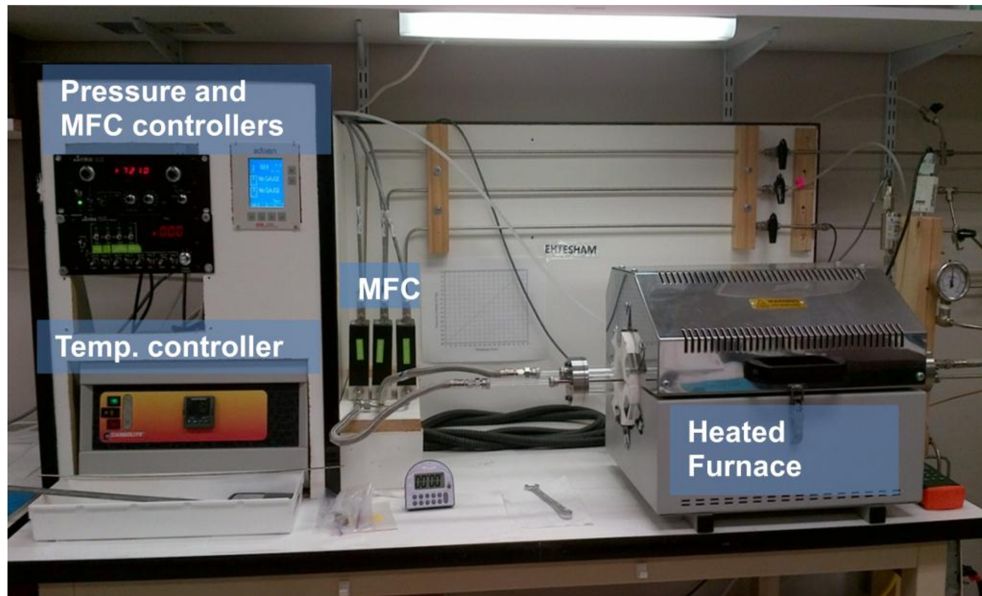

Figure 4.4: CVD system setup, Pressure and MFC controllers, MFCs, Temperature controllers and heated furnace

High quality single crystalline InN NWs were observed to grow along the plane of the substrate in the [110] direction and diameter and length varying in the range from 10-100 nm and 5-50 µm respectively. A systematic study was performed to obtain the best optimized condition for the synthesis of these high quality nanowires. The high quality single crystalline InN NWs are obtained by carefully choosing the optimum combination of various

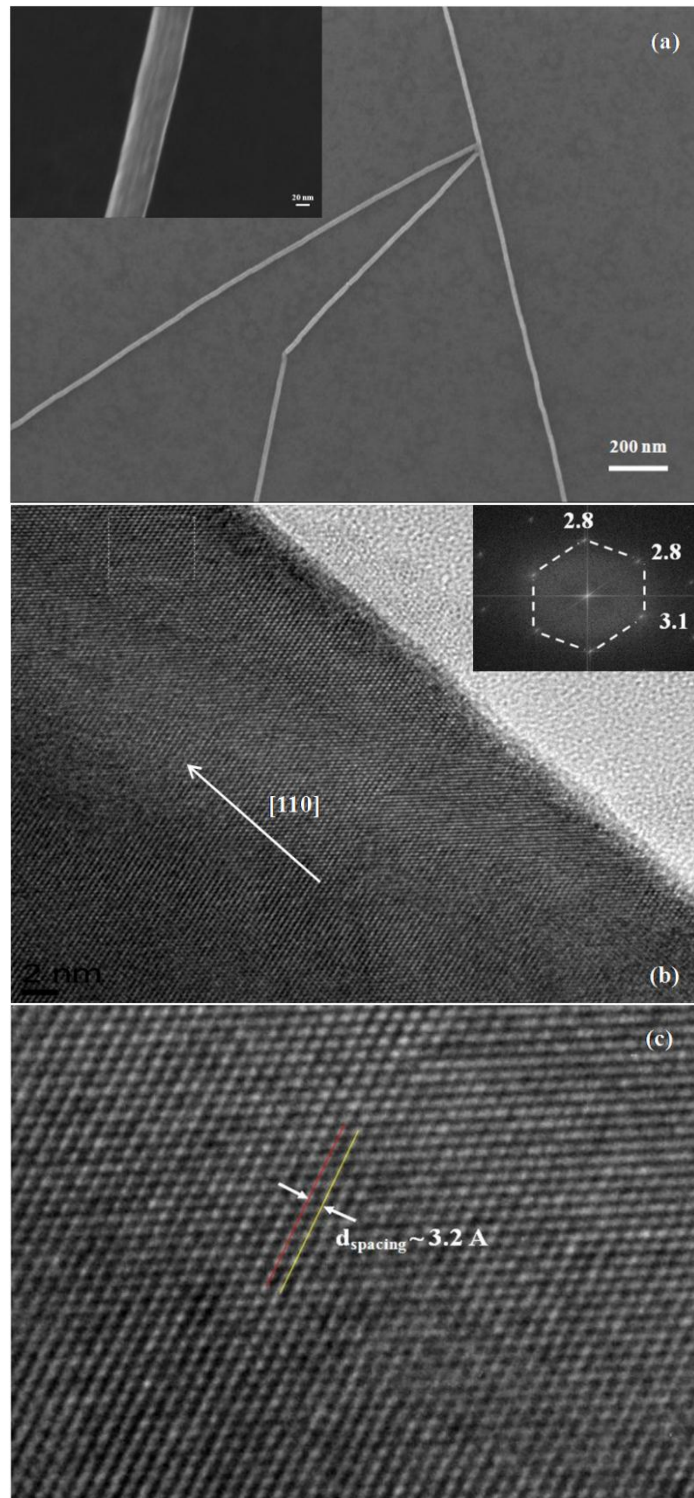

Figure 4.5: (a) A typical SEM image of InN nanowires as-synthesized on a Si/SiO2 substrate. Inset shows a single NW, scale bar is 20 nm. (b) High resolution TEM image of a single NW growing along [110] direction, the inset shows the hexagonal FFT spectrum. (c) Atomic resolution shows the lattice spacing of the NW.

growth parameters including controlled gas mixture between diluted O_2 and UHP N_2, precursor gas NH_3, temperature and pressure as well. Figure 4.5(a) shows an SEM image of typical NWs and deflection and formation of K- junction caused by another NW; the inset shows magnified image of a single NW, the diameter is around 50nm. The single NW on the left side exhibited spontaneous and forced/ barrier-induced bending (the barrier here was another single NW) at angles multiples of 30^0. Figure 4.5(b) shows a lattice resolved TEM image on section of a NW growing along [110] direction, inset shows the hexagonal FFT spectrum with lattice spacing where the wurtizite structure of InN with [001] zone axis and the [110] growth direction are identified. From the HRTEM image (Fig 3.2(b)) there was no outer sheath observed in the NW, which means even in the oxide-assisted growth method there is no evidence of the synthesis of core/shell type of structure where usually a layer of In_2O_3 is coated outside the InN core. Figure 4.5(c) demonstrates the atomic arrangements of InN NW. The lattice spacing of the (100) lattice planes calculated is around 0.32 nm, which is very close to that of bulk InN.

4.4.1 Elemental mapping

To further verify that these NWs are made of high quality InN even in the oxygen environment we have performed Energy Dispersive Spectroscopy (EDS) mapping on section of a nanonetwork. Figure 4.6 (a) shows the Scanning Transmission Electron Microscopy (STEM) image of the chosen nanonetwork, (b), (c), and (d) demonstrate the mapping of In, N- and O- elements respectively. The mapping was done at In-L: 87% FWHM (3.285keV), N-K: 30% FWHM (0.392keV), O-K: 50% FWHM (0.525keV). These images are background subtracted and deconvoluted to account for close overlap

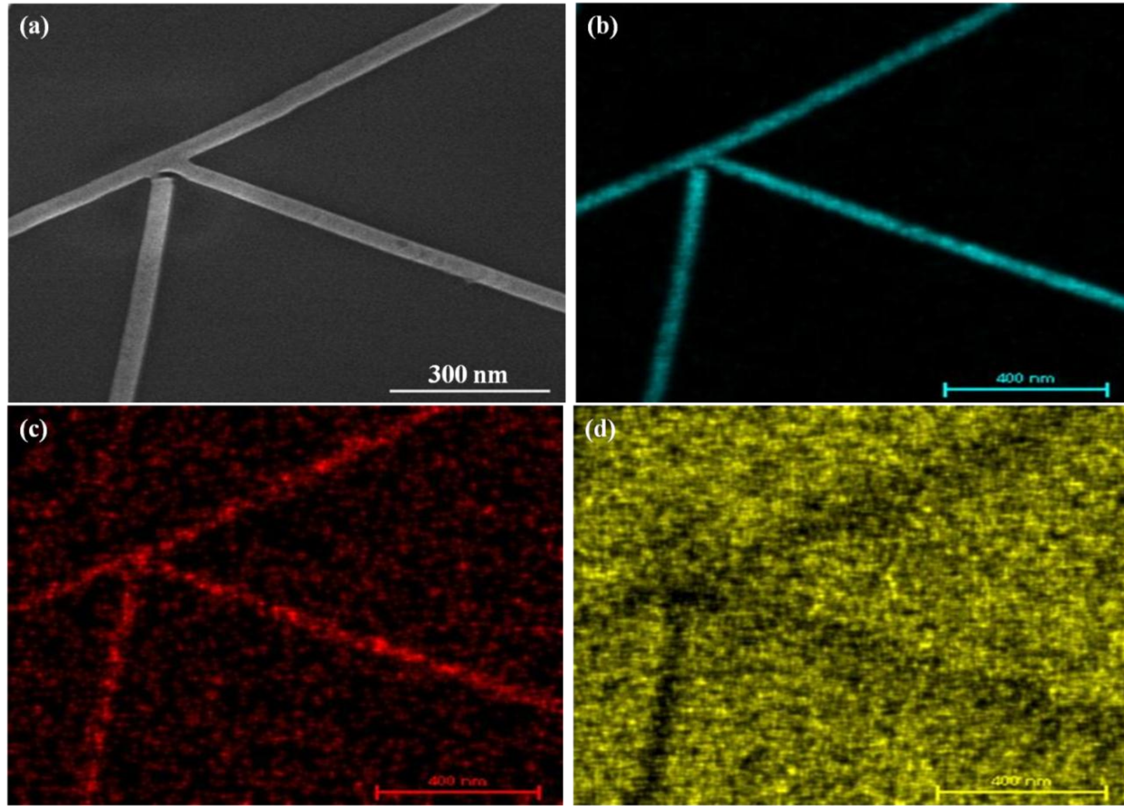

Figure 4.6: Energy Dispersive Spectroscopy (EDS) mapping on section of a nanonetwork. (a) STEM Image. (b) In elemental mapping, (c) N elemental mapping and (d) O elemental mapping along the nanonetwork.

between In-M peak (0.366keV) and N-K peak (0.392keV). However for N- and O- map the background noise was visible due their lighter elemental weight and was not completely removed. For In metal, along the NW growth direction distinct elemental map is clearly seen while for N distinct peaks as well as random peaks are observed due to the previously mentioned reason. A void region along the NW direction making black shade refers to the absence of O peak. Since the NWs were synthesized on thin SiO_2 membrane, peaks are observed in a complementary fashion; along the NW there is vacancy of O peaks and in other area, presence of O peaks.

4.4.2 Raman Characterization

It has been proved that InN has an electron accumulation at the surface that is due to the presence of occupied surface states at the conduction band minimum. Raman spectroscopy is a nondestructive, no contact characterization tool that can be used to determine surface properties of semiconductors. In most cases, Raman spectra shows the coupled LO phonon from bulk (ω_{LO}) band and surface electron induced LO phonon

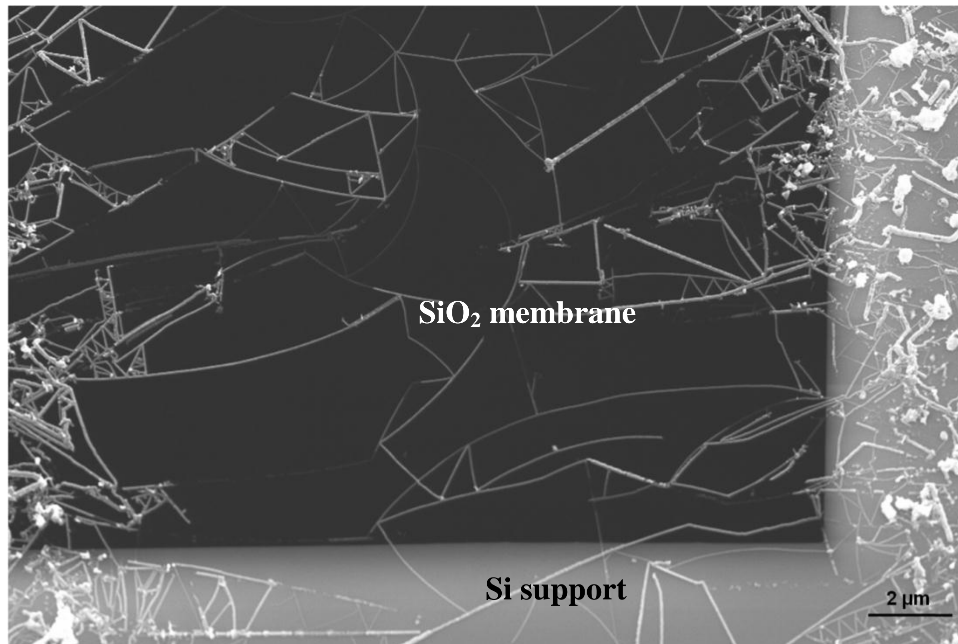

Figure 4.7: NWs growing on a 40 nm thick SiO_2 membrane from catalyst patterns outside the membrane (Si support).

(ωS_{LO}) band if the penetration depth is higher than the width of surface accumulation layer. Jeganathan et al reported Raman spectra peaks for InN NWs for both phonon

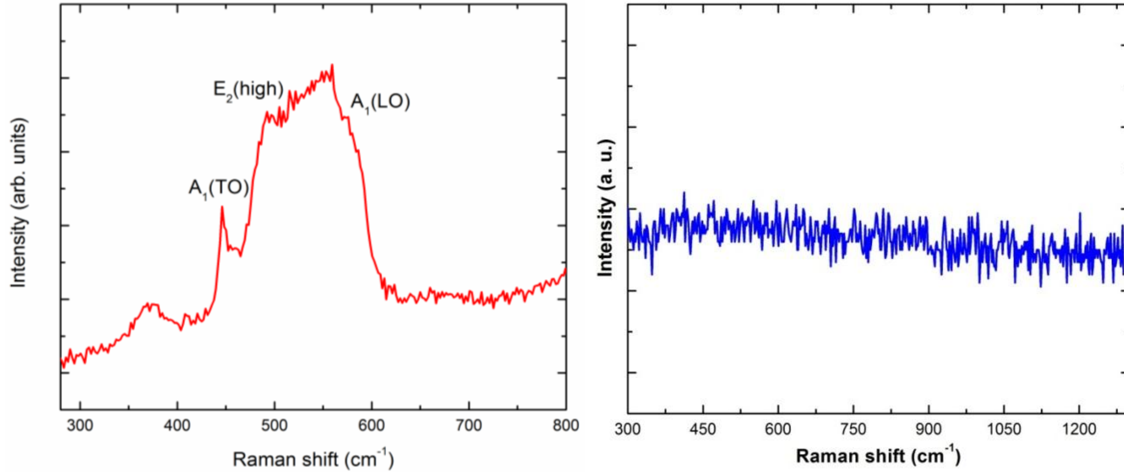

Figure 4.8: (a) Raman spectrum of the InN NW junction showing the A_1 (TO), E_2 (high) and A_1 (LO) phonon peaks at 443, 491 and 594 cm-1. The E_1 (TO) phonon peak at 475 cm-1 is hidden. (b) Raman spectrum of the SiO_2 membrane without InN NW.

modes (E_2(high) and A_1(LO)) at 491 cm^{-1} and 594 cm^{-1} [189]. Due to the electron accumulation they also reported a peak at 627.2 cm^{-1}, spectra taken perpendicular to c-axis of the wires [190]. For InN thin films grown at 500°C, Agulló-Rueda *et al.* also reported strong peaks corresponding to the E_2(high) and A_1(LO) at 491 cm^{-1} and 591 cm^{-1} respectively. The other two peaks found at 443 cm^{-1} and 475 cm^{-1} correspond to A_1(TO) and E_1(TO) phonons of the hexagonal phase [191]. In this study, raman spectroscopy was also performed (Horiba, LabRam 1B) to further obtain verification of the formation of InN nanowires on both the 40 nm SiO_2 membrane TEM grid and on the SiO_2/Si sample. It was observed that the usage of the membrane sample as opposed to NWs grown on the SiO_2/Si sample eliminated the interference from the strong Raman peak from the Si substrate, which occurs in the same wavelength range as the InN peaks. Raman spectra was also taken on the membrane, where NWs were not grown to show that the background does not interact with our results and that only InN peaks are shown. Raman spectra peaks for InN NWs for both phonon modes, E_2 (high) and A_1 (LO), occur at 491

cm^{-1} and 594 cm^{-1}. Two additional peaks can be found at 443 cm-1 and 475 cm-1 correspond to A_1(TO) and E_1(TO) phonons of the hexagonal phase. The Raman spectrum obtained from one region containing an InN NW junction is shown in Fig. 4.8. A junction was used to maximize the area covered by the Raman laser beam so that the signal intensity can be maximized. From Fig. 4.8 (a), we can clearly see the expected E_2 (high), A_1(LO) and A_1(TO) peaks, which confirms the presence of InN NWs. The reference Raman spectra taken on bare SiO_2 surface is shown in Fig. 4.8(b). We observe that in the region where there is no InN NW, there are no peaks, indicating (i) the peaks that we find in Fig. 4.8(a) are indeed coming from InN only.

4.5 Growth optimization: Role of oxygen in the synthesis

Series of experiments were performed to obtain the best growth conditions including flow rates of different gases, process temperature and pressure. Among all different conditions and parameters, gas flow of diluted O_2 and temperature are the most important factors that affect the growth and quality of NWs significantly. The optimum growth condition was obtained with a mixture of 8 sccm oxygen (3% in balance N_2) and UHP N_2, and ammonia flow at a fixed rate. The optimum temperature was found to be 690 ºC while the pressure was not that critical and kept at 170 Torr. The decomposition temperature of InN was reported to be around 550 ºC while the NH_3 break down temperature is more than 700 ºC which suggests that it is necessary to find the appropriate growth temperature and NH_3 cracking mechanism prior to trying other growth parameters. Synthesis in a two zone furnace, where NH_3 cracking occurs at an elevated temperature and growth happens in a lower temperature, is a popular process for InN NWs. Availability of N free radicals and the nucleation; both are the key steps that

affect the quality and growth rate. These two steps are not simultaneous and occurred in two different places which results slower growth rate and non uniform cross section along the diameter and also poor material quality. In our case we are using a single zone furnace where the ammonia cracking and growth occurs at the same chamber.

Ammonia, being a toxic component in the waste streams, can be removed potentially by its selective oxidation processing with oxygen. Ammonia dissociation by dehydrogenation and oxidation has been extensively studied for the potential solution for several ammonia spills. This dissociation technique has been applied here in the synthesis of high quality InN NWs. Depending on the reaction conditions, the dissociation process leads to the formation of atomic nitrogen, molecular nitrogen, NO, N_2O and even water, hydrogen. There have been several reports of using different catalysts for the dissociation of ammonia by oxygen including Fe, Pd, Pt, Au, etc. [192-196]. Among them activation of ammonia dissociation by oxygen on platinum sponge and palladium are the most common [193, 194]. Recently, Lopez et al. reported the oxidation of ammonia on Oxygen covered Au catalyst [195]. In our catalyst mediated growth Au is used as two fold catalysts, one forming Au-Si liquid alloy for the nucleation of NWs and another as catalyst for the dissociation of ammonia. Unimolecular dissociation of ammonia on the surface is difficult and needs a proton scavenger to drive the decomposition. Adsorbed O atoms or OH- hydroxyl groups on the Au surface provides the basis to attract the first H atom from the molecule and are also significant for the consecutive dehydrogenation steps. Prior to starting the growth, 10 sccm of diluted 3% O_2 was flown inside the chamber to pre-cover the 2nm thick Au surface with adsorbed O atoms. This was done by degassing the chamber with a pump at room temperature at around 10 mT pressure and

then the introduction of O_2 and ramping up the furnace temperature up to the growth temperature simultaneously. By the time the temperature raises up to the growth temperature, O atoms are adsorbed on the Au surface. Again, above the eutectic temperature of Au-Si alloy, 2 nm thick Au catalyst deforms and breaks down into Au nanoclusters. These Au nanoparticles initiate the growth of NWs after the super saturation of In vapor and atomic N-obtained from dehydrogenated NH_3 in the Au-Si alloy phase while NWs are observed to have the Au catalysts at tip.

The reaction scheme for the dissociation of ammonia involves three major steps, activation, dehydrogenation and termination step [196]. The 1st step is the activation step where the first hydrogen is stripped off and resulting product NH_2 are attached between Au atoms. In the 2nd or dehydrogenation step, second hydrogen atom is abstracted by a unimolecular or bimolecular reaction and only N atoms sit between Au atoms. It is believed that in this step subsequent reaction happens between the vapor phase-already been adsorbed In metals in the Au-Si alloy and the stripped off N atom, which dictates the nucleation of solid phase InN followed by the supersaturation of both metallic In and lonely N atoms near the surface of Au-Si interface. However this phenomenon is still under investigation and needs further verification. In the last step of ammonia dissociation, left out N atoms which have been formed on the Au surface are eliminated by either N-N or N-O recombination as N_2 or NO by product.

Ammonia dissociation is difficult under Au surface in normal conditions due to the fact that energy barrier for ammonia activation corresponding to the direct reaction on a clean Au surface is higher than the O pre-adsorbed Au surface. To verify the role of

oxygen, systematic experiments were performed with different O_2 flow rates (3% in balance N_2) varying from 0 sccm up to 20 sccm. The concentration of oxygen is

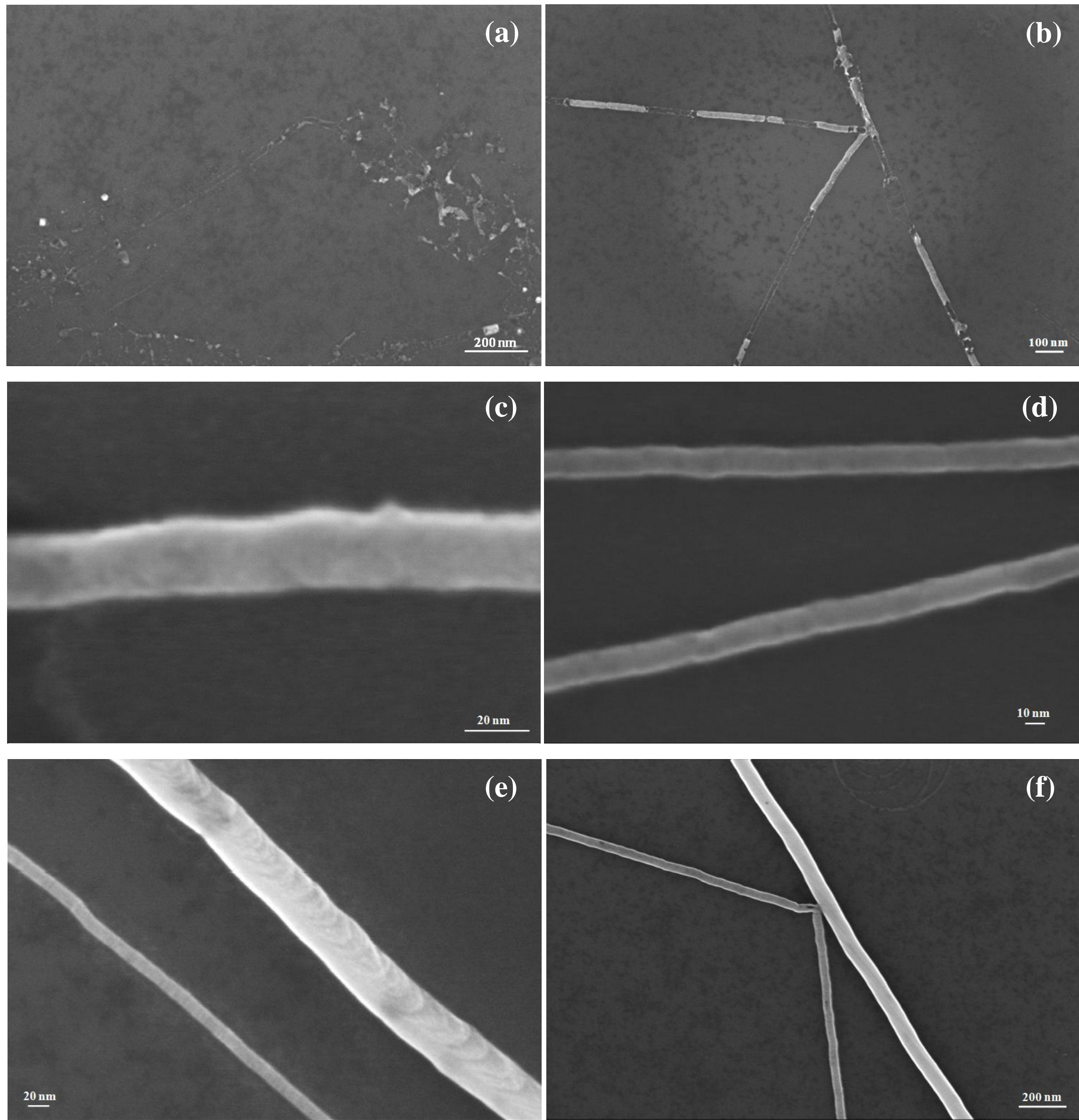

Figure 4.9: The morphologies obtained at different oxygen (3% in balance N2) flow rates in sccm: (a) 0 sccm; (b) 2.0 sccm; (c) 4.0 sccm; (d) 8.0 sccm; (e) 10.0 sccm; (f) 14.0 sccm.

presumed to be increased with increasing flow rates under balance conditions where other parameters are unchanged. Representative images of nanowires synthesized at different oxygen concentrations are shown in Fig 4.9. Figure 4.9 (a) shows the SEM image of a section of a nanowire network synthesized at 0 sccm of oxgen flow. Usually in this condition with zero or no oxygen, there is no nanowire growth, only catalyst areas can be located in SEM; sometimes some traces of decomposed NWs are observed. As stated earlier the dehydrogenation of ammonia is not activated on clean Au surface, however high enough temperature (690 ºC) was able to dissociate some ammonia, and released small amount of atomic N that initiated the nucleation and growth of InN NWs but later on were decomposed due to the fact of having higher growth temperature and at the same time due to not having higher N overpressure that could potentially prevent the decomposition. It is well known that InN starts to thermally dissociate at low temperatures due to the loss of nitrogen partial pressure. From Fig. 4.9 (b) at 2 sccm of O_2, there are portions of solid and decomposed NW along the NW growth direction. The reason may still lie on the verge of having just enough amount of N atom by the ammonia dehydrogenation on oxygen covered Au surface and InN decomposition. Figure 4.9 (c)-(f) show the SEM images of the NWs synthesized at 4 sccm, 8 sccm, 10 sccm and 14 sccm of oxygen flow rates respectively. Significant dissociation of ammonia is activated by the O pre-adsorbed Au surface at or above 4 sccm of oxygen flow rates and the NWs are observed with good crystalline quality and non uniform cross sections. Increased oxygen concentration i.e. flow rate ensures the continuous supply of N atoms at the Au-Si surface and thus the subsequent nucleation and rapid growth of InN NWs which inhibits the decomposition of InN regardless of the effect of higher temperature. It was observed

that higher the oxygen flow rate better is the quality of the NWs and in this report up to 20.0 sccm of oxygen flow rates were observed while after 14.0 sccm the quality does not change much. The atomic configuration of the NWs synthesized at different oxygen concentrations was investigated by HRTEM to identify the material type. Fig 4.10 (a)-(d)

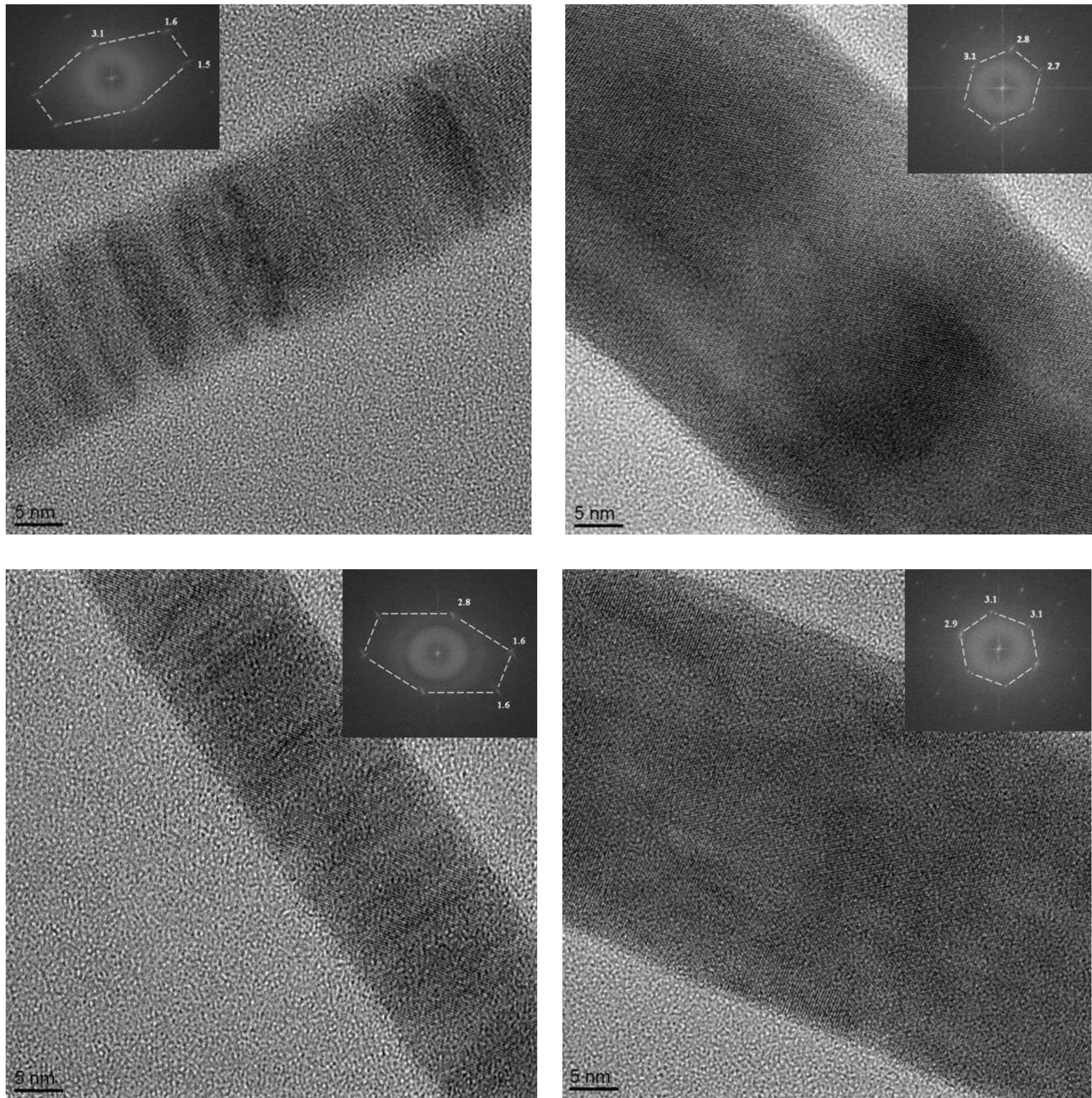

Figure 4.10: HTREM images of single NWs at different oxygen (3% in balance N2) flow rates in sccm a) 2 sccm; (b) 4.0 sccm; (c) 10.0 sccm; (d) 14.0 sccm. Insets show the hexagonal FFT spectra respectively.

show the HRTEM images of the NWs for 2.0 sccm, 4.0 sccm, 10.0 sccm and 14.0 sccm of oxygen flow rates respectively, the insets show the FFT spectra. Even in the oxide mediated growth, the lattice resolved TEM images depict the crystalline quality of the NWs and the FFT spectra indicate the hexagonal wurtzite structure for all different

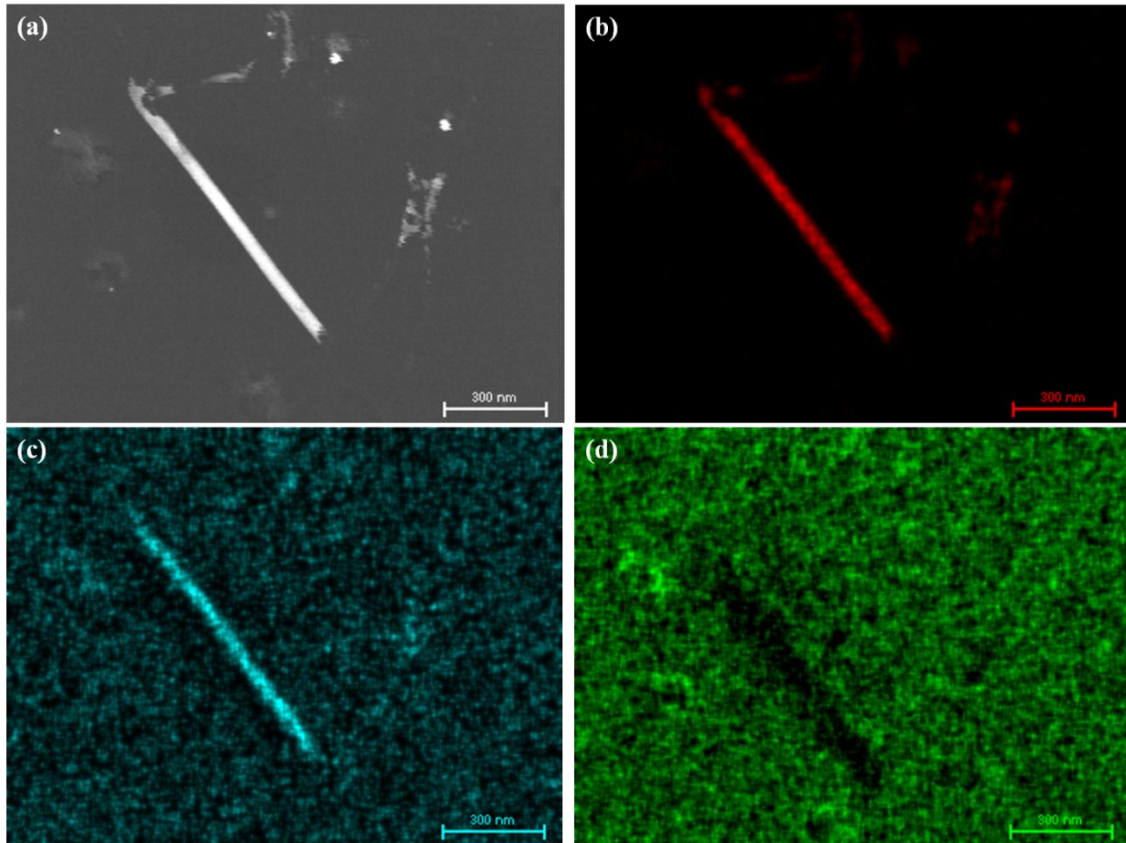

Figure 4.11: Energy Dispersive Spectroscopy (EDS) mapping on section of a nanowire. (a) STEM Image. (b) In elemental mapping, (c) N elemental mapping and (d) O elemental mapping along the nanowire for 4 sccm of O2 concentration.

oxygen concentrations. To further verify the presence of oxygen content, NWs at different oxygen concentrations were investigated by Energy Dispersive Spectroscopy (EDS). The results are shown in Fig. 4.11 (a)-(d) and Fig. 4.12 (a)-(d) for 4.0 sccm and 14.0 sccm of O_2 concentrations respectively. Other concentrations were studied also but

not reported here since they exhibit similar results. For all different oxygen concentrations only In and N elemental peaks are observed but no O peaks can be seen which verifies the material as of pure InN.

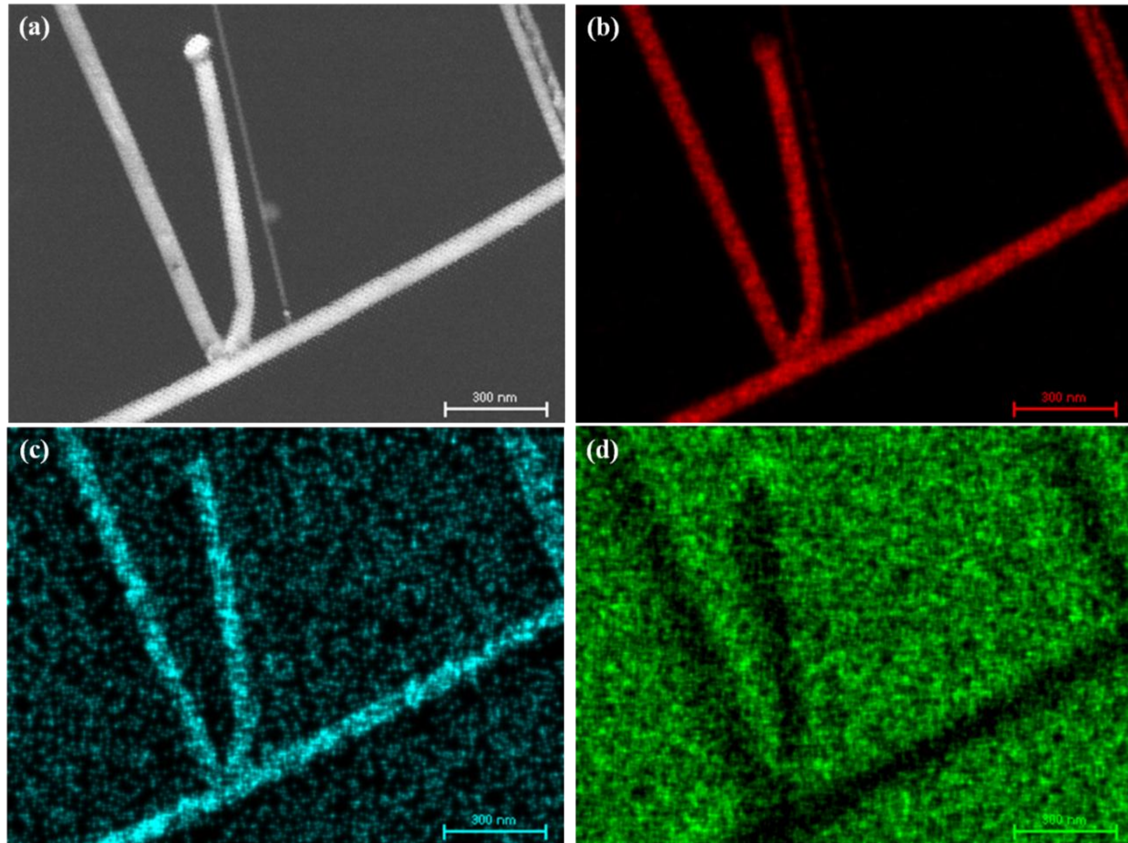

Figure 4.12: Energy Dispersive Spectroscopy (EDS) mapping on section of a nanonetwork. (a) STEM Image. (b) In elemental mapping, (c) N elemental mapping and (d) O elemental mapping along the nanonetwork for 10 sccm of O2 concentration.

4.6 Growth direction modulation

The synthesized InN NWs exhibit two distinctive properties: (i) they are almost always coplanar, especially when growing on the plane of the substrate, and (ii) they change their growth direction either spontaneously or upon meeting an obstacle in their growth path [182]. Figure 4.13 (a) shows an example of spontaneous bending of the NW,

where it bends by an angle of ~30°. Barrier-induced multiple bending of InN NWs can be seen in Fig. 4.13 (b), where the growth of the middle NW is guided by multiple deflections from two other guiding NWs with nanoscale precision. It should be noted here that, for multiple deflections to occur, it is necessary that all three NWs be in the same plane with precise positional accuracy better than a few nanometers, and the guiding NWs should be parallel to or at a slight angle to each other. The angles of deflection of the NWs were generally found to be close to 30°, 60° or 90°.

The geometrical precision of the NW growth and deflection indicates that this is not a random behavior exhibited by the NWs, but is determined by NW material properties. The bending of the NWs at multiples of 60° can be understood from the fact that InN wurtzite crystal has hexagonal symmetry with equivalent free energy of growth along equivalent <110> or $<1\bar{1}0>$ directions [see inset of Fig. 4.13 (d) for the equivalent directions]. The 30° (or 90°) bending of the NWs happens due to a change in the NW growth direction from <110> to $<1\bar{1}0>$ direction (and vice-versa), which is possible if the free energies in these growth directions are similar.

To find out if the NWs can also be guided by lithographically patterned barriers, we deposited 100 nm thick SiO_2 barriers along with adjacent Au catalyst spot as shown in Fig. 4.13 (c). We find that an InN NW indeed deflects back and forth several times at specific angles (~90°) forming nanoscale V-shaped patterns. If catalyst pattern is deposited right at the edge of the lithographic barrier, and the growth is performed for a short enough duration, a single deflection resulting in a V-shaped structure can result. These special V-shaped structures can be readily used to make V-shaped nanocantilevers

(VNCs), by etching the underlying SiO_2 layer; the detail of the fabrication process is discussed later on section 5.8.

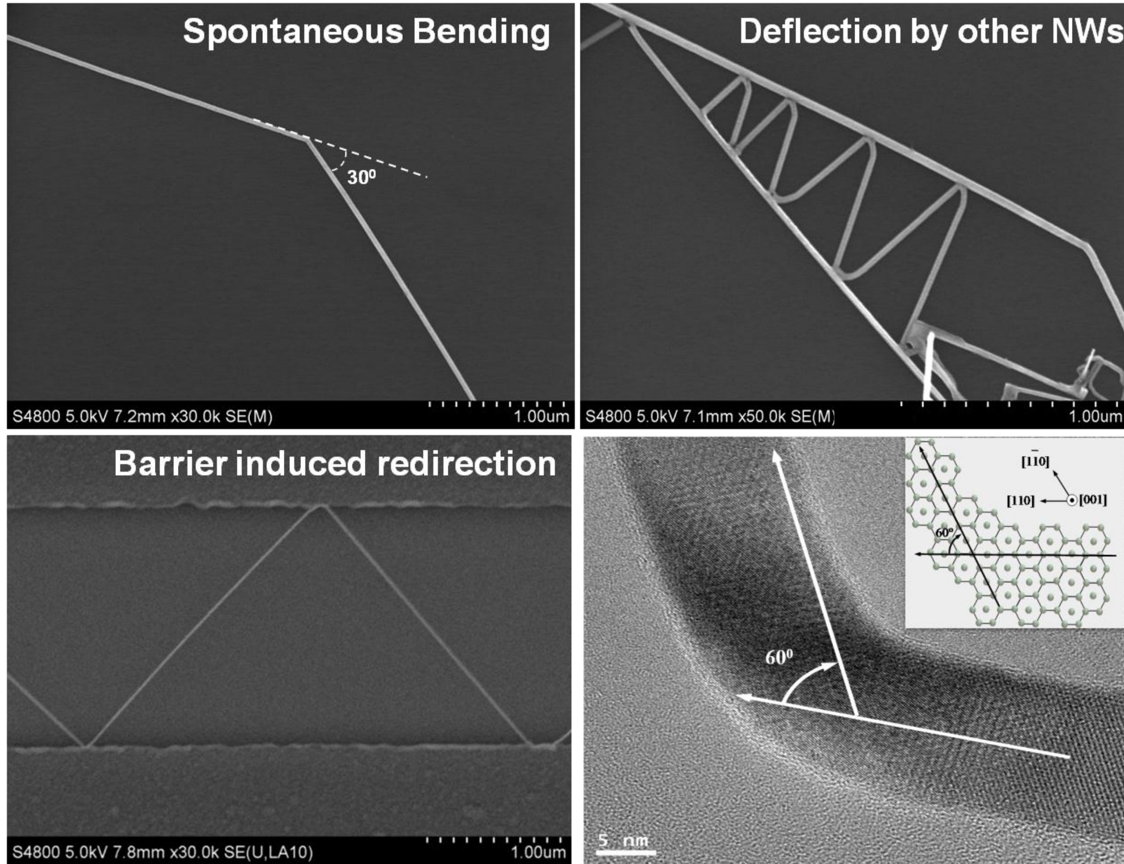

Figure 4.13: SEM images showing (a) spontaneous bending of InN NW, as well as bending caused by (b) two InN NW guides (c) lithographically deposited 100 nm SiO2 barriers and (d) Lattice resolved TEM images of a NW showing atomic arrangement as the growth direction is changed from [110] to another [1$\bar{1}$0], inset shows schematic diagram of atomic configurations for 60° (similar to 120°) bend.

4.7 Electrical Characterization and Diameter-dependent mobility

The electron mobility for InN NWs have been found to be a few tens of cm^2/Vs [197, 198] which is generally much smaller than that in large area thin films (usually

1000 – 2000 cm^2/Vs for carrier concentrations of 5×10^{17} - 10^{18} cm^{-3}) [199-201]. This is in contradiction with GaN NWs which have electron mobility comparable to or exceeding that of GaN thin films [202]. Another intriguing property of InN NWs observed in several past studies is the variation in conductance with NW diameter [203-206]. While some studies reported an increase in conductance with decrease in NW diameter, and proposed theoretical models for the behavior [204] other studies found that the conductance can decrease with decrease in NW diameter [205, 206].

The electrical properties of the NWs were measured by fabricating FETs in a back-gated configuration, with the highly doped Si substrate acting as the back gate. The NWs used to fabricate FETs were grown from a central Au catalyst spot of 2 μm diameter, which allowed only a few NWs to grow from it [207]. Following growth, pre-aligned ohmic contacts consisting of Ti/Al/Ti/Au metal stacks were deposited at the center (covering the catalyst spot) as the source contact, and in a thin surrounding circular strip, as the drain contact [see Fig. 4.14 (a)]. This special device geometry helped the NWs to connect the source and the drain contacts with high probability, alleviating the need for meticulous post-growth alignment [208]. For these NWs the contact resistance was found to be quite small, usually ~1 KΩ [209] which is much less than the NW resistance of hundreds of KΩ, so the device characteristics were obtained from two terminal (i.e. source-drain) measurements only. Our measured contact resistance agree very well with that of ~850 Ω

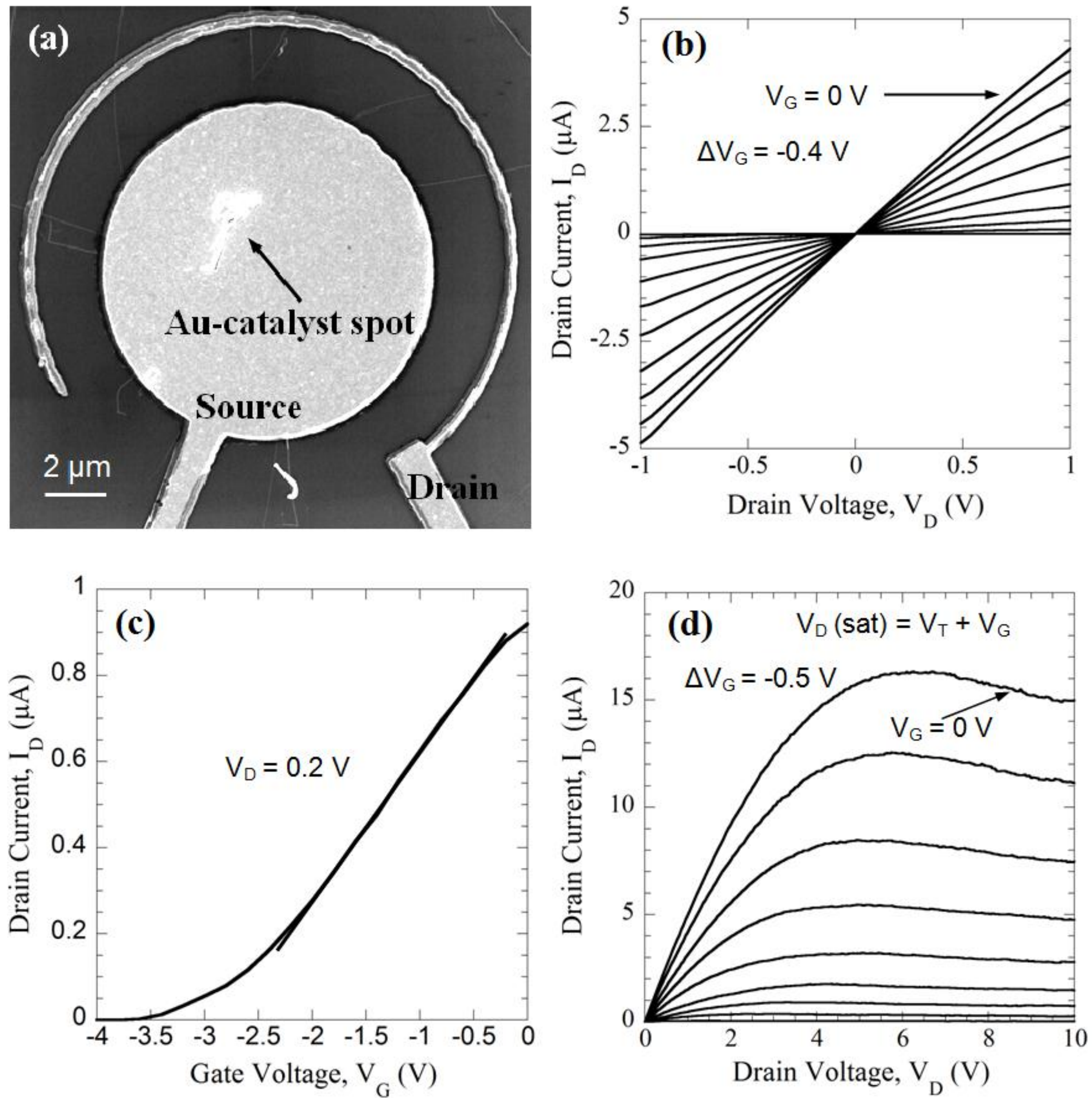

Figure 4.14: (a) SEM image of a 3 NW FET in a back-gated configuration. (b) Id-Vd curves for the InN NW FET at gate bias voltages between 0 V to -3.6 V at intervals of -0.4 V. (c) An Id-Vg curve measured at Vd = 0.2 V, with the dId/dVg slope shown by a straight line. (d) I_d-V_d saturation curves measured for gate bias voltages between 0 V and -4.0 V at intervals of -0.5 V.

reported recently by Werner et al. [206] SEM image of a typical fabricated device containing 3 source-drain connecting NWs is shown in Fig. 4.14 (a). The diameters of the NWs were found to be 17, 39 and 31 nm with a measurement uncertainty of ±1 nm from

SEM images. The measured I_d-V_d and I_d-V_g characteristics of the NW FET are shown in Figs. 4.14 (b) and (c), respectively. The I_d-V_d characteristics show excellent gate control, while the I_d-V_g characteristics indicate a threshold voltage V_{th} = -3.7 V. The I_d-V_d characteristics obtained for larger drain biases are shown in Fig. 4.14 (d). We find that drain current saturates beyond a certain V_d, which although very typical for FETs, has not so far been observed for any InN NW based FET, possibly due to very high carrier density in these NWs [197, 198]. However, the saturation of the drain current is important as it reveals the maximum current possible to obtain from a device under a given biasing condition. From Fig. 4.14 (d), we observe that the saturation drain current reduces with larger V_d, especially for lower gate biases. This is most likely due to heating of the NWs under high current, as observed earlier for GaN [208] and InAs [210] NWs.

The electron mobility μ_e is related to the device transconductance dI_d/dV_g by the equation [202]:

$$dI_d / dV_g = \mu_e (C/L^2) V_d . \tag{4.01}$$

For an FET with multiple conducting NWs, Eq 4.01 can be modified as (assuming a constant mobility for all the NWs):

$$dI_d / dV_g = \mu_e \left(\sum_{i=1}^{n} C_i / L_i^2 \right) V_d \tag{4.02}$$

Here L_i and C_i are the length and capacitance of the ith NW in the FET, and V_d is the drain bias. The capacitance C_i is given as [211]

$$C_i = \frac{2\pi\varepsilon_{eff}\,\varepsilon_0 L_i}{\ln(2h/r_{nw,i})}, \tag{4.03}$$

where ε_{eff} is the effective dielectric constant accounting for the curvature of the NW, h is the thickness of oxide layer, and $r_{nw,i}$ is the radius of the ith NW. Putting the value of the slope 0.33 μA/V obtained from straight line fit to the middle section of the I_p - V_{bg} curve [see Fig. 4.14 (c)] into Eq 4.02, the mobility and carrier concentration are calculated as ~395 $cm^2V^{-1}s^{-1}$ and 2.0×10^{18} cm^{-3}, respectively. It should be noted that the mobility and carrier concentration determined here are averaged over 3 NWs with different diameters, assuming the mobility is constant and independent of the NW diameter. However, while studying several FETs containing multiple NWs with different diameters we noticed that FETs having thicker NWs have lower average mobility than those having thinner NWs. The mobility of NW FETs containing only one NW, or multiple NWs with same diameter, were also found to exhibit similar diameter dependent mobility. This was an interesting observation, based on which we assumed a unique radius dependent mobility $\mu_e(r)$ for the NWs, which enabled us to extract mobility for many different diameters even from devices that contain multiple NWs (see discussion below). Although dependence of NW conductance on diameter has been proposed earlier [203-205], to the best of our knowledge, dependence of mobility on NW diameter has not been proposed or investigated so far, mainly due to the difficulty in determining carrier mobility in InN NWs (through back-gate modulation of charges in a FET configuration) arising out of high carrier density [197, 198].

The overall transconductance for a set of n NWs connecting the source and drain contacts follows from Eq 4.01 as:

$$\frac{\partial I_d}{\partial V_g} = V_d\left(\sum_{i=1}^{n}\frac{\mu_e(r_i)C_i}{L_i^2}\right), \tag{4.04}$$

where the capacitance C_i for the ith NW is given as, $C_i = 2\pi\varepsilon_{eff}\varepsilon_0 L_i / \ln(2h/r_i)$. Here L_i, r_i, and $\mu_e(r_i)$ are the length, radius, and radius dependent mobility of the ith NW, respectively. Thus, separate equations for each FET can be obtained with the right hand side containing a linear combination of $\mu_e(r_i)$. Assuming same electron mobility for NWs with similar diameters (varying within ±2 nm), these equations can be solved uniquely to obtain the mobility corresponding to each radius. Similarly, the drain conductance of the FET, which can be found out from the I_d-V_d characteristics of the NWs, can provide information on the carrier concentration of individual NWs, if we also assume unique radius dependent conductivity $\sigma(r_i)$. The total drain conductance of the FET is the sum of the individual conductance of the NWs in the FET, and is then given as

$$\frac{\partial I_d}{\partial V_d} = \sum_{i=1}^{n}\frac{\sigma(r_i)A_i}{L_i} = \sum_{i=1}^{n}\frac{n_i q\mu_e(r_i)A_i}{L_i} \tag{4.05}$$

Here $\sigma(r_i)$ and A_i are the radius dependent conductivity and cross-sectional area of the ith NW. Once again, assuming NWs with similar radii (varying within ±1 nm) have similar conductivity, they can be calculated as a function of radius from the conductance data of all the devices [similar to the calculations of $\mu_e(r_i)$ discussed above].

To verify the proposed idea of diameter dependent mobility, NW FETs were fabricated in two separate batches several months apart. In the first batch, there were 3 FETs with either one NW or 2 NWs with same diameter. There were 5 other FETs

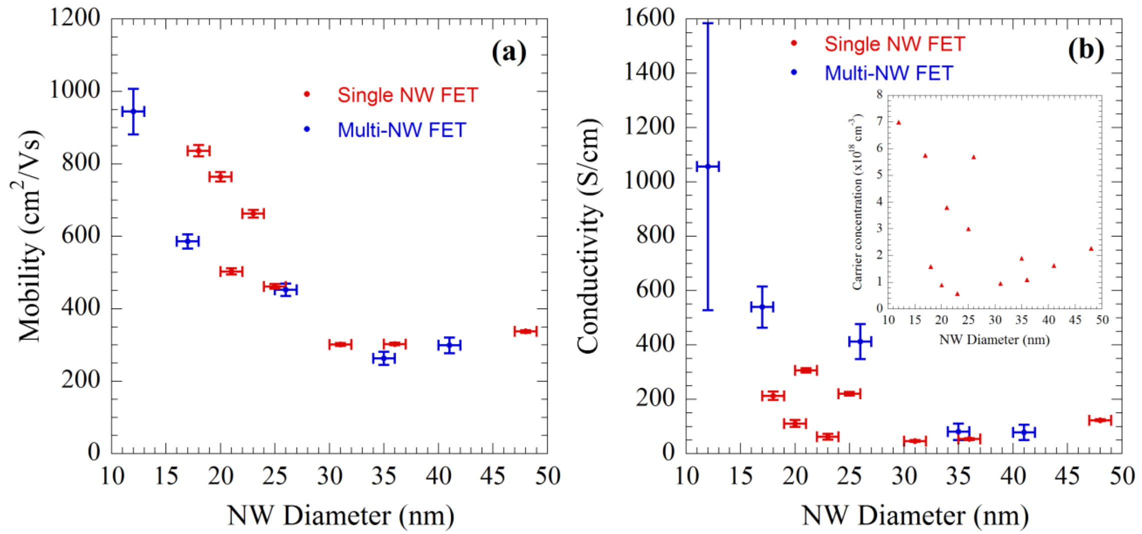

Figure 4.15: Variation of (a) mobility and (b) conductivity of InN NWs as a function of the diameter obtained from single and multi-NW FETs. The respective error bars are also shown. Inset of (b) shows the variation in carrier concentration with NW diameter.

containing multiple NWs with different diameters. By assuming similar mobility for NW with diameter within ±2 nm, the mobility values were solved from Eq 4.04 (see supplementary material for additional information on the NW FETs). The second batch of 5 devices, fabricated several months after the first batch, had either single NW or 2 NWs with same diameter. The mobility $\mu(r)$ of the NWs plotted as a function of their diameter are shown in Fig. 4.15 (a), with the mobility values obtained from FETs with single NW (or with 2 NWs with same diameter) shown with separate symbols from the ones calculated from multiple NW devices using Eq 4.04. As we can see, the mobility decreases regularly as the NW diameter increases from 12 nm to 50 nm. The reduction is very steep from 12 to ~35 nm, after which the change is slower. Interestingly, the variation of $\mu_e(r)$ is very similar regardless of whether it is calculated from single NW or from multiple NW FETs (using equation 4), which clearly supports our proposition of

diameter dependent electron mobility. The conductivity $\sigma(r)$ plotted as a function of NW diameter is shown in Fig. 4.15 (b). Once again we observe a trend of decreasing conductivity with increase in NW diameter, however, the variation is not as regular as that for mobility. The variation of carrier concentration n(r) with NW diameter was determined using the relationship $\sigma(r_i) = \sigma(r_i)n(r_i)q$ for the ith radius, and is shown as an inset in Fig. 4.15 (b). Like $\sigma(r)$ and $\mu(r)$, n(r) also increases with decrease in NW diameter, but not as regularly as mobility. Since conductivity and carrier concentration varies as square of the NW radius (as opposed to mobility where the NW radius appear in a logarithmic term), their variations due to inaccuracies in diameter can be quite large. This could be partly responsible for the less regular variation of the conductivity and carrier concentration with NW diameter compared to mobility.

It is worth mentioning here that in most of the studies reported so far on electrical characterization of InN NWs, only the variation in conductivity with diameter has been reported, but not carrier mobility, since carrier mobility could not be determined experimentally in most cases. Therefore, it was difficult to conclude whether the carrier concentration, or the carrier mobility, or both, were responsible for the observed conductivity variation with NW diameter. Our experimental results reveal that both carrier concentration and mobility changes strongly with NW diameter and contributes to the conductivity variation. The measurement uncertainty for NW diameter and diameter grouping would lead to uncertainty in the calculated mobility, carrier concentration, and conductivity values. For single NW devices, the error is mostly from the uncertainty in diameter measurement from SEM images of ±1 nm. For multi-NW devices, the errors are larger and are contributed by diameter measurement uncertainty and the effect of

grouping. Procedures for calculating the errors are described in detail in the supplementary information. The calculated error bars in mobility and conductivity are shown in Figs. 4.15 (a) and (b).

The observed variation of carrier mobility with NW diameter was modeled by assuming two parallel conduction channels in InN NWs, one formed by the surface accumulated electrons, and the other by the core electrons, following earlier propositions [204, 206]. Accumulation of electrons at the surface of InN thin films has been experimentally verified [212, 213], and the same is also believed to hold true for InN NWs [197, 214, 215]. In our model, we consider that the surface electrons are confined to a depth of only a few nm, and have different density and mobility compared to the core electrons. Since the confinement of the carriers is determined by the Fermi pinning at a level above the conduction band [212, 213] when the diameter of the NW changes, the distribution profile of the carriers with distance beneath the surface can generally be expected to remain the same. For InN thin films, this charge distribution has been determined numerically by solving Poisson's equation within modified Thomas-Fermi approximation [212]. For our simulations, we approximated the carrier profile reported in [213] to describe the variation of surface carrier density n_s, which is found to approximately vary as $n_s = n_0 e^{-\sqrt{x/4}}$, where x is the distance inside the surface of the NW in nm, and n_0 is the density (areal) of charges at the NW surface. The total surface carriers denoted as N_s and the total core carriers denoted as N_b, are given as,

$$N_s = L\int_0^{r_0} 2\pi(R-x)n_s(x)dx, \qquad N_b = n_b\pi(R-r_0)^2 L \qquad (4.06)$$

Assuming that the surface and core electrons N_s and N_b, move with mobility of μ_s and μ_b, respectively, the average mobility μ_{eff} is given as: $\mu_{eff} = (N_s\mu_s + N_b\mu_b)/(N_s + N_b)$. The conductivity is then calculated as: $\sigma = q\mu_{eff}(N_s + N_b)/(\pi R^2 L)$. The simulated electron mobility and conductivity as a function of NW diameter are shown in Fig. 4.16. In our simulations, we used $r_0 = 2$ nm, $n_b = 5.67\times10^{18}$ cm^{-3}, $n_0 = 1.15\times10^{19}$ cm^{-3}, $\mu_s = 1400$ and $\mu_b = 10$ cm^2/Vs, to obtain the least square fit to the mobility data. Interestingly, the mobility of the surface electrons of 1400 cm^2/Vs used in our simulations is much larger than the mobility expected for thin films for n = 5×10^{18}-10^{19} cm^{-3}, which should only be a few 100 cm^2/Vs, based on measurements on InN thin films [199-201]. The high mobility could be due to better screening of charge carriers from remote ionized impurities by high density of surface electrons, which is generally observed for two-dimensional electron gas (2DEG) systems [217, 218]. The core carrier mobility of 10 cm^2/Vs is comparable to what has been generally measured on larger diameter InN NWs [197, 198].

From Fig. 4.16 (a), we observe that the carrier mobility calculated from experimental data fits quite well with the mobility vs. diameter plot determined from equation (4.04). However, measured NW conductivity deviates significantly from the simulated values as seen in Fig. 4.16 (b). This could be partly due to the presence of a few nm thick oxide layer on the NW surface, which would underestimate the conductivity of the NWs by increasing the NW diameter used in our calculations compared to the actual diameter of the conducting core. Our TEM images have shown

presence of these oxide layers [207], which have been observed by other researchers as well [206]. For mobility calculations, the

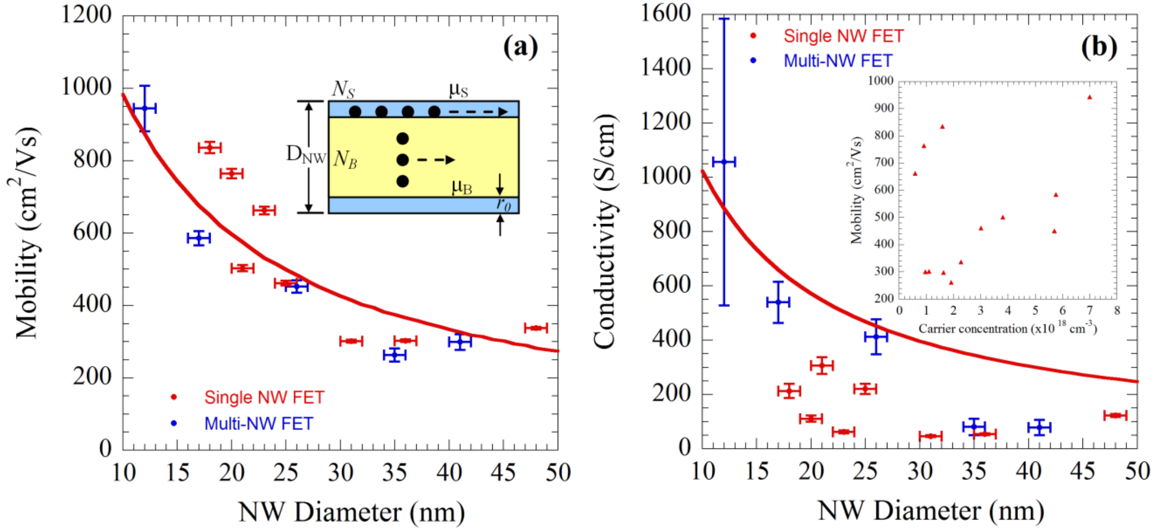

Figure 4.16: Variation of (a) mobility and (b) conductivity of InN NWs as a function of NW diameter fitted with diameter-dependant mobility and conductivity obtained from theoretical modeling (solid lines). Inset of (b) shows the variation of mobility with carrier concentration.

diameter appears in the logarithmic term in Eq 4.03, so small deviations do not cause a significant error in the calculated mobility. The inset of Fig. 4.16 (b) shows the variation of mobility with carrier concentration in the NWs. As we can see, the mobility increases fairly monotonically with increase in carrier concentration, except for a few data points (i.e. 18, 20, and 23 nm diameters) that belong mostly to the NW FETs fabricated in the later batch, where NWs might have developed thicker overgrown oxide layer. In spite of some deviations, the overall trend clearly supports our model, which predicts higher mobility and carrier concentration for lower diameter NWs, where properties of the surface electrons dominate. It should be noted that the increase in mobility with carrier

concentration is quite unique, and similar to that observed for 2DEG systems in modulation doped heterostructures [216, 217]. Since in these systems the mobility is mainly determined by remote ionized impurity scattering, it is possible that the later also plays a dominant role in determining surface electron transport in the InN NWs. Notably, the trend is opposite to that observed for InAs (with similar material properties as InN) NWs [218, 219], and also InN thin films [200, 201], where mobility has been found to decrease for increasing electron concentration.

CHAPTER 5

INDIUM NITRIDE NANOCANTILEVERS

This chapter briefly discusses the details of the fabrication steps and related issues in realization of novel V-shaped InN NW based nanocatilever (VNC) sensors using Ebeam lithography. First, the development of InN nanoresonators and then the fabrication steps of the NEMS nanocantilevers are explained. The mechanical properties, noise sensitivity are presented also with theoretical models.

5.1 Introduction

In recent years, one of the most significant applications based on nanowires is nanoelectromechanical devices. A typical example of a silicon nanowire based nanoelectromechanical device is shown in Fig. 5.1. Nanoelectromechanical systems (NEMS) are electromechanical systems, much like microelectromechanical systems (MEMS), mostly operated in their resonant modes with dimensions in the nanoscale [219]. In nanoscale regime, they come with extremely high fundamental resonance frequencies, diminished active masses, and tolerable force constants. The quality (Q) factors of resonance are in the range from 10^3 to 10^5—significantly higher than those of electrical resonant circuits. These attributes collectively make NEMS suitable for a multitude of technological applications including resonant sensors for ultrahigh-

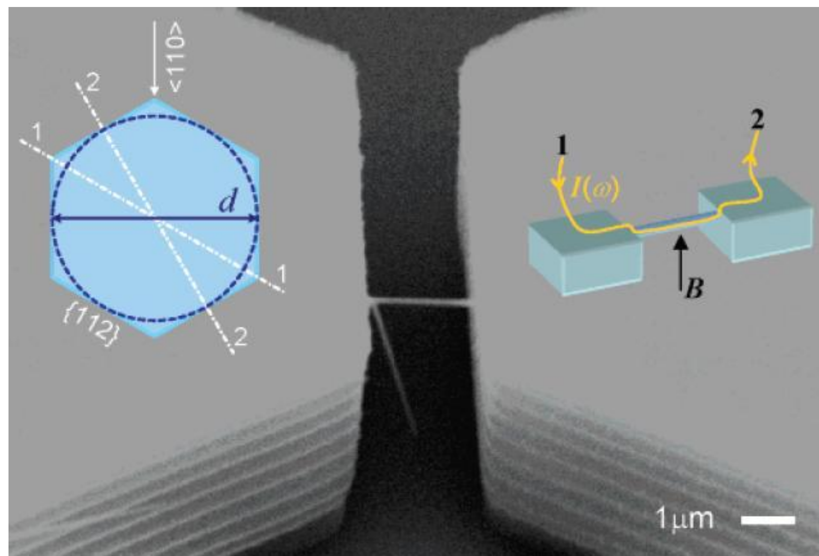

Figure 5.1: A typical example of a silicon nanowire based NEMS resonator (Ref. [224]).

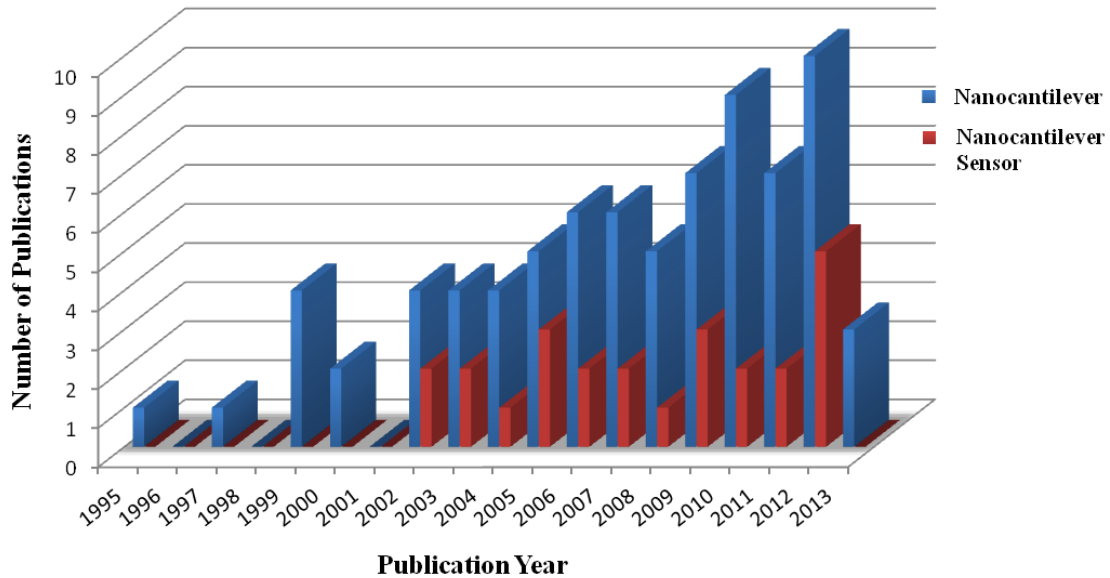

Figure 5.2: Plots showing the number of yearly peer reviewed publications as obtained from Web of Search with a key “nanocantilever” and “nanocantilever sensor”.

resolution mass sensing [220], force detection [221], quantum electromechanics [222], electromechanical signal generation and processing [223], and high-speed logic and computation [224].

In NEMS based sensors the system stimulation and transduction is sought to perform by electrical means, but the actual sensing is performed mechanically, taking advantage of the exceptionally high quality factors (in resonance) available in these systems that are normally not possible to achieve in electrical systems. There have been attempts to fabricate NEMS devices based on NWs and NTs. However, in addition to the problem of integration as mentioned above, NEMS sensors in general, and those based on NWs (or NTs) in particular, suffer from the problems of transduction of the mechanical signal into electrical form. Unlike MEMS based cantilever sensors, research activity in the area of NEMS sensors has not witnessed a rapid progress in the last two decades due

to the aforementioned reasons, as evidenced by the results of a Web of Science literature search of peer reviewed papers published by year for the period of 1990-2013, using the keywords “nanocantilever,” and “nanocantileve sensors”, shown in Fig. 5.2.

Various techniques have been employed to transduce the mechanical deflection of the NEMS device, which includes optical, electron beam, magnetic, radio-frequency transmittance, and piezoresistive [221-225]. However, with the exception of piezoresistive transduction, none of these techniques are applicable for simultaneous deflection transduction of multiple NEMS devices in an integrated circuit. Another significant limitation with most NEMS sensors reported in the literature is they almost invariably have a linear geometry (due to obvious ease in fabrication and alignment), and are fixed at both ends, acting as a beam resonator rather than a cantilever resonator. This geometry greatly reduces the sensitivity of these devices to changes in physical quantities that needs to be measured. If instead, a V-shaped nanocantilever (VNC) is used as the sensor, it will not only dramatically improve detection sensitivity, but will also provide ready means for signal transduction (based on resistance change caused by deflection) through contacts established at the two arms.

This research focuses on the development of VNC probes utilizing the special properties of InN NWs. The special shape of the InN NWs will be achieved inexpensively through barrier patterning which will allow us to not only use them as true cantilever resonators, but also transduce their deflection from change in resistance between the two arms (caused by deflection in an electric field as well as possible piezoresistive effects). The small diameter attainable for these NWs along with the high density and mobility of the carriers (discussed in the previous chapter) allows them to be

densely packed in a small area, and use them in multimodal detection of analytes based on measured changes in multiple parameters, like SWF, mass, and electrical conductivity due to molecular attachment.

5.2 InN Suspended nanostructures

Viable processing of V-shaped nanocantilever relies heavily on expensive and complicated electron-beam lithography technique. It also requires extensive understanding of various processing steps including PECVD oxide deposition and etching of Oxide. As a realization of VNCs we will first start with fabricating and characterizing InN based nanoresonators (InN suspended nanostructures) which is described in the following section. Nanoelectromechanical systems (NEMS) resonators have the potential to have significant impact in

- ❑ Resonant sensors for ultrahigh-resolution mass sensing
- ❑ Force detection
- ❑ Electromechanical signal generation and processing
- ❑ Biosensor applications

5.3 Fabrication of InN NEMS resonators

There have been few reports of top-down lithographic technique and surface nanomachining for the fabrication of NEMS resonators but it's not very well developed technique. To date, most NEMS resonators have been fabricated using chemical-synthesis-based bottom-up approach and here in this research the bottom-up technique has been adapted with as grown coplanar InN NWs. Apart from the well known bottom up approach, our InN NWs have certain distinct advantages over other type of

nanostructures due to having high crystalline quality, perfectly terminated surfaces and sizes down to the molecular scale.

Fabrication steps

InN NW based resonators are fabricated on Si/SiO_2 samples. 300nm SiO_2 is grown thermally on p typed doped Si. The whole process is done by E Beam lithography. The details of the processing steps are described below:

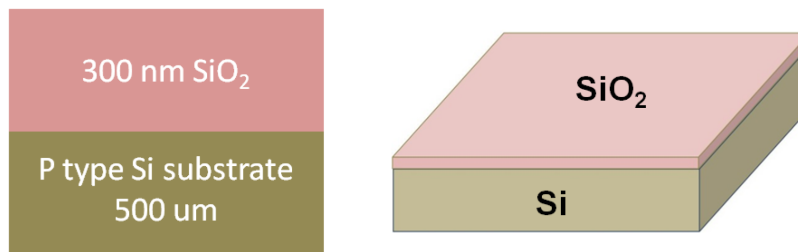

Figure 5.3: Wafer information for the processing of InN NEMS resonators

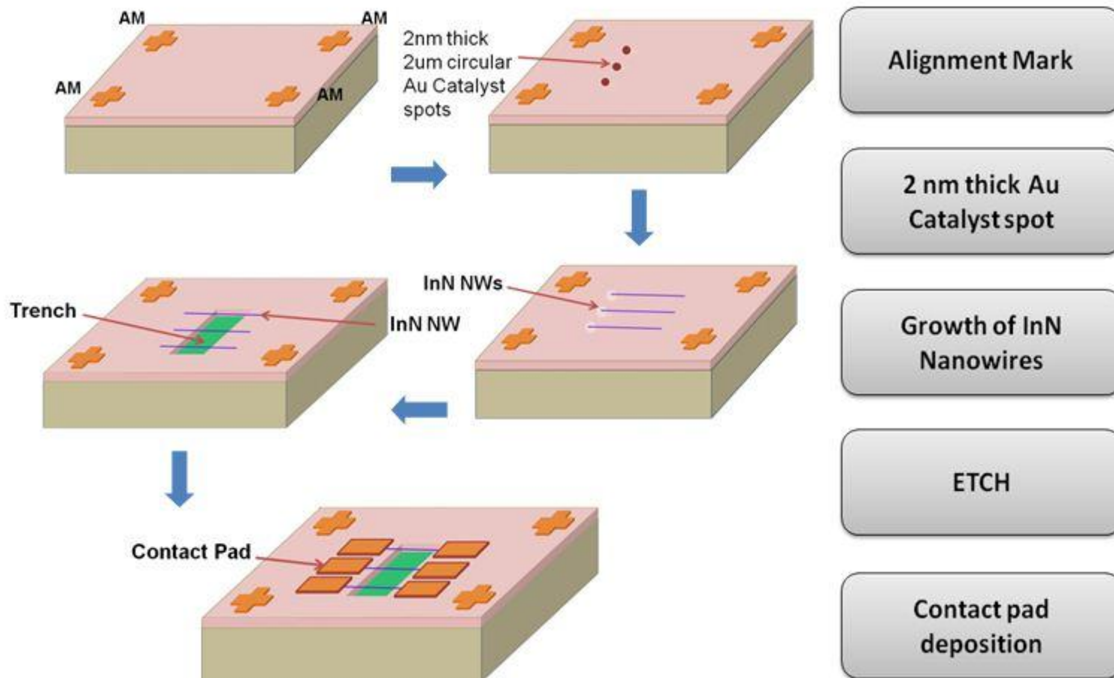

Figure 5.4: The fabrication process flow of nanoresonators

Step 1: Alignment Mark

Si/SiO_2 2 inch wafer is diced into a number of 3x3 mm^2 small pieces for the processing of NEMS resonator. Each of these sized samples can have arrays of resonators with optimize designing. DesignCad software was used for the mask design which is interfaced with the Jeol SEM. “Plus” alignment marks are designed and patterned on sample as the reference layer for subsequent lithography steps. These alignment markers are patterned by E-beam lithography and thick metallization was done in the E-beam evaporator. To make sure that during the synthesis process of InN NWs there is no growth from these AMs, metals other than Au is preferred to have different eutectic temperature, for our case thick Ti /Al/Ti/Au metal stacking was done.

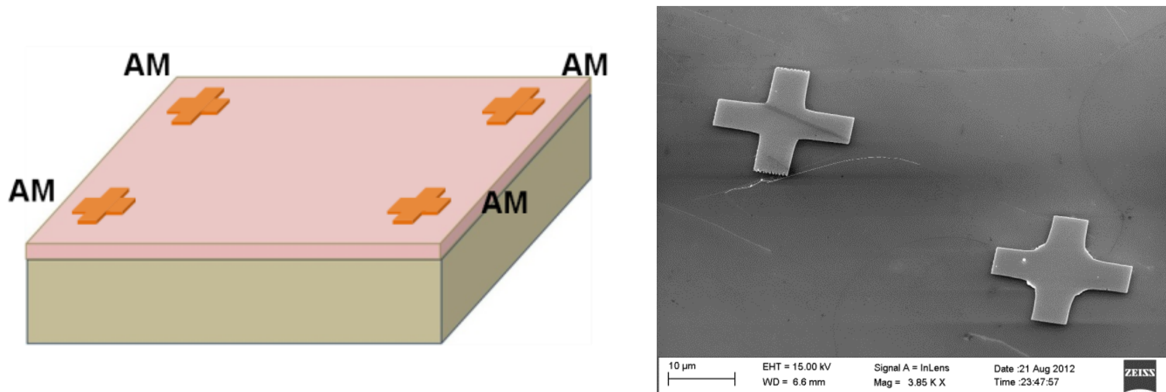

Figure 5.5: (a) Schematic representation and (b) SEM image of alignment mark

Step 2: Catalyst patterning

2 um diameter catalyst spots were patterned by E beam lithography near the AMs and then 2 nm thick Au was deposited by E beam evaporation.

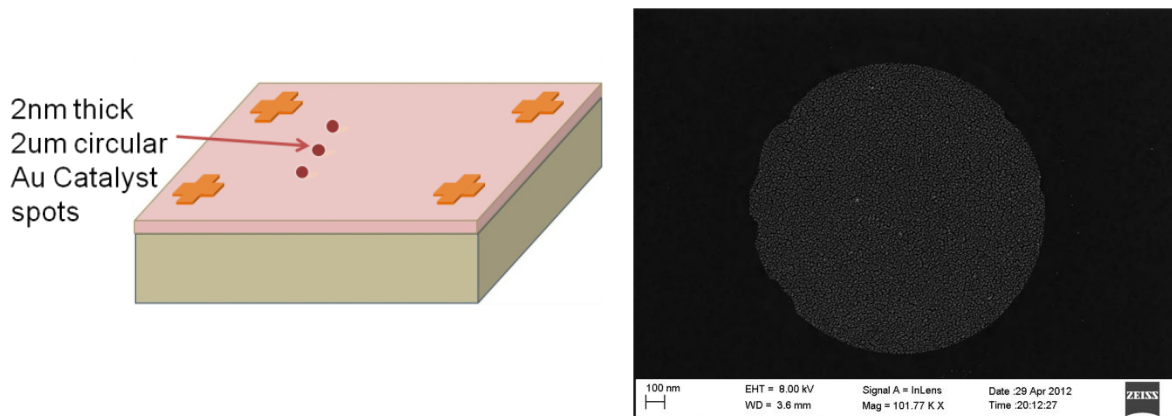

Figure 5.6: (a) Schematic representation and (b) SEM image of 2 nm thick, 2um diameter catalyst spots

Step 3: Growth of InN Nanowires

InN NWs were synthesized from the catalyst spots by VLS mechanism in the CVD chamber as discussed previously in the NW synthesis section (previous chapter). The growth condition needs to be perfectly optimized to obtain horizontal coplanar NWs for the subsequent process steps.

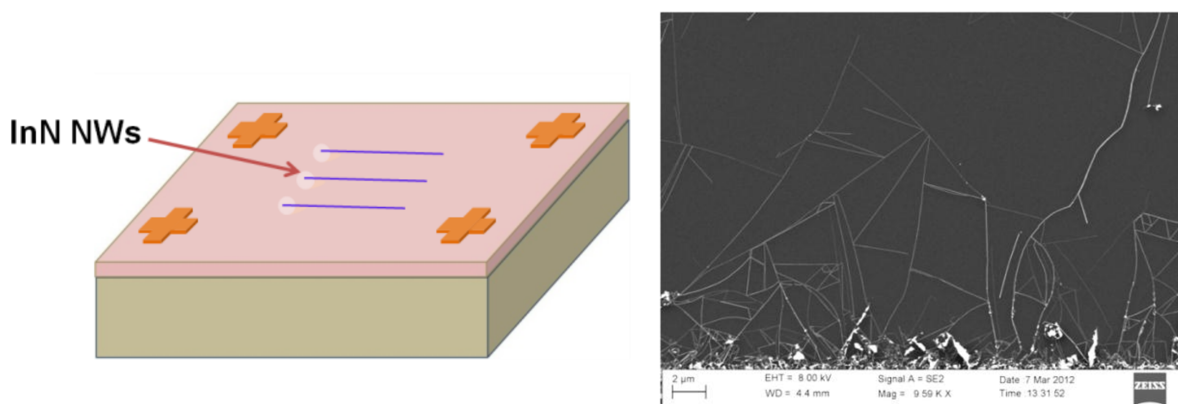

Figure 5.7: (a) Schematic representation and (b) SEM image of NWs grown from catalyst spot

Step 4: Trench Etching

After the growth, the sample is characterized by SEM to find suitable NWs close to Alignment marks. The trenches are designed by Design Cad according to the position and coordinates of the NWs referenced from the AMs. E beam lithographically pattered 2 um wide trenches were then etched by wet Buffered Oxide etching technique in this step. The depth of the trench is usually 70-100nm.

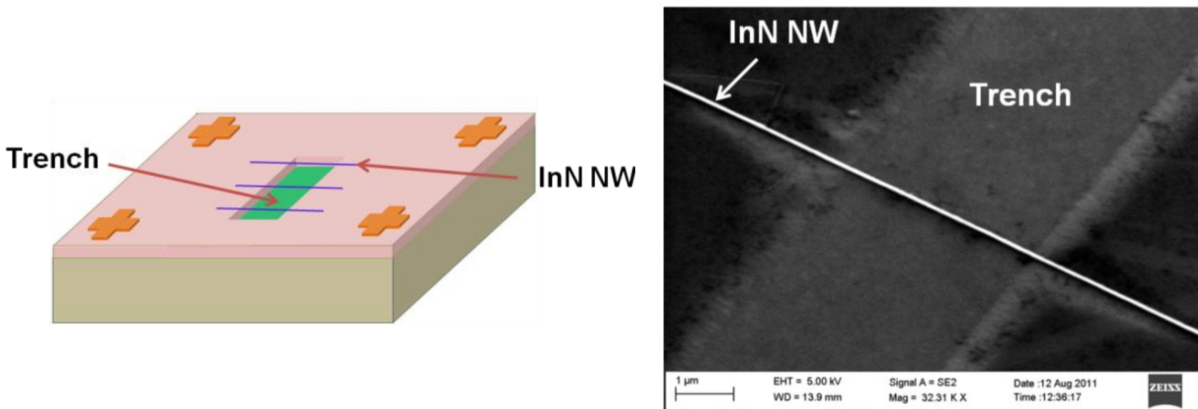

Figure 5.8: (a) Schematic representation and (b) SEM image of NW and etched trench

Step 5: Contact pad deposition

This last step involves connecting the suspended NWs to the outside world by means of metal contact pads. A Ti/Al/Ti/Au metal stack layer was deposited by E beam evaporation technique and the probe contacts and contact pads are patterned in this same step by E beam lithography.

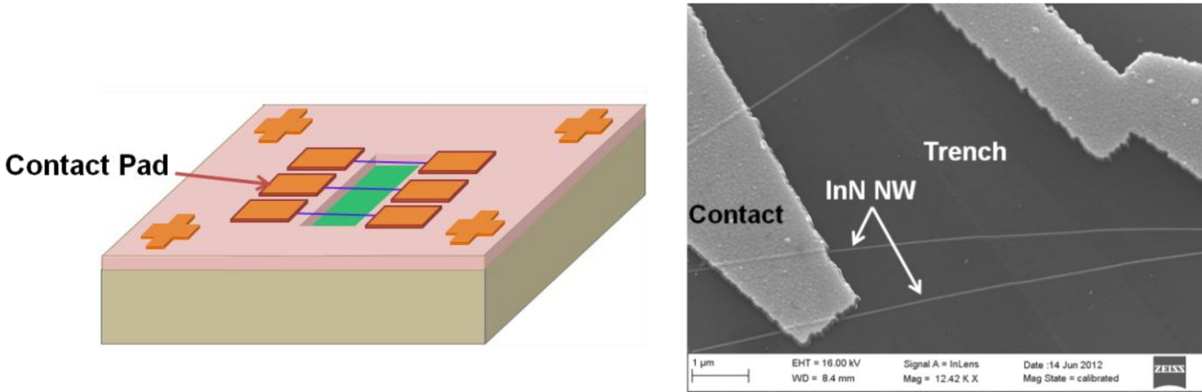

Figure 5.9: (a) Schematic representation and (b) SEM image of NW, trench and probe contact

5.4 DC characteristics of InN NEMS resonator

The dc characteristics of InN nanoresonator devices were taken for both the cases in back gate configuration: before trench etching (NW on the Oxide surface) and after etching (NW suspended across the trench, over the doped Si). Figure 5.10 shows the output characteristics (I_d-V_d) of the same devices before and after trench etching. The electron mobility μe can be calculated from $I_d - V_g$ curve using the relationship: $dI_D/dV_G = \mu e\ (C/L^2)V_D$, where C and L are the capacitance and length of the NW, respectively. The mobility obtained from the I-V characteristics are 30 cm^2/Vs which is much lower than the previously reported mobility values (Chapter 4), possibly due to the processing steps affecting the surface of the NW.

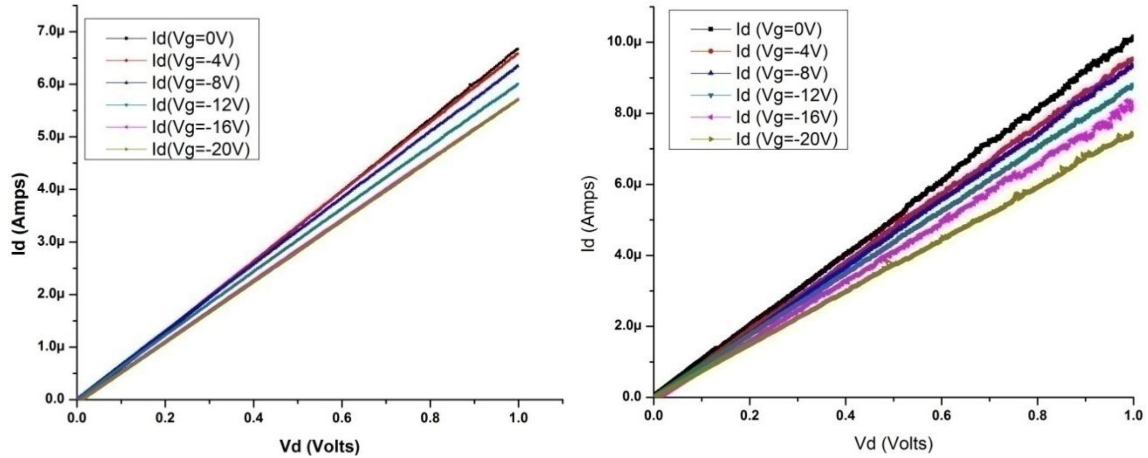

Figure 5.10: The dc characteristics curves for InN nanoresonators, (a) before trench etching and (b) after trench etching.

The drain current at zero gate bias and also the percentage change of gate modulation both show increasing trend after etching the trench. It was observed that after etching the trench, the NW tends to fall inside the trench surface due to the surface tension of BOE and DI. This makes the NW resting very close the p-doped Si surface which increases the capacitance and hence the drain current. Also there is another possibility of the NW conducting through the back gate doped Si and adding the leakage current at higher negative gate bias.

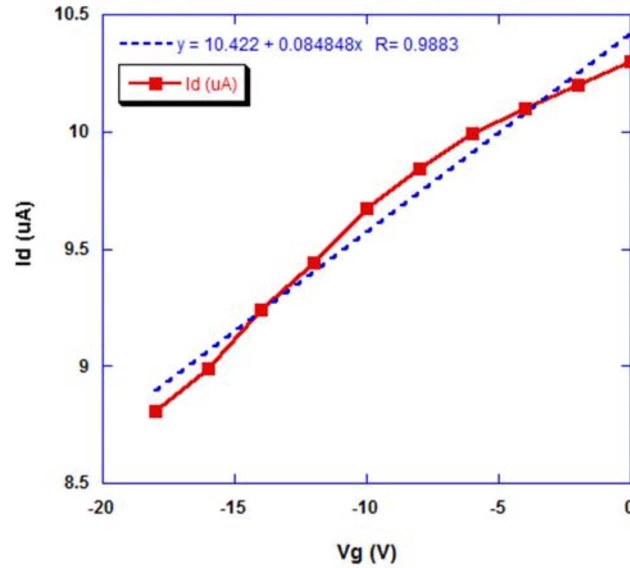

Figure 5.11: $I_d - V_g$ characteristics of InN NEMS resonator, from this curve we calculated the mobility of the InN NW.

5.5 Optimization of the release process of suspended Nanostructures

Releasing NWs by etching the oxide is one of the most critical process steps for any NEMS based suspended nanoscale devices. There are mainly two approaches to etch the underneath SiO_2, one is BOE wet etching and the other one is dry ICP etching; both of them are discussed in the next section.

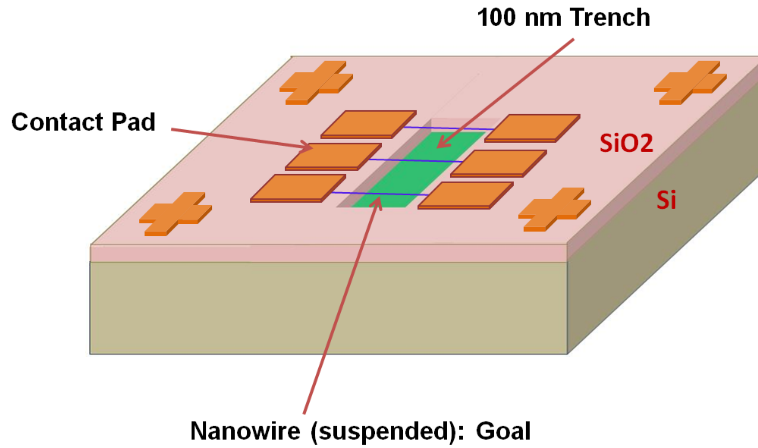

Figure 5.12: The schematic representation of the final NEMS resonator, NWs should be going across the trench with no sagging.

5.5.1 Buffered Oxide Etch (BOE) Wet Etch

Buffered oxide etch (BOE), also known as buffered HF or BHF, is a wet etchant used in micro- and naono-fabrication. Its primary use is in etching thin films of silicon dioxide (SiO_2) or silicon nitride (Si_3N_4). It is a mixture of a buffering agent, such as

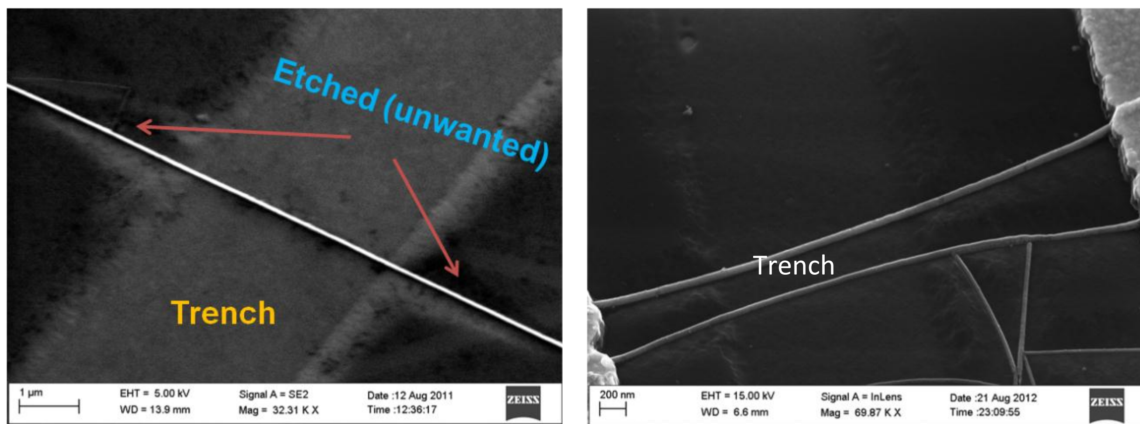

Figure 5.13: SEM images of InN NWs on the trenches, both cases the NWs fell down inside the trench.

ammonium fluoride (NH_4F), and hydrofluoric acid (HF). Buffered oxide etch can have different concentrations; the common buffered oxide etch solution comprises a 6:1 volume ratio of 40% NH_4F in water to 49% HF in water. This solution is used to etch our SiO_2 and the etch rate for thermally grown oxide is approximately 2 nm/second at 25 ˚C. Temperature can be increased to raise the etching rate. BOE usually etches uniformly by removing etched material from the surface. BOE etches SiO_2 isotropically; etches along the NW growth direction and ultimately the NW lands on the trench surface.

5.5.2 Inductively Coupled Plasma (ICP) Dry Etch

The ICP tools are characterized by high etch rates due to the dense plasma that can be produced and good sidewall angle control with highly anisotropic etch profile. They are thus well-suited for fabrication of high aspect ratio structures since the structures can be etched in a reasonable time and with well-define walls. In the case of ICP dry etch, which makes anisotropic etching, the NW acts as the mask for underneath SiO_2 and protects it from being etched. The result is shown is Fig. 5.14 where we see the NW sitting on top of the unetched oxide region while other part of the trench is etched.

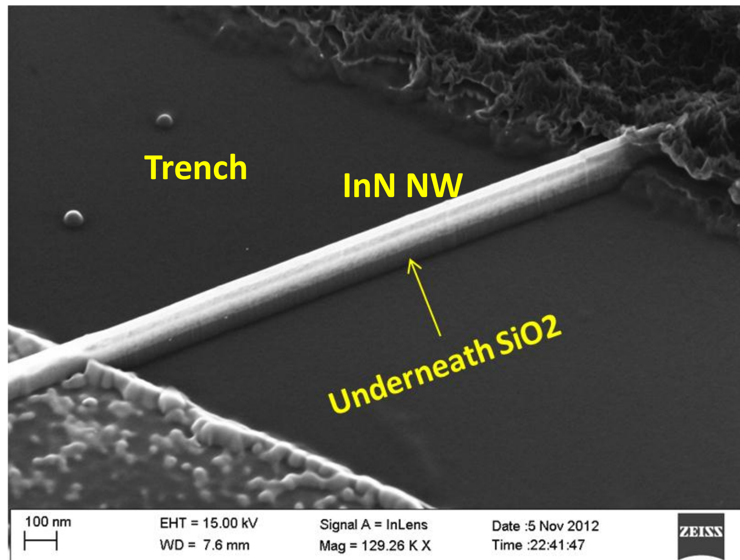

Figure 5.14: SEM image of an InN NW across a trench, the trench was etched by Inductively Coupled Plasma (ICP) dry etch recipe.

5.6 InN Nanoresonators: Focused Ion Beam (FIB) technique

Due to the limitations of not having optimized recipe for perfectly suspended NWs by either of the wet etch or dry etch technique, a different approach has been pursued which does not need any lithography steps to make final devices rather metal contacts are deposited . In this approach the NWs are synthesized on post growth trench, which means the trenches are already patterned by E beam lithography and etched by BOE wet etch. After that the contact are made by Electron Beam Induced Deposition equipped in a dual beam FIB machine.

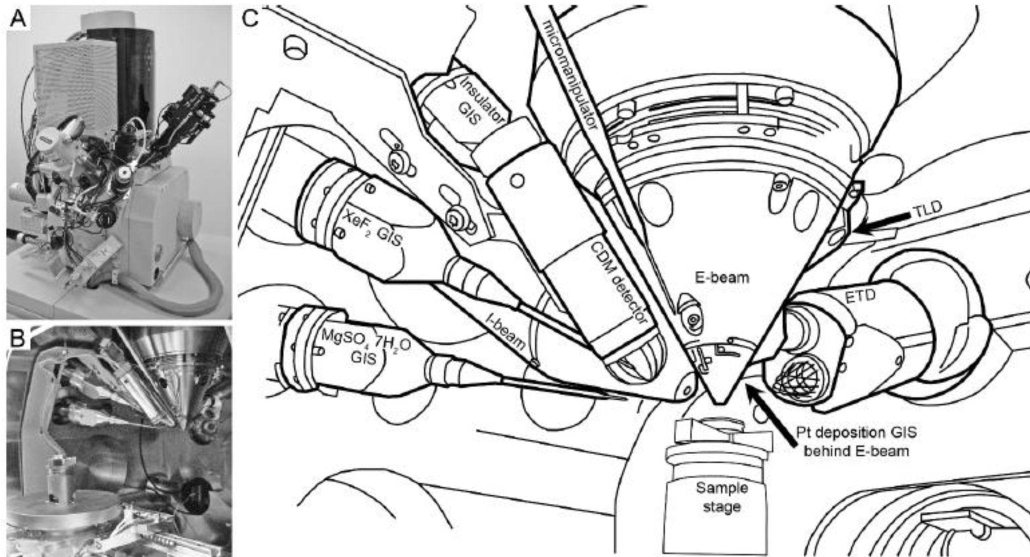

Figure 5.15: (a) Image of a Dual beam FIB, (b) Inside of the dual beam FIB and schematics of different components of a dual beam FIB

5.6.1 Focused ion beam and Dual Beam microscopy

A focused ion beam (FIB) microscope is similar to a SEM except the electron beam is replaced by a beam of ions, usually positively charged gallium (Ga+). A FIB can provide high resolution imaging (with resolution as good as a few nanometers), and because the ions are much more massive than electrons, the FIB can also be used to sputter (remove) material from the sample with very precise control. A FIB may be combined with a SEM in a single instrument (FIB/SEM). In FEI's DualBeam™ FIB/SEM instruments, the electron and ion column are positioned to allow the SEM to provide immediate high resolution images of the surface milled by the FIB.

5.6.2 Electron beam-induced deposition

Electron beam-induced deposition (EBID) is a process of decomposing gaseous molecules by electron beam leading to deposition of non-volatile fragments onto a nearby substrate. The electron beam is usually provided by a scanning electron microscope that results in high spatial accuracy (below one nanometer) and possibility to produce free-standing, three-dimensional structures.

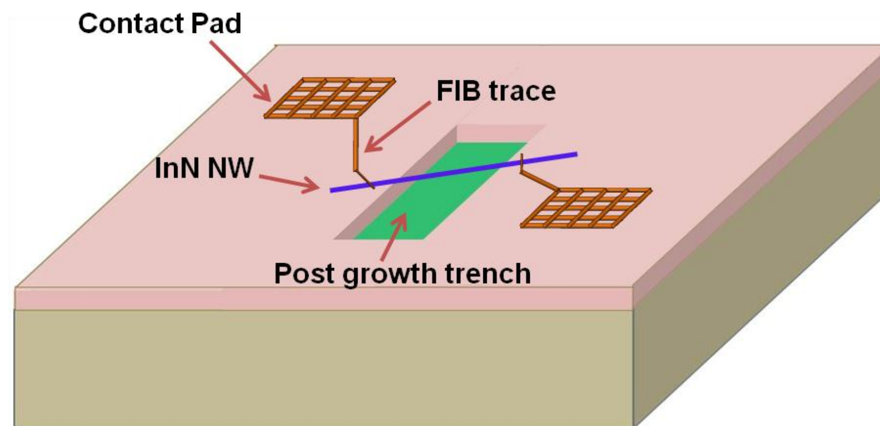

Figure 5.16: The schematic representation of the final NEMS resonator with FIB; NWs are going across the trench with no sagging and the probe contacts are not solid filled.

Processing Steps:

- ❑ Pre-growth trench
- ❑ NW growth
- ❑ FIB trace deposition
- ❑ FIB contact pad deposition (mesh)

- FIB milling
- Wire bonding

Prior to depositing Au catalyst spots and NW synthesis, trench is etched on the small 3x3 mm^2 samples by E-beam lithography as shown in figure. The trenches can be patterned and etched on 1 cm^2 sized sample by Optical lithography as well. BOE wet etch is performed to etch 300 nm trenches for around 3 mins. 2 µm Au catalyst spots are aligned and patterned near the trenches by E beam lithography or by optical lithography. Figure 5.17 (a) shows the SEM image of the pre growth trench and (b) shows the SEM image of trench and 2nm thick catalyst spots.

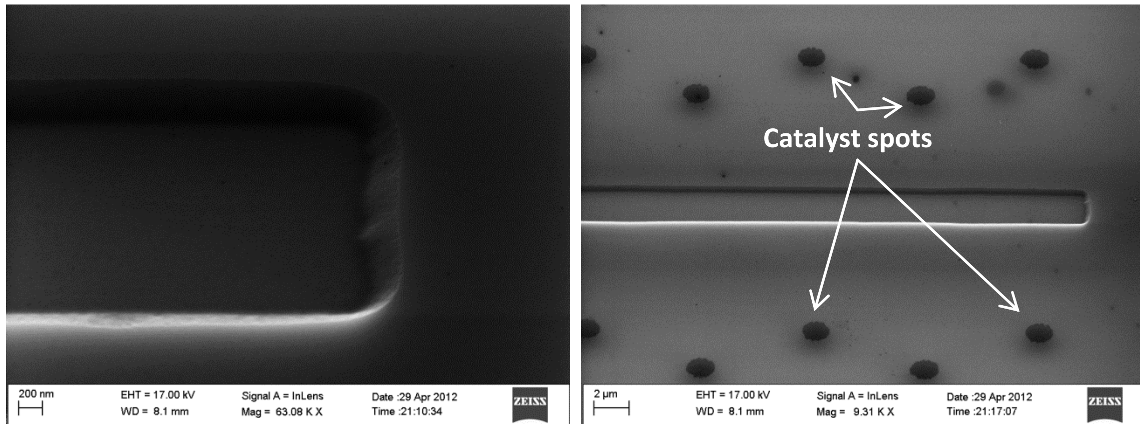

Figure 5.17: (a) SEM image of a pre-growth trench and (b) the SEM image of a pre growth trench and 2nm thick catalyst spots

In this step, InN NWs are synthesized from the catalyst spots by VLS mechanism in the CVD chamber as discussed previously in the NW synthesis section (previous chapter).

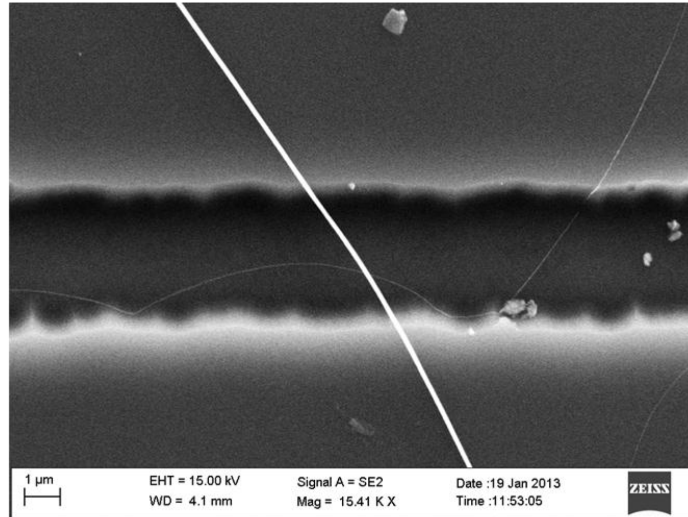

Figure 5.18: SEM image of a pre growth trench and a suspended NW crossing across the trench

Once the suspended NWs are located on specific trenches on a sample then we can design and pattern the FIB contact traces. The contact traces were done by depositing Pt on the designed pattern inside the FEI dual beam FIB/SEM instrument.

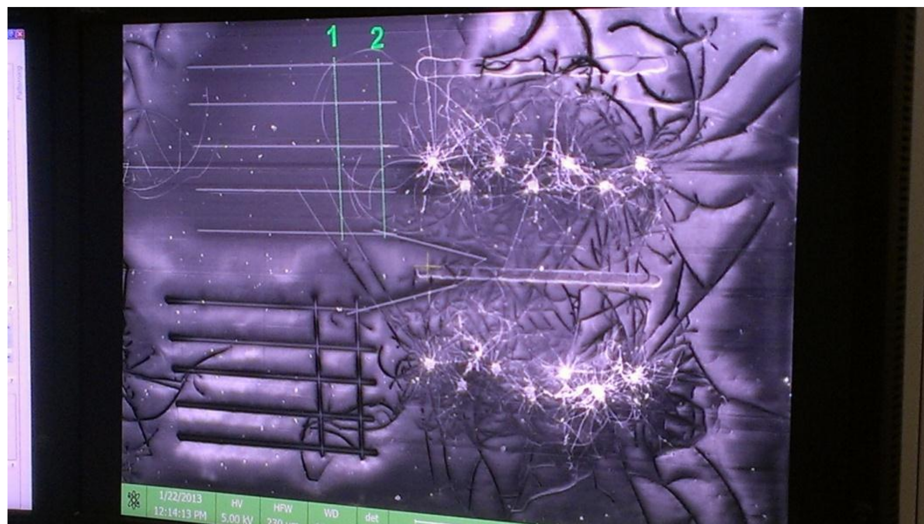

Figure 5.19: Image of the designing of contact pads via FIB software

We deposited Pt traces as the contacts to the NWs; the two traces connect between the NW contact and the metal pad. Instead of having metal filled contact probes we deposited contact pads as horizontal and vertical lines like mesh grid pattern to shorten the writing time span. Each horizaontal or vertical line consists of Pt trace of 70 um x 300 nm dimension and 300 nm thick.

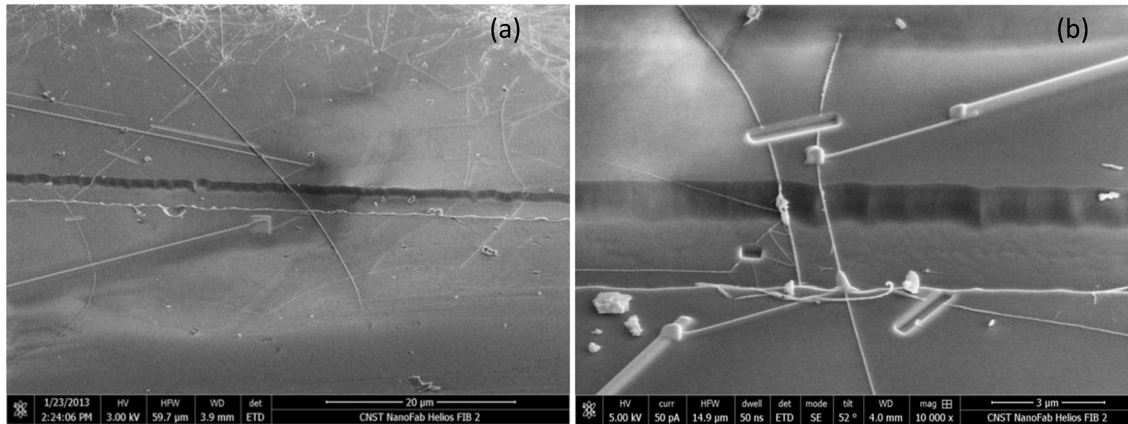

Figure 5.20: (a) SEM image of a suspended NW and the patterned and deposited FIB traces, (b) SEM image (close view) of another suspended NW, the etched profile can be seen as a measure to disconnect or cut down the NW from conducting through other NWs.

Focused Ion Beam milling of NWs are performed to cut down unwanted NWs for securing the conduction of a single suspended NW. In the last step wire bonding is done on the grid like contact pads for electrical characterization of the devices.

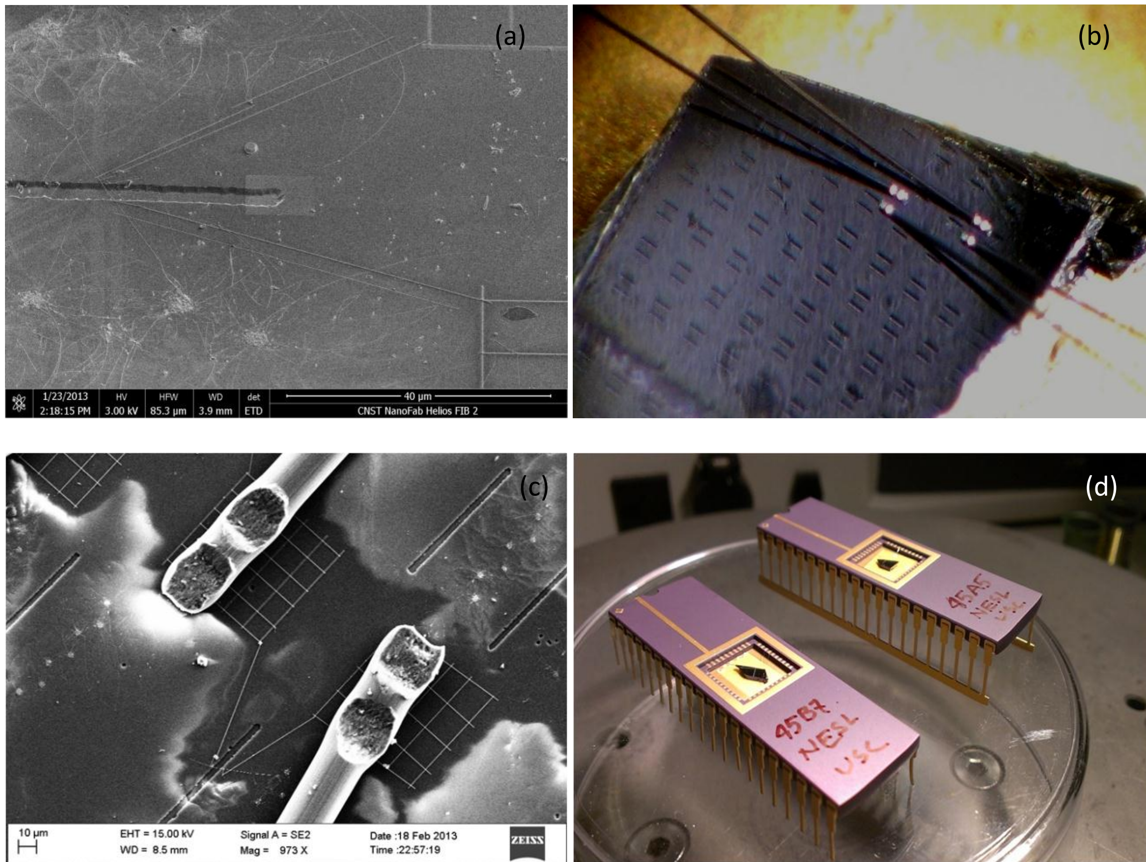

Figure 5.21: (a) SEM image of a NEMS resonator by dual beam FIB technique, the traces and pads are seen, (b) optical micrograph image of the wire bonding, (c) SEM image of the wire bonded contact pads and (d) image of the final 40 pin DIP Chip containing active devices.

5.7 InN Nanowire Based V-shaped Cantilever Sensors

The V-shaped Nanocantilevers (VNCs) can be technologically very significant with potential applications in Nanoelectromechanical systems (NEMS), scanning probes, and sensor arrays. From the success of fabricating nanoresonators (previous section) and understanding of growth direction modulation (discussed in chapter 4), we can realize V shaped nanocantilevers from InN NWs. The detail processing steps will be discussed here, before that we will begin with theoretical aspects of InN V-shaped nanocantilevers.

5.7.1 Theoretical Modeling of InN V-shaped Nanocantilever Sensors

Microscale materials and resonators have been investigated in terms of the electrical and mechanical properties using COMSOL and ANSYS finite elements simulation software [226, 227]. There are very few reports regarding simulations of nanoscale materials using finite element analysis (FEA), exploring their electrical and mechanical properties, and almost none exist for III-V semiconductor materials. Only a handful of studies are reported on carbon nanotubes or Si nanowires, one of the two most widely studied nanoscale materials. For a complete understanding of the nanoscale electromechanical system, both the electrical and mechanical aspects need to be studied in detail. In addition, investigation of the applicability of these nanoscale sensors has not been studied through finite element simulation. For example, one of the most important aspects of nanoscale materials, i.e. prediction of charge and mass resolution of these structures has not been thoroughly investigated.

Through use of computer aided finite element analysis we examine the resonant and electrostatic properties of our InN V-shaped NW (VSN) as well as investigate its feasibility as a sensor. We have found these structures to have high quality factors in vacuum (279×10^3) and atmospheric quality factors near 250, as well as high mass sensitivity (4 Hz per oxygen molecule). The results show that given the small nature of the device, these structures may be fabricated in arrays to present an alternative nanoscale mass detection solution.

5.7.1.1 Finite Element Simulations

We construct a model using finite element analysis (FEA) to conduct electrical, thermal, and mechanical simulations which determine the static and dynamic

characteristics of this device to examine the plausibility of its use as a sensing device. Below we discuss the model and simulation limitations, several mechanical properties of the structure including sensitivity to mass attachments, the effects of temperature variations, and electrostatic response.

5.7.1.2 Device Model

The device shown in Figure 5.22 is modeled to characterize the nano-cantilever shown in Figure 1 while bound to a substrate. This allows us to properly model strains as well as electrostatic and thermal effects related to the final device anchoring method for a more realistic assessment of the final sensor's performance. The InN nanowire is attached to the substrate consisting of a SiO_2 layer over crystalline silicon with Au Contacts deposited on top. Where the "arms" of the cantilever meet the substrate they are considered bound to the SiO_2 layer.

The cantilever has a cross-sectional diameter of 30 nm and an arm length of 4μm with the angle of the arms maintained at 60°. The metal contacts have the dimensions of 1 μm × 2 μm (for simplicity) with a thickness of 60 nm. Simulation parameters related to material constants may be found in Table I. Additionally an "air box" three-dimensional domain which encompasses the entire model may be toggled to allow electrostatic based simulations.

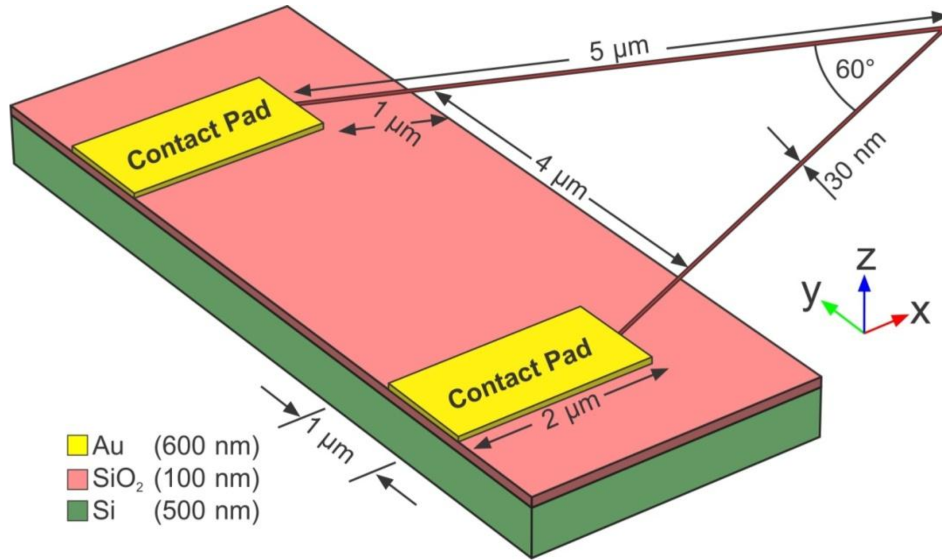

Figure 5.22: Three-dimensional model used to perform analyses.

Table 5.1 Simulated material constants

	InN	Au	Si	SiO_2	
Heat Capacity (C_p)	320	129	700	730	J/kg/K
Relative Permittivity (ε_r)	15.3	6.9	11.7	4.2	
Thermal Conductivity (k)	55.6	317	130	1.4	W/m/K
Density (ρ)	6780	19300	2329	2200	kg/m^3
Coeff. thermal expansion (α)	32E-6	14.2E-6	2.6E-6	0.5E-6	K^{-1}
Young's modulus (E)	200	70	170	70	GPa
Poisson's Ratio (v)	0.3	0.44	0.28	0.17	
Resistivity (ρ_0)	50E-6	22.14E-9	640	10^{14}	Ωm
Resistivity temp. coefficient	3.7E-3	3.715E-3	-0.075	0	K^{-1}
Reference Temperature (T_{ref})	300	300	300	300	K

Table 5.2 Simulated Model Properties

Parameters	**Value**
Suspended VNC Volume	5.61×10^{-21} kg
Suspended VNC Mass (m)	38×10^{-18} kg
Normalized Effective Mass (M^*)	0.243

5.7.2 Mechanical Response

5.7.2.1 Mechanical Properties

Known analytical equations must be used to verify the usefulness of the developed computer model. Using data from Table 5.1, Table 0.2, and [227], we find a calculated spring constant (*k*, Eq. 5.01, [227]) of 1.69×10^{-3} N/m and a resonant angular frequency (ω_0, Eq 5.02, [228]) of $2\pi\times2.15$ MHz.. A major source of error in the analytical-simulation comparison is derived from the approximation errors that equations 1 and 2 assume. Equation 5.01, derived for atomic force microscopy (AFM) cantilevers, gives the spring constant (*k*) of a v-shaped cantilever with a square cross section. Here *E* is the Young's modulus, *d* is the arm diameter, *L* is the length of a single arm, and θ is half of the angle at the tip. Also, Eq 5.02, where mass is represented by *m*, assumes a normalized effective mass (M^*) approximation of 0.243 [227]. The proper theoretical normalized effective mass value may be difficult to find for the model given that there is no experimental data to derive it. Because M^* is normally derived experientially for this type of structure it can be a large source of error [229] between analytical and simulated models.

$$k=\frac{Ed^4}{2L^3}\cos(\theta) \tag{5.01}$$

$$\omega_0=\sqrt{\frac{k}{M^*m}} \tag{5.02}$$

5.7.2.2 Damping and Quality Factor

An accurate real-world resonating model must also consider the avenues of energy loss. In this study we examine our resonant model using air damping, and thermo-elastic damping. Internal acoustic losses will be ignored because it is one of the least dominant of the loss types and its dependence on imperfections and the fabrication process [230]. We will also ignore the damping contribution of anchor loss because our small attachment footprint also makes its contribution negligible [231]. The observed avenues of energy loss are summed reciprocally to provide the system's total energy lossfrom TED, squeezed-film (SF), and air damping as shown by the equation below.

$$Q_t^{-1}=Q_{therm}^{-1}+Q_{SF}^{-1}+Q_{air}^{-1} \tag{5.03}$$

Beam bending causes compression and expansion on opposite sides of the beam relative to the direction of bending. These repeated volume changes will cause a temperature difference which in turn creates a dissipative heat flow [232, 233]. Energy loss from thermoelastic heat flow is given by equation 5.04 [234] which consists of both temperature dependent and frequency dependent parts. Here α is the thermal expansion coefficient, while $\rho$is density, and C_p is heat capacity (Eq. 5.07). Thermal relaxation time (τ) is satisfied by Eq 5.05 where κ is the thermal conductivity. Simulating this source of energy loss is accomplished by coupling structural mechanics with heat transfer physics, using the structural stresses formed during oscillation as a source of heat which then in-turn creates localized thermal expansions.

$$\frac{1}{Q_{TED}}=\left(\frac{E\alpha^2T_0}{\rho C_p}\right)\left(\frac{\omega_0\tau}{1+(\omega_0\tau)^2}\right) \tag{5.04}$$

$$\tau = \frac{\rho C_p d^2}{\pi^2 \kappa} \tag{5.05}$$

For the air damping case we observe energy loss through both the standard fluid damping model and through SF losses. The fluid damping model presents energy loss from air viscosity and ambient pressure. This damping, presented in Eq 5.06 [235] is computed to be a negligible avenue of energy loss. Here μ is viscosity (Pa/s) and ρ is the air density (kg/m^3).

$$C_{damping} = 2\pi\mu d \left(\frac{2\mu}{\rho_{air}\omega_0}\right)^{\frac{1}{2}} \tag{5.06}$$

The squeeze-film damping case presents itself as the largest contributor of energy loss in the system. Fairly accurate SF models have been found which applies to models that share our proximity to the bottom surface but do not translate well to our geometry [236]. Because of its extreme proximity to the bottom plane this form of damping must be accounted for, and as shown in Fig 5.23 accounts for most of the system's energy loss at normal atmospheric levels. Figure 5.23 shows that for simulations run at pressures higher than about 200 Pa we may exclude the other forms of energy loss to free up resources.

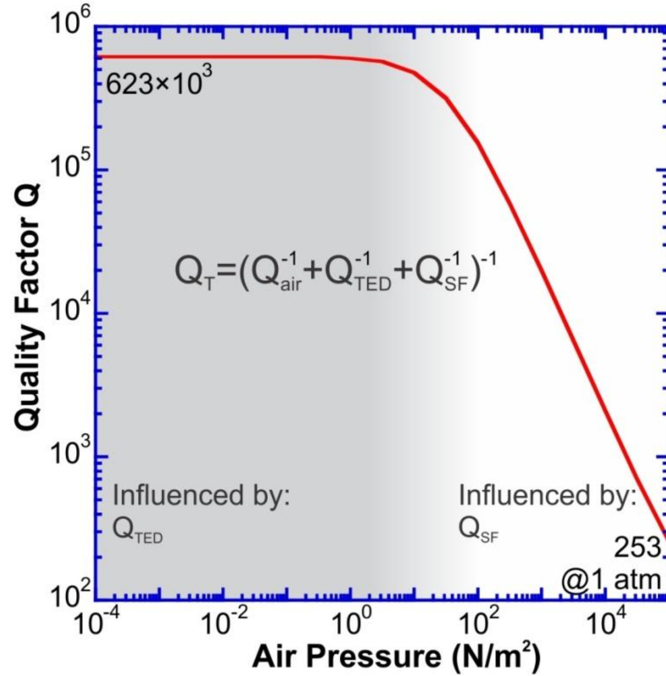

Figure 5.23: System quality factor (Q_T) as a function of ambient air pressure. After about 200 Pa, damping is predominantly determined by squeeze-film losses.

Results given for eigenvalue simulations are given in complex form and translate to resonant angular frequency and quality factor given Eq 5.07, where λ is the complex eigenvalue output. This simulation run gives us details needed to set up a frequency response simulation. The response, shown in Fig 5.24, will help us determine our sensor's resolution given the system's noise, which is accounted for later.

$$\omega_0=|Re(\lambda)|,\ Q_T=\left|\frac{Re(\lambda)}{2Im(\lambda)}\right| \quad (5.07)$$

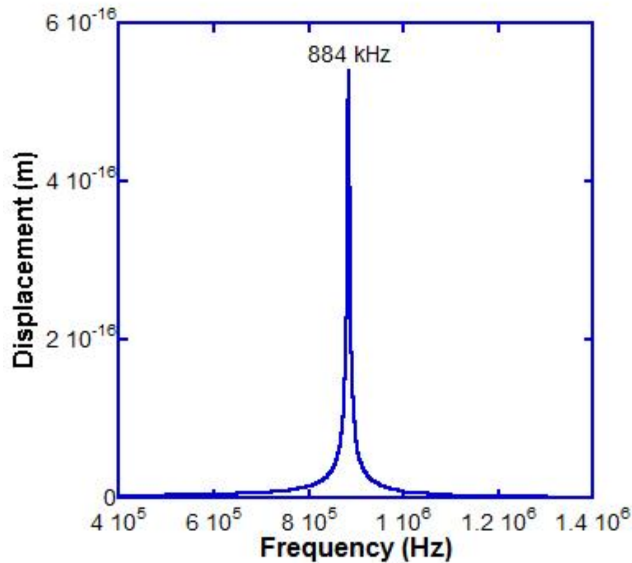

Figure 5.24: Frequency sweep output of the model structure. Displacement is measured at the cantilever tip.

5.7.3 VNC for Sensing Applications

The InN VNC sensors are capable of performing highly sensitive detection based on changes in 3 different physical parameters: *SWF* ($\Delta\varphi$), *conductivity* ($\Delta\sigma$), *and surface stress* (ΔS). Of these, detection based on $\Delta\varphi$ is the most versatile and widely applicable, where various types of analyte molecules can be sensed by simply changing the functionalization layer on the substrate during fabrication.

For detection based on ΔS, the VNC, just like a microcantilever, needs to be coated on one side with appropriate selective layers, which requires more functionalization steps. $\Delta\sigma$ based detection also requires the presence of selective layers on the VNC, and the overall change in conductivity can be measured for detection. The choice of either of these modes, either individually, or in combination (for multimodal

detection), depends on the properties of the functionalization layer corresponding to a target analyte, although, sensing based on $\Delta\varphi$ measurements can always be utilized unless the functionalization layer is a solid with low melting point (such as a polymer). Even then, a thin layer of the selective film can be deposited on the VNC post-fabrication, if the coating does not significantly alters the resonance characteristics of the VNC. The other two modes depend on modifying the VNC specifically, which however, does not pose a significant problem (except when a highly conducting material needs to be deposited), since they detect in the static mode. However, simultaneous measurements of any two of these parameters (for multimodal detection), using the same functionalization layer, can be more restrictive. In the future study, we will determine $\Delta\varphi$ from the resonance amplitude change Δa measured using an RF lock-in amplifier [$\Delta\varphi$ and Δa are related by $\Delta a = (Q/k)(\partial C/\partial z)(\Delta\varphi)V_{ac}$].

Change in conductivity, either due to surface depletion caused by direct molecular adsorption, or due to bending induced depletion caused by electric field (former related to $\Delta\sigma$, and the later to ΔS) will be measured using a dc picoamperemeter. A single VNC sensor with the relevant electrical connections is shown in Fig. 5.25. The dc bias to the substrate will be used to compensate for the natural difference in SWF between the probe and the functionalization layer, as well as, to create depletion in VNCs due to bending in static sensing modes. The pulsed bias will be used for VNC calibration.

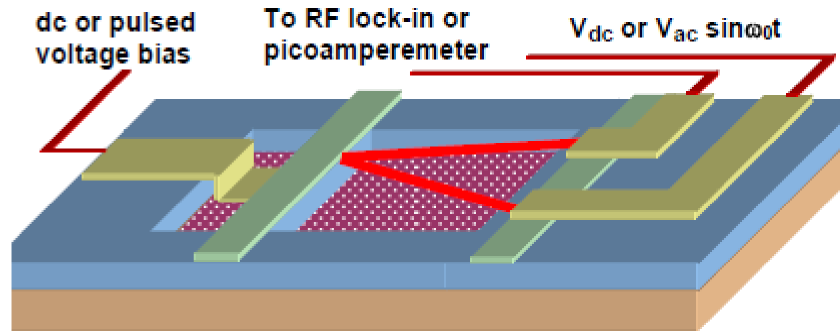

Figure 5.25: Sensing configuration for the VNC sensor.

5.7.3.1 Mass Attachment Based Simulations

Resonating micro-cantilevers have been considered attractive for performing molecular detection based on the attached mass of absorbed molecules. The VNC's low mass (10^{-12}g range) is suitable for detecting exceptionally small attachments.

To observe the resonance shift from various magnitudes of mass attachments we ran mass parametric Eigen-frequency simulations. Here the model is altered to incorporate an increased mass at the tip, simulating an absorbed molecule. Inset shows that the frequency variation from an attached mass of 3x 10^{-23}g is 2 Hz. At this resolution we may detect an attachment of one oxygen molecule to the resonating structure. Provided it is absorbed at the tip.

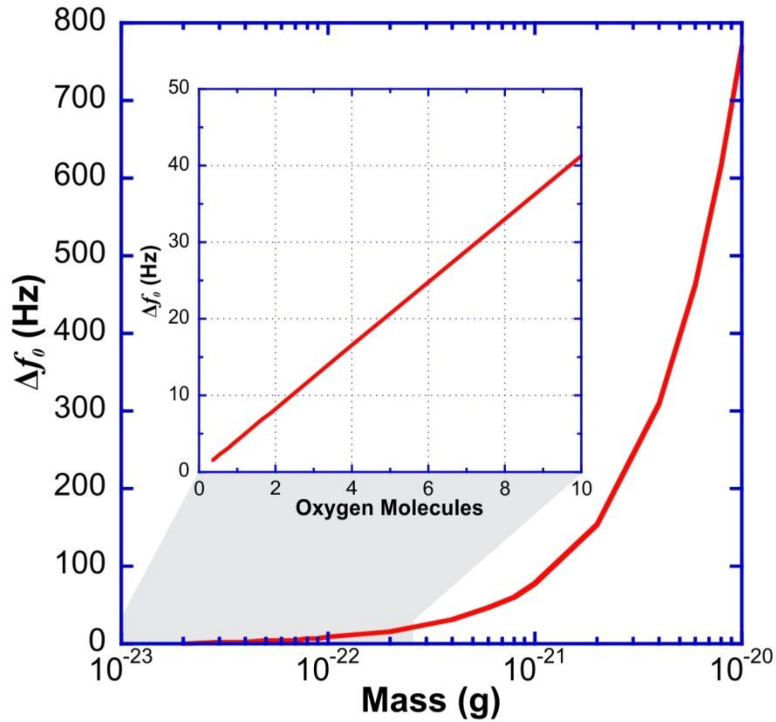

Figure 5.26: Fundamental resonant frequency change given a mass attachment at the cantilever tip. The inset shows greater detail in the 10^{-23} g decade mass range.

5.7.3.2 Electrostatics

The three dimensional model used is similar to that of the one used in the structural mechanics model. In addition it has a semi-spherical air domain surrounding the cantilever. The bottom of the air domain is designated as the ground plane and is spaced 100 nm below the bottom of the cantilever. The capacitance for this structure may be estimated through existing analytical equations [237] by multiplying the outcome by two (to account for each arm), resulting in Eq 5.08 where C is capacitance, ε_0 and ε_r is vacuum and relative permittivity, and g is the gap between the cantilever and the ground plane.

$$C = \frac{4\pi\varepsilon_0\varepsilon_r L}{\cosh^{-1}\left(\frac{2g}{d}\right)} \tag{5.08}$$

Furthermore we may approximate the force field magnitude given Eq 5.09, where *V* is the applied voltage bias to the cantilever. This field, which applies to the entire cantilever, will cause the cantilever to deflect, changing the cantilever's capacitance.

$$F = \frac{V^2 C}{2g} \tag{5.09}$$

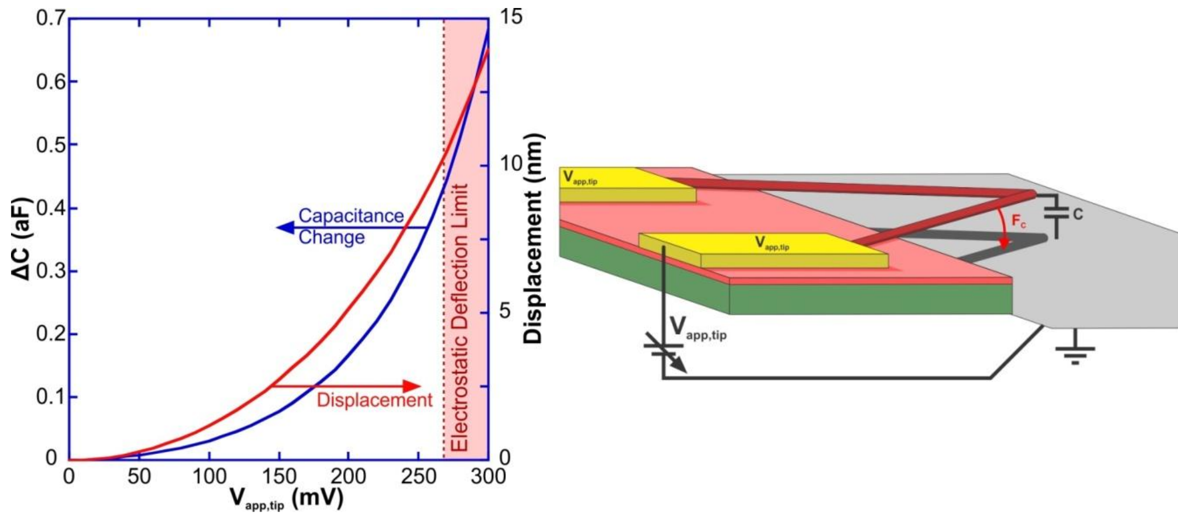

Figure 5.27: Capacitance (blue) plotted against the bias applied to the cantilever. Deflection (green) is also present to compare with the device deflection limitation (red) of the dielectric strength of air breakdown point (3×10^6 V/m).

Figure 5.27 shows simulation output for voltages up to 300 mV. Output capacitance and force magnitude was verified against analytical equations to have ~16% and ~33% error respectively. This graph gives us a reasonable operating voltage of ~250 mV to prevent dielectric breakdown while achieving the highest possible displacement (8.6 nm) and thus highest possible capacitance change (3.36×10^{-19} F).

5.7.3.3 Sensing Based on Surface Work Function Change

Through Eq 5.10 we may observe a change in sizable change in resistance due to the change in capacitance. *R* is the simulated resistance as observed during the joule heating effects simulations (867 kΩ). Because the capacitance changes are so small sensing bending through resistance change is much more preferable. Here we may observe resistance changes around1 kΩ which is much easier to sense than capacitance changes in the 10^{-19} F range. Figure 5.28 shows this relationship.

$$\frac{\Delta C}{C} = \frac{\Delta R}{R} \qquad (5.10)$$

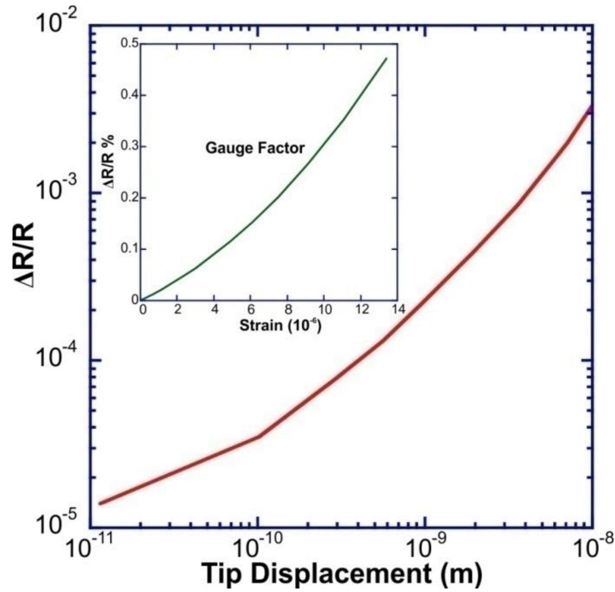

Figure 5.28: Resistance change from displacement. The charged cantilever, when subjected to bending (induced or through capacitive force) will exhibit a change in charge, which may be translated into a change in resistance.

5.7.3.4 Joule Heating Effects

Joule heating simulations were run to examine the reaction of the structure given an electric potential across its arms. With an active current flow through the device some resistive heating and resulting thermal expansions are expected. Coupled simulations accommodate these problems well because they take into account all of the interrelations between these properties. A current flow is induced which causes joule heating. This in-turn causes the structure to deform. The deformation, along with localized heating causes the structure's resistance to change further. At this point we may observe a resonant frequency shift in our operating structure.

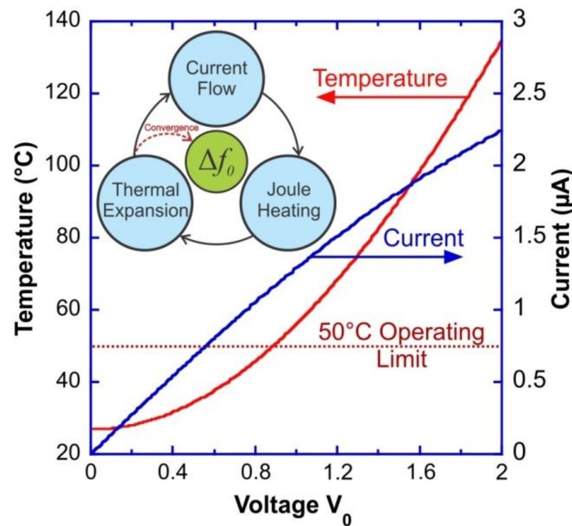

Figure 5.29: Temperature and current response across a small range of input voltages.

This model considers that the system starts at a temperature of 300 K before start time. The voltage bias will be applied to the top surface of the gold contacts and current flow observed. Heating is expected so the system is set to include a heat transfer

coefficient of 5 $W/m^2/K$ for air under normal conditions. A sink is placed on the bottom of the substrate set to remain at the initial temperature of 300K. Current flow through the nanowire should be limited not to let the temperature rise above 50 °C (323 K). Parametric simulations helped find a maximum operating voltage for this case. Voltages are swept from 100 mV to 2 V so that the temperature and current at the tip may be measured.

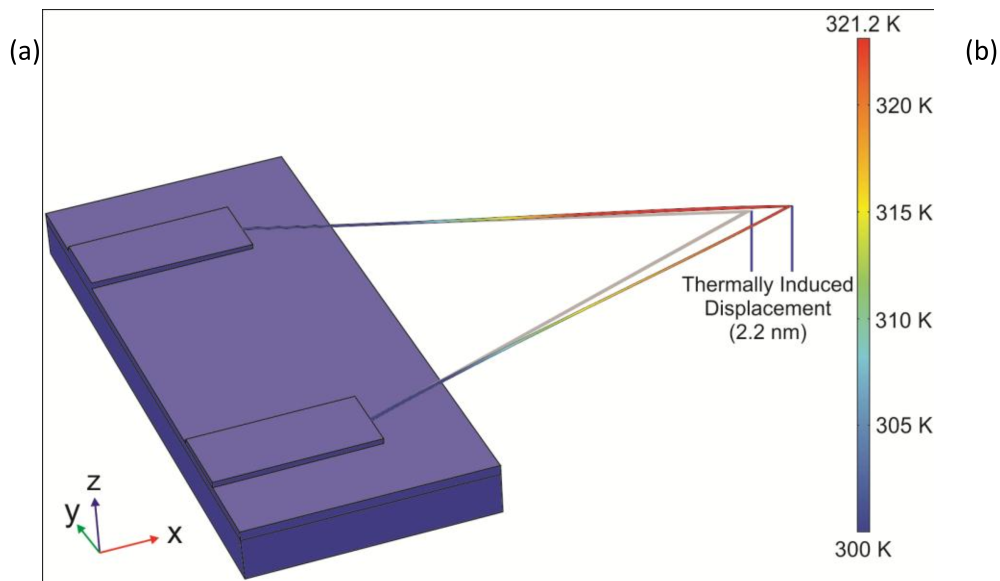

Figure 5.30: (a) Scaled (by 190) increase in length of the VNC due to temperature rise caused by an applied bias of 850 mV, and (b) displacement across a range of temperatures given by an applied voltage.

From the data given, in we find a thermal maximum voltage to be near 850 mV, which is where the temperature at the tip (maximum temperature) of the cantilever approaches 50 °C. This is much lower than our electrostatic maximum of 200 mV. Structure deformations due to heating effects are shown in Fig **Error! Reference source not ound.**5.30 (a) along with the horizontal displacement plotted against tip temperature (Fig

5.30 (b)). The displacement geometry is scaled (by 190) to allow the deformation to be easily seen, however the actual displacement is very small in relation to the structure.

5.7.4 Noise and Sensor Resolution

White Noise and Thermo-mechanical Noise

In piezoresistive microcantilevers there are two types of noises: electrical noise and vibration noise. Electrical noise consists of Johnson noise (White noise) and 1/*f* low frequency noise (Flicker noise), while vibration noise consists of thermo-mechanical noise. For our proposed cantilever, the total noise consists in finding the Johnson and thermo-mechanical noises. Thermo-mechanical (TM) noise for a microcantilever that is in a viscous medium, like air or water and at resonant frequency, is given by the equation [238]

$$rms_{noise_{TM}} = \sqrt{\frac{4k_B TBQ}{k\omega_0}} \quad (5.11)$$

Where B is the measurement bandwidth and $k_B$is the Boltzmann's constant.

Johnson noise, known as the white noise of a resistive element is due to the random thermal motion of carriers and it is dependent on temperature and resistance and is given by [239]

$$rms_{I<noise>} = \sqrt{\frac{4k_b T\Delta f}{R}} \quad (5.12)$$

Where T is temperature, K_B is Boltzmann's constant, Δf is measurement bandwidth and R is resistance of the resistor. Eq. 5.11 represents rms noise in terms of

current and to find the rms value in terms of deflection the deflection sensitivity needs to be calculated.

The total deflection noise for our nanocantilever can be calculated by taking in account both types of noises as:

$$rms^2_{total}=rms^2_{Elect<noise>}+rms^2_{Vib<noise>} \quad (5.13)$$

By applying the dimensions of our nanocantilever, and for a simulated quality factor Q = 253, measured bandwidth B = 1 Hz, temperature T = 302.8 K, resonant frequency f_0 = 1.52 MHz and spring constant 2.83 x 10^{-3} N/m and applying equation 10 the thermo-mechanical noise can be estimated to 0.0125 nm. Using Eq. 5.11 and a resistance of 783 kΩ (from the simulation results) the rms value in terms of current can be estimated to 0.15116 pA. The theoretical sensitivity was found to be equal to 45948 /m, which gives us a white noise of 0.0095 nm and a total rms noise of 0.0157 nm.

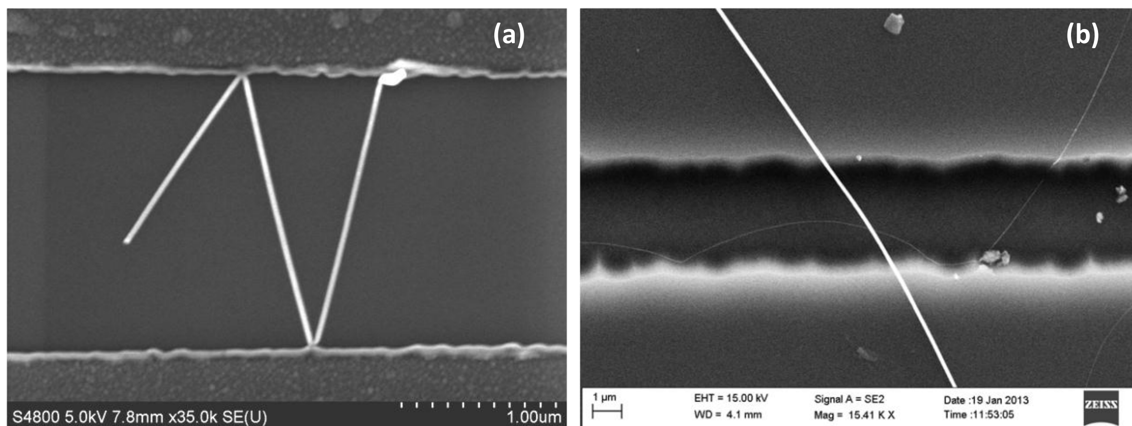

Figure 5.31: (a) SEM image of a V-shaped NW deflected back and forth by oxide barriers and (b) SEM image of a suspended NW across the trench.

5.8 Fabrication steps of InN nanocantilever sensors

The InN NWs were observed to suffer growth redirections either spontaneously, or when obstructed by a barrier, at angles that are multiples of 30°. Examples of spontaneous and obstacle (InN NW or lithographically patterned SiO_2 barriers) induced bending of InN NWs are discussed in the previous chapter. Presence of two parallel barriers can make the NW suffer multiple growth redirections that can be quite symmetric and repeatable [Fig. 5.31 (a)]. As can be observed, the deflection angles are

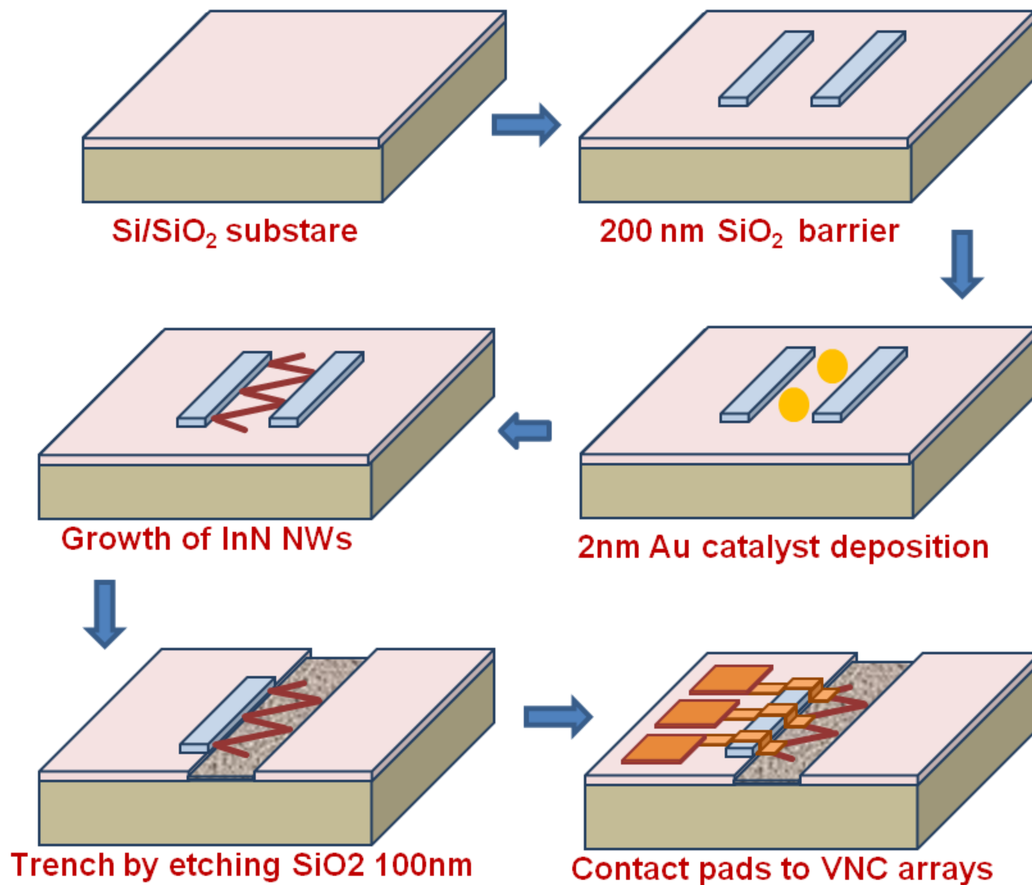

Figure 5.32: The fabrication process flow of V-shaped nanocantilevers.

very close multiples of 30°. Again, with the optimization of the etch recipe (both wet and dry) suspended InN NWs can be obtained very regularly. These highly significant attributes, the growth direction modulation and fabrication of NEMS resonators, provide a direct to access to the processing of InN NW based nanocantilevers.

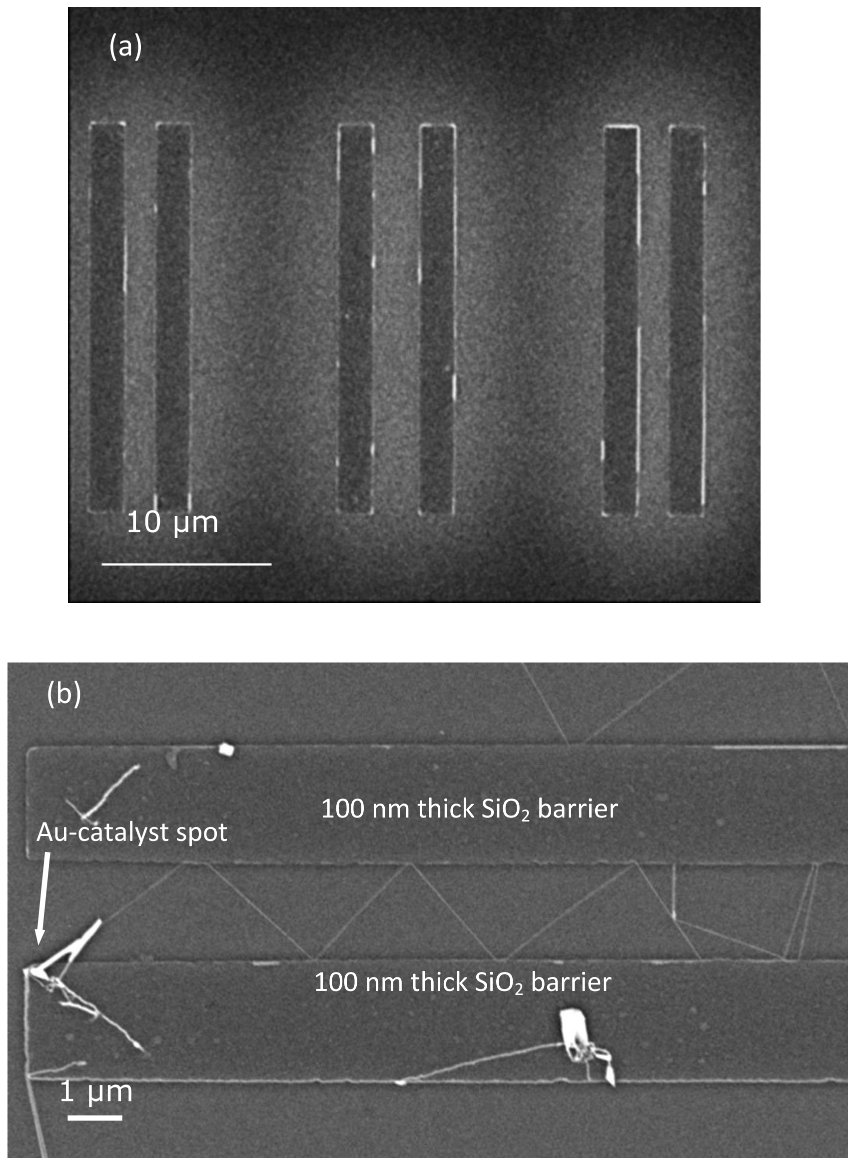

Figure 5.33: (a) SEM image of 200nm thick SiO_2 barriers and (b) SEM image of a V-shaped NW deflected back and forth by SiO_2 barriers

All the process steps (Fig. 5.32) are very similar to the nanoresonator process steps except the patterning and deposition of 200nm thick SiO_2 barriers. Figure 5.32 shows the fabrication process flow for fabricating V-shaped nanocantilevers. 200nm thick SiO_2 barriers are deposited by Plasma Enhanced CVD (PECVD) for better smoothness of the barrier wall. Figure 5.33 (a) shows multiple SiO_2 barriers. The Au catalyst spots are patterned and thermally deposited to 2nm thickness inside the SiO_2 barriers so that the NWs get deflected by the inside wall of the barriers after the synthesis process as discussed in section 4.4. An SEM image of V-shaped NW deflected back and forth by barriers is shown in Fig 5.33 (b). Later on the etching is performed to etch away the underneath SiO_2 (100nm thermal oxide) to release the V shaped NW and

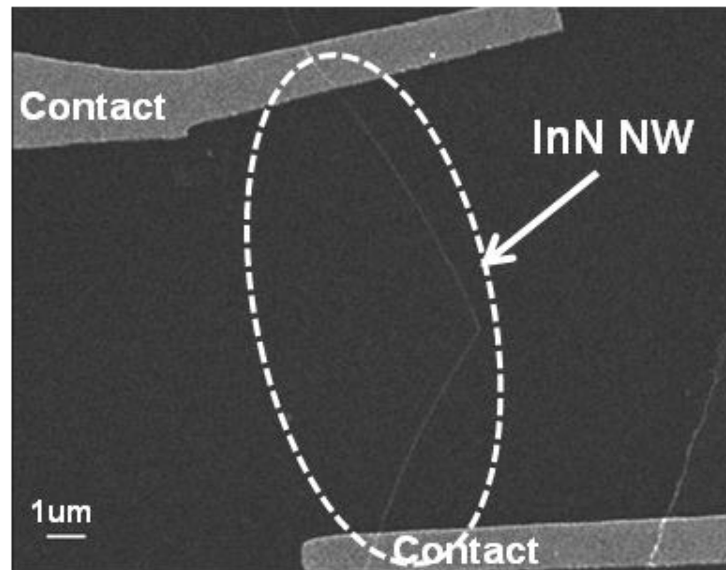

Figure 5.34: SEM image of a V-shaped NW device, the etching of the underneath SiO_2 is not performed yet (not V-shaped nanocantilever). The contacts are seen in the SEM image.

finally metallization layer was deposited to make the VNCs connected with external circuitry for characterization. Figure 5.34 shows an SEM image of a V shaped InN NW connected between drain and source contacts, the underneath SiO_2 is not yet etched.

CHAPTER 6

ALGAN/GAN HETEROSTRUCTURES

This chapter deals with the theoretical framework of the GaN material system. A brief introduction to AlGaN/GaN heterostructure and its importance is demonstrated at first, and then some theoretical aspects are presented. The origin of the Two Dimensional Electron Gas (2DEG) is presented briefly in this chapter as well.

6.1 Introduction

Due to its abundance and mature technology, Silicon (Si) has captured most of the semiconductor industries of the world. However, application of Si has shown limitations in sensing applications in harsh environmental conditions. Si cannot be used for high temperature applications (intrinsic carrier concentration increases more than 100 times above 100°C, loses the mechanical reliability at 500 ◦C) [240], is attacked by corrosive media and exhibits low biocompatibility. One of the main advantages of the wide band gap semiconductors is the very high mechanical, thermal, chemical and biochemical stability, which enables such applications. Moreover, materials with a high Young's modulus can better maintain a linear relationship between applied load and the

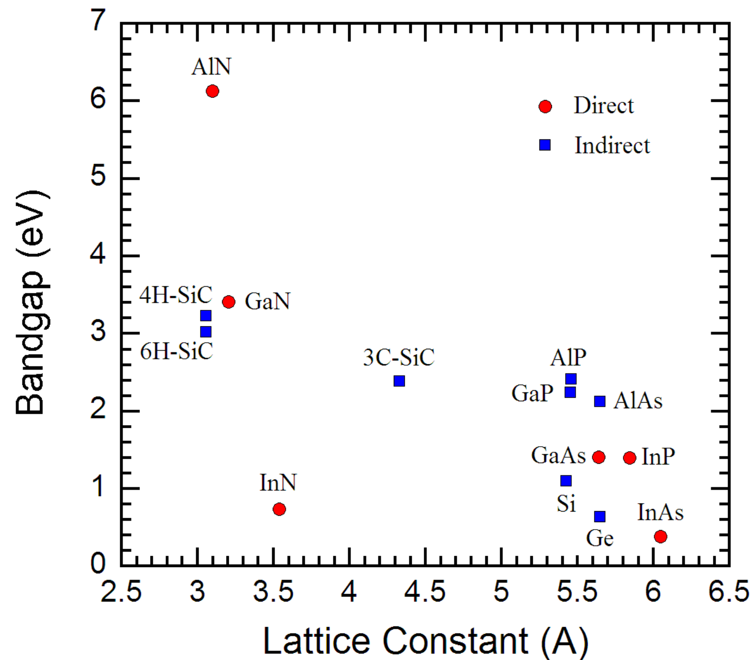

Figure 6.1: Bandgap of common semiconductors at room temperature plotted against their lattice constant, Ref. [241].

induced deformation [240]. This particularly favors group-III nitrides, which has high Young's modulus. AlGaN/GaN heterostructure has high density 2DEG very close to the surface (Fig. 6.2 (a)) similar to that of InN NW surface charge accumulation layer. This strain dependent 2DEG at the interface is sensitive to mechanical load as well as to chemical modification of the surface and can be used for novel sensing principles and as transducers for MEMS applications. 2DEG in AlGaN/GaN heterostructures are polarization-induced (Fig. 6.2 (b)) and no intentionally doping is needed. Presence of such a 2DEG is unique to AlGaN/GaN heterostructure, and is often attributed to polarization doping, since it arises because of the strong polarization properties of the nitrides.

Table 6.1 Electronic properties of some common semiconductors, Ref. [241]

Properties	**Si**	**GaAs (AlGaAs/ InGaAs)**	**InP (InAlAs/ InGaAs)**	**4H- SiC (3C-SiC/ 6H-SiC)**	**GaN (AlGaN/ GaN)**
Bandgap (eV)	**1.11**	**1.42**	**1.35**	**3.26**	**3.42**
Electron Mobility (cm^2/Vs)	**1350**	**8500 (10000)**	**5400 (10000)**	**700 (2000)**	**900 (2000)**
Saturation velocity ($\times 10^7$ cm/s)	**1**	**1 (2.1)**	**1 (2.3)**	**2**	**1.5 (2.7)**
2DEG density (cm^{-2})	**NA**	**$< 4\times10^{12}$**	**$< 4\times10^{12}$**	**$< 3\times10^{12}$**	**$1\text{-}2 \times10^{13}$**
Critical Breakdown field ($\times 10^6$ V/cm)	**0.3**	**0.4**	**0.5**	**2**	**3.3**
Relative dielectric constant	**11.8**	**12.8**	**12.5**	**10**	**9**

Among the most common semiconductors (see Fig. 6.1) AlN (6.13 eV) and GaN (3.42 eV) have much higher bandgap compared to others. Due to such wide bandgaps, their critical electric fields for breakdown are much higher than other III-V semiconductors. Though GaAs has much higher low field mobility, GaN is clearly superior in terms of saturation velocity (see Table 6.1). Together with high bandgap, high saturation velocity

and high mobility makes nitrides ideal contenders for high power microwave application. The presence of a direct and wide bandgap in AlGaN/GaN also make them very suitable for optoelectronic applications, especially in the green, blue, and UV regions of the spectrum, where there are virtually no other contenders.

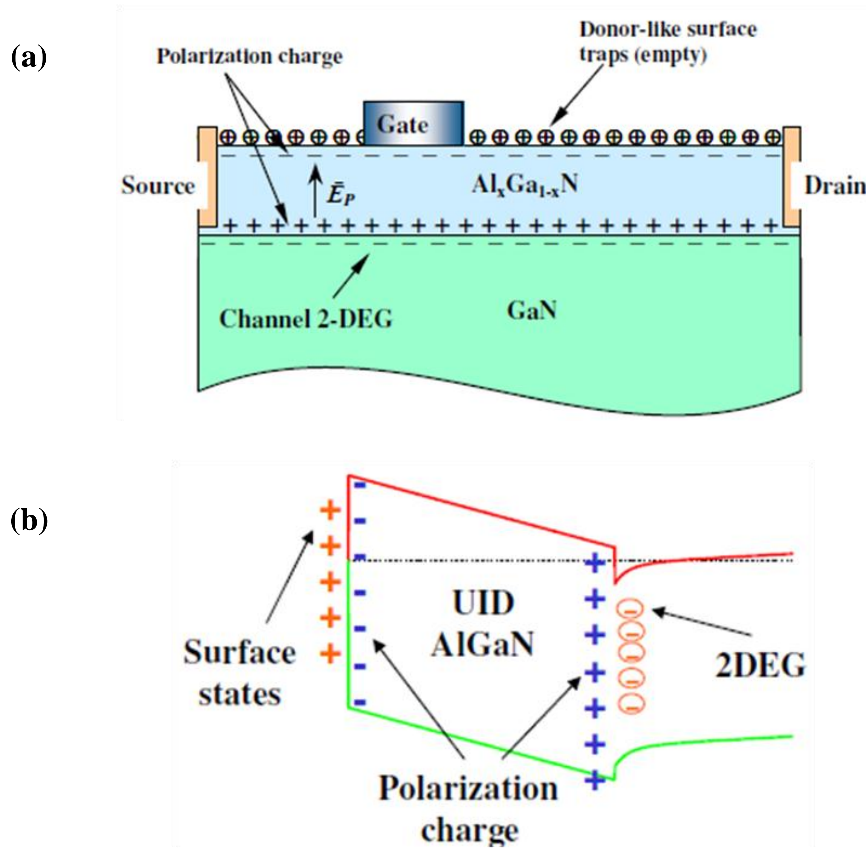

Figure 6.2: (a) 2DEG in AlGaN/GaN interface, (b) band diagram and surface states of AlGaN/GaN heterostructure

Unlike bottom-up approach, the top-down microfabrication approach for multimodal sensor development using AlGaN/GaN heterostructures is well established and less complicated. Thus, we exploited these attributes of AlGaN/GaN and took advantage of microfabrication to make microcantilever based sensors.

6.2 Gallium Nitride crystal structure

At ambient temperature, the thermodynamically stable structures for AlN, GaN and InN are wurtzite. Though under special conditions they can also be grown with zinc blende structure, the wurtzite nitrides are grown and studied almost exclusively. In wurtzite structure, there are two interpenetrating hexagonal close-packed lattices, each displaced from the other ideally by 3/8 c_0. Each atom is tetrahedrally bonded to four atoms of the other type, and the primitive unit cell is simple hexagonal with a basis of four atoms, two of each kind. There is no inversion symmetry in this lattice along the [0001] direction (same holds true for zinc blende structure along [111] direction), resulting in all atoms on the same plane at each side of a bond being same. Hence, a GaN crystal has two distinct faces, the Ga-face and the N-face.

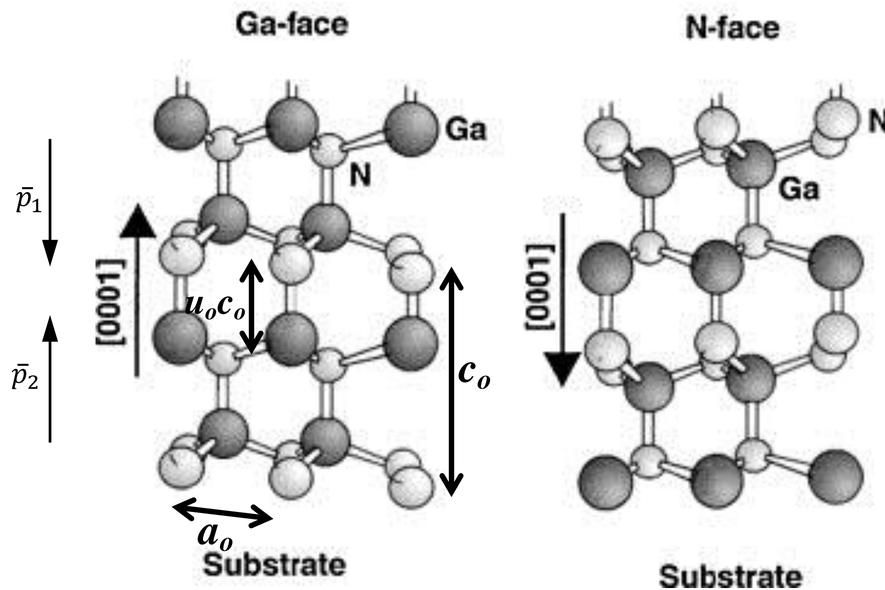

Figure 6.3: Atomic arrangement in Ga-face and N-face GaN crystals. The arrow pointing from N to Ga atom shows the direction of the spontaneous polarization.

The arrangement of atoms for Ga-face and N-face GaN are shown in Fig. 6.3. Note that for Ga-face the N-atom is stacked directly over the Ga- atom and vice-versa for the N-face. The wurtzite lattice is characterized by three parameters: the edge length of the basal hexagon (a_0), the height of the hexagonal lattice cell (c_0), and the cation-anion bond length ratio (u_0) along the [0001] axis in units of c_0. The subscript "$_0$" indicates these values are those of the equilibrium lattice. These dimensions are marked in Fig. 6.3. In an ideal wurtzite crystal, the c_0/a_0 ratio is 1.6330 and u_0 is 0.375. Because of the different metal cations, the bond lengths and the resultant c_0/a_0 ratio of AlN, GaN and InN are different (as listed in Table 6.1). It is obvious from Table 6.2 that among the group-III nitrides, GaN is closest to the ideal structure, followed by InN and AlN. This fact is very important because the degree of non-ideality is an important factor in determining the strength of polarization in group-III nitrides.

Table 6.2 Structural parameters for AlN, GaN, and InN.

Parameter	Ideal	AlN	GaN	InN
a_0 (Å)[a]	-	3.112	3.189	3.54
c_0 (Å)[a]	-	4.982	5.185	5.705
c_0/a_0 (exp.)[a]	-	1.6010	1.6259	1.6116
c_0/a_0 (cal.)[b]	1.6330	1.6033	1.6297	1.6180
u_0[c]	0.375	0.380	0.376	0.377

[a]Ref. [242], [b]Ref. [243], [c]Ref. [244]

6.3 Spontaneous and piezoelectric polarization

Group III-nitride has nitrogen which is the smallest and the most electronegative group-V element. The metal in these compounds create metal-nitrogen covalent bond which is strongly attracted by the coulomb potential of the nitrogen atomic nucleus. This

means that the metal-nitrogen covalent bond will have stronger ionicity compared to other III-V covalent bonds. This localized ionicity will combine together to generate macroscopic polarization in AlN, GaN or InN crystals as the c_0/a_0 ratio deviates from the ideal value [245, 244]. Since this polarization is produced without any external strain and only due to the property of crystal, this is called *spontaneous polarization* (P_{SP}) [244]. In III- nitrides, the covalent bonds parallel to the c-axis and the other three covalent bonds in the tetrahedral structure are strongly ionic and are primarily responsible for the spontaneous polarization. As seen from Fig. 6.3, the microscopic polarization created by the metal-nitride bond that is parallel to c-axis is $\bar{p}_1$. While the other three metal-nitride bonds add up vectorically in space and exhibit microscopic polarization of $\bar{p}_2$. For ideal wurtzite crystal this two polarizations cancel each other as they are equal and opposite in direction. However, as the c_0/a_0 ratio decreases (c_0 decreases and a_0 increases), these three covalent bonds will be at a wider angle from the c-axis, and their resultant compensation polarization will decrease, giving rise to a stronger macroscopic spontaneous polarization (see Fig 6.3 and Table 6.3).

Table 6.3 The dependence of spontaneous polarization on the c_0/a_0 ratio, Ref. [243]

Parameter	AlN	GaN	InN
c_0/a_0	1.6033	1.6297	1.6180
P_{SP} (C/m^2)	-0.090	-0.034	-0.042

As described in the previous section, we can see that the polarizations of AlN, GaN, and InN strongly depend on the c_0/a_0 ratio. Now, if this ratio is changed further by applying external stress, the ideal lattice parameters c_0 and a_0 of the crystal structure will change to accommodate the stress. Thus the polarization strength will be changed. This

additional polarization in strained III-nitride crystals, in addition to the spontaneous polarization already present, is called *piezoelectric polarization* (P_{PE}). For example, if the nitride crystal is under biaxial compressive stress, the in-plane lattice constant a_0 will decrease and the vertical lattice constant c_0 will increase, making the c_0/a_0 ratio increase towards the ideal lattice value of 1.6330. This will decrease the polarization strength of the crystal; since the piezoelectric polarization and the spontaneous polarization will act in opposite directions [see Fig. 6.4 (a)]. On the other hand, if the nitride crystal is under tensile stress, the in-plane lattice constant will increase and the vertical lattice constant

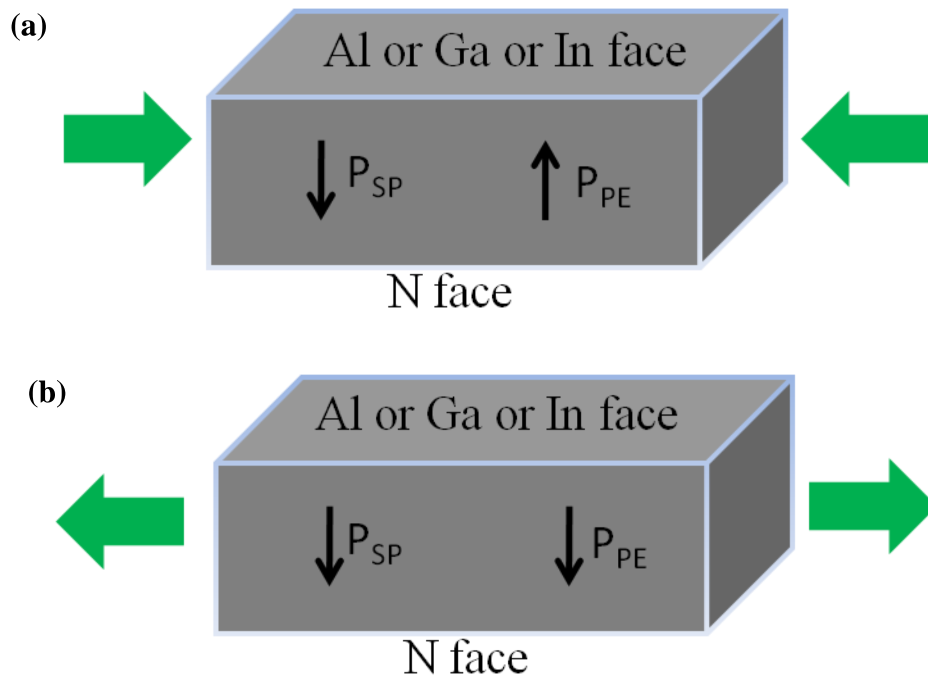

Figure 6.4: The direction of piezoelectric polarization with (a) compressive, and (b) tensile stress on Al(/Ga/In)N layer.

will decrease, lowering the c_0/a_0 ratio further away from 1.6330. This will increase the overall polarization, since the piezoelectric and the spontaneous polarizations now act in

the same direction [see Fig. 6.4 (b)]. When a biaxial stress is applied to the crystal along the direction perpendicular to *c*-axis, the piezoelectric polarization is expressed as [244] ,

$$P_{PE} = e_{33}\,\varepsilon_z + e_{31}(\varepsilon_x + \varepsilon_y) \tag{6.01}$$

where, e_{33} and e_{31} piezoelectric constants of the wurtzite material (Table 6.4). If the lattice parameters are changed to c and a due to external strain, then the z- direction strain,

$$\varepsilon_z = (c - c_0)/c_0 \tag{6.02}$$

If the material has same strain along x and y direction (isotropic), the strain can be expressed as,

$$\varepsilon_x = \varepsilon_y = (a - a_0)/a_0 \tag{6.03}$$

The shear related strain is not considered in this work. The z and x axis strains can be related as,

$$\varepsilon_z = -2\left(\frac{C_{13}}{C_{33}}\right)\varepsilon_x \tag{6.04}$$

Where, C_{13} and C_{33} are elastic constants.

Table 6.4 List of elastic and piezoelectric constants used for calculation

Parameters	AlN	GaN
C_{13} (GPa)[a]	108	106
C_{33} (GPa)[a]	373	398
e_{31} (C/m^2)[b]	-0.53	-0.34
e_{33} (C/m^2)[b]	1.50	0.67

[a]Ref. [242] [b]Ref. [243]

A list of reported values of the piezoelectric and elastic constants can be found in Ref. [245]. Moreover, Vurgaftman *et al.* reviewed all the band parameters of nitrogen containing compounds and summarized the recommended parameters for simulation [244]. Equations (6.01) and (6.04) can be combined together to obtain,

$$P_{PE} = 2\left(\frac{a - a_0}{a_0}\right)\left(e_{31} - e_{33}\frac{C_{13}}{C_{33}}\right) \tag{6.05}$$

It should be mentioned here that, Eq. (6.05) is only applicable when the x and y axis strain values are same (for as grown AlGaN on GaN). Therefore this is widely used to find out the piezoelectric polarization AlGaN layers grown pseudomorphically on GaN where AlGaN layer faces tensile stress during growth (lattice constant of AlGaN is smaller than that of GaN). However, if an AlGaN/GaN heterostructure is embedded on a GaN microcantilever, where the strain during cantilever bending is not biaxial, the Eq. (6.05) is not valid.

6.4 Growth of AlGaN/GaN heterostructures

Unlike Si, the bulk growth of GaN is not possible due to huge amount of defect which hinders any device operation. This limits GaN growth to only epitaxial growth which was not optimized and perfected until the 80's. At present the growth and quality of GaN is good enough to fabricate reliable electronic and optoelectronic devices. Due to the lack of any native substrate, GaN is grown on foreign substrate that has a close lattice match. 6H-SiC is the most ideal choice because of the lattice mismatch of less than 3.5%. However, sapphire (Al_2O_3) is most extensively used because of its low cost (lattice mismatch with GaN is 13.9%) [246]. Though SiC is better than sapphire in several

respects, including higher thermal conductivity (3.7 W/ $cm^{-1}K^{-1}$ compared to 0.23 W/$cm^{-1}K^{-1}$ for sapphire) and better lattice match, it does suffer from several disadvantages. The surface finish of SiC is usually not good (about ten times rougher than sapphire) as it is very hard material and difficult to polish. Also, there are intrinsic defects in the SiC substrate that might affect the GaN crystal quality. In addition, thermal expansion coefficient mismatch between SiC and GaN or AlN give rise to strain in the GaN layer, which is also complicated by the smaller but significant lattice mismatch between SiC and GaN. To make compatible with Silicon electronics, Si substrates (111) were also investigated for GaN. GaN grown on (100) Si is predominantly cubic. The layers grown on (111) Si are predominantly wurtzite which is the ideal match for epitaxial growth. Though the use of Si substrate has not matured to the point that it can be commercialized reliable electronics or optoelectronics, Si substrates are widely used for nitride based MEMS application [247, 248]. GaN is mostly grown by a two-step process (Metal Organic Chemical Vapor Deposition (MOCVD) described by Amano *et. al.* [249] where a nucleation layer (also sometimes called the buffer layer) of AlN at is grown lower

\

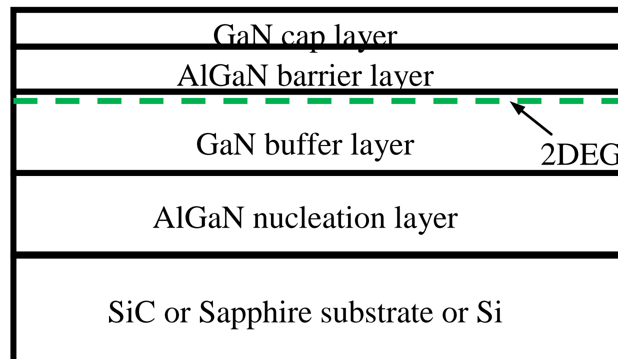

Figure 1: Typical layer structures of nitride heterostructures grown by MOCVD.

temperature on c-plane sapphire before growing the main GaN film at a higher temperature. Development of the growth of GaN by Molecular Beam Epitaxy (MBE) was also been done, however it was slow and tedious due to several problems [246]. Since III-nitrides can grow in either N-face and Ga-faced structure (which is discussed in next section), and growth is always along the [0001] axis along which the crystals are non-centrosymmetric. It has been observed that III-nitride layers grown by MOCVD are almost always Ga-face irrespective of the growth conditions, or the nature of the intervening layers. However, growth by MBE can result in either Ga-face or N-face material depending on the nature of the nucleation layer [241]. For microwave device applications, the Ga-face material turns out to be most important, and has been studied almost exclusively in this work. A typical layer structure grown by MOCVD on sapphire or SiC is shown in Fig. 6.5. Typically, the GaN buffer layer is ~2 μm thick and totally relaxed, while the AlGaN barrier is pseudomorphic assuming the in-plane lattice constants of the GaN layer. Please note that there is a cap layer (1 – 2 nm thick) grown on top of the regular AlGaN/GaN heterostructure layer with Ga-face polarity. The effect of the cap layer (10 – 20 Å) in the Ga-face heterostructure is to enhance the surface barrier height and will be discussed later in the chapter. The 2DEG is formed at the AlGaN/GaN heterostructure interface on the GaN side for both N-face and Ga-face material (similar to the Ga-face MBE and MOCVD materials) as expected, due to smaller bandgap of GaN. However, the important difference is that in the Ga-face material the 2DEG is formed at the AlGaN/GaN hetero-interface, while in the N-face material it is formed at the GaN/AlGaN hetero-interface. It should also be pointed out, that for 2DEG to actually

form in the N-face heterostructure, the GaN top layer should be much thicker than the GaN cap layer (Ga-face case), typically ~25 nm.

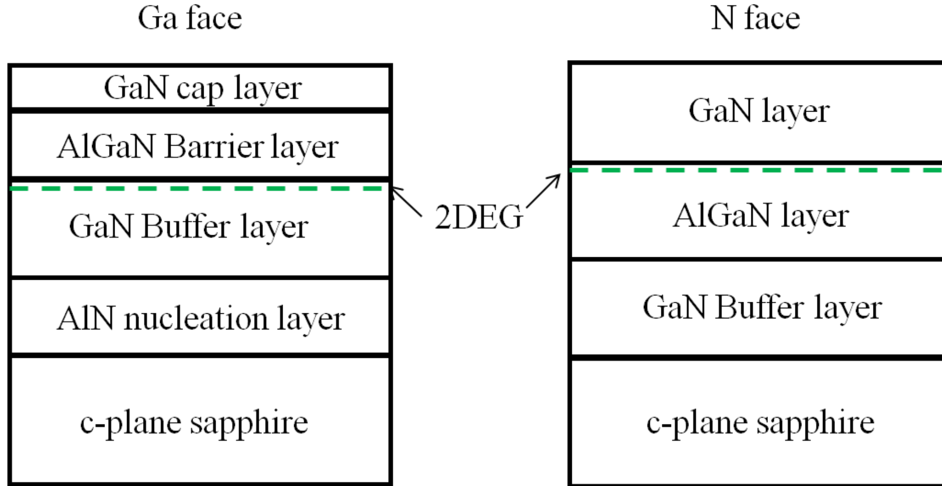

Figure 6.6: Layer structures of Ga-face and N-face nitride heterostructures grown by MBE on sapphire. Note that the N-face structure does not have a nucleation layer (a low temperature GaN nucleation layer can also be used to get N-face polarity).

6.5 Formation of 2DEG

The two dimensional electron gas (2DEG) is generated at the interface of AlGaN and GaN. The exact location of the 2DEG is dependent on the face on which AlGaN is grown. In general, if the polarization P changes in space then there will be a charge density ρ associated with such a change and given by the negative divergence of the polarization vector as, $\rho = -\nabla \cdot P$. For the wurtzitic III-nitrides, polarization is always directed along the growth axis ([0001] direction), perpendicular to the heterostructure interface. In such a case, there will be a bound sheet charge σ_{int} formed at the interface of the two layers (assumed to be planar and abrupt), and is given by,

$$\sigma_{\text{int}} = P_{tot,AlGaN} - P_{tot,GaN} \tag{6.06}$$

And therefore, $$\sigma_{\text{int}} = (P_{SP} + P_{PE})_{AlGaN} - (P_{SP} + P_{PE})_{GaN} \qquad (6.07)$$

Due to interface roughness or unintentional composition gradient, heterojunctions are rarely totally abrupt. However, as long as the gradient of the heterojunction is not over a large distance (e.g. > 20 Å), a sheet density (σ) given by Eq. (6.07) is a quite good approximation [245]. This bound charge induced by a change in polarization of the two layers will attract compensating mobile charge at the interface. If the bound charge is positive, it will create a negative mobile sheet charge, and vice versa. With this understanding we will focus on the calculation of bound charge, and the corresponding 2DEG at the AlGaN/GaN interface.

To find out the 2DEG concentration, all the band parameters of AlGaN (which are dependent on Aluminum mole fraction, x) need to be calculated. The following set of linear interpolations (as done in Ref. [245]) between the corresponding values of GaN and AlGaN are used for calculation.

Lattice constant, $$a(x) = (-0.077x + 3.189)\times 10^{-10} \text{ m} \qquad (6.08)$$

Elastic constants, $$C_{13}(x) = (2x + 106) \text{ GPa} \qquad (6.09)$$

$$C_{33}(x) = (-25x + 398) \text{ GPa} \qquad (6.10)$$

Piezoelectric constants, $$e_{31}(x) = (-0.19x - 0.34) \text{ C/m}^2 \qquad (6.11)$$

$$e_{33}(x) = (0.83x + 0.67) \text{ C/m}^2 \qquad (6.12)$$

Spontaneous polarization, $$P_{SP}(x) = (-0.056x - 0.034) \text{ C/m}^2 \qquad (6.13)$$

From the previous section, during pseudomorphic growth of AlGaN layeron GaN, the GaN buffer layer is relaxed, therefore GaN will have only spontaneous polarization component in the layer. However, as AlGaN has smaller lattice constant it will feel a tensile force when assuming the in plane lattice constant of GaN. Hence, AlGaN will

have both spontaneous and piezoelectric polarization. So, polarization induced sheet charge density,

$$\sigma_{\text{int}} = (P_{SP})_{GaN} - (P_{SP} + P_{PE})_{AlGaN}$$

$$= P_{SP}(x) + 2\left(\frac{a(0)-a(x)}{a(x)}\right)\left(e_{31}(x) - e_{33}(x)\frac{C_{13}(x)}{C_{33}(x)}\right) - P_{SP}(0) \qquad (6.14)$$

Figure 6.7 shows the variation of different polarization in $Al_xGa_{1-x}N$ with aluminum mole fraction. As seen in Fig. 6.7, though the variation of spontaneous polarization is linear, the piezoelectric polarization and hence the total polarization does not vary linearly.

The total polarization in AlGaN (pseudomorphically grown on GaN-face GaN) can be found out by calculating all the parameters mentioned from Eqs. (6.08)-(6.14). However, all these equations can be combined together into one polynomial equation in the following form,

$$P_{\text{total, AlGaN}} = P_{\text{SP, AlGaN}} + P_{\text{PE, AlGaN}} = M_0 + M_1x + M_2x^2 + M_2x^3 \qquad (6.15)$$

where the co-efficients are M_0 = -0.034, M_1 = -0.081, M_2 = -0.0211, and M_3 = -0.0014 (found out from 3rd order polynomial curve fitting of the data shown in Fig. 6.7).

Free electrons tend to compensate the high positive polarization induced sheet charge at the AlGaN/GaN interface for Ga(Al)-face or at the GaN/AlGaN interface for N-face material. Figure 6.8 shows the conduction band diagram, and charge densities at the interface and the surface. The maximum sheet carrier concentration located at these interfaces of the nominally undoped structures is expected to be,

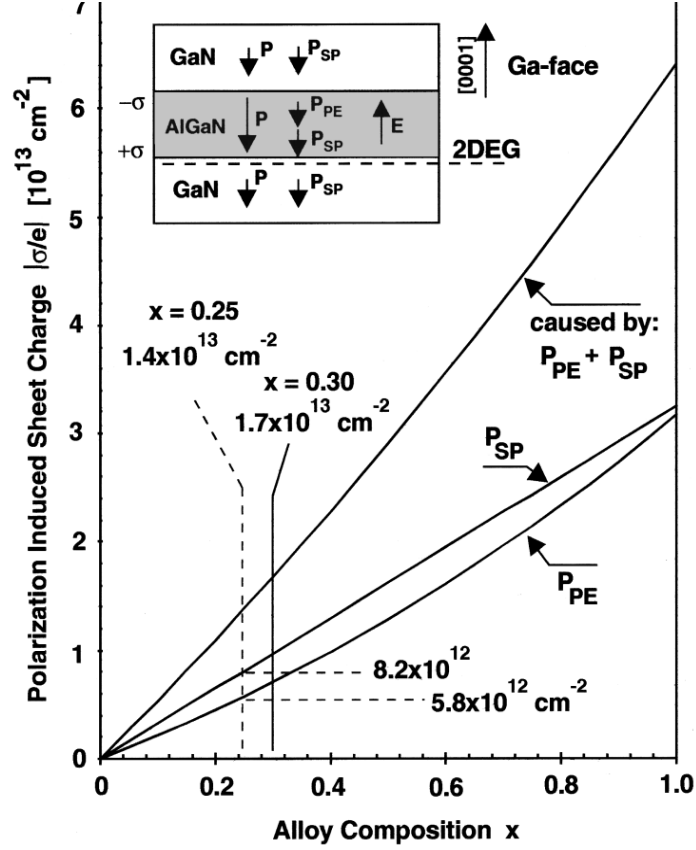

Figure 6.7: Variation of the spontaneous and piezoelectric polarization of $Al_xGa_{1-x}N$ and the bound charge at AlGaN/GaN interface plotted against aluminum mole fraction of $Al_xGa_{1-x}N$ [245].

$$n_s(x) = \frac{\sigma_{\text{int}}(x)}{q} - \left(\frac{\varepsilon_0 \varepsilon(x)}{dq^2}\right)\left[q\phi_b(x) + E_F(x) - \Delta E_C(x)\right] \qquad (6.16)$$

where σ_{int} is the bound polarization sheet charge (as plotted in Fig. 6.6), q is the electron charge, ε_0 is the permittivity of free space, $\varepsilon(x)$ is the relative dielectric constant of AlGaN, d is the thickness of the AlGaN layer. ϕ_b is the Schottky barrier height, E_F is the Fermi level at the heterointerface with respect to the GaN conduction band edge, and ΔE_c is the conduction band offset at the AlGaN/GaN interface. To determine the sheet carrier concentration from the polarization induced sheet charge density from Eq. (6.14), we use the following approximations:

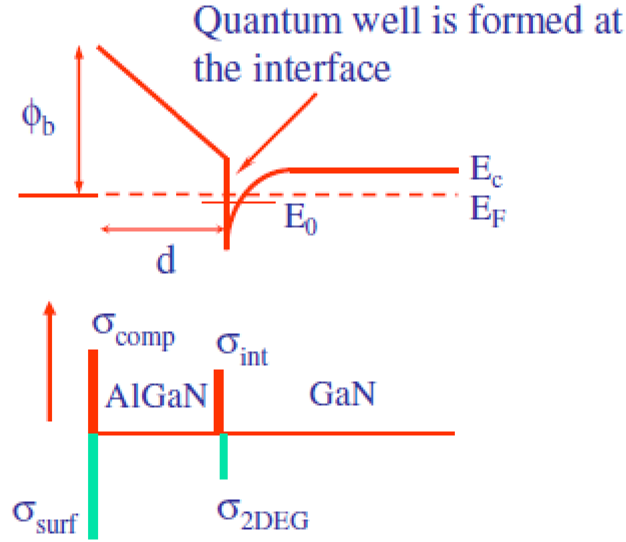

Figure 6.8: Conduction band diagram, sheet charge densities at the surface and interface of AlGaN/GaN heterostructure.

Dielectric constant: $\varepsilon(x) = (-0.5x + 9.5)$ (6.17)

Schottky barrier: $\phi_b = (1.3x + 0.84)$ eV (6.18)

Where, the Fermi energy level can be expressed as [245],

$$E_F(x) = E_0(x) + \frac{\pi\hbar^2}{m^*(x)} n_s(x) \tag{6.19}$$

where the ground sub-band level of the 2DEG is given by,

$$E_0(x) = \left[\frac{9\pi\hbar q^2}{8\varepsilon_0 \sqrt{8m^*(x)}} \frac{n_s(x)}{\varepsilon(x)} \right]^{2/3} \tag{6.20}$$

the, electron effective mass is $m^*(x) \approx 0.20m_0$ [250], where m_0 is the rest mass of an electron. And the conduction band offset is,

$$\Delta E_C(x) = 0.7\left[E_g(x) - E_g(0)\right] \tag{6.21}$$

The bandgap of $Al_xGa_{1-x}N$ is express as,

$$E_g(x) = xE_g(AlN) + (1-x)E_g(GaN) - x(1-x)1.0 \text{ eV}$$

$$\therefore \quad E_g(x) = x6.13 + (1-x)3.42 - x(1-x)1.0 \text{ eV} \qquad (6.22)$$

Equation (6.16) is a result of simple semiclassical electrostatic analysis assuming charge neutrality condition to hold between the sheet charge densities at the surface and the interface. Using equations (6.12) through (6.17), the free electron concentration can be calculated as a function of Al alloy composition or the thickness of the barrier layer (assuming the surface barrier to be constant). Calculated free electron sheet density versus aluminum mole fraction is shown in Fig. 6.9. Two different AlGaN barrier layer thickness (100 Å and 300 Å) are plotted to illustrate the effect of barrier thickness variation. We find that as the AlGaN barrier thickness is decreased, the 2DEG density drops due to increased Schottky barrier depletion. For example, the 2DEG density for 30% Al composition is 1.45×10^{13} cm^{-2} for a 300 Å barrier and is 1.06×10^{13} cm^{-2} for a 100 Å barrier. We notice from Fig. 6.9 that as the AlGaN barrier thickness is increased, the 2DEG density approaches the fixed polarization induced charge density. This can be easily understood, since the dipolar charge ($\sigma_{int}+n_s$) across the AlGaN barrier required to produce a fixed surface barrier decreases as the thickness increases, as the gate schottky barrier is assumed to be constant for a particular Al composition irrespective of the AlGaN layer thickness. However, we note that as a

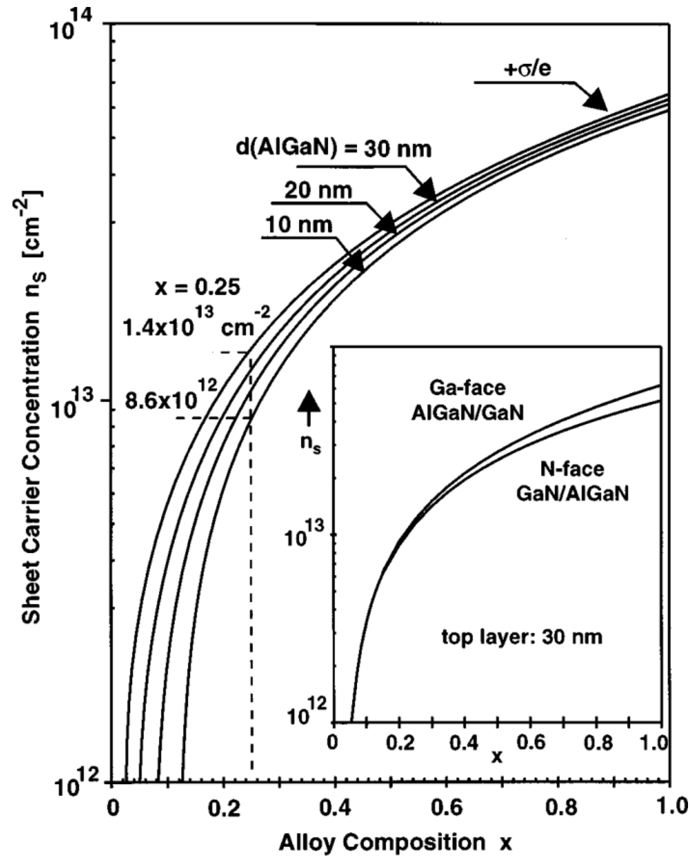

Figure 6.9: Sheet carrier concentration of the 2DEG confined at a Ga-face (GaN/AlGaN/GaN) or N-face (GaN/AlGaN/GaN) interface for different thickness of the AlGaN barrier. The insert shows the maximum sheet carrier concentration of a pseudomorphic grown Ga-face AlGaN/GaN and a N-face GaN/AlGaN heterostructure.

consequence of a constant barrier height, there is a lower bound of the Al composition of the AlGaN layer for the formation of the 2DEG at the interface. This has been found to be 2% for 300 Å, and 8% for 100 Å AlGaN layer thickness. To understand the effect of the AlGaN thickness on the 2DEG density more clearly, it is plotted against barrier layer thickness for 35% Al alloy composition in Fig. 6.9. It is seen that the 2DEG increases monotonically with AlGaN thickness and asymptotically reaches the sheet carrier concentration of 1.98×10^{13} cm^{-2} (equal to the polarization induced bound charge density for 35% Al composition for the barrier layer). In addition, there exists a minimum AlGaN

thickness of 20 Å below which there exists no 2DEG at the interface. This is due to the presence of a constant schottky barrier height, and is very similar to having a lower bound for Al composition with constant AlGaN thickness as discussed above. Note that the surface barrier height (schottky barrier height if there is a schottky contact or the bare surface barrier height) controls the charge dipole across the AlGaN barrier, which in turn controls the magnitude of the 2DEG, and any change in surface barrier is reflected as a change in the 2DEG.

CHAPTER 7

ALGAN/GAN MICROCANTILVERS

This chapter discusses AlGaN/GaN based V-shaped microcantilevers exclusively. Design, theoretical calculations, simulations are presented thoroughly. Then detail of the cantilever fabrication processes are explained with related issues and problems. Experimental results, sensing characteristics are also covered in this chapter.

7.1 Introduction

The development of AlGaN/GaN microcantilevers starts from designing the cantilever models, simulating the cantilevers in COMSOL and then fabricating them in the final step. In this section AlGaN/GaN microcantilevers are designed and discussed for the fabrication purpose. The performance of microcantilevers is determined by various parameters such as stiffness, quality factor and resonant frequency. With the goal of improving the performance, various researchers have studied and developed models for understanding cantilever behavior. There is always a trade-off between parameters such as deflection and the resonant frequency. In AFM, cantilevers sense forces and when the deflection of the cantilever is measured optically, good deflection capability is required. For biological applications, surface effects play an important role and the binding can be related to changes in the resonant frequency. High sensitivity is prevalent in systems with higher resonant frequency. The active region available on the upper surface of the cantilever is also an important parameter for chemical or biological sensors. Different cantilever parameters are weighted according to the requirements of the application for optimizing the performance. Rectangular, V-shaped and T-shaped cantilevers are the most commonly used cantilever geometry for sensors. Cantilevers of different geometries can be manufactured with any desirable spring constant and resonance frequency. The main difference is their torsional stiffness. V-shaped cantilevers have significantly larger torsional and lateral stability compare to rectangular and T-shaped geometries.

We have designed two different types of AlGaN/GaN microcantilevers for multifunctional detection of analyte molecules. The first one is HFET embedded V-

shaped microcantilever and the second one is V-shaped heated microcantilever, they will be discussed in the next sections.

7.2 HFET embedded V-shaped AlGaN/GaN microcantilever

The 2DEG formed at the AlGaN/GaN interface becomes modulated by the stress induced change in piezoelectric polarization. This stress induced piezoelectric response of AlGaN/GaN heterostructures is converted to piezoresistive response and the HFET acts as the piezoresistive deflection sensor which is integrated at the base of the cantilever. Because of the V-shaped design of the cantilever, there are two this kind of HFETs embedded at the base of each of the two arms of the cantilevers. This has distinct advantages over rectangular cantilevers as it enables not only conductometric mode of sensing through the arms but also the HFETs get utilized as the transduction elements for transducing the mechanical oscillation into electrical signal.

7.2.1 Cantilever dimensions

The V-shaped cantilever can in fact be approximated by two rectangular plates joined in parallel [229]. The initial design parameters, specially the length and arm width, were chosen from standard tipless rectangular microcantilevers (350 μm × 25 μm × 1 μm) purchased from Mikromasch Inc. Therefore the dimensions of these rectangular cantilevers were taken as the reference for this design. The GaN layer (cap layer, AlGaN layer, GaN layer and the transition layer) in the wafer had a thickness of 3.22 μm. The thickness of the cantilever was also 3.22 μm. Though GaN can be etched

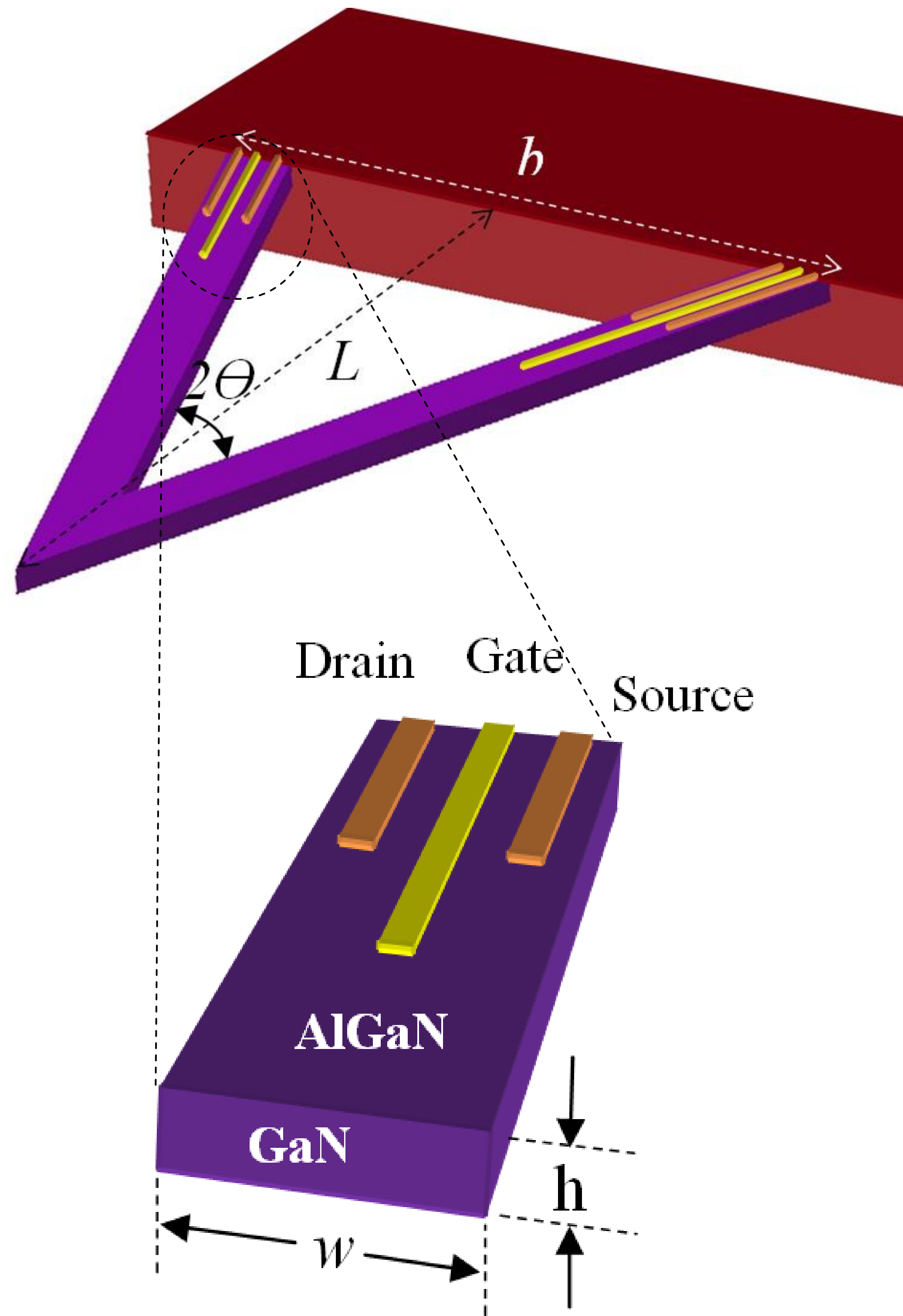

Figure 7.1: Schematic diagram of the AlGaN/GaN HFET embedded V-shaped microcantilever.

Table 7.1 Dimension of the AlGaN/GaN HFET embedded microcantilevers and calculated *k* and *f*.

L **(μm)**	***b (μm)***	***w*** **(μ*m*)**	***h*** **(μ*m*)**	**2Θ *(deg)***	***k*** **(N/m)**	***f*** **(kHz) ***
350	250	25	3.221	39	1.6257	37.2

*COMSOL simulation

Table 7.2 Dimension of the AlGaN/GaN HFET

Source		**Drain**		**Gate**	
Length (μm)	Width (μm)	Length (μm)	Width (μm)	Length (μm)	Width (μm)
4	37.2	4	37.2	3	73.3

down to reduce thickness, there is a possibility of the surface becoming rough and deteriorating the quality factor of the cantilever. Lower width gives lower *k*, however an AlGaN/GaN HFET would be fabricated at the base of the cantilever and reasonable width is needed to accommodate the HFET safely on the microcantilever. 25 μm is a safe choice considering the fabrication issues during photolithography (Fig. 7.1). GaN microcantilever with longer length bends downward after the cantilever release during fabrication process [142] (discussed in the next sections); again increasing L decreases the angle between arms, θ. Both effects reduce *k*, therefore long cantilever was not considered in the design.

7.2.2 HFET dimensions

As shown in Fig. 7.1 the AlGaN/GaN HFETs are situated at the base of each of the arms of the microcantilever where maximum strain is found [see next sections]. All the dimensions of the cantilever and the dimension of the HFET are shown in Table 7.1 and 7.2. Source or drain to gate distance is kept 5 μm in order to protect gate overlapping on the source/drain during litho and metallization. The bonding pads of 350 μm × 350 μm (not shown here) connect the source, drain and gate. The outline of the V-shaped cantilever (the arms) is actually the MESA outline, i.e. there is a continuous AlGaN layer from base to base of the cantilever.

7.2.3 Analytical model for resonant frequency and spring constant

In chapter 3 we have discussed the mechanical properties of the more common rectangular cantilever. In the case of V-shaped microcantilevers the equations need to be modified to fit the geometry.

7.2.3.1 2nd Moment of cross-sectional area

The 2nd moment of cross-sectional area, I can be express as,

$$I = \int_A z^2 dA \tag{7.01}$$

where, z is the distance from the centroid axis to the area dA. Therefore, I depends upon the cross sectional area of the cantilever [see Fig. 2.1 (a)].

For triangular beam,

$$I = \frac{wh^3}{6}\left[1 + 4\left(\frac{w}{b}\right)^3\right] \tag{7.02}$$

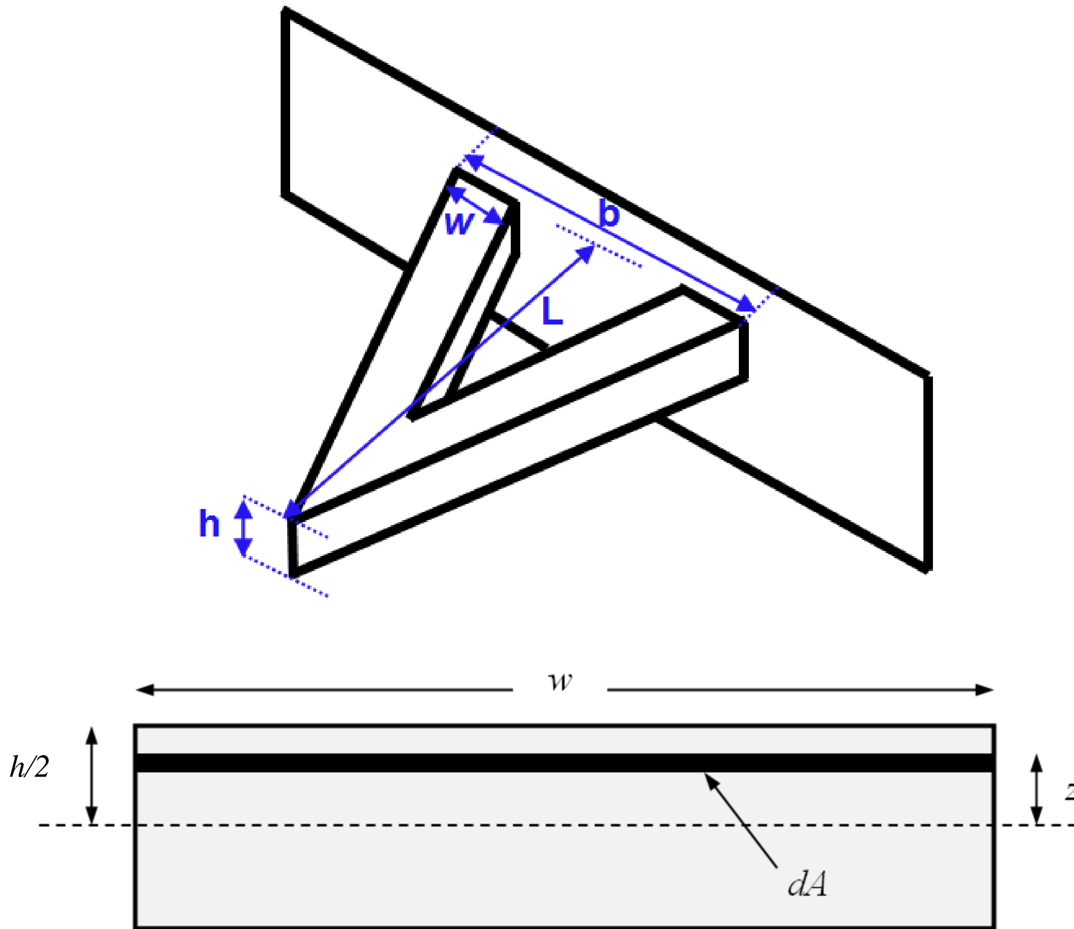

Figure 7.2: (a) Geometrical parameters of a triangular cantilever, (b) Calculation of *moment of cross-sectional area, I* for one rectangular arm of a V-shaped cantilever.

7.2.3.2 Spring constant

For the V-shaped cantilever, the most popular, conventional, and simplistic approach to the analytical evaluation of its normal spring constant is the use of the parallel beam approximation (PBA). The fundamental principle of the PBA is as follows: (a) Fist, the basic assumption is made that the V-shaped cantilever can be approximated by two rectangular cantilevers joined in parallel; (b) then, by using the well-known analytical result for the rectangular cantilever**,** [251] the spring constant of the V-shaped

cantilever can be trivially determined. However, to obtain the spring constant k (defined to be the force required per unit length deflection at the end tip) of the equivalent cantilever, we implement the zeroth order method presented in Ref. 4, from which we obtain the new PBA result,

$$k = \frac{Eh^3 w}{2L^3}\cos\theta\left[1+\frac{4w^3}{b^3}\left(3\cos\theta-2\right)\right]^{-1} \tag{7.03}$$

7.2.3.3 Natural frequency of oscillation

The V-shaped cantilever, with linear arms, has been equated as the difference of two solid triangles and the resonant frequency has been obtained using energy balancing principles and the Rayleigh–Ritz (RR) method [252]. Considering a linear V-shaped cantilever with E as theYoung's modulus, ρ as the density, h as the cantilever thickness, $W(x)$ as the varying width and l_1 as the length, from the symmetry of the V-shaped cantilever and by using the RR method the resonant frequency and $W(x)$ are given as [252],

$$f(W(x)) = \frac{h}{2\pi}\sqrt{\frac{3E}{\rho}}\sqrt{\frac{\int_0^L W(x)(l_1-x)^2\,dx}{\int_0^L W(x)x^4(3l_1)^2\,dx}} \tag{7.04}$$

$$W(x) = \begin{cases} \frac{W_1}{2}(1-\frac{x}{l_1}) - \frac{W_0}{2}(1-\frac{x}{l_0}), & x\in[0,l_0] \\ \frac{W_1}{2}(1-\frac{x}{l_1}), & x\in[l_0,l_1] \end{cases} \tag{7.05}$$

where W_1 is the width of the outer triangle, W_0 is the width of the inner triangle and x is the distance along the direction shown in Fig 7.3. The V-shaped cantilever is

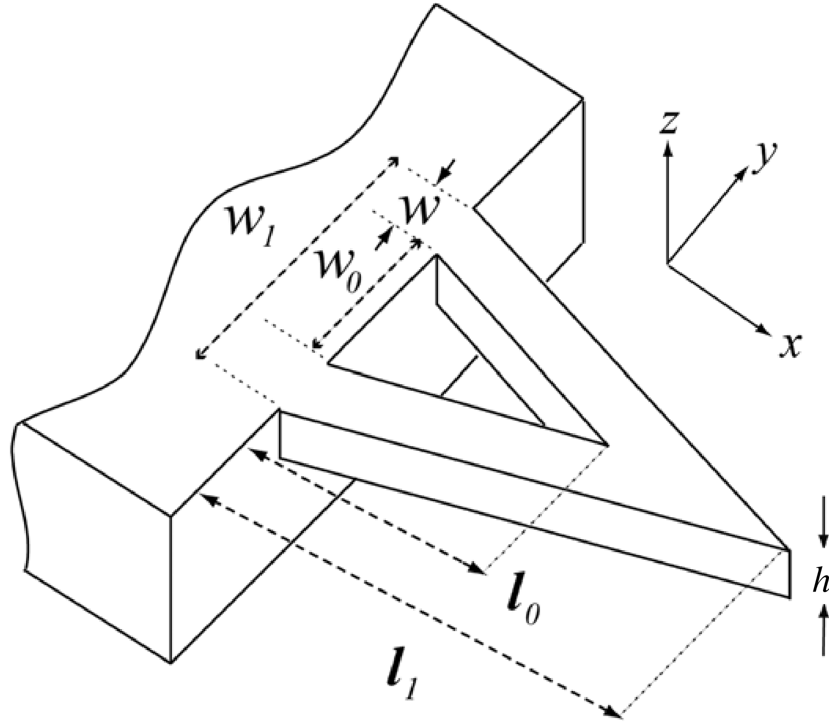

Figure 7.3: Structure of a general V-shaped microcantilever.

assessed as the difference of a smaller triangle from the outer triangle. L_1 is the length of the outer triangle and L_0 is the length of the inner triangle.

7.2.4 COMSOL simulation

7.2.4.1 Calculating resonant frequency

In contrast to the analytical calculations for rectangular cantilevers, the corresponding calculations for the V-shaped cantilevers (Fig. 7.4) are not easily performed. Nevertheless, some analytical expressions are found in the literature,8–14 which are useful for simplified V-shaped cantilever geometry. However, for special cases

of HFET embedded V-shaped cantilever the analytical calculation is not well established. In this section we will calculate and discuss the resonance frequency of the designed microcantilever by simulating a developed model in *COMSOL Multiphysics*. For the simulation the length, width and thickness are considered in x, y, and z directions respectively. The properties of material of GaN and AlGaN used for simulations are listed in Table **7.3.** COMSOL has the option of incorporating anisotropic elasticity, however for simplicity we only considered bulk elastic constant for both GaN and AlGaN.

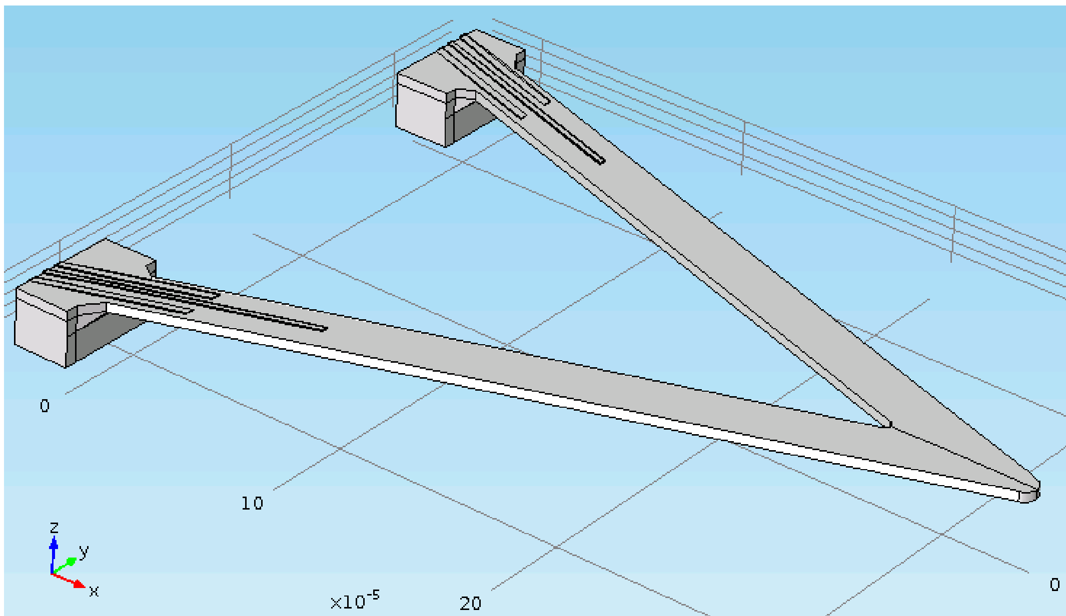

Figure 7.4: The model used for COMSOL simulation for the AlGaN/GaN HFET embedded V-shaped microcantilever

Table 7.3 Properties of GaN and AlGaN used for COMSOL simulations ([Ref. 253])

	GaN	AlGaN
Young's Modulus (*E*)	**210 GPa**	**185 GPa**
Density (ρ)	**6150 kg/m^3**	**5740 kg/m^3**

We calculated the resonant frequency using the *k*-spring constant calculation which is a parallel-beam approximation. We also looked into a different method, the Rayleigh-Ritz (RR) method, of calculating the first resonant frequency which does not rely on an effective mass constant like the parallel beam approx does. The output follows:

```
COMSOL Eigenf Output, f0 = 28.29 [kHz]
Parallel beam approx, f0 = 25.42 [kHz]  (-10.11%)
Rayleigh-Ritz method, f0 = 31.11 [kHz]  (+9.99%)
```

The COMSOL output lies almost directly between the two different approximation method outputs. Given this confirmation we were comfortable to move forward with the model to see how much non-idealities contribute to frequency shift.

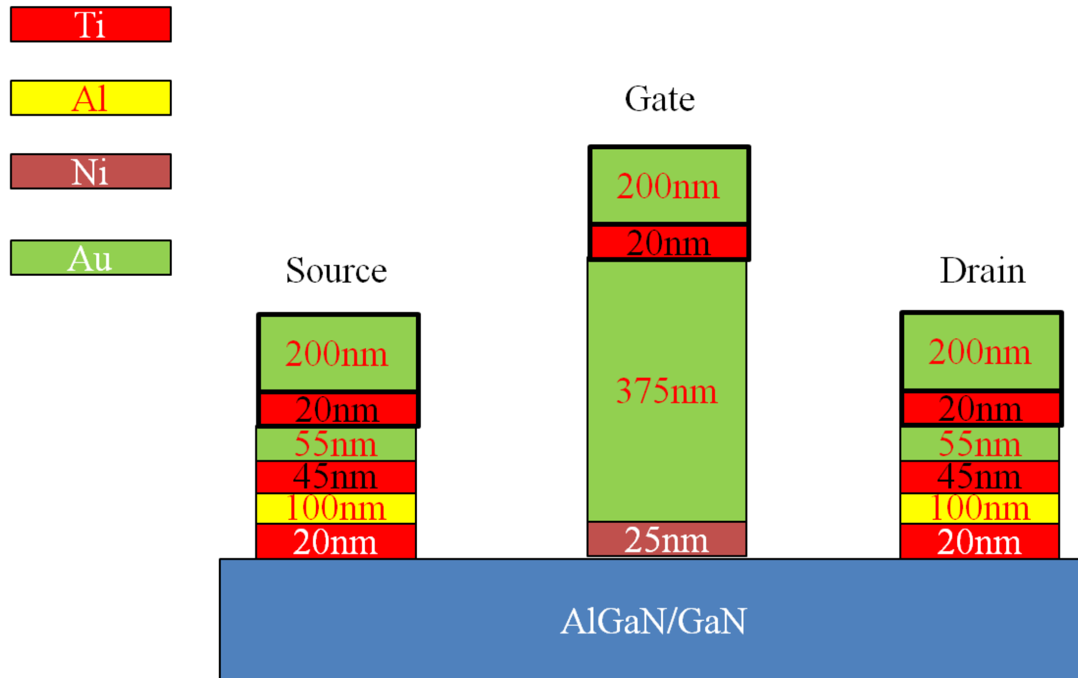

Figure 7.5: Cross section of a HFET embedded AlGaN/GaN V-shaped microcantilever showing different metal stacks (not drawn to scale).

Non-ideality factors

Several non-idealities were added to the model in order to attempt to account for frequency shift in the experimental setup from our calculated values. From the model shown in figure we have modeled the metal stacks as well as adding chamfering/fillets at the base and tip. Also, the standard bulk Young's modulus of 210 GPa is replaced with its orthotropic elasticity matrix. Given all of the model changes we observe a shift from 28.3 [kHz] up to 37.2 [kHz].

Interpreting the model

We take 37.2 [kHz] as our resonant "starting point" here we can assume that all non-idealities have caused a frequency shift from theoretical approximations without

considering thickness differences. We should consider the 4 [kHz] shift observed from re-orienting the material as our "error" while viewing the thickness addition table.

Factors not considered

In this simulation the largest avenues of frequency shift are observed. The following factors were not considered and may add to further resonance change:

- Mechanical property changes due to ambient temperatures.
- Where on the cantilever additional thickness may occur.

  Ex. 500 [nm] of thickness increase located on the half end closest to the base will cause a comparatively marginal (~100 Hz range), but nonetheless greater upward frequency shift than if the 500 [nm] thickness addition was located throughout the cantilever.
- Arm-width inconsistencies.

7.2.4.2 Simulating mechanical properties

A V-shaped HFET embedded cantilever is modeled using Finite Element Analysis (FEA) and Matlab programming. The microcantilever is applied at a constant force F = 1 nN as shown in Fig 7.6 (a) . Deflection and stress distribution of the cantilever is modelled using COMSOL 3.5a, Figure 7.6 and Fig. 7.7 show simulation results through modelling. With a distributed uniform force of 1 nN at the free end of the microcantilever a vertical displacement of 2.93×10^{-10} m was observed. We observe that the high stress region is located at base of the cantilever, which is in agreement with analytical models.

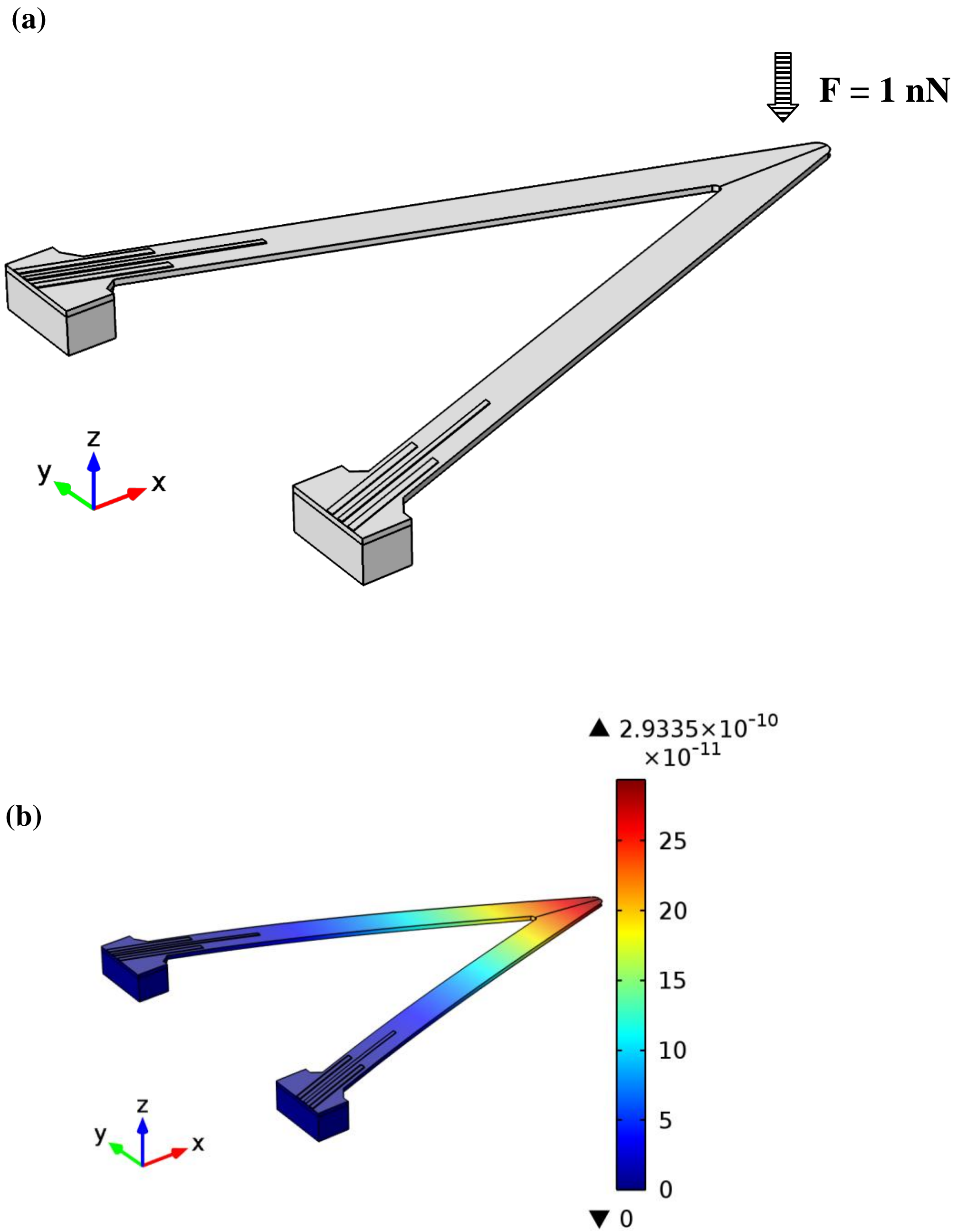

Figure 7.6: (a) The model used for COMSOL simulation for the AlGaN/GaN HFET embedded V-shaped microcantilever, the position of the applied force of 1 nN is shown by arrow and (b) the deflection result with the applied force.

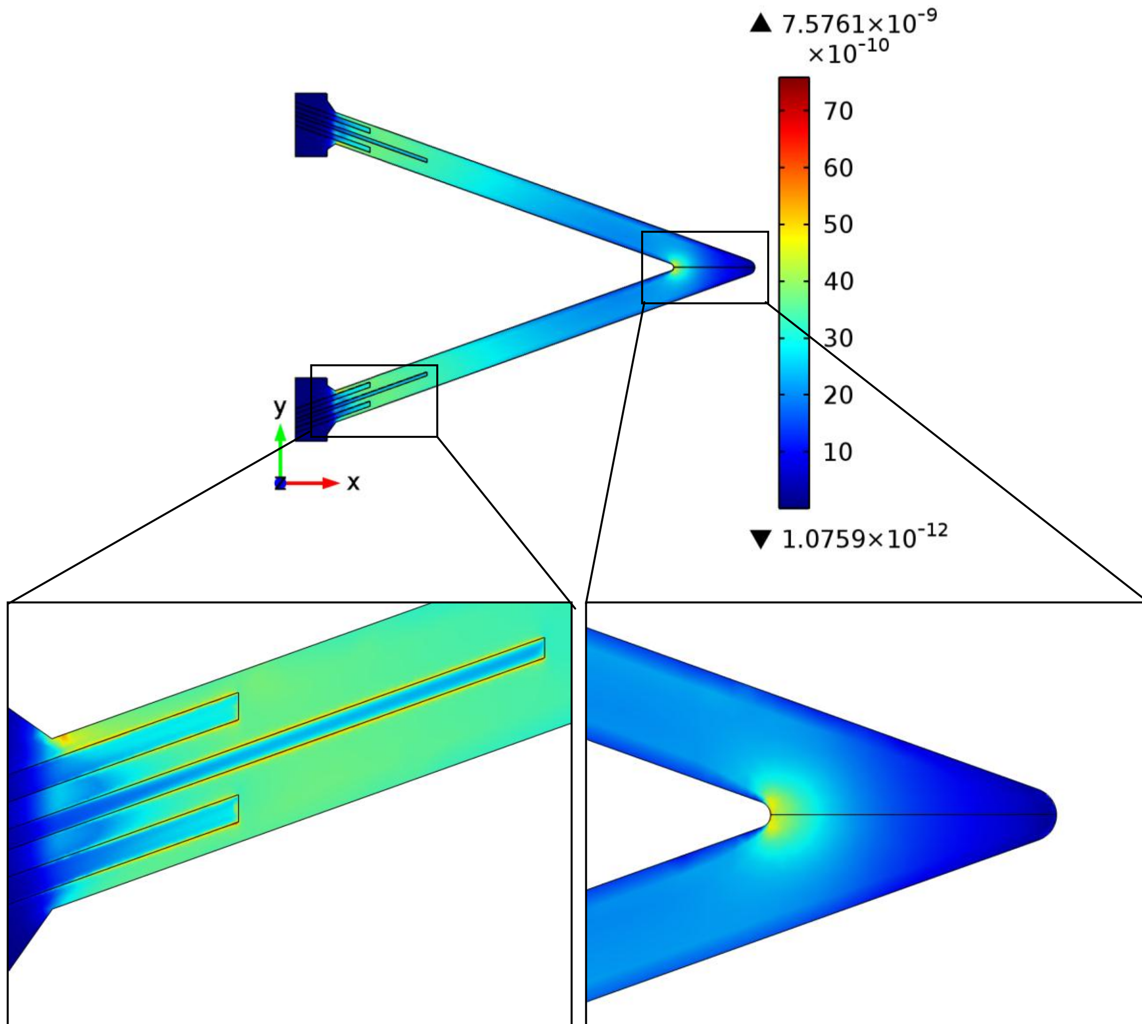

Figure 7.7: The *x*-direction strain distribution on the surface of the cantilever. Insets show expanded view of the base area.

7.3 V-shaped AlGaN/GaN micro heater cantilever

Microcantilevers, as we have discussed previously, offer outstanding opportunities for bio/ chemical sensors, as they can be highly sensitive to specific bio/chemical analytes [84, 255]. In addition, micro heated cantilevers (a.k.a. microhotplates) have been shown to be extremely useful for calorimetry [256, 257] and chemical sensing [258]. While several studies have shown that microcantilevers can be fabricated with internal resistive heaters [259, 260], little work has been done to converge microcantilevers with microhotplates for sensing applications. Microfabricated hotplates have previously been used for various sensing applications, including as a Pirani gauge [261], gas sensor [262], and a flow-rate sensor [263]. In some cases, the method or materials of microsensor fabrication limit its performance. The main design considerations for microhotplates are thermal isolation and temperature uniformity that can be achieved through free standing heatable microstructures, which are either bridges or cantilevers. King *et al.* fabricated micro hotplates which were made of Silicon microcantilevers. Fig. 7.8 (a) shows scanning electron microscope (SEM) image of a microcantilever heater and (b) infrared (IR) microscope IR microscope image of the heater cantilever during steady electrical excitation. The IR image is approximately 0.5 mm^2. The doped silicon cantilever is fabricated in a “U” shape such that it forms a continuous electrical path. The region near the cantilever free end is a highly resistive heater and the legs have lower electrical resistance such that they carry electricity. The IR image confirms substantial heating only near the free end of the cantilever.

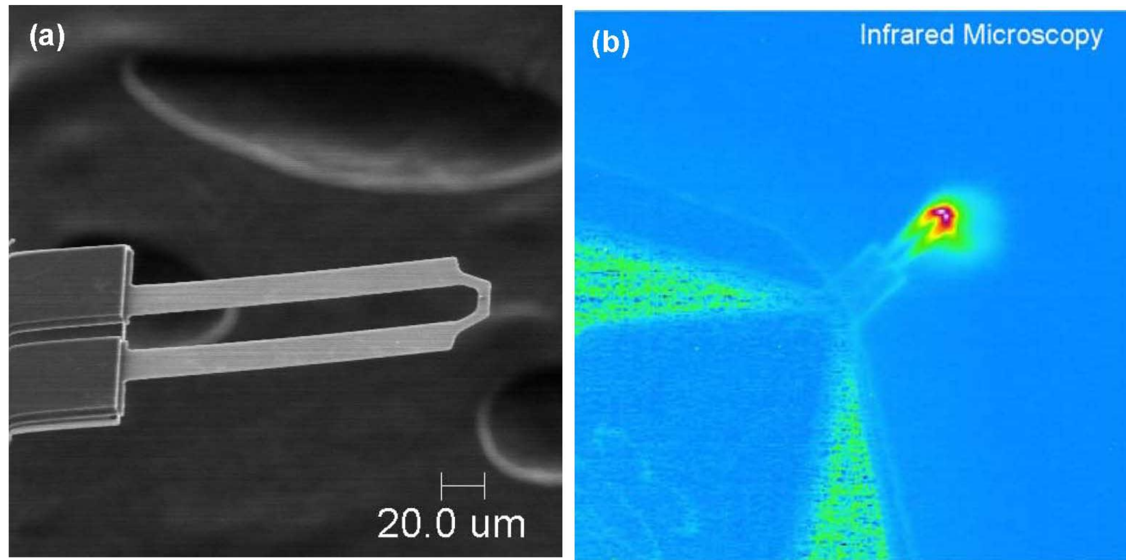

Figure 7.8: (a) scanning electron microscope (SEM) and (b) infrared (IR) microscope images of the fabricated heated cantilever, indicating heating only near the free end of the cantilever [265].

For heat conduction through mechanical links, porous silicon has been introduced for low power microhotplate arrays [264]. Microhotplates made from thin-film platinum heater-thermometers [265] could not be integrated with on-chip circuitry since platinum is not compatible with conventional silicon microelectronics fabrication. Microhotplates made from polysilicon [265] have poor long-term stability at high temperature since the grain boundary of polysilicon is highly reactive. Microcantilever heaters made from doped single-crystal silicon overcome these drawbacks, as integrated electronics could be produced in the same silicon layer, but suffer from poor deflection sensitivity.

Microcantilevers having both heaters and piezoresistive sensors would be useful in a number of applications. One example is thermal nanomanufacturing [264, 265], where the tip heating would perform writing, but piezoresistive topography sensing would be preferred in the presence of a thermally reactive substrate. A second example is

topography sensing where cantilever heating could be used to perform local materials synthesis [266], chemical reaction [267], or to clean the tip [268]. Finally, such a cantilever could be used to sense temperature-sensitive biochemical binding events [269].

The capability to heat microcantilevers is useful for cantilever-based sensors. Recently, heatable microcantilevers have demonstrated explosives detection with part-per-trillion sensitivity [270]. The cantilever heating caused deflagration of the chemical adsorbed to the cantilever, which in turn induced measurable cantilever deflection. For these experiments, commercial piezoresistive cantilevers were used to provide heating and laser and photodiode were used to detect induced deflection.

AlGaN/GaN based V shaped heated microcantilevers in this work will be designed to provide a highly uniform temperature to the analyte. Faster response time of less than 1ms and the highly sensitivite piezoresistive (discussed previously) deflection make this kind of AlGaN/GaN based V-shaped cantilevers ideal for microscale explosive vapor detection.

7.3.1 Cantilever dimensions

The novel AlGaN/GaN V-shaped heated cantilevers are tapered in shape as shown in Fig. The base of the cantilever is 25 μm, where as the tip width is reduced to only 3 μm, thus the tip is highly resistive. The outer arm length is 257 μm and the inner length is 252 μm. Arm to arm distance is 100 μm. The thickness of the cantilever is 3.221 μm, same as the HFET embedded cantilevers. Instead of having HFETs at the base, these tapered V shaped cantilevers have ohmic contacts at the base. The metal stacking is also the same as the source or drain stacking for the HFET embedded ones.

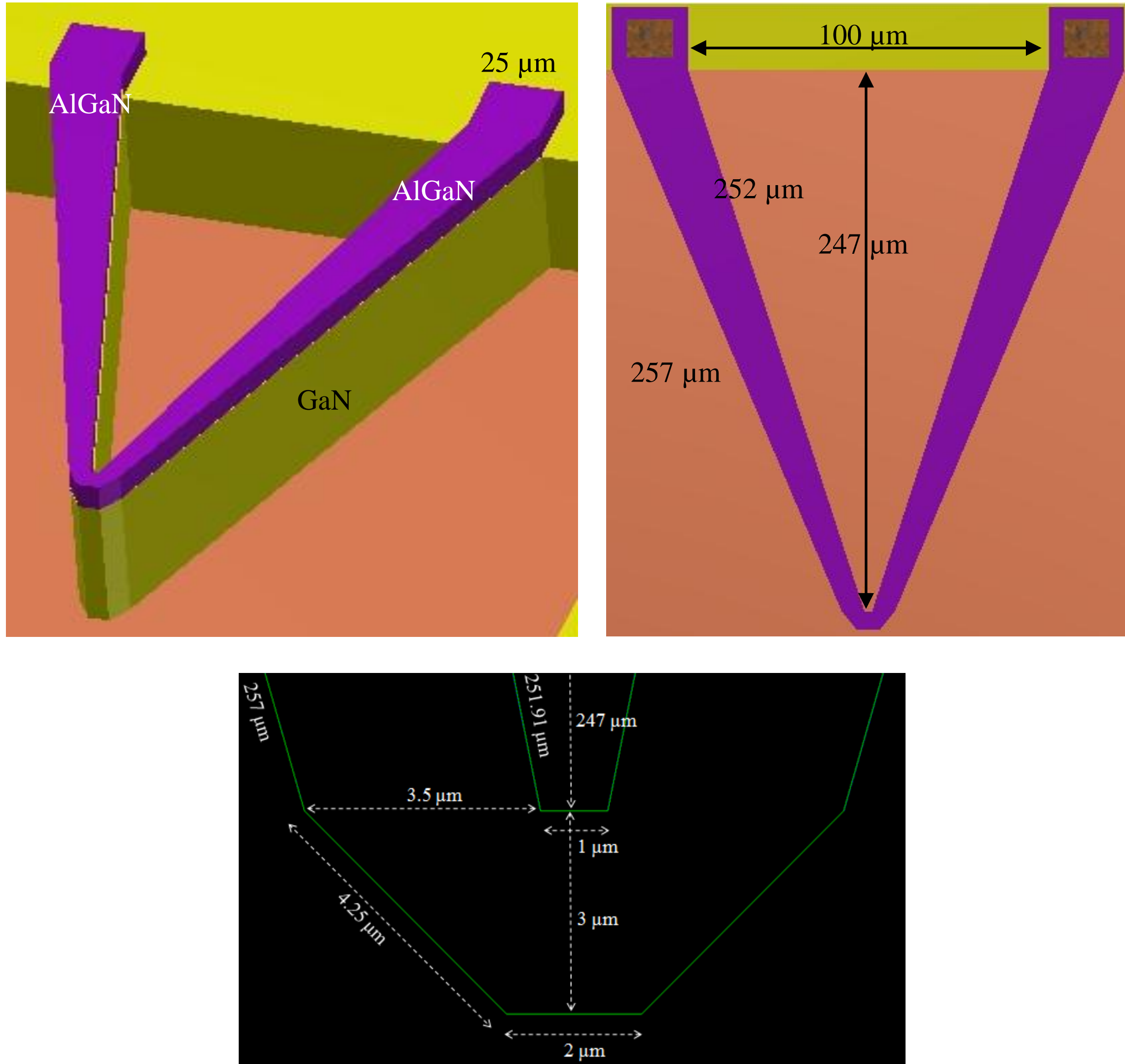

Figure 7.9: Design of the tapered V-shaped AlGaN/GaN microcantilevers (a) the GaN and AlGaN layer, (b) dimensions of the cantilever and (c) tapered tip dimension from the AutoCad design

7.3.2 COMSOL simulation

7.3.2.1 Calculating resonant frequency

Finite Element Aanalysis is the only way of calclating resonant frequency theoreically snice there is no straight analytical model of this kind of cantilever structure in the litertaure. The properties of the material for GaN and AlGaN used for the COMSOL simulations of these cantilevers are listed in Table 7.2**.**

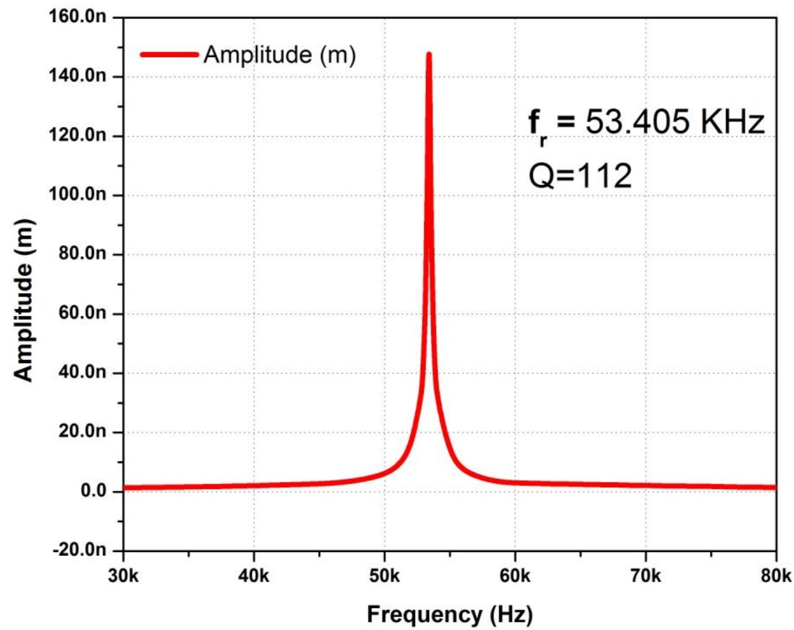

Figure 7.10: COMSOL simulated frequency response of the heated microcantilever.

The simulation was run using an isotropic loss factor n=1/200 (Q = 200) and a periodic force of 1 [nN] applied to the tip. The static displacement for a 1 [nN] tip force for this model is 0.81023 [nm]. z_static * Q = 0.81023 [nm] * 200 = 162 [nm].

7.3.2.2 Simulating mechanical properties

The tapered V-shaped heated microcantilever is also modeled using Finite Element Analysis (FEA) and Matlab programming. Here also a constant force of F = 1 nN was

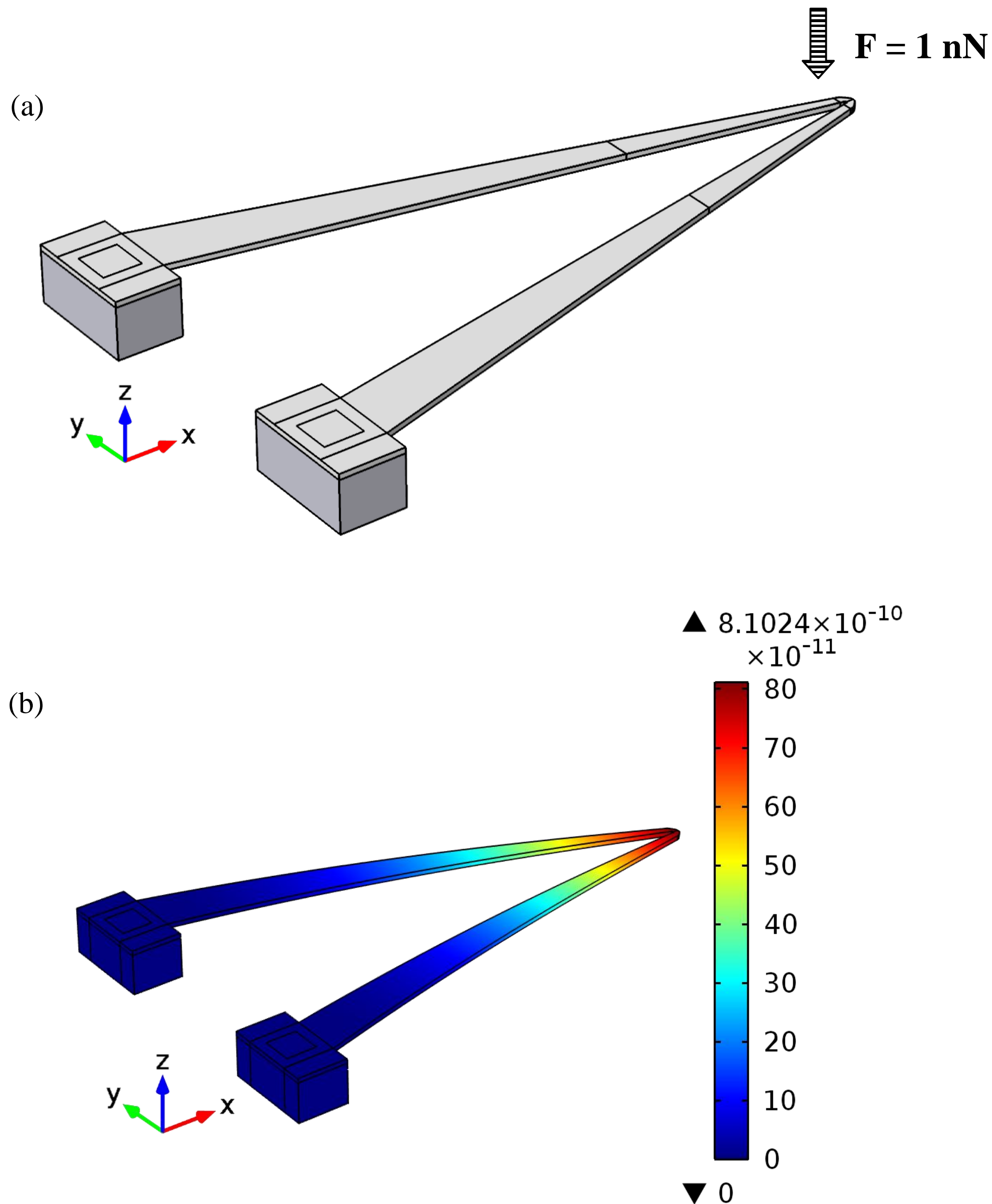

Figure 7.11: (a) The model used for COMSOL simulation for the tapered V-shaped AlGaN/GaN heated microcantilever, the position of the applied force of 1 nN is shown by arrow and (b) the deflection result with the applied force.

applied at the tip (Fig. 7.11 (a)). Deflection and stress distribution of the cantilever is modeled using COMSOL 3.5a, Figure 7.11 and Fig 7.12 show simulation results through modeling. With a distributed uniform force of 1 nN at the free end of the microcantilever a vertical displacement of 8.1×10^{-10} m was observed.

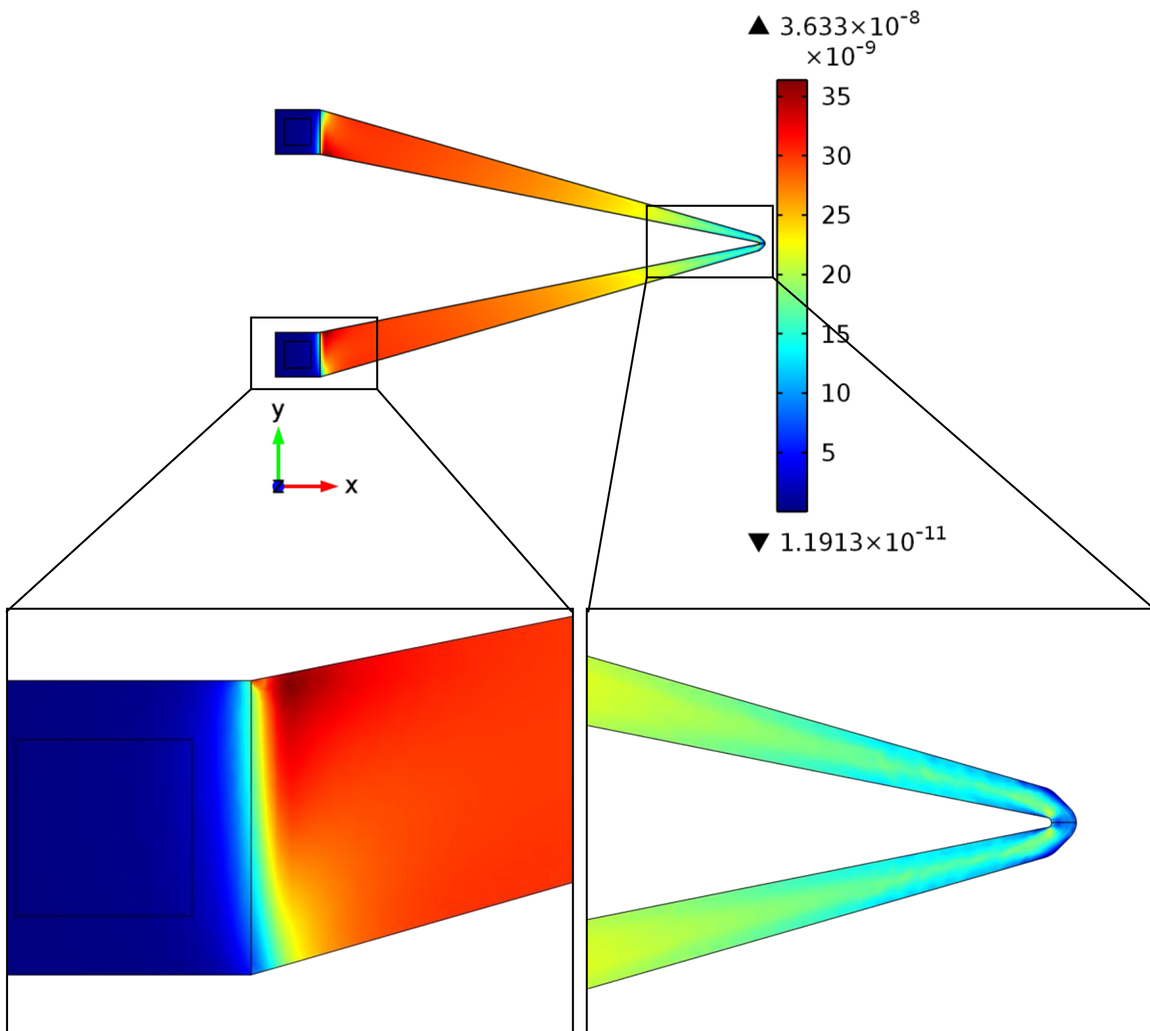

Figure 7.12: The *x*-direction strain distribution on the surface of the cantilever. Insets show expanded view of the base area.

7.3.3 Temperature dependence of Raman scattering in single crystal GaN films

Raman spectroscopy, a widely used noncontact method for the characterization of semiconductors, measures the inelastic scattering of light from materials which results from changes in the polarizability of the atoms. Thus, any effect such as stress or temperature which may change the lattice spacing and polarizability of nonmetallic solids will change the Raman signature. When a small portion of the incident photons on a crystal lattice experiences inelastic scattering through interaction with phonons, the inelastic scattering shifts the frequency of the scattered photons to longer wavelengths (Stokes peak shift) or shorter wavelengths (Anti-Stokes peak shift). Local temperature of these cantilevers can be measured by intensity ratio of Stokes and Anti-Stokes peak, line width (full width at half maximum, FWHM) of Stokes peak, or the shift of Stokes peak.

The temperature dependent Raman scattering has been successfully measured in studies on Si [271], Ge [272], diamond [273] and GaAs [274] etc. The effect of temperature and the temperature dependence of the optical phonons in GaN on single crystal GaN films were reported previously. Here we will illustrate the use of Raman scattering for characterizing the cantilever heater temperature calibrated with dc excitation on AlGaN/GaN cantilevers, before that we will cover the theoretical modeling of the temperature dependence briefly.

Modeling of the Temperature dependence

A simple empirical equation was used to describe the temperature of the phonon frequencies. This has the advantage of allowing determination of a simple but accurate

temperature frequency relationship of use in the measurement of temperature from the phonon frequencies.

The empirical formula to fit experimental data is

$$\omega(T) = \omega_0 - \frac{A}{\exp(Bhc\omega_0 / k_B T) - 1} \tag{7.06}$$

Where $\omega(T)$ is the phonon frequency at temperature T and ω_0, A and B are fitting parameters. Cui *et al.* [273] first proposed this empirical equation and successfully modeled the temperature dependence of the Raman modes of diamond and this equation was subsequently used for GaN by Liu *et al.* [275]. At higher temperature equation simplifies to $\Delta\omega \approx -(Ak_B/Bhc\omega_0)\Delta T$ where $\Delta\omega$ is the change in the phonon frequency induced by a temperature change in the phonon frequency induced by a temperature change ΔT.

The Raman line position of the E_2 mode and the $A1$(LO) mode of GaN as a function of temperature in the range of 78–800 K are shown in Figs. 7.13 (a) and 7.13 (b), respectively. The open circles refer to data from free-standing GaN films and the open triangles refer to data taken from the films still attached to the sapphire substrate. Also shown is the empirical fitting of the temperature dependence in freestanding GaN.

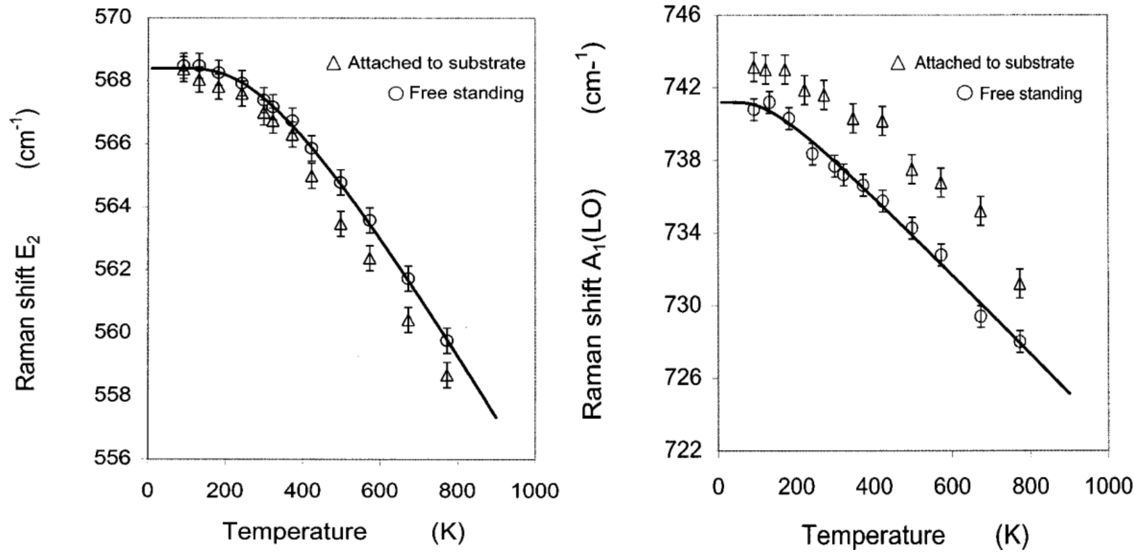

Figure 7.13: (a) Temperature dependence of the Raman frequency for the active E_2 mode in GaN still attached to the substrates (Δ) and free-standing GaN (O) respectively. (b) Temperature dependence of the Raman frequency for the active A_1(LO) mode in GaN still attached to the substrates (Δ) and free standing GaN (O), respectively. The solid curves give the best fitting using Eq. 7.06 (Ref. [275]).

7.4 Fabrication of AlGaN/GaN V-shaped microcantilevers

Following the discussion in the previous sections, the two types of microcantilevers, the AlGaN/GaN HFET embedded V-shaped microcantilevers and AlGaN/GaN V-shaped tapered heated microcantilevers, were fabricated using common photolithography techniques. This section describes the steps for fabricating these microcantilevers along with the fabrication issues, problems and solutions. All the fabrication processes were carried out in the Institute of Electronics and Nanotechnology (IEN) facility at Georgia Institute of Technology, Atlanta, GA.

7.4.1 Fabrication Outline

For AlGaN/GaN based MEMS fabrication there are several techniques to release the cantilever [276]. In this work, we chose the technique based on deep anisotropic silicon etch; here silicon is the sacrificial layer. A 4 inch AlGaN/GaN HEMT Epi wafer grown on Silicon (111) substrate was purchased from DOWA Semiconductor Akita Co.,

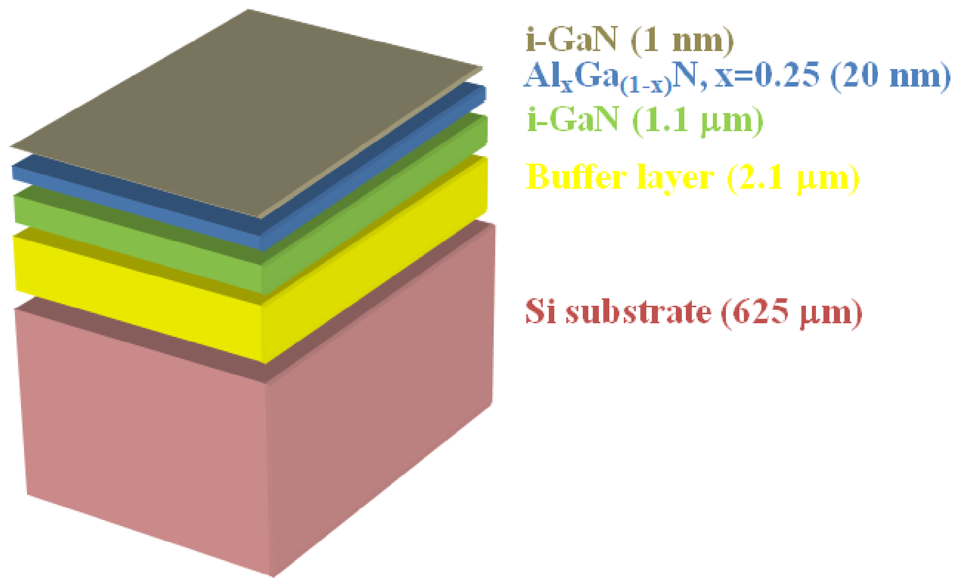

■Specifications
- -Classification : AlGaN/GaN HEMT epiwafers
- -Part Description : 4inch AlGaN/GaN HEMT Epi Wafer on Si Substrates
- -Specification :
  - ・Epi structure

Layer #	Composition	Thickness	X	Dopant	Carrier Concentration
4	GaN	1nm	–	–	–
3	AlxGa1-xN	20nm	0.25	–	–
2	GaN	1.1um	–		
1	Buffer	2.1um	–		
Substrate	Sillicon	625um	–		

・Substrate
- -Material : Silicon
- -Orientation : 〈111〉
- -Growth method : FZ
- -Conduction Type : P or N
- -Size (inch) : 4
- -Thickness(µm) : 625
- -Backside : Rough
- -Resistivity(Ωcm) : 〉6000

Figure 7.14: Layer information and spec of the AlGaN/GaN wafer.

Ltd, Japan for this work. The wafer was diced into 32 (1.4 cm by 1.4 cm) pieces. Before dicing, the wafer was spin coated with photo resist (Shipley 1827) and then baked for 5 mins at 110˚C. This is done to avoid contaminating the wafer surface with dust particles generated during dicing. The different layers of the wafer are shown in Fig. 7.14. Silicon substrate (111) of 625 μm thickness was used to grow the AlGaN/GaN layer [153]. A 2.1 μm thick layer consisting of AlN and AlGaN graded layer was used as a transition layer before growing 1.1 μm undoped GaN layer. On the top of the GaN layer, AlGaN barrier layer of 20 nm thickness was grown. This AlGaN layer and the transition layer along with the undoped GaN form the thickness of our microcantilevers. The Aluminum mole fraction was $x = 0.25$. A 1 nm undoped GaN cap layer was grown on that.

The final optimized mask used for the fabrication was 4”×4”×0.09” chrome material on quartz substrate and ordered from *Photo Sciences Inc., USA.* All the different layers of the mask was designed in *AutoCAD 2007*. There are 6 lithographic layers in the fabrication process and all the layers could be designed and housed in a single mask due to the smaller dimension of processing samples (1.4 cm by 1.4 cm). The mask was a clear field mask and both positive and negative photoresists were used as per the layer contents (features).

Total three pockets (2.8 mm by 1.2 mm) were patterned on each sample, each pocket houses 2 sets of different cantilever devices [see Fig. 7.15 (b)]. The other part was dedicated for Disc resonators for multimodal pressure sensing (not in the scope of this dissertation). Large plus (+) shaped feature was added to perform automatic dicing of a sample into 4 smaller pieces (discussed later) [see Fig. 7.15 (b)] during through wafer Si etch. Figure 7.15 (c) shows the V-shaped HFET embedded microcantievers whereas Fig

7.15 (d) shows the tapered V-shaped heated microcantilevers. Each of the blocks is designed with own set of TLM and CV pads. Red plus (+) and square (□) patterns are the

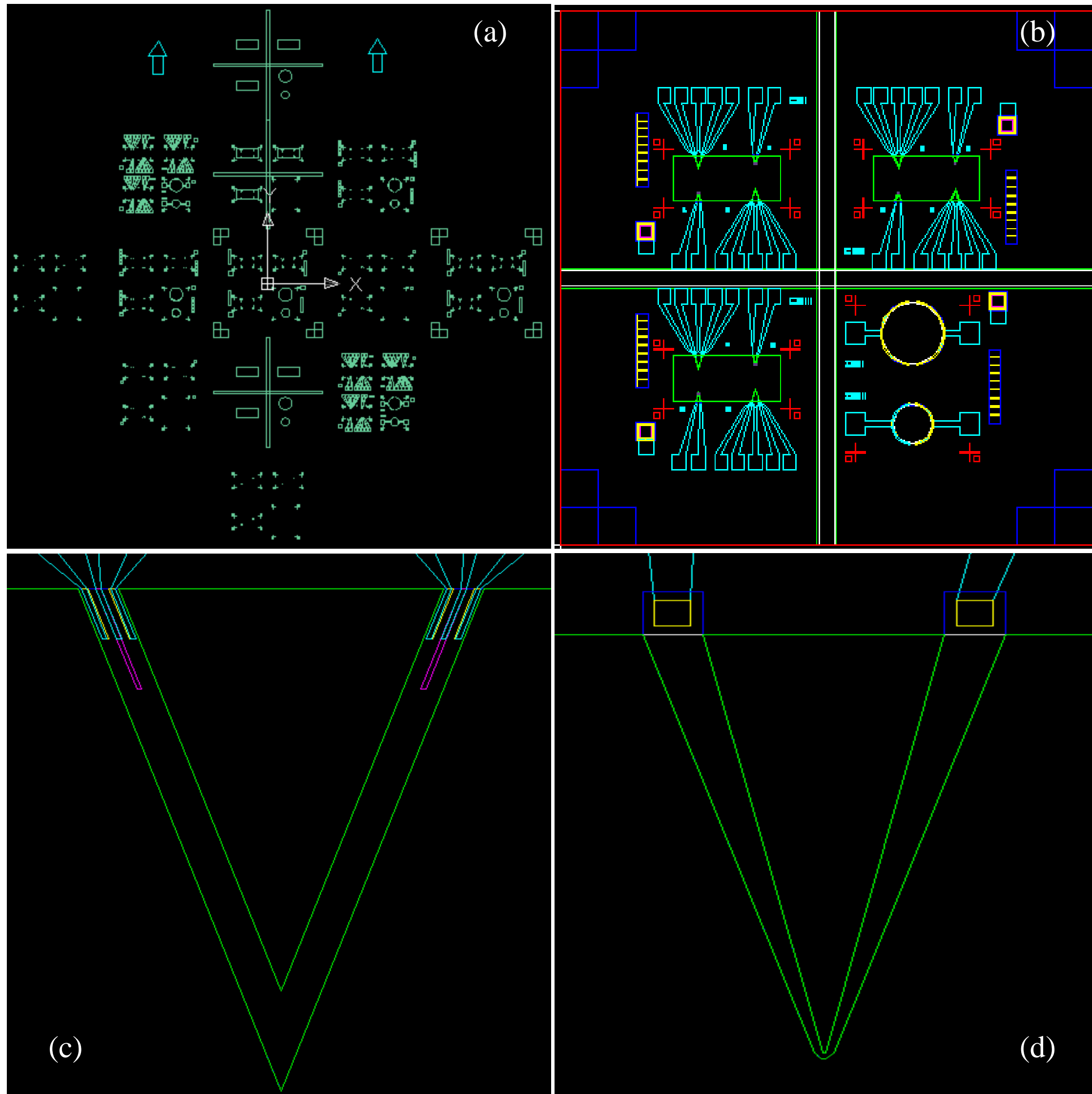

Figure 7.15: (a) View of the complete mask (4” by 4”) with various photolithographic layers. (b) View of the all lithography layers of mask superimposed into one single area equal to the sample size of 1.4 cm by 1.4 cm. (c) Partial view of the single V-shaped HFET embedded microcantievers device. (d) Partial view of the single tapered V-shaped heated microcantilevers.

alignment marks for multiple layers of lithography. Figure 7.15 (a) shows the CAD design of the whole 4 inch chrome mask where all the layers are housed; some of the layers are repeated for convenience.

7.4.2 Fabrication steps details

This section deals with the fabrication related issues, problems and solutions. The section is segmented into six sub-sections where each lithographic layer is discussed. Positive photo resist (PR) was used for the first process step, whereas negative photo resist was used for the rest.

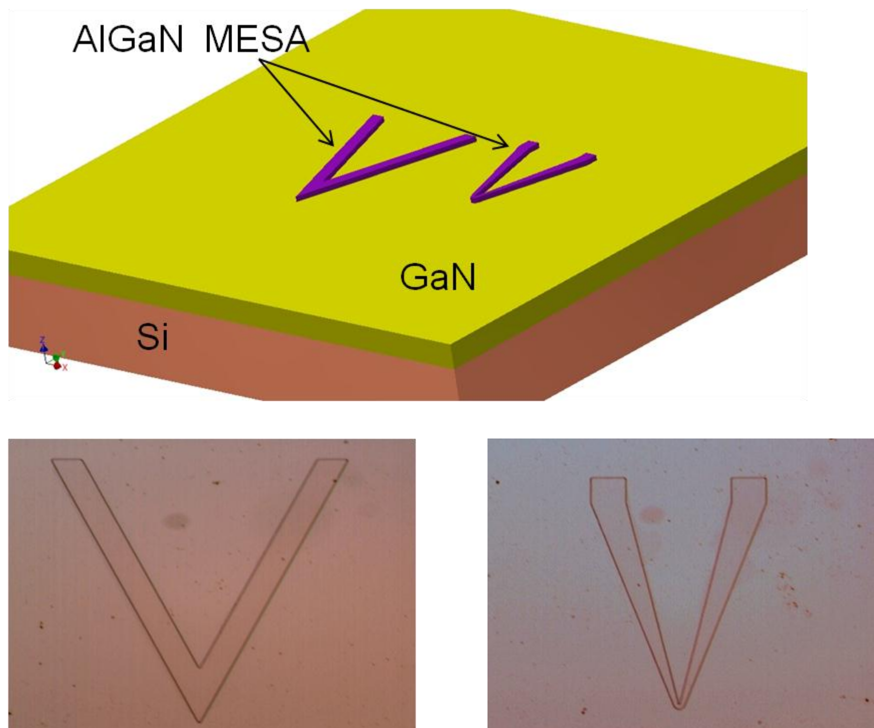

Figure 7.16: Schematic diagram and optical images for MESA Etching.

7.4.2.1 Step1: MESA Etch

MESA is a table shaped area on which the AlGaN/GaN HFET is fabricated. This is because AlGaN/GaN layer has 2DEG throughout the wafer, therefore it is conductive all over. To fabricate HFET device the active region of the device needs to be isolated from other patterns on the sample. To fabricate devices the active region of the device needs to be isolated from other patterns on the sample. We used BCl_3/Cl_2 based dry
etching recipe of GaN in Inductively Coupled Plasma (ICP) etcher to isolate mesa. 230 nm was etched down to ensure complete isolation. Same recipe was used for both the AlGaN and GaN etch. The height was verified by Tencor Profilometer.

7.4.2.2 Step2: Defining shape of cantilever

In this step, GaN is etched down to make an outline for the cantilevers. GaN is etched down in the pocket area up to the substrate where silicon acts as the etch stop. To protect the 2DEG of the mesa, a 1 um thick PECVD SiO_2 was deposited, it was eventually etched away by ICP at first and then the GaN also in ICP. While doing the ICP etching of GaN, SiO_2 acts as the mask. Later on SiO_2 was etched away by BOE wet etching.

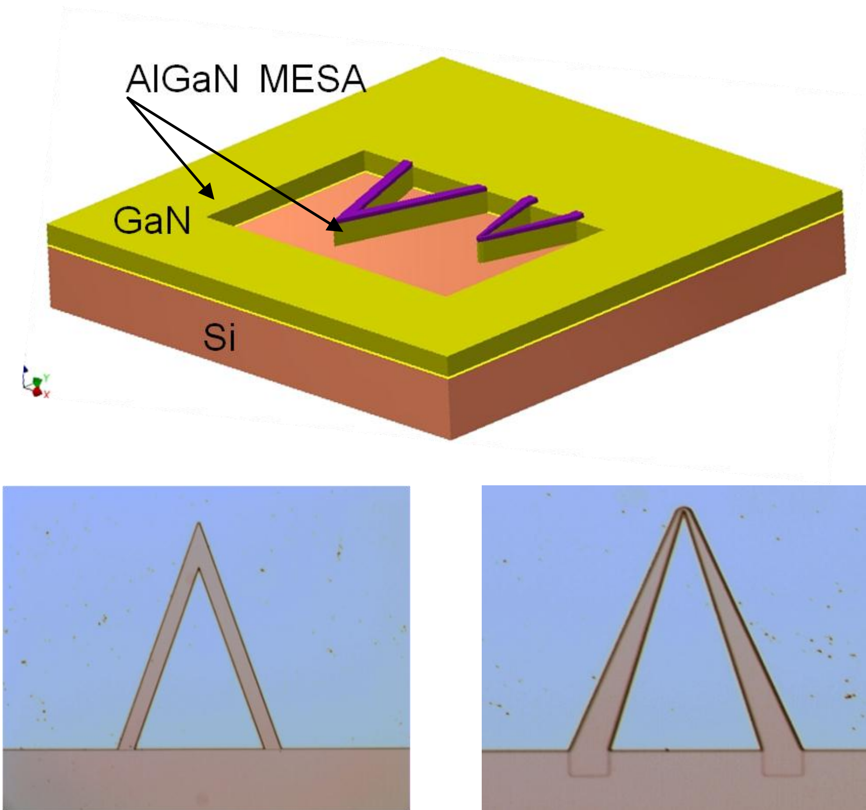

Figure 7.17: Schematic diagram and optical images for top cantilever outlining.

7.4.2.3 Step3: Ohmic contact deposition

For ohmic contact (needed for source, drain and TLM pads) multilayer gate metal stack of Ti/Al/Ti/Au was used. 20/100/45/55 nm was the thickness of the stacking. It was annealed at 800˚C in presence of N_2 for about 60 sec. Both the V-shaped structures will have ohmic contacts at the bases. Due to the wide bandgap of GaN, getting a good ohmic has always been a challenge. Multilayer metal stack has already proven to be a good choice with low contact resistance. Ti is chosen to be the first layer because it has low work function creating low Schottky barrier with GaN. Ti reacts with the GaN to form TiN and in doing so creates N vacancies in the GaN that acts as donors, thereby increasing the doping level at the metal–semiconductor interface to reduce the

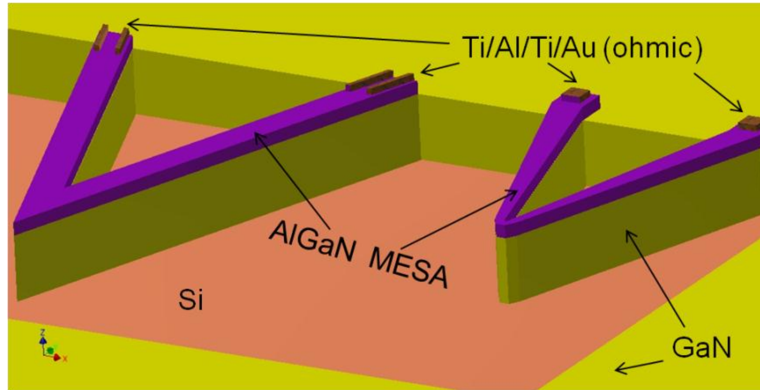

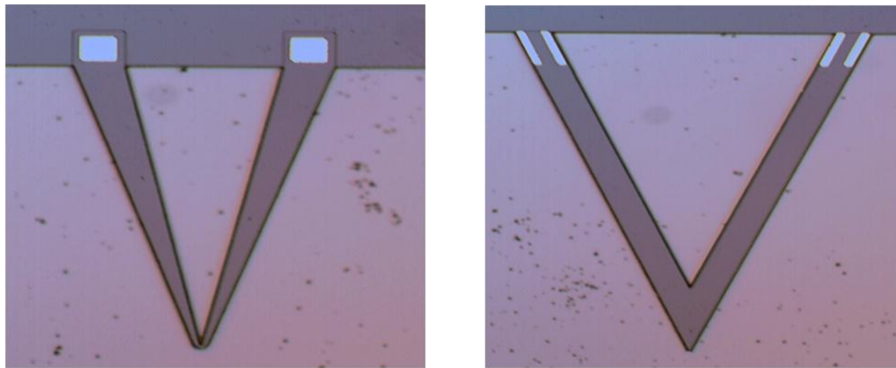

Figure 7.18: Schematic diagram and optical images for Ohmic contact deposition.

resistivity at the contact. This occurs as long as Ga is also not lost from the GaN. The primary role of the Al layer is to ensure that this does not happen by impeding the out diffusion of the Ga. However, at higher temperature during annealing Al gets oxidized. To prevent that, an inert metal (Au) can be covered on the top of Al with a Ti layer in between. Ti acts as a barrier to prevent Au from diffusing to Al [277].

7.4.2.4 Step4: Schottky contact deposition

The HFET embedded microcantilevers and the CV blocks have Shottky contacts only. In contrast to the metallization scheme for ohmic contacts on AlGaN/GaN, the

Schottky contacts should have higher work function and create high Schottky barrier with nitride

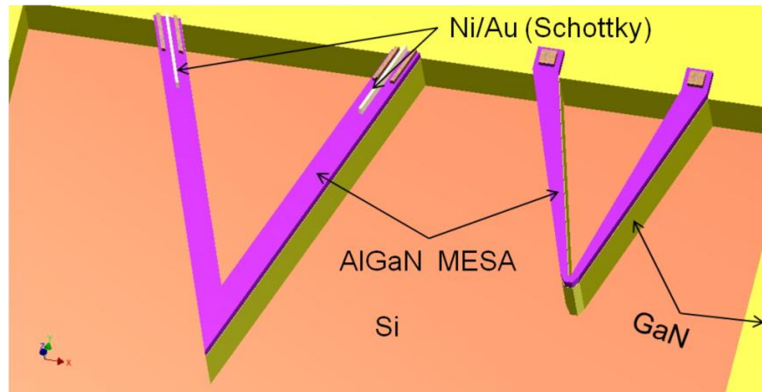

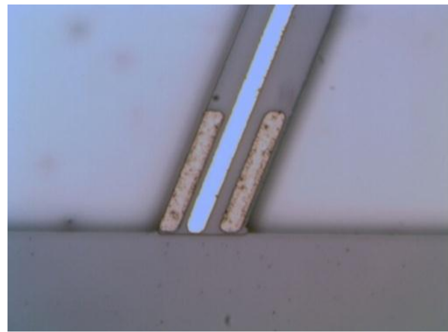

Figure 7.19: Schematic diagram and optical image for Schottky Contacts (HFET embedded catilever).

surface [278]. Both Pt and Ni are ideal choices for Schottky contact metal with high work function and both are extensively investigated [278]. Ni is a preferred choice due to its higher adhesion property with nitrides. Also Ni does not react with the GaN surface until a temperature of above 600°C. Therefore we used a Ni/Au (25/375 nm) metal stack for Schottky contacts for the HFET gates.

7.4.2.5 Step5: Probe contacts

Large metal pads (350 μm by 400 μm) are deposited for characterization which connect to the drain, source, gate and cantilever tip. Au with adhesion layer of Ti was used for this metal deposition step. The metal deposited in this step is only to create contact to the metal layers already deposited in the previous steps.

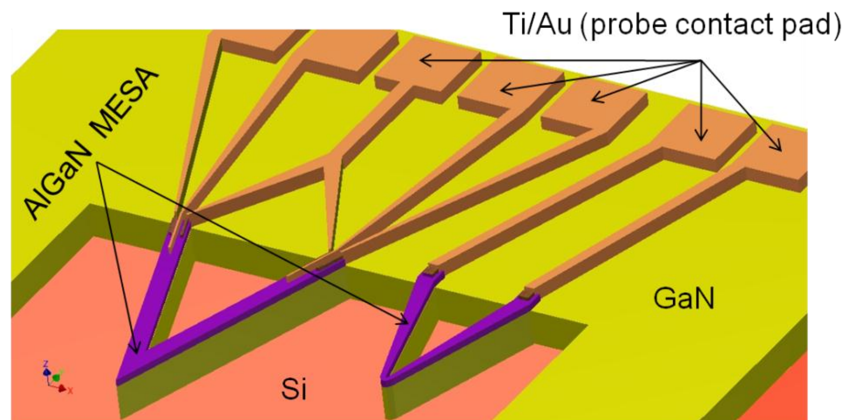

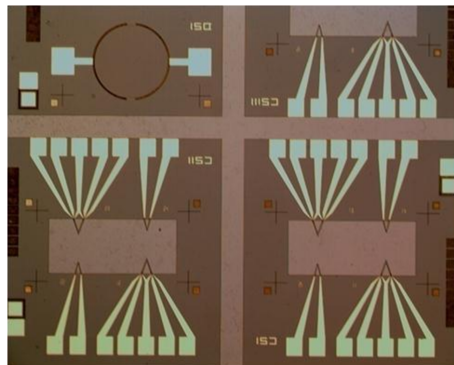

Figure 7.20: Schematic diagram and optical image for probe contact.

7.4.2.6 Step6: Back pocket etch

This step involves several sub steps: 10 um thick SiO_2 was deposited by PECVD from the back side which will act as the mask while doing Si deep trench etching. The

back pocket, aligning with top pocket, was patterned and then the SiO_2 was etched by Wet

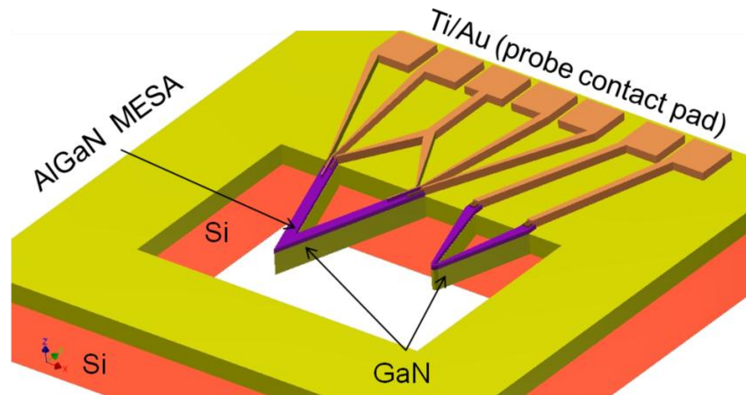

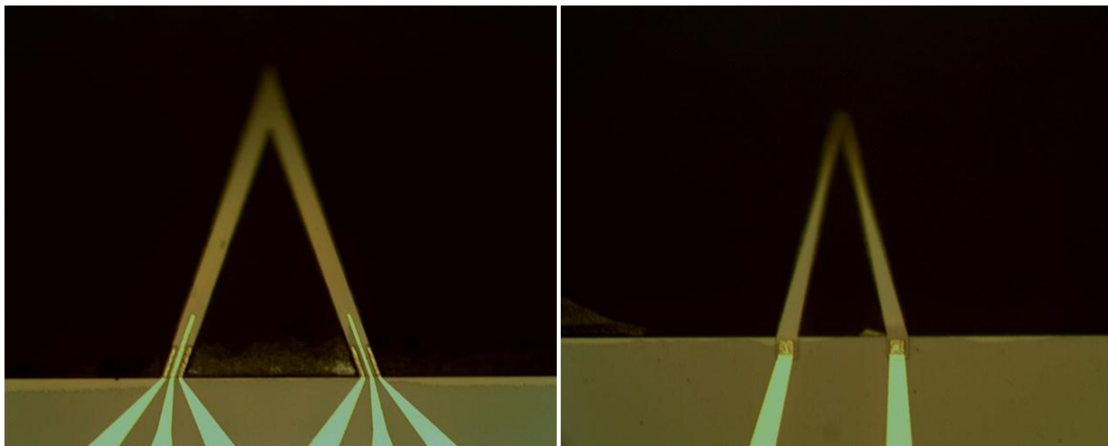

Figure 7.21: Schematic diagram and optical images for back pocket etching.

BOE etching (10um). Then through wafer Si etching from backside was done. The cantilever is released through a long (~7 hr) through wafer etching of Si using ICP etcher. We used "Bosch process" where the etcher alternates between an etch cycle and deposition cycle. During the etch cycle, Si is isotropically etched using SF_6. Then the etched region is deposited with a polymer (C_4F_8). In this next etch cycle, due to the RF power and the nature of the polymer the bottom region is etched more readily than the

sidewall. The whole process continues alternatively, resulting in a high aspect ratio Si etch with vertical side walls. The sample is auto diced during this step.

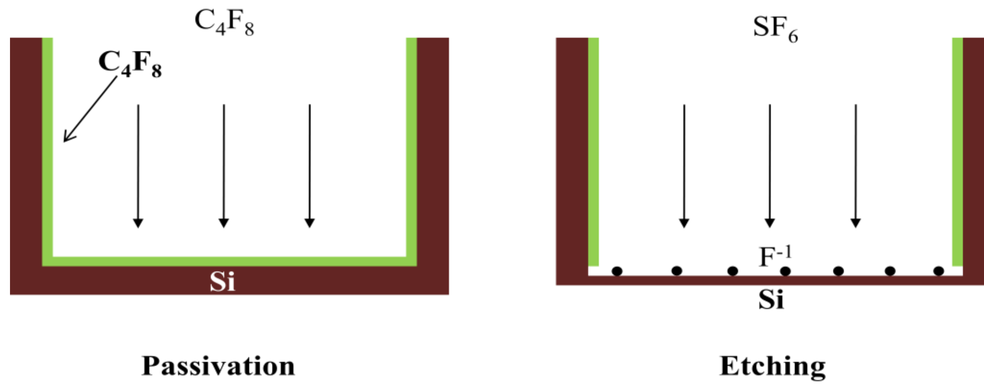

Figure 7.22: Basics of ICP Bosch process including a passivation and etching step.

7.4.2.7 Auto dicing feature

To integrate fabricated samples and for testing purpose wire bonding is necessary; hence the samples need to be diced down into smaller pieces. However for our case, we already released the cantilevers before dicing the samples small enough for wire bonding. The option was to dice them further after release of cantilever. However, it is not possible to PR-coat the samples that has fabricated and released cantilevers and then dice them. This will damage the cantilevers. To solve this issue, we designed a plus (+) feature in the last fabrication step so that the through wafer etching of Si automatically dices the sample into pieces. In Fig. 7.23 we can see the sample after cantilever release, being diced automatically into four pieces.

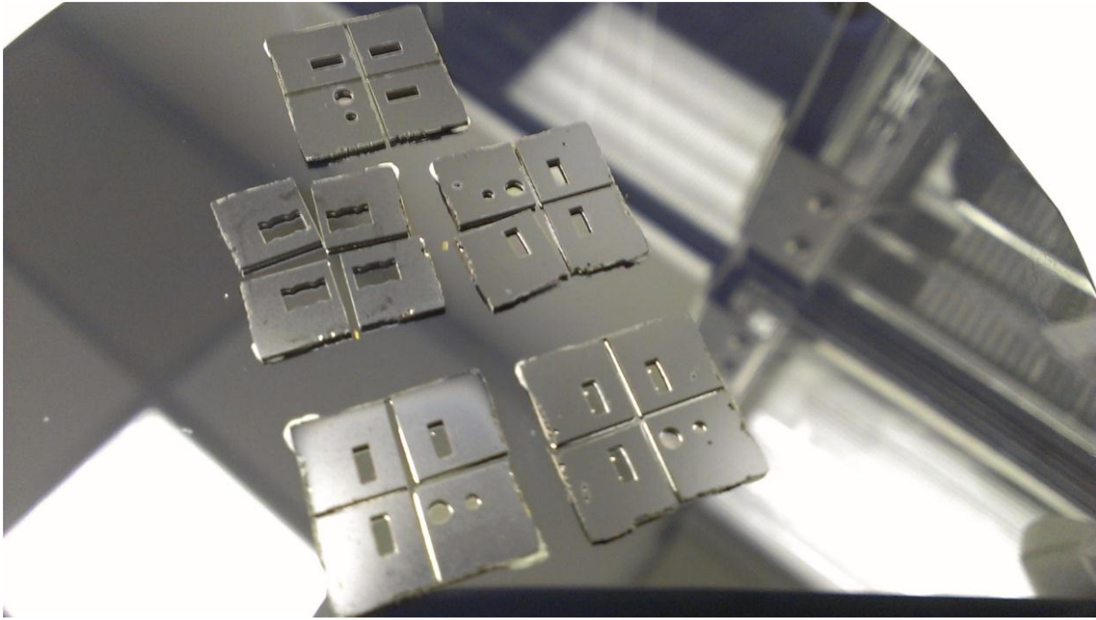

Figure 7.23: Image of the auto diced cantilever samples after the last step (Bosch process) of dry etching. The samples are still mounted on the carrier wafer by Cool grease.

7.4.3 SEM Images

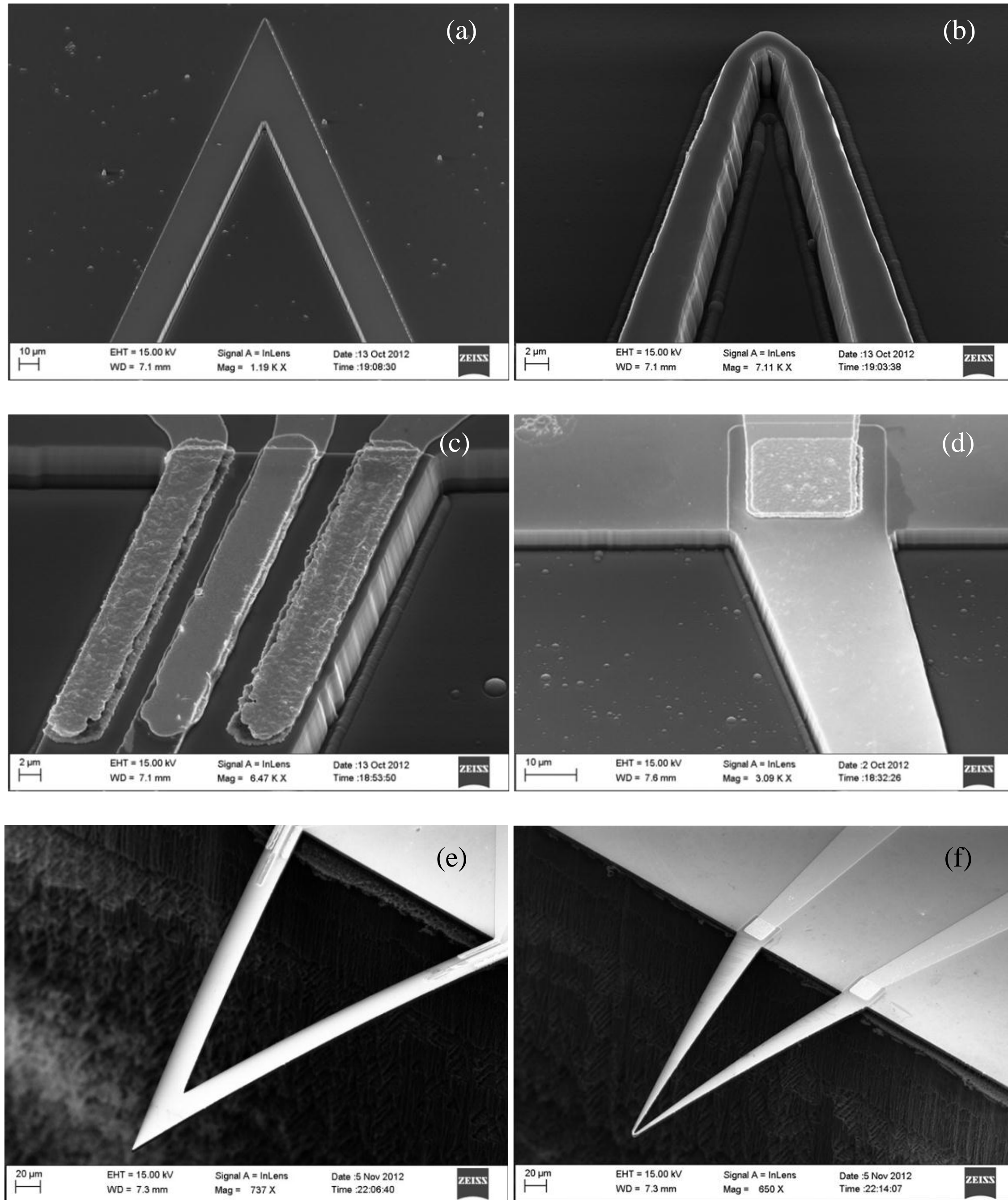

Figure 7.24: Scanning Electron Microscopy images of fabricated AlGaN/GaN V shaped microcantilevers. (a) shows the tip of HFET embedded cantilever, whereas (b) the tapered shaped tip of the heated cantilever, (c) shows the HFET in one arm of the HFET embedded V cantilever, (d) the base of the heated cantilever and ohmic contact, (e) HFET embedded suspended V shaped cantilever and (f) suspended heated cantilever after through wafer etching.

7.4.4 Fabrication challenges

There are enormous challenges throughout the entire process of fabrication. I will list main problems during my fabrication. The development of features using photolithography appeared initially troublesome, the problem was resolved through multiple testing runs by optimizing exposure duration and development duration, respectively. Furthermore, releasing of microcantilever is one of most challenging issues since it is the final step of processing. In the last step of cantilever release there are few sub steps involved. The first one is thick 10um SiO_2 etching. This 10um SiO_2 was deposited by PECVD in the back side of samples and acts as the mask for deep Si trench etching. As a first choice to etch the oxide, I tried dry ICP etching, but it takes time to etch 10 μm. While doing dry etching for a longer time that cool grease (cool grease is a thermal glue and applied on a carrier wafer to stick the 1.4 mm by 1.4 mm small samples) comes off from the carrier wafer and deposited in the pocket as blackish spots which further hinders the etching. So I tried to do BOE wet etching instead of dry etching. The etching is done from the back side and in the top side active devices are there and also the metal bonding pads which is of Ti/Au. BOE attacks Ti and lifts off the whole metal bonding pads just like a film. I solved the problem by coating the top side by thick PR and then mounted the sample on an already PR coated carrier wafer. After that the carrier wafer with the samples was baked for 5 mins at 80 ˚C to cure the PR. BOE does not attack most of the PRs and there was no sipping through of BOE and thus no etching of Ti. Then, BOE droplets were poured by pipettes on the back side of the attached samples and there was no lift off of metal pads. The Bosch process is very critical and it took

several testing runs to optimize the ICP Bosch process recipe to release microcantilever successfully.

7.5 Measurements of AlGaN/GaN Microcantilevers

7.5.1 Electrical characteristics

7.5.1.1 Transmission Line Measurement (TLM) technique

TLM is used to determine the quality and characteristics of the metal-semiconductor contact. The metal contacts must supply the required device current. It should also have a voltage drop across the contact that is small compared to the voltage drop across the active device region. The metal contacts are either referred to as Schottky or Ohmic based on a distinctly non-linear or linear I-V characteristic, respectively where an ohmic contact is desirable. The TLM test measures different electrical parameters including the contact resistance, transfer length and sheet resistance. Figure 7.25 (a) shows a portion of the TLM pattern before the Rapid Thermal Annealing (RTA). The separation of the pads were 2.5, 5, 10, 15, 20, 25, 30 and 35 μm and the dimension is 200 μm by 300 μm. Figure 7.25 (b) shows the same TLM pattern shown in Fig. 7.25 (b) after the RTA was done. As seen from Fig. 7.26 the total resistance has a fairly linear relationship with the contact distance. Generally the resistance versus contact distance has a linear relation in the form,

$$R = \frac{R_{sheet}}{Z} d + 2R_C \tag{7.07}$$

where, R is the total resistance between two adjacent contacts, R_{sheet} is the sheet resistance of the channel, and R_C is the total contact resistance of each contact. Applying a linear fit for the graph in Fig. 7.26 we get the following relation,

$$R = 1.56d + 46.12 \tag{7.08}$$

here, R and d are expressed in Ω and μm.

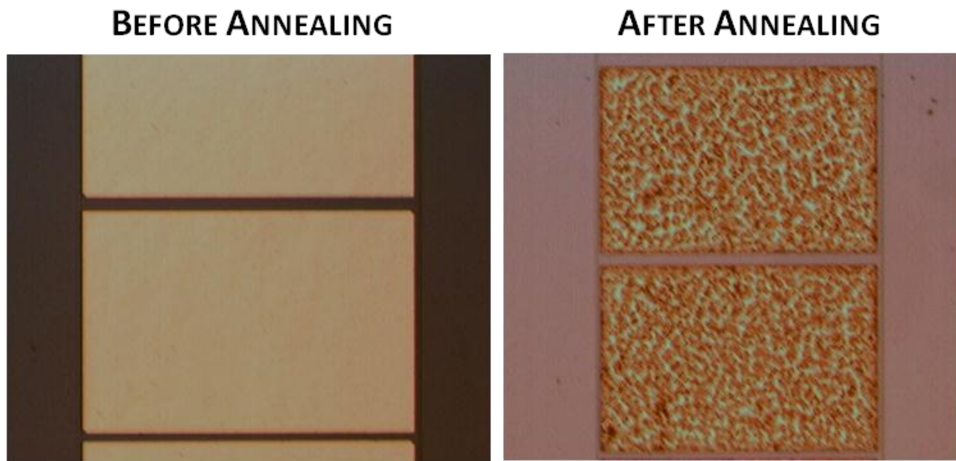

Figure 7.25: TLM contact pads, before annealing and after annealing

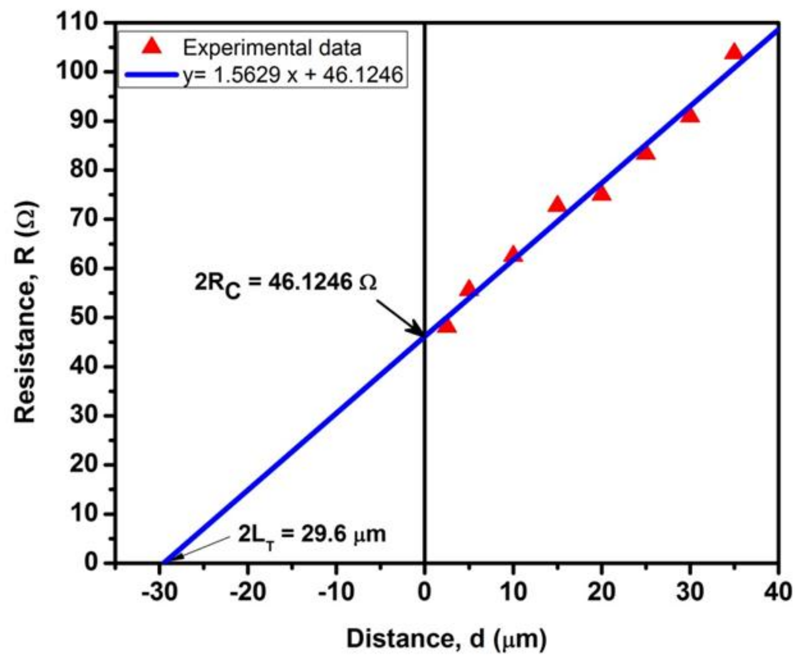

Figure 7.26: The total resistance between contacts as a function of distance

Table 7.4 Calculated parameters from the TLM test

Width, W (μm)	**Contact resistance, Rc (Ω)**	**Sheet resistance, Rsh (Ω/□)**	**Transfer length, L_T (μm)**	**Contact resistivity, ρc (Ω-cm^2)**
300	23.06	468.9	14.75368	1.02E-03

As shown in Fig. 7.26 the *x*-axis intercept is $2L_T$ where L_T is the transfer length. Transfer length is the distance below the contact where the applied voltage gets attenuated by $1/e$ factor ($e = 2.718$). Moreover, the specific contact resistivity, ρ_c can be expressed as,

$$\rho_c = L_T^2 R_{sheet} \tag{7.09}$$

All the calculated value found out from our TLM test is shown in Table 9.2. As observed from the calculated values the contact resistivity is low which shows that the contacts in these TLM patterns are ohmic.

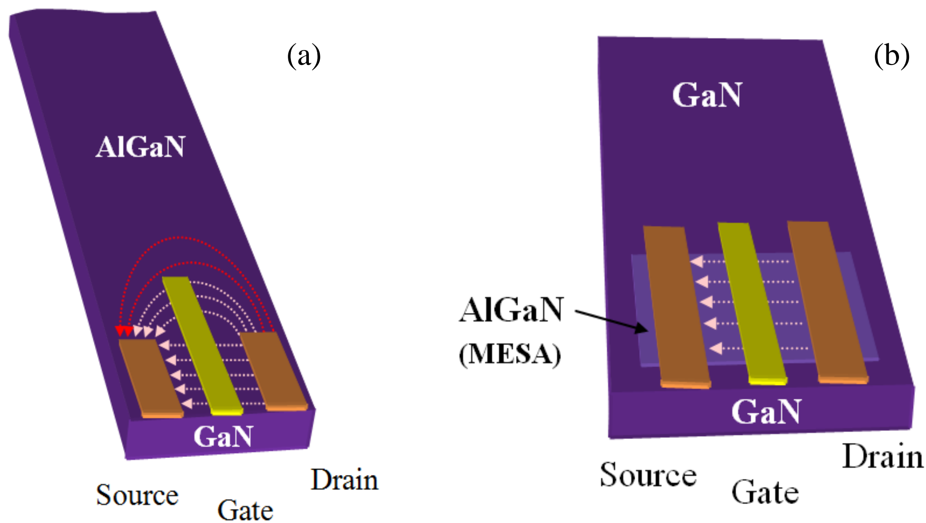

Figure 7.27: Current flow of HFET embedded (a) V-shaped and (b) rectangular cantilever

7.5.1.2 DC characteristics of AlGaN/GaN HFETs

Gate of the V-shaped HFET embedded microcantilever does not completely turn off the channel since the cantilever has 2DEG all over the cantilever arms. Gate is designed as three times wider than the source/drain width and is supposed to modulate the channel but not turn off the drain current completely as can be seen from the red arrows from drain to source in Fig 7.27 (a). To find the typical HFET behaviour we have fabricated HFET embedded AlGaN/GaN rectangular cantilevers in the same processing

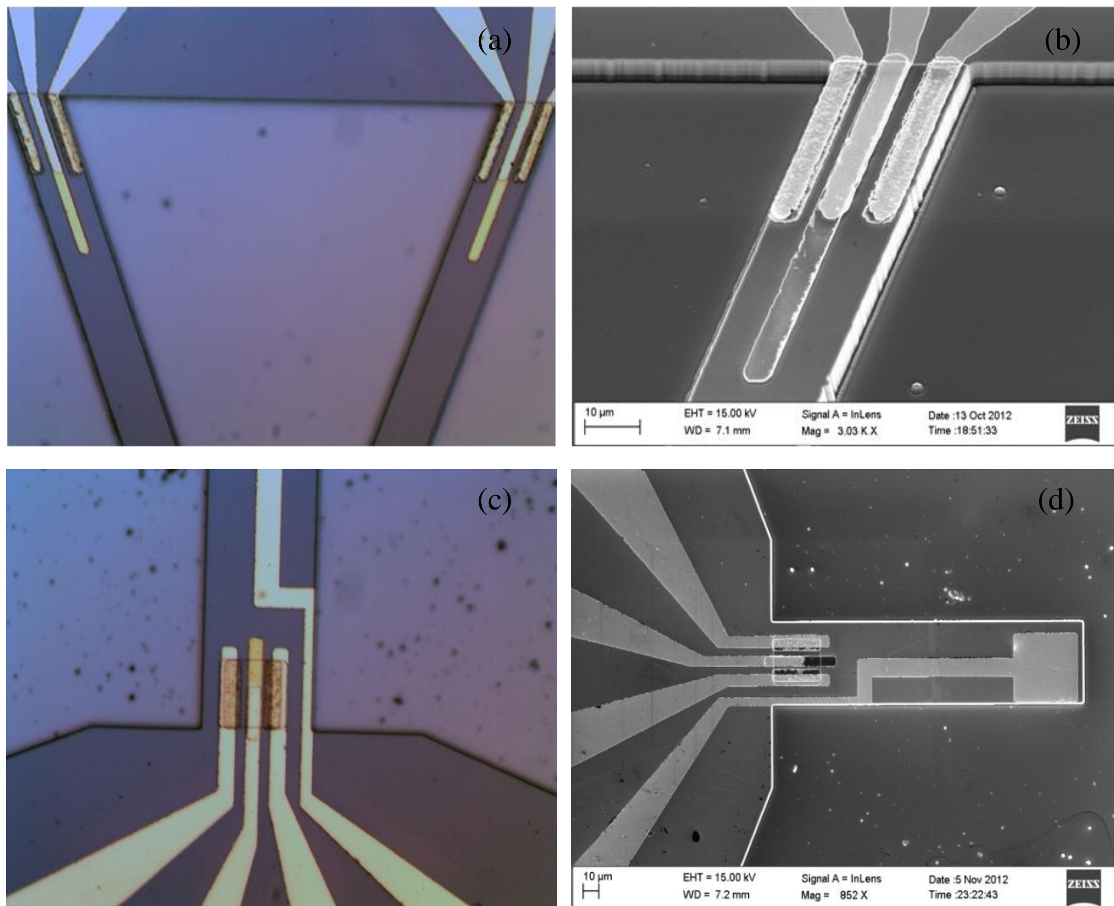

Figure 7.28: (a) Optical micrograph image of fabricated AlGaN/GaN HFET embedded V shaped microcantilever, (b) SEM image of fabricated AlGaN/GaN HFET in one arm of the V cantilever. (c) Optical micrograph image of the HFET embedded rectangular microcantilever, and (d) the SEM image of the rectangular cantilever.

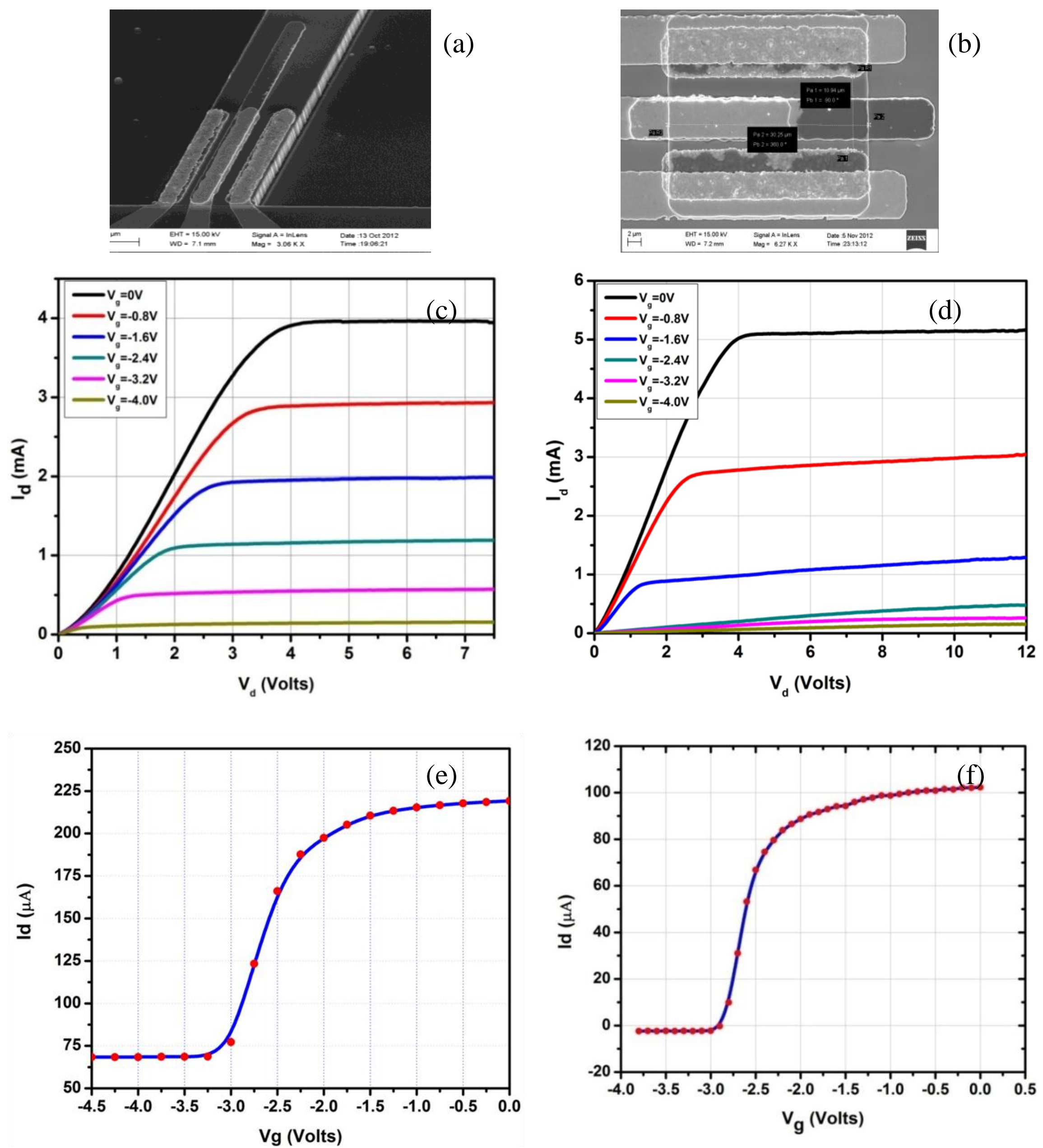

Figure 7.29: (a), (c), (d) and (b), (d), (f) SEM images, family of curves and I_d-V_g plots for HFET embedded V-shaped cantilevers and rectangular cantilevers respectively.

batch with other V-shaped cantilevers. In this rectangular structure there is a Mesa of AlGaN at the base of the cantilever and the HFET is located on this area. Gate has now the full control of turning off the channel as can be seen from Fig 7.26 (b). Figure 7.28

shows the optical image of HFET embedded V-shaped microcantilever, the HFET is shown in the SEM image in Fig 7.28 (b). The optical micrograph and SEM image of the embedded HFET in the recntagular cantilever is shown in Fig 7.28 (c) and 7.28 (d) respectively.

From the family of curves for V-shaped microcantilever (Fig 7.29) we see that the drain current is increasing slowly with drain bias even with large negative gate bias rather than showing saturation behavior. However for rectangular cantilever the drain current is saturated and is even turned off completely with large negative bias. The threshold voltage V_{th} for the rectangular cantilever is -2.8 V. The transconductance, $g_{m=}$ dI_D/dV_{GS} from I_D-V_{GS} curve is 220 μA/V, from this we found out the calculated mobility around 830 $cm^2/V.s$.

7.5.1.3 C-V measurements

The capacitance-voltage (*CV*) profiling was carried out to find the information about the 2DEG electron concentration. The profiling was done between Schottky and Ohmic contact (each pocket i.e. each block of 4 V-shaped cantilever devices has one C-V pad). A small ac voltage (500 mV) of 10 kHz was superimposed on a variable dc using a summing amplifier was applied to the gate. Both the ac and dc voltages were provided and the C-V measurements were performed with HP 4280A 1MHz LCR Meter. The dc voltage was varied from 0 to -8 V. Through further MATLAB processing the capacitance per unit area versus dc bias is obtained from the Schottky contact area of 300 μm × 300 μm. Figure 7.30 (a) shows the capacitance per unit area plotted against dc bias on the Schottky contact. With the application of more negative bias on the Schottky contact, the

electron move away from the AlGaN/GaN interface reducing the capacitance. However, at V = -2.8 V, there is a sudden decrease in the capacitance as seen in Fig. 7.30 (a) indicating the total loss in 2DEG. Therefore this graph also gives us the threshold voltage of the AlGaN/GaN heterostructure which is -2.8 V. The *C–V* profiling technique allows one to measure the carrier concentration [259],

$$N_{C-V} = \frac{C^3}{q\varepsilon_0\varepsilon_{AlGaN}}\frac{dV}{dC} \tag{7.10}$$

as a function of depth,

$$z_{C-V} = \frac{\varepsilon_0\varepsilon_{AlGaN}}{C} \tag{7.11}$$

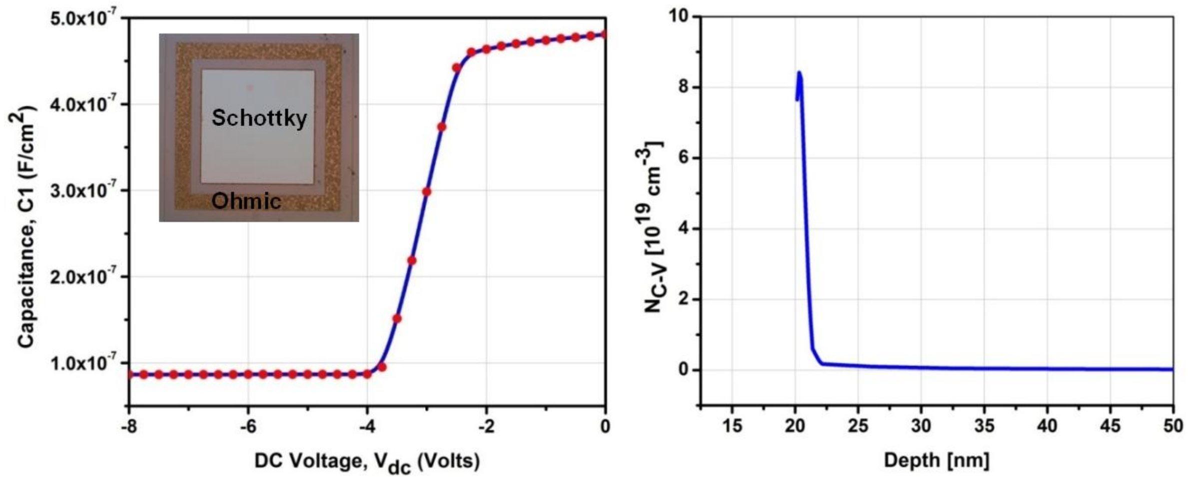

Figure 7.30: Capacitance voltage profiling, (a) Capacitance per unit area versus applied dc bias on the Schottky contact, (b) Distribution of electron concentration as a function of depth.

where V is the voltage applied to the Schottky contact, C is the measured differential capacitance per unit area, and ε_{AlGaN} is the dielectric constant of AlGaN, the absolute permittivity, $\varepsilon_0 = 8.85 \times 10^{-14}$ F/cm, and electronic charge, $q = 1.6 \times 10^{-19}$ C. The

$N_{C\text{-}V}$ is plotted against the depth and shown in Fig. 7.30 (b). As seen in Fig. 7.30 (b), the carrier concentration peaks near the interface of AlGaN/GaN and decays very quickly within few nanometer depth. This is an expected distribution of 2DEG where the electron is concentrated at the very interface. Here, N_{C-V} equals the free carrier concentration [176]. Where the 2DEG carrier concentration n_s,

$$n_s = \int_{-\infty}^{\infty} N_{C-V}(z_{C-V})dz_{C-V} = \int_{-\infty}^{\infty} n(z)\, dz \tag{7.12}$$

From the data shown in Fig. 7.30 (b) and using Eq. (7.12) we obtain the 2DEG carrier concentration, $n_s = 1.044 \times 10^{13}$ cm^{-2} (with aluminium mole fraction, $x = 0.25$, AlGaN barrier layer thickness 20 nm with a 1 nm i-GaN cap layer). The theoretical value of the 2DEG carrier concentration found out in the previous chapter is around 1.15×10^{13} cm^{-2}.

7.5.1.4 Electrical characterization results: Summary

Conductivity Mobility	
Sheet resistance from TLM, R_{sh}	**468.9 Ω/□**
2DEG carrier concentration from CV plot, n_s	***1.0443 x 10^{13} cm^{-2}***
Mobility	***1275 cm^2/V.s***
FET Mobility	
Transconductance, $g_m = dI_D/dV_{GS}$ from I_D-V_{GS} curve	**220 µA/V**
Mobility	***830 cm^2/V.s***

2DEG carrier concentration	
Theoretical with 25% Al mole fraction	**1.385×10^{13} cm^{-2}**
2DEG carrier concentration from CV plot	**1.044×10^{13} cm^{-2}**

7.5.2 Frequency Analysis and Quality Factor

The resonant frequency of the fabricated microcantilever is measured by an optical transduction system. Figure 7.31 shows the schematic diagram of the experimental setup used for measuring the frequency response of the microcantilever. The motion of the cantilever is transduced using optical transduction as it has better resolution. A laser beam is incident on the microcantilever. The incident beam is adjusted by viewing through a top microscope arrangement. The reflected beam is positioned on to a position sensitive photo detector (PSPD) which is mounted on *XYZ* translation stage having micrometer movement resolution (purchased from Thorlab Ltd.).

A micropositioner needle is brought within few millimeters of the microcantilever free end using a top and side microscope (see Fig. 7.31). The needle is biased by ac voltage with varying frequency from a digital lock-in amplifier (Stanford Research Systems SR850). The frequency sweep was performed by the lock-in amplifier. The ac voltage applied on micropositioner needle creates a capacitive force that forces the cantilever to oscillate. The cantilever oscillation is converted to corresponding voltage signal out of PSPD and the output is fed back to the lock-in amplifier where RMS value of the oscillation is extracted by the lock-in amplifier and recorded.

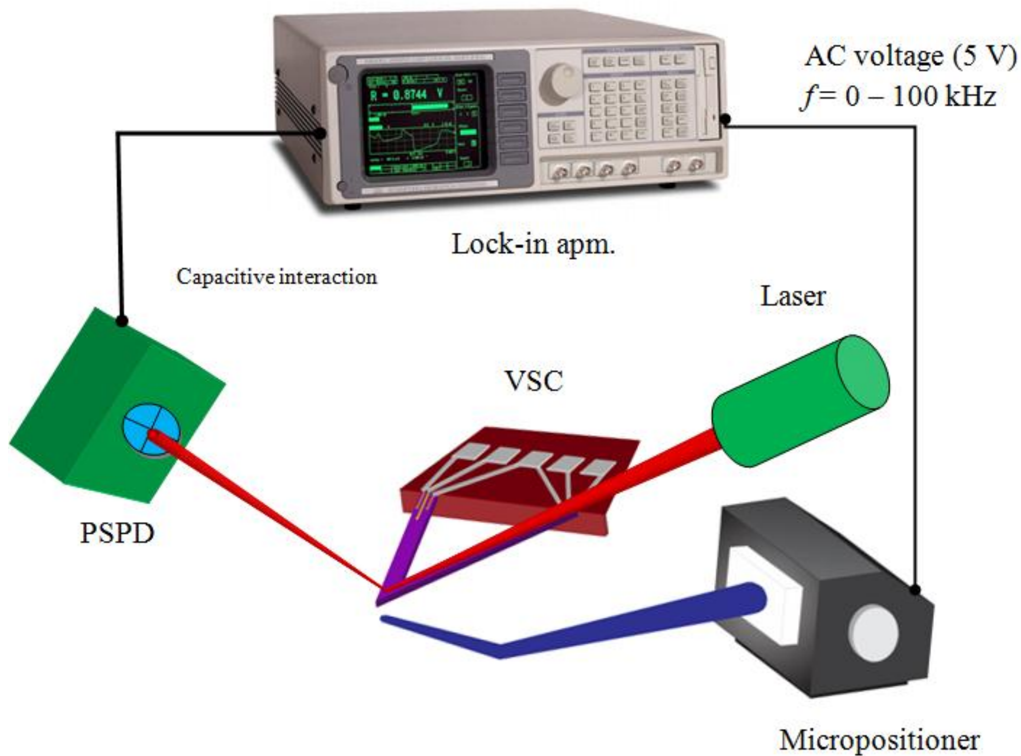

Figure 7.31: Schematic diagram of the measurement setup for finding resonant frequency of V-shaped microcantilever using an optical transduction approach and capacitive coupling by a micropositioner needle.

The V-shaped cantilever (HFET embedded or the tapered heated) has continuous 2DEG from one arm base to another arm base very close to the surface, within few nm, so the cantilever itself acts like metal plate or an electrode. When the cantilever is applied an ac bias very close to its resonant frequency the oscillation amplitude is Q/k times the maximum capacitive force between cantilever and the ground electrode. Therefore it is obvious that for sensing operation and prediction of sensitivity it is important to know the resonant frequency, f_0 and the quality factor, Q of the fabricated cantilever. Figure 7.32 shows the experimental frequency response of AlGaN/GaN HFET embedded V shaped

microcantilever. The *quality factor*, which is a measure of losses an oscillating cantilever has, was found out from the following relation,

$$Q = \frac{f_0}{f_2 - f_1} \tag{7.13}$$

where, f_0 is the resonant frequency of the cantilever. f_1 and f_2 are the two frequencies for which half of the maximum amplitude occurs in the frequency response. As seen from Fig. 7.32 the measured resonant frequency and quality factor for the HFET embedded V shaped cantilever is 36.3 kHz and 312 respectively which are very close to the COMSOL simulated results incorporating the non-ideality factors (source, drain and gate contacts).

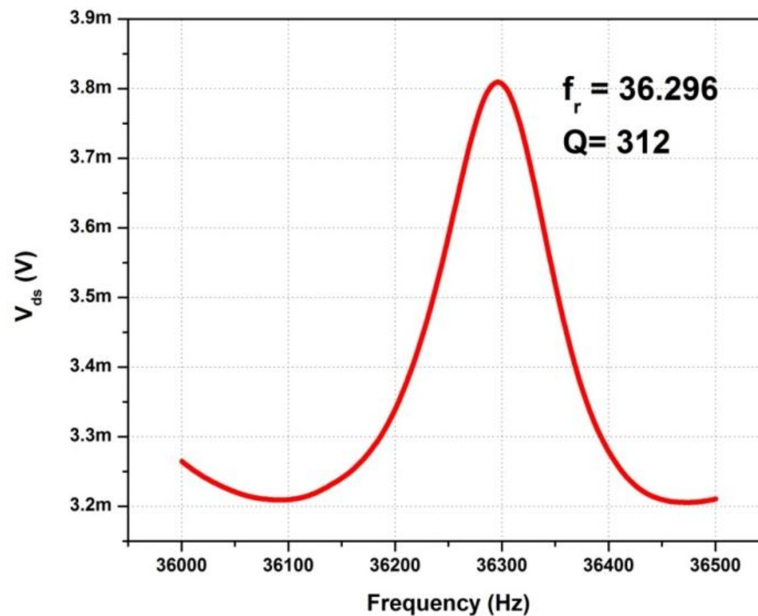

Figure 7.32: Experimental frequency response of the V-shaped AlGaN/GaN microcantilever

The slight difference between theoretical and experimental values might occur due to the non-ideal etch and metal deposition profile during the fabrication. We can assume that thickness differences have caused a frequency shift from theoretical approximations.

Table 7.5 Comparison between theoretical and experimental resonant frequency

	Theoretical	***Experimental***
Resonant frequency (f_0)	**37.2 kHz**	**36.3 kHz**

7.5.3 Microcantilever bending measurements

7.5.3.1 Experimental setup

The bending experiments on the cantilevers were performed using a Piezo-based Z-axis Nanopositioner from Physik Instrumente, PI (PI-611 Z). The nanopositioner is attached upside down with a XYZ translation stage (Thorlabs. Inc.) to allow coarse maneuverability in three axes. The nanopositioner has a range of up to 100 μm movement with a closed loop resolution of 2 nm. A long cantilever shaped piece made from Delrin plastic will be attached to the top surface of the nanopositioner to keep the sample few inchs away from the nanopostioner [see Fig. 7.33]. A micropositioner needle (tip diameter 12 μm) attached to the end of the Delrin piece with spring loaded arrangement is shown in Fig. 7.33. The nanopositioner is controlled from a computer interface designed in LabView.

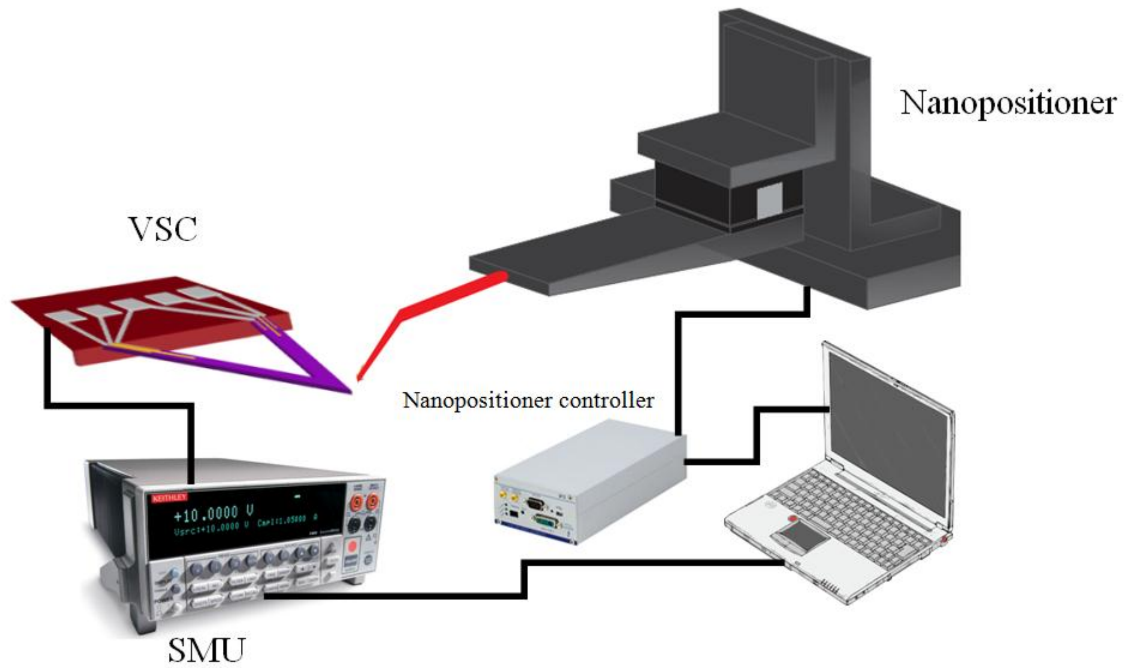

Figure 7.33: Experimental Setup for microcantilever static bending test

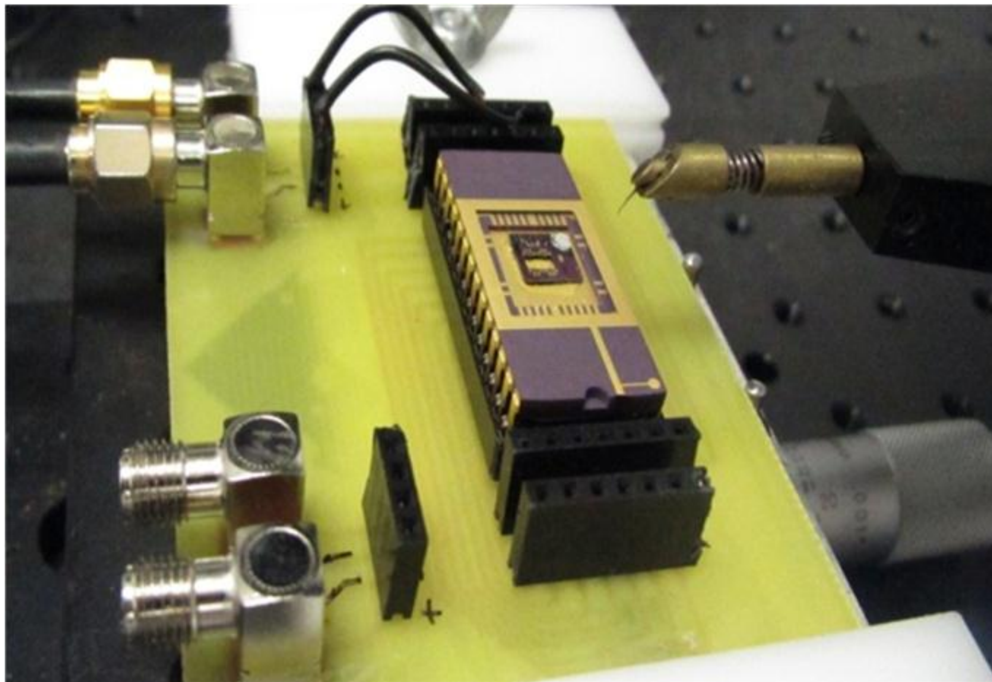

Figure 7.34: Microcantilever bending test measurement

7.5.3.2 Static bending: HFET dc current transients with cantilever bending

The drain current transients of AlGaN/GaN HFET embedded V shaped microcantilevers were measured over time. V shaped microcantilevers have two embedded HFETs per cantilever and each arm has one HFET with drain, source and gate contacts. Figure 7.34 shows an image of a wire bonded chip containing array of microcantilevers. Figure 7.35 shows the top view of the bonding pads and wires on one side of the sample. The SEM image of a HFET embedded microcantilever denoted "HFET cantilever AB" is shown in Fig**.** 7.36. Each of the two arms "Arm A" and "Arm B" of the cantilever has one HFET; Drain A, Gate A and Source A for Arm A and Drain B, Gate B and Source B for Arm B respectively. For the DC bending test one of the HFETs (one arm) was kept active (drain, source and gate bias) while the other HFET (another arm) was inactive i.e. no biasing provided. Figure 7.37 (a) shows the drain current response for 10um upward bending of a cantilever with no gate bias applied, and (b) shows 10 um downward bending response with -4V gate bias.

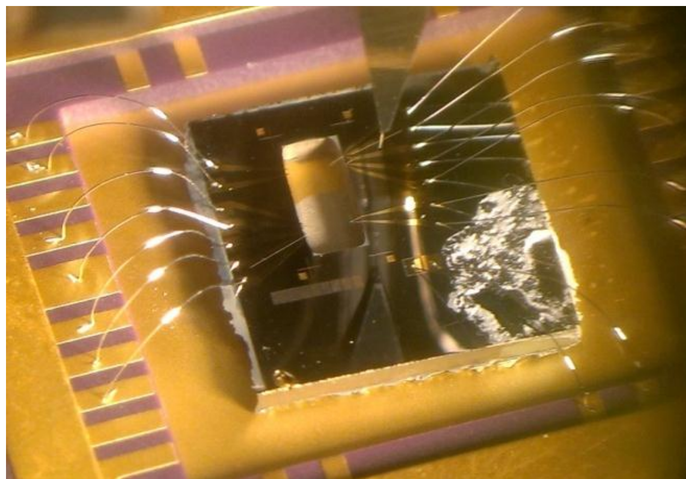

Figure 7.35: Top view of a wire bonded chip containing arrays of cantilevers

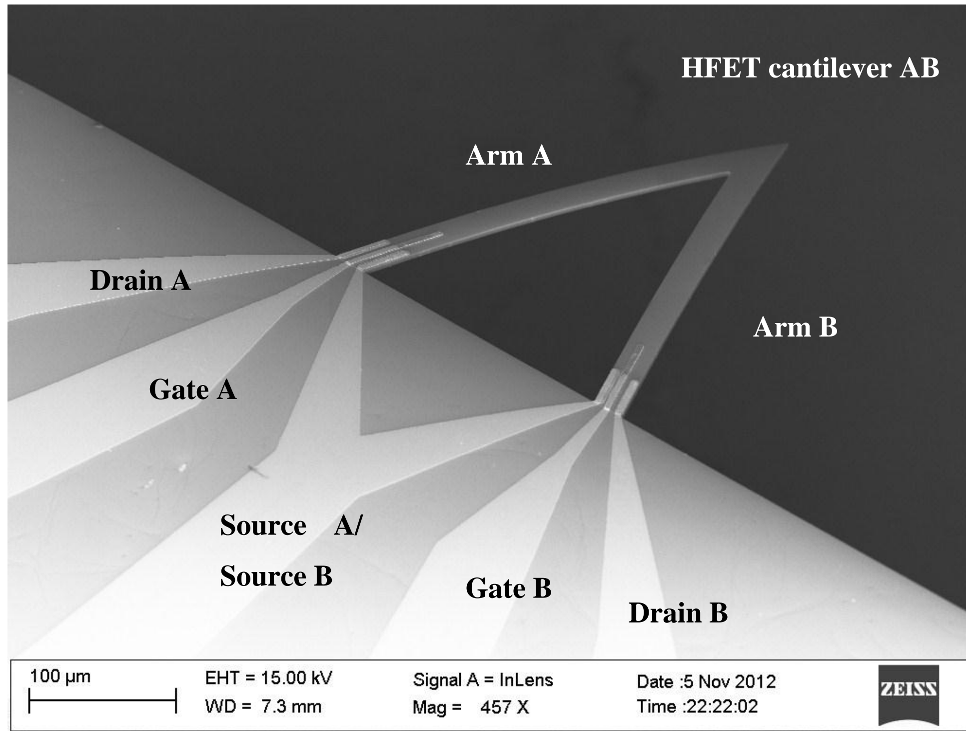

Figure 7.36: SEM image of a HFET embedded suspended cantilever showing source, drain and gate contacts

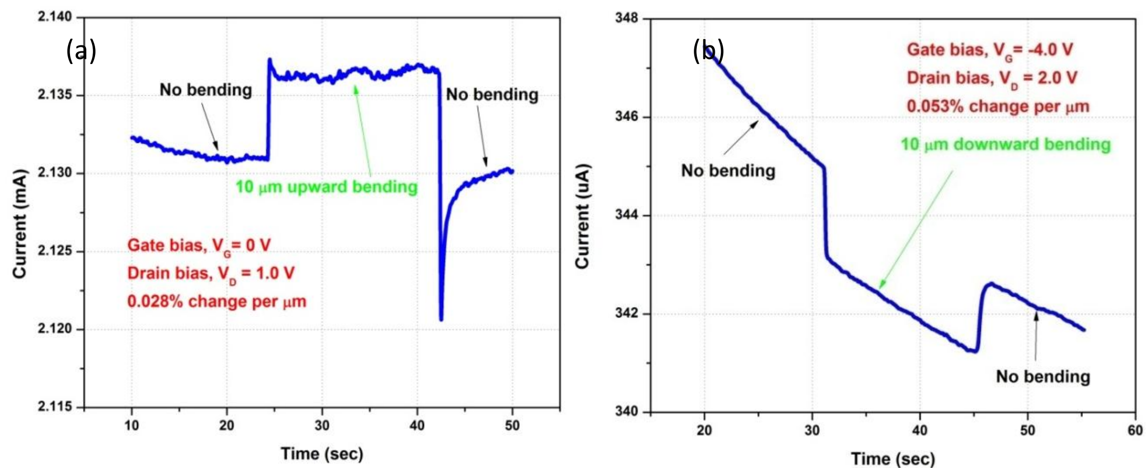

Figure 7.37: (a) DC drain current transients with 10 µm upward bending applying zero gate bias. (b) DC drain current transients with 10 µm downward bending at V_G = -4 V.

From Fig 7.37 (a) and (b) we can see that the change in the drain current when the cantilever is bent upward is not same as it is for same magnitude of downward bending.

7.5.4 Thermal characteristics of AlGaN/GaN Microcantilever hotplates

Raman spectroscopy to measure the temperature of the cantilever

Raman spectroscopy was performed on AlGaN/GaN heated cantilever to measure the local temperature of the cantilever with electrical excitation. In this work the Raman data is taken at room temperature with a micro-Raman setup by Olymus Raman microscope as shown in Fig 7.38 (a) and (b). The sample excitation utilized a 632 nm HeNe laser while the collection was performed with an 800 cm^{-1} spectrometer and an 1800 l/mm grating. The slit was set at 200 μm to maximize the spectral resolution. An 80x objective was used to collect the Raman signature of the devices which provided a focal spot of 2 μm. Figure 7.38 (c) shows an SEM image of a heated microcantilever.

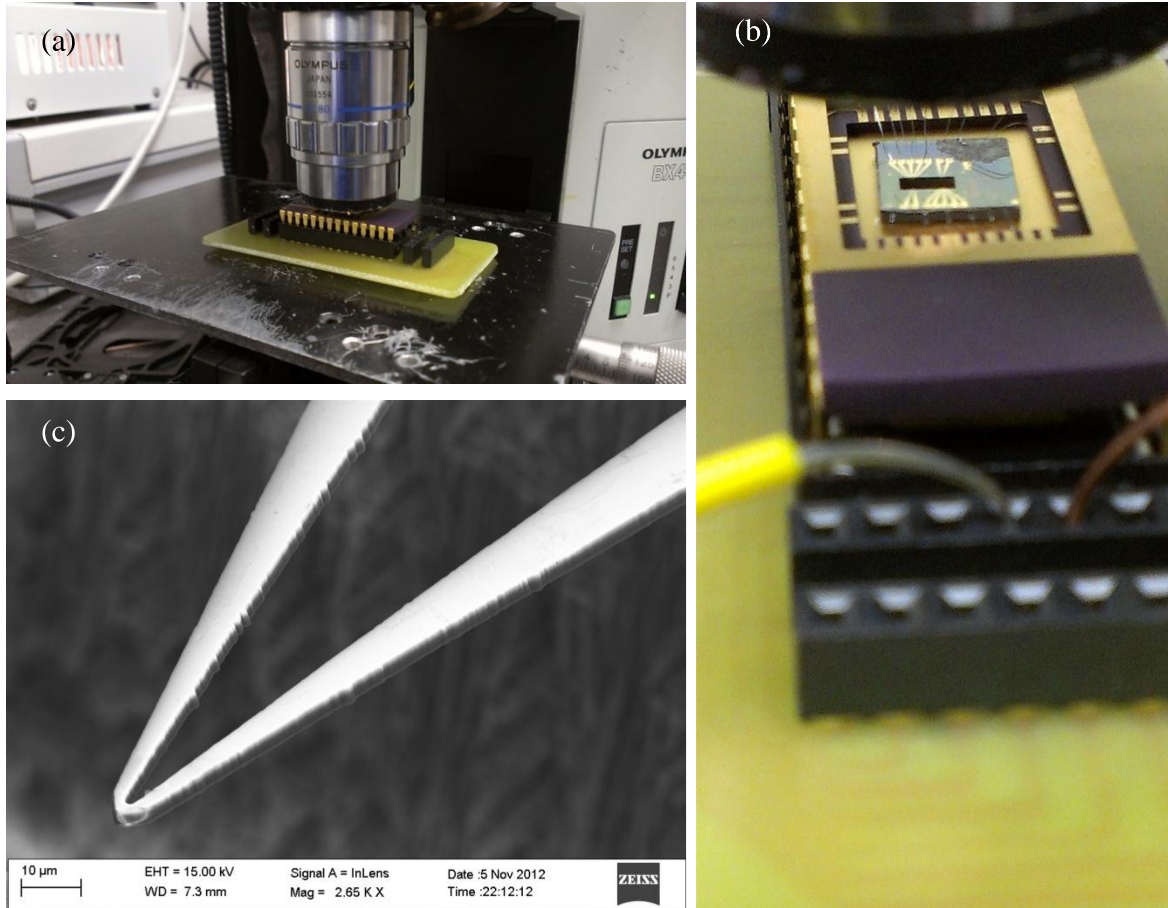

Figure 7.38: (a)-(b) Experimental setup of Raman spectroscopy for measuring the temperature of tapered V shaped heated cantilever, (c) SEM image of a heated cantilever

In Fig. 7.39 (a), we show typical Raman spectra of free standing AlGaN/GaN at seven different excitations in the backscattering z(xx)ź geometry. Each different electrical excitation corresponds to different temperature of the cantilever. The Raman line position of the E_2 mode and the AlGaN/GaN as a function of temperature in the range of 0–1000 K are shown in Fig. 7.39 (b).

The effects of temperature on the phonon energy measured by Raman scattering are primarily due to the thermal expansion of the lattice, thus a downshift of phonon frequency with temperature is observed as shown in Fig 7.39 (a). There is no generally

accurate method to describe the temperature dependence of the phonon frequencies in the crystal.

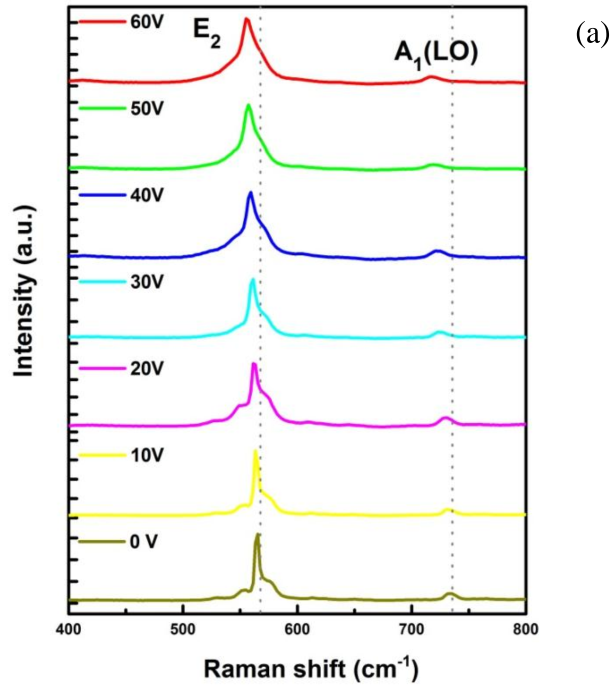

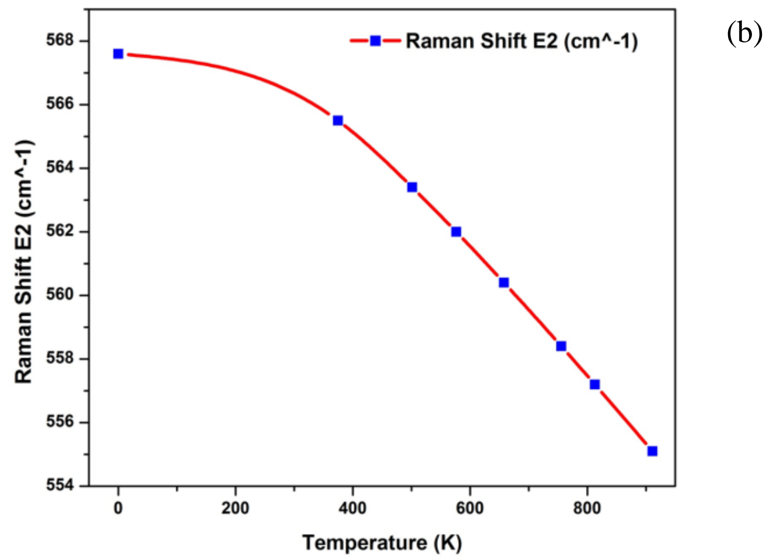

Figure 7.39: (a) Typical Raman scattering of AlGaN/GaN free standing film and (b) Raman shift as a function of cantilever temperature.

Following the discussion in the previous section (7.3.3) it was found that the Cui formula could be employed to interpret our experiments. Thus the function form of the temperature dependence of the Raman shift in AlGaN is given by

$$\omega(T) = \omega_0 - \frac{A}{\exp(Bhc\omega_0 / k_B T) - 1} \tag{7.14}$$

where ω_0 is the Raman phonon frequency at 0 K, and *A* and *B* are fitting parameters. The fitting parameters were found from hotplate calibration of the heated microcantilever, for the E_2 mode, we have $A=21\ cm^{-1}$ and $B=1.10\ cm^{-1}$. By inverting Eq (7.14), the cantilever temperature is obtained from the line position $\omega(T)$ according to

$$T = \frac{Bhc\omega_0}{k \ln\left\{1 + \frac{A}{[\omega_0 - \omega(T)]}\right\}} \tag{7.15}$$

Using Raman spectroscopy, the cantilever heater temperature was calibrated with dc excitation. Fig. 7.40 shows the cantilever heater temperature based on Stokes peak position as functions of the cantilever power. The cantilever heater temperature increases almost linearly with the cantilever power as a result of a linear temperature coefficient of resistance (TCR).

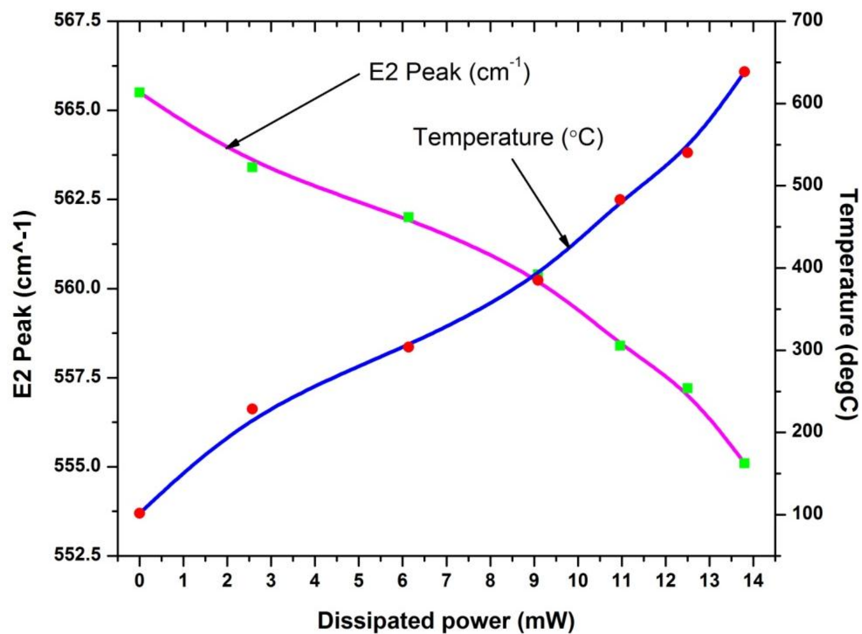

Figure 7.40: Heated microcantilever temperature as a function of the cantilever power, measured using Raman spectroscopy, where the temperature is based on Stokes peak position.

Following cantilever heater temperature characterization, temperature distribution from the cantilever heater along one of the arms was examined based on Stokes peak position. Fig. 7.41 (b) plots temperatures at three specific locations with respect to the E_2 phonon shift. The temperature gradient also plotted along different position at a power level of 7 mW and we can see an 84 ˚C temperature spatial difference in the arm from tip to bottom of the cantilever.

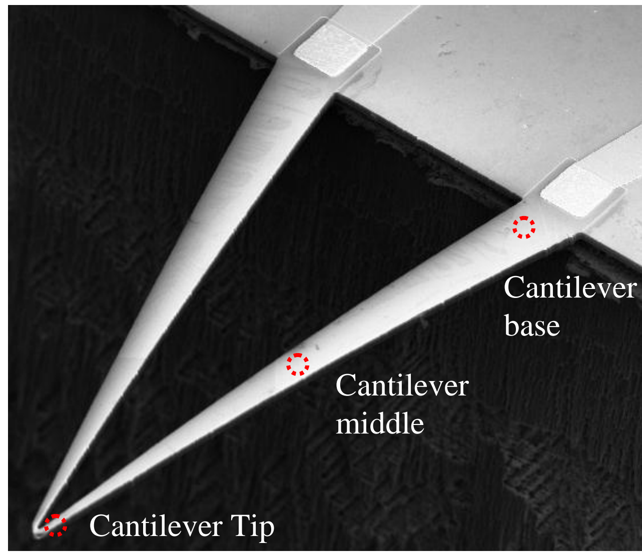

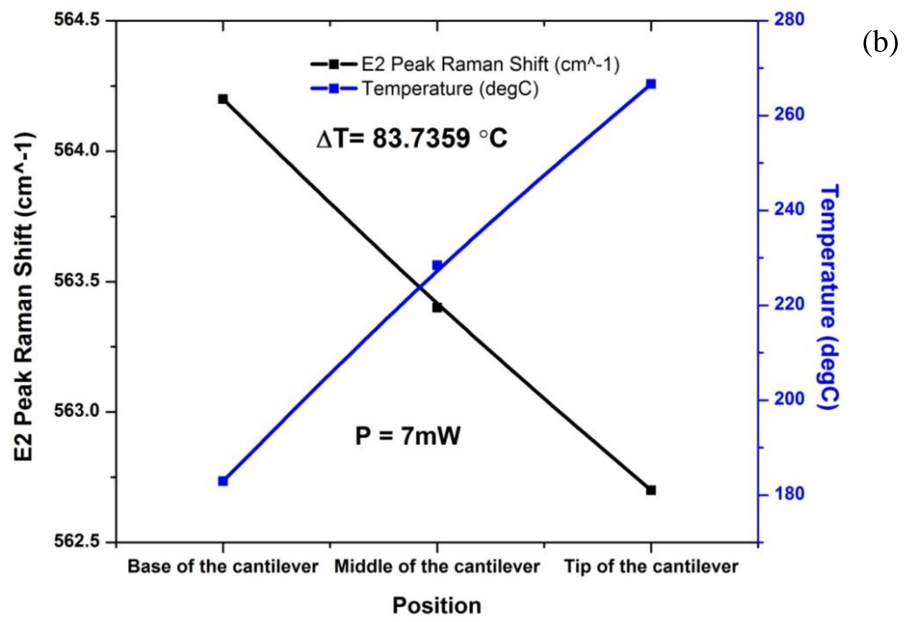

Figure 7.41: (a) Temperatures at three specific locations with the cantilever power of 7 mW based on Stokes peak position.

7.5.5 Sensor characteristic: AlGaN/GaN Microcantilever hotplates

Transient electrical measurements and VOC sensing

The capability to heat AlGaN V-shaped heated microcantilevers as we have seen in the previous section is very useful for cantilever-based sensing. In our lab these heated microcantilevers have demonstrated detection of Volatile Organic Compounds (VOCs) with high sensitivity. The cantilever heating caused deflagration of the chemical adsorbed to the cantilever, which in turn induced measurable cantilever deflection. This deflection in the piezoresistive AlGaN/GaN based microcantilevers can be transduced to electrical signal easily.

When a voltage pulse is applied to the cantilever, the cantilever temperature increases and, if the pulse is sufficiently long, may eventually reach a steady value. After the pulse has elapsed, the cantilever temperature drops and recovers the initial temperature exponentially. Square pulse excitation can provide insight into how the cantilever behaves and responds to electrical excitation in short time periods. We performed transient/pulse electrical measurements that can monitor the cantilever heating (τ_h) and cooling time constant (τ_c). Square pulses of 2 ms duration were applied to the cantilever to monitor the cantilever resistance before and after the square pulse. From this measurement we have seen the cantilever is heated to as high as 700 ˚C in just 500 μs (Fig 7.42 (b)). With increased excitation voltage, the cantilever resistance and generated power increased, reached the maximum, and then decreased until the cantilever reached steady state. For increased voltage, the heating and cooling happen quickly as compared to low excitation voltage.

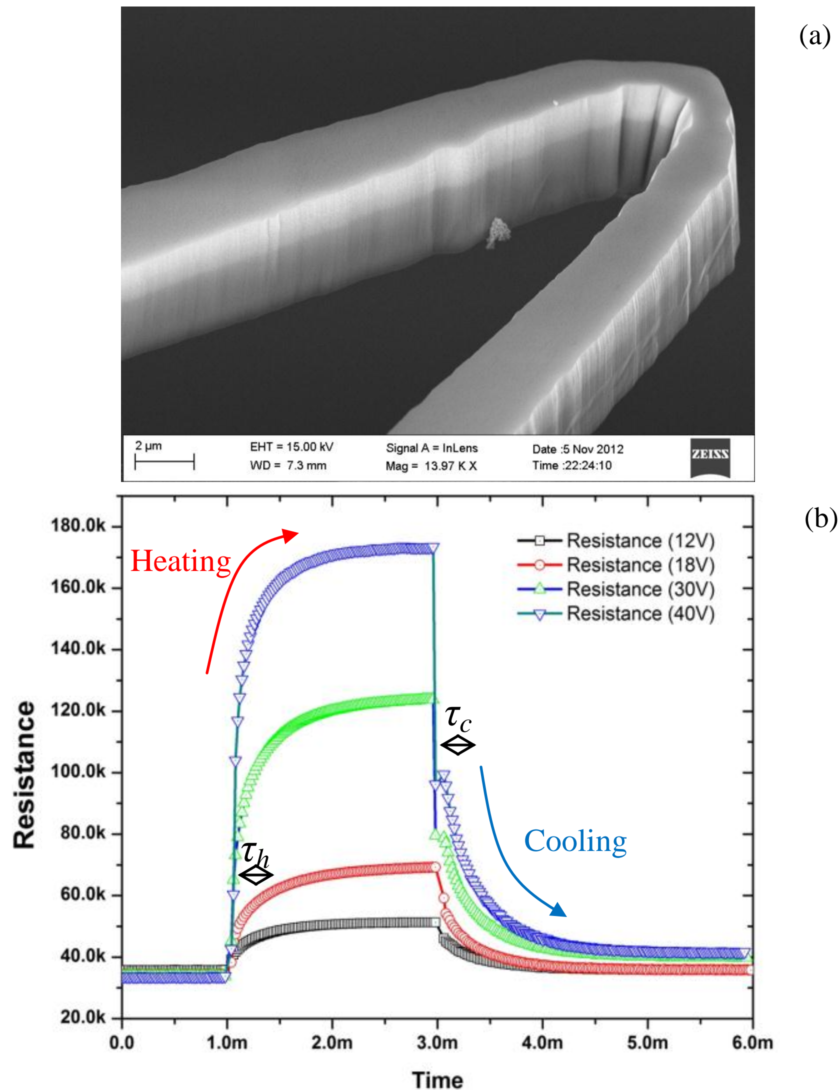

Figure 7.42: (a) SEM image of the tip of the heated micro cantilever and (b) resistance depending upon the voltage level V where square pulses of 2 ms duration are applied to the cantilever. With higher V, the cantilever resistance and generated power increase, reach the maximum, and then decrease until the cantilever reaches steady state.. Heated cantilevers can reach approximately 700˚C within 500µs.

The transient heat can be used to deflagrate volatile organic compounds (Fig 7.42 (a)). This deflagration drives the thermal gradient change around the cantilever tip which in turn changes the conductivity (Fig 7.44). This way VOCs can be sensed efficiently; again each VOC has different auto ignition temperature, thus VOCs can be detected selectively using the heated cantilevers (Fig 7.44 (a)). VOC methanol has the auto

ignition temperature of 385 ˚C whereas IPA and acetone have 399 ˚C and 465 ˚C respectively. The cantilever temperature can be tuned by setting up desired voltage (dissipated power, please refer to Fig 7.42) to detect a specific VOC.

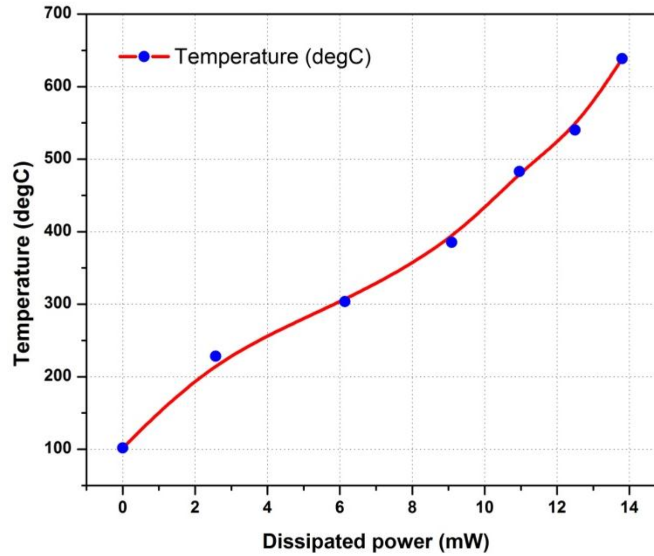

Figure 7.43: V-shaped heated cantilever temperature profiling with dissipated power.

Figure 7.44 (b) shows the sensing of different VOCs at different excitation voltages (dissipated power) of the cantilever. At 25 V voltage the average dissipated power is 6.5 mW which corresponds to 320 ˚C at the tip of the cantilever (Fig 7.44 (a)). At this low temperature, which is below the auto ignition points of the VOCs, no sensing is observed. At 35 V or 8.7 mW power level where the temperature of the cantilever tip is close to 400 ˚C we observe change in current (hence dissipated power) for Methanol and IPA but no change for Acetone since the temperature is below the Acetone auto

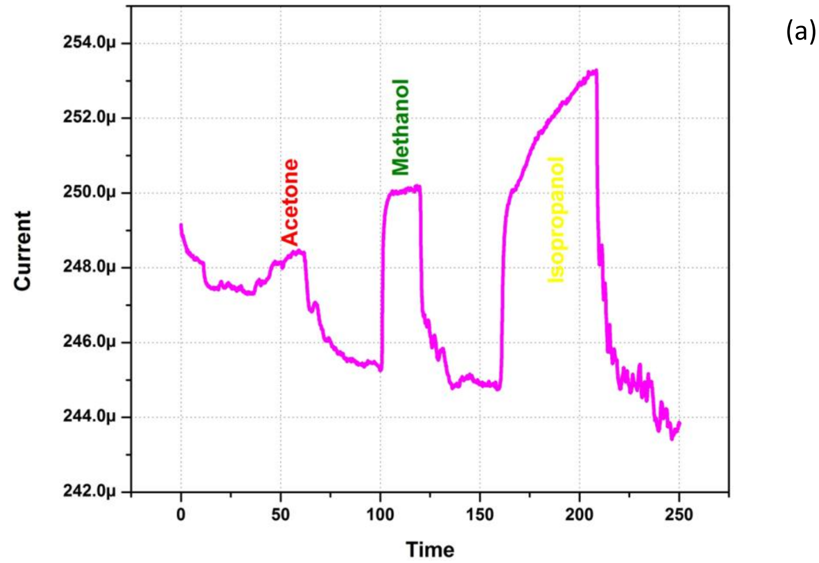

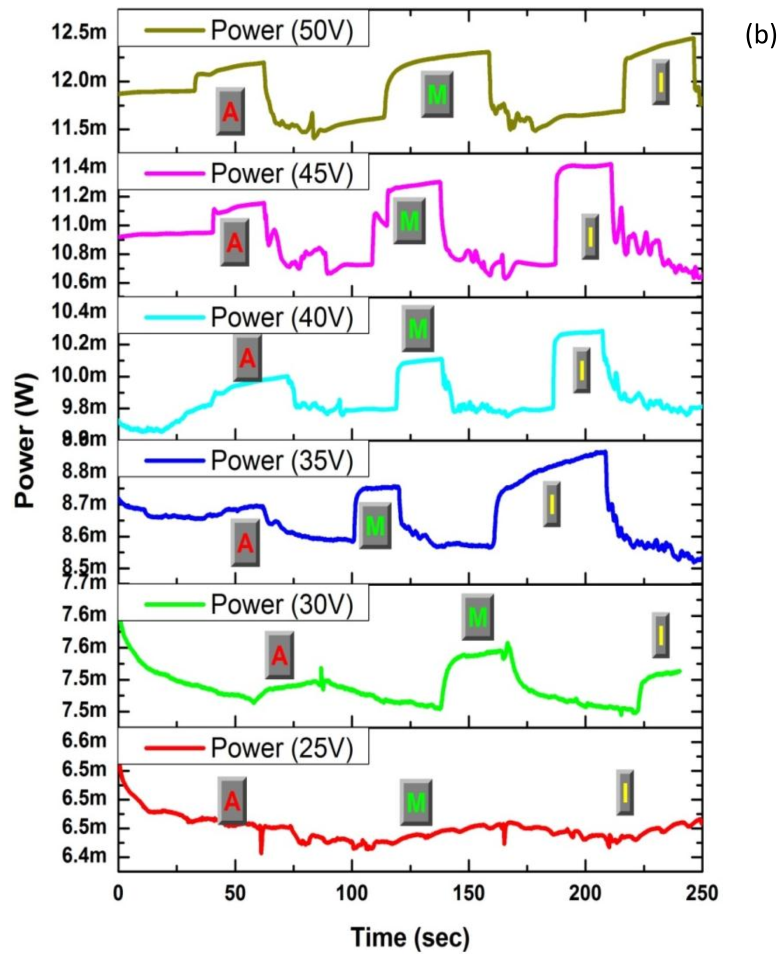

Figure 7.44: (a) Sensing of different Volatile Organic Compounds (VOCs) at the fixed voltage of 35V and (b) nature of sensing for different VOCs with different voltages (dissipated power).

ignition temperature as shown in Fig. 7.44 (a). For higher voltages and dissipated power the VOCs can be selectively detected from the nature of the peak change in dissipated power plot.

CHAPTER 8

CONCLUSION AND FUTURE PLAN

This chapter will give a concluding overview of the dissertation. The achievements earned so far in this work are also presented briefly. The future work plan is presented at the end.

8.1 Summary

The synthesis of high quality InN is challenging due to its low thermal decomposition temperature and the high equilibrium vapor pressure of nitrogen. In this work we have seen that with the contribution of controlled amount of oxygen we can overcome this challenge and we reported successful synthesis of high quality, coplanar, small diameter and long InN NWs.

Charge carrier mobility and conductivity were found to be strongly dependent on NW diameter. The observed mobility and conductivity variations have been modeled by considering NW surface and core conduction paths. Both the mobility and conductivity increase with the decrease of diameter.

Morphological control of nanostructures by photolithographic patterns by utilizing the NW growth redirection has been studied extensively. Successfully fabricated nanoresonators using InN NWs, also the process steps for V-shaped nanocantilevers have been realized.

Fabrication of V-shaped HFET embedded AlGaN/GaN microcantilever and heater microcantilever has been successfully optimized. Preliminary HFET characterization results show excellent mobility, 2DEG density and gate control.

8.2 Future work

8.2.1 Multimodal detection using InN Nanocantilever sensors

Sensing CWAs

Detection of CWAs will be performed using In_2O_3 functionalization layer which has very high responsivity to DCP and DIMP. The selection of In_2O_3 for detection is advantageous since it is fairly easy to grow In_2O_3 shell layer on InN VNCs by thermal oxidation in O_2/Ar mixture. Since the VNCs can be used as nanoheaters by passing appropriate current through them, the oxidation can be performed quite easily and selectively after they are fully fabricated. Thermally grown In_2O_3 functionalization layer also allows all three sensing modes to be utilized enabling unique identification of analytes, although for ΔS based detection, one side of the VNC needs to be covered with a thin SiO_2 layer to create asymmetric stress due to molecular attachment. Although

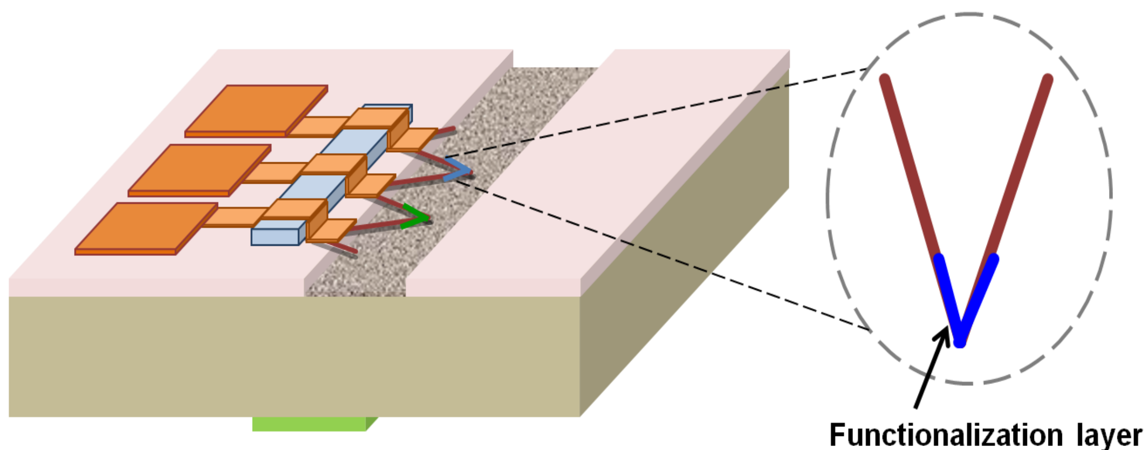

Figure 8.1: V-shaped nanocantilever array and functionalization layer coating.

detection of CWAs is possible at room temperature, best sensitivity is obtained at higher temperatures in the range 300 – 400 °C. Fortunately, all the detection modes require passing current through the VNC for transduction, and we will adjust the level of current used in each mode to achieve the required temperature of the NW.

Sensing explosives

Detection of explosives (TNT and PETN) will be performed using mercaptobenzoic acid (MBA) and mercaptonicotinic acid (MNA) self assembled monolayers (SAMs) to functionalize the adsorption surface taking advantage of the strong interaction between the - COOH and -NO2 groups. We will use a bi-modal detection scheme based on $\Delta\varphi$ and ΔS measurements, and determine unique signature $S_{G2} = \Delta\varphi/\Delta S$ of the anytes. For $\Delta\varphi$ measurement, we will deposit Au/Cr film during fabrication process, which will be functionalized later with the SAM layer, by simply putting a drop of MBA or MNA using a micropipette on the particular VNC pit. For functionalizing the VNC for measurement of ΔS, we will first deposit a thin (3 – 5 nm) insulating layer of SiO_2 on the VNC followed by a thin layer (~5 nm) of Au, which will finally be functionalized using the MBA or MNA SAM. Obviously, the thickness of the VNC will increase, making it somewhat less sensitive to ΔS. To compensate for this, we may increase the length of the VNCs during growth process as appropriate (determined from actual testing). Similar to CWA sensing, we will also test the detection limits of $\Delta\varphi$ and ΔS based sensing, individually, and use the most sensitive mode to determine the concentration of analyte TNT or PETN vapors. We will determine the S_2 signatures of other -NO2 containing analytes such as DNT, nitro-toluene, and nitro-benzene and use them for comparison and unique identification of TNT or PETN vapors. The explosive

vapor for testing will be generated by first isolating the Sensor Test Bed (STB) chamber after filling it with air, and then producing a calibrated vapor pressure by controlling the temperature (above or below 300 K) of the container housing the explosive powder, which will be placed inside the STB chamber in close proximity to the VNC sensors arrays.

In summary,

For sensing CWAs,

DMMP (Dimethyl methylphosphonate) => Sarin Gas

2,4-Dichlorophenol (2,4-DCP) => Chlorinated Gas

The *functionalization layer* is **Indium Oxide (In_2O_3)**

For Sensing Explosives,

Pentaerythritol Tetranitrate (PETN)

TNT (Trinitrotoluene)

The *functionalization layer* is **Mercaptobenzoic acid (MBA) and Mercaptonicotinic acid (MNA) self assembled monolayers (SAMs)**

The functionalization layers will be deposited on the tip of the VNCs by E beam lithography prior to the etching of underneath SiO_2.

8.2.2 Multimodal sensing using AlGaN/GaN microcantilevers

Though the fabrication and preliminary characteristics are done and the piezo-response of the AlGaN/GaN HFET embedded microcantilevers is observed through various experiments, the molecular sensing with these kinds of microcantilevers are not done yet. Again for heated microcantilevers, VOC sensing are done but the chemical warefare agents (CWAs) and explosive detection are not preformed yet. The work can be extended by sensing various molecules with gas sensitive layers by multimodal detection technique on both kinds of cantilevers.

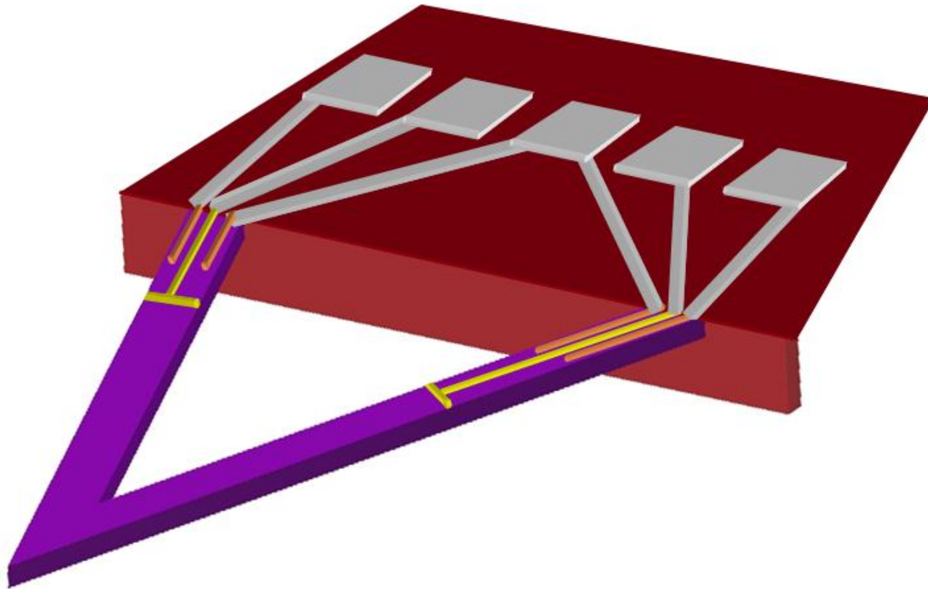

Figure 8.2: Redefined T-gates for the second generation of HFET embedded V-shaped microcantilevers for complete channel turn off, maximum gate modulation.

The design of the V-shaped cantilevers can be improved well for increasing the sensitivity. As for example the HFETs can be redesigned to completely turn off the channel to get better peizoresponse. Such a design is illustrated in Fig 8.2 for the second

generation of V-shaped cantilevers. The gate is "T" shaped, which will have complete controllability to modulate the 2DEG carriers.

Furthermore, the microcantilevers can be placed inside a vacuum chamber and the testing can be done by positioning the sensing layer outside the chamber and flowing the test gases. With appropriate controlling of the chamber pressure, the enhancement of the quality factor and hence the sensitivity can be monitored and studied.

REFERENCES

[1]. M. M. Ayad and N. L. Torad, Talanta78 (4-5), 1280-1285 (2009).

[2]. H. Sohn, M. J. Sailor, D. Magde and W. C. Trogler, J. Am. Chem. Soc.125 (13), 3821-3830 (2003).

[3]. M. H. Yun, N. V. Myung, R. P. Vasquez, C. S. Lee, E. Menke and R. M. Penner, Nano Lett.4 (3), 419-422 (2004).

[4]. J. Gere, Mechanics of materials, 6 ed. Pacific Grove: Brooks/Cole, 2004.

[5]. W. Weaver, Jr., S.P. Timoshenko, D.H. Young, Vibration Problems in Engineering,5 ed. New York: Wiley, 1990.

[6]. N. V. Lavrik, M. J. Sepaniak, and P. G. Datskos, Rev. Sci. Instr., 75, pp. 2229-2253, 2004.

[7]. C. Ziegler, Anal. BioAnal.Chem.,379, pp. 946-959, 2004.

[8]. R. Raiteri, G. Nelles, H. J. Butt, W. Knoll, and P. Skladal, Sens. Actuators B, B61, pp. 213-17, 1999.

[9]. D. Lange, C. Hagleitner, A. Hierlemann, O. Brand, and H. Baltes,Anal.Chem.,74, pp. 3084-3095, 2002.

[10]. K. M. Goeders, J. S. Colton, and L. A. Bottomley, Chemical Reviews, 108, pp.522-542, 2008.

[11]. P. E. Nokes and E. G. Carr, Mech. Eng., 69, pp. 117-119, 1947.

[12]. R. M. McClintock, Rev. Sci. Instr., 30, pp. 715-718, 1959

[13]. F. P. Burns, J. Acoust. Soc. Am., 29, pp. 248-253, 1957.

[14]. M. Traite, W. Welkowitz, and R. Downs, Rev. Sci. Instr.,31, pp. 987-991, 1960.

[15]. L. M. Roylance and J. B. Angell, IEEE Trans. Elec. Dev., 26, pp. 1911-17, 1979.

[16]. P. L. Chen, R. S. Muller, R. D. Jolly, G. L. Halac, R. M. White, A. P. Andrews, T.C. Lim, and M. E. Motamedi, IEEE Trans. Elec. Dev., 29, pp. 27-33,1982.

[17]. G. Binnig, C. F. Quate, and C. Gerber, Phys. Rev. Lett., 56, pp. 930-3, 1986.

[18]. Y. Martin, C. C. Williams, and H. K. Wickramasinghe, J. Appl. Phys. , 61, pp. 4723-9, 1987.

[19]. R. Erlandsson, G. M. McClelland, C. M. Mate, and S. Chiang, J. Vac. Sci. Technol.A,6, pp. 266-70, 1988.

[20]. R. Garcia and R. Perez, Surf. Sci. Rep.,47, pp. 197-301, 2002.

[21]. G. Binnig, C. F. Quate, and C. Gerber, Phys. Rev. Lett. 56, 930 (1986).

[22]. Yang, Y. T.; Callegari, C.; Feng, X. L.; Ekinci, K. L.; Roukes, M. L. Nano Lett. 2006, 6, 583.

[23]. Rugar, D.; Budakian, R.; Mamin, H. J.; Chui, B. W. Nature 2004, 430, 329.

[24]. Schwab, K. C.; Roukes, M. L. Phys. Today 2005, July, 36.

[25]. Feng, X. L.; White, C. J.; Hajimiri, A.; Roukes, M. L. 2007, *Nature Nanotechnology* **3**, 342 - 346 (2008)

[26]. Roukes, M. L. In Technical Digest 2004 IEEE International Electron Devices Meeting, San Francisco, CA, December 13-15, 2004; p 539.

[27]. Cleland, A. N.; Roukes, M. L. Appl. Phys. Lett. 1996, 69, 2653.

[28]. He, R. R.; Gao, D.; Fan, R.; Hochbaum, A. I.; Carraro, C.; Maboudian, R.; Yang, P. D. Adv. Mater. 2005, 17, 2098.

[29]. San Paulo, A.; Bokor, J.; Howe, R. T.; He, R.; Yang, P.; Gao, D.; Carraro, C.; Maboudian, R. Appl. Phys. Lett. 2005, 87, 053111.

[30]. He, R. R.; Yang, P. D. Nat. Nanotechnol. 2006, 1, 42.

[31]. Karabacak, D.; Kouh, T.; Huang, C. C.; Ekinci, K. L. Appl. Phys. Lett. 2006, 88, 193122.

[32]. Truitt, P. A.; Hertzberg, J. B.; Huang, C. C.; Ekinci, K. L.; Schwab, K. C. Nano Lett. 2007, 7, 120.

[33]. Knobel, R.; Cleland, A. N. Appl. Phys. Lett. 2002, 81, 2258.

[34]. Cleland, A. N.; Roukes, M. L. Sens. Actuators, 1999, 72, 256.

[35]. Huang, X. M. H.; Feng, X. L.; Zorman, C. A.; Mehregany, M.; Roukes, M. L. New J. Phys. 2005, 7, 247.

[36]. Lavrik, N.V., M.J. Sepaniak, and P.G. Datskos, Rev. Sci. Instr., 2004. 75(7): p. 2229-2253.

[37]. Ziegler, C., Anal Bioanal Chem, 2004. 379(7-8): p. 946-59.

[38]. Carrascosa, L.G., et al., Trac-Trends inAnal.Chem., 2006. 25(3): p. 196-206.

[39]. Lang, H.P., M. Hegner, and C. Gerber, Materials Today,2005(April), p. 30-36.

[40]. Baller, M.K., et al., Ultramicroscopy, 2000.82(1-4): p. 1-9.

[41]. Lange, D., et al., Anal Chem, 2002.74(13): p. 3084-95.

[42]. Tang, Y.J., et al., Anal.Chem., 2004. 76(9): p. 2478-2481.

[43]. Mertens, J., et al., Sens. Actuators B, 2004. 99(1): p. 58-65.

[44]. Yan, X.D., et al., Instr. Sci. Technol., 2004. 32(2): p. 175-183.

[45]. Alvarez, M., et al., Langmuir, 2004. 20(22): p. 9663-9668.

[46]. Monchev, B., et al., Appl. Phys. A, 2007. 87(1): p. 31-36.

[47]. Filenko, D. and I.W. Rangelow, Kassel,B1, 91 (2004).

[48]. Abedinov, N., et al., Appl. Phys. A, 2004. 79(3): p. 531-536.

[49]. Abedinov, N., et al., J. Vac. Sci. Technol.B, 2003. 21(6), p. 2931-2936.

[50]. Abedinov, N., et al., J. Vac. Sci. Technol. A, 2001. 19(6): p. 2884-2888.

[51]. Zambov, L.M., et al., Adv. Mater., 2000. 12(9): p. 656.

[52]. Yum, K., et al., J. Appl. Phys., 2004. 96(7):p. 3933-3938.

[53]. Kooser, A., et al., Sens. Actuators B, 2004. 99(2-3): p. 474-479.

[54]. Fadel, L., et al.,J. of Micromechanics and Microengineering, 2004. 14(9): p. S23-S30.

[55]. Fadel, L., et al., Sens. Actuators B,2004. 102(1): p. 73-77.

[56]. Gunter, R.L., et al., IEEE Sensors Journal, 2004. 4(4): p. 430-433.

[57]. Pei, J.H., F. Tian, and T. Thundat, Anal.Chem., 2004. 76(2): p. 292-297.

[58]. Yan, X.D., H.F. Ji, and Y. Lvov, Chem. Phys. Lett., 2004. 396(1-3):p. 34-37.

[59]. Zhang, Y.F., et al., Biosens.Bioelectron., 2004. 19(11): p. 1473-1478.

[60]. Lee, J.H., T.S. Kim, and K.H. Yoon, Appl. Phys. Lett, 2004. 84(16): p. 3187-3189.

[61]. Lee, J.H., et al., Biosens.Bioelectron., 2004. 20(2): p. 269-75.

[62]. Yinon, J., Anal.Chem., 2003. 75(5): p. 99a-105a.

[63]. Pinnaduwage, L.A., et al., Sens. Actuators B, 2004. 99(2-3): p. 223-229.

[64]. Pinnaduwage, L.A., et al., J. Appl. Phys., 2004. 95(10): p. 5871-5875.

[65]. Zhang, J. and H.F. Ji, Anal. Sci., 2004. 20(4): p. 585-587.

[66]. Gfeller, K.Y., N. Nugaeva, and M. Hegner, Biosens.Bioelectron., 2005. 21(3) p. 528-533.

[67]. Ke, L. and H.-F. Ji, Anal. Sci., 2004. 20.

[68]. Zhang, Y.F., et al., Instr. Sci. Technol., 2004. 32(4), p. 361-369.

[69]. Tian, F., et al., Ultramicroscopy, 2004. 100(3-4): p. 217-23.

[70]. Bottomley, L.A., M.A. Poggi, and S.X. Shen, Anal.Chem., 2004. 76(19):p. 5685-5689.

[71]. Ryu, W.H., et al., Sens. Actuators B,2004. 97(1): p. 98-102.

[72]. Ren, Q. and Y.P. Zhao, Microsystem Technologies-Micro-and Nanosystems-Information Storage andProcessing Systems, 2004. 10(4): p. 307-314.

[73]. Khaled, A.R.A. and K. Vafai, J. of Micromechanics and Microengineering, 2004. 14(8): p. 1220-1229.

[74]. Zhang, Y., Q. Ren, and Y.P. Zhao, J. Phys. D, 2004. 37(15): p. 2140-2145.

[75]. Tang, Y.J., et al., Sens. Actuators B, 2004. 97(1): p. 109-113.

[76]. Hu, Z.Y., et al., Rev. Sci. Instr., 2004. 75(2): p. 400-404.

[77]. Jeon, S. and T. Thundat, Appl. Phys. Lett, 2004. 85(6): p. 1083-1084.

[78]. Bambu, G.-G. and e. al., Macromol. Chem. Phys., 2004. 205(13): p. 1713.

[79]. McFarland, A.W., et al., Rev. Sci. Instr., 2004. 75(8): p. 2756-2758.

[80]. Ilic, B., et al., J. Appl. Phys., 2004. 95(7): p. 3694-3703.

[81]. Sharos, L.B., et al., Appl. Phys. Lett, 2004. 84(23): p. 4638-4640.

[82]. Lin, R., P. Boggild, and O. Hansen, J. Appl. Phys., 2004. 96(5): p. 2895-2900.

[83]. Yue, M., et al., J. of Microelectromechanical Systems, 2004. 13(2): p. 290-299.

[84]. Thundat, T., et al., Anal.Chem., 1995. 67(3): p. 519-521.

[85]. Boltshauser, T., et al., J. Micromech. Microeng., 1992. 2: p. 205-207.

[86]. Thundat, T., et al., Appl. Phys. Lett, 1995. 66(13): p. 1695-1697.

[87]. Hierlemann, A., et al., Sens. Actuators B, 2000. 70(1-3): p. 2 11.

[88]. Maute, M., et al., Sens. Actuators B, 1999. 58(1-3): p. 505-511.

[89]. Lange, D., et al., Digest of Technical PapersTRANSDUCERS, 1999. Sendai, Japan: p. 1020-1023.

[90]. Lange, D., et al., Proc. SPIE, 1998. 3224: p. 233-243.

[91]. Lange, D., et al., Proc. IEEE MEMS, 2000(Myazaki, Japan): p. 547-552.

[92]. Britton, C.L., Jr., et al., Ultramicroscopy, 2000. 82(1-4): p. 17-21.

[93]. Kim, B.H., et al., Sens. Actuators B, 2001. 78(1-3): p. 12-18.

[94]. Koll, A., et al., Proc. SPIE, 1999.

[95]. Hagleitner, C., et al., Technial Digest TRANSDUCERS, 1999(Sendai, Japan): p. 1012-1015.

[96]. Kerness, N., et al., Proc. IEEE MEMS, 2000(Myazaki, Japan): p. 96-101.

[97]. Vu. Thien Binh, N. Garcia, and A. L. Levanuyk, Surf. Sci. Lett. 301, L224 (1994).

[98]. F. A. Nichols and W. W. Mullins, J. Appl. Phys. 36, 1826 (1965).

[99]. M. Drechsler, A. Piquet, R. Uzan, and Vu Thien Bihn, Surf. Sci.14, 457 (1969).

[100]. Vu Thien Binh, M. Chaudier, J. C. Couturier, R. Uzan, and M. Drechsler, Surf. Sci. 57, 184 (1976).

[101]. M. Drechsler, S. Ramadani, A. Claverie, and A. Maas, J. Phys. Colloq. C6-209 (1987).

[102]. Saya, D, Fukushima, K, Toshiyoshi, H, et al., Jpn. J. Appl. Phys. 39 (2000) pp. 3793-3798

[103]. Binh, Vt; Garcia, N; Levanuyk, Al, surf. Sci., 301,Jan 1994.

[104]. Datskos PG, Thundat T, J Nanosci Nanotechnol. 2002 Jun-Aug;2(3-4):369-73

[105]. William L. Hughes and Zhong L. Wang, Appl. Phys. Lett.,82(17), April 2003

[106]. Z. W. Pan, Z. R. Dai, and Z. L. Wang, Science291, 1947 (2001).

[107]. C. Ma, D. Moore, J. Li, and Z. L. Wang, Adv. Mater. (in press).

[108]. M. Ferrari, Nature Reviews Cancer, 5 (161-171), March 2005

[109]. Shao-Min Zhou, Xiang-Min Meng, Xiao-Hong Zhang, Xia Fan, Kai Zou, Shi-Kang Wu, Shuit-Tong Lee, Micron36 (2005) 55–59

[110]. Llic, B., Yang, Y., Aubin, K., Reichenbach, R., Krylov, S., Craighead, H.G. (2005) Nanoletters,5(5), pp. 925-929.

[111]. http://www.nsti.org/Nanotech2006/showabstract.html?absno=488

[112]. Gupta, A.K., Nair, P.R., Akin, D., Ladisch, M.R., Broyles, S., Alam, M.A., Bashir, R. Proc. Natl. Acad. Sci.USA, 103(36), 13362-13367 (2003).

[113]. S. M. Han, H. Benaroya, and T. Wei, J. of Sound and Vibration225, 935-988 (1999).

[114]. W. Weaver, Jr., S.P. Timoshenko, D.H. Young, Vibration Problems in Engineering, 5 ed. New York: Wiley, 1990.

[115]. C. M. Harris, Harris's shock and vibration handbook, 5 ed. New York: McGraw-Hill, 2002.

[116]. C. A. Desoer and E. S. Kuh, Basic circuit theory. New York: McGraw-Hill, 1969.

[117]. L. E. Kinsler, Fundamentals of acoustics, 3rd ed. New York: Wiley, 1982.

[118]. S. D. Senturia, Microsystem Design. Boston: Kluwer Academic 2001.

[119]. R. R. Archer, N. H. Cook, S. H. Crandall, N. C. Dahl, F. A. McClintock, E. Rabinowicz, and G. S. Reichenbach, An introduction to the mechanics of solids. New York: McGraw-Hill, 1959.

[120]. J. Gere, Mechanics of materials, 6 ed. Pacific Grove: Brooks/Cole, 2004.

[121]. J. L. Arlett, J. R. Maloney, B. Gudlewski, M. Muluneh, and M. L. Roukes, Nano Lett., 6, pp. 1000-1006, 2006.

[122]. N. E. Jenkins, L. P. DeFlores, J. Allen, T. N. Ng, S. R. Garner, S. Kuehn, J. M. Dawlaty, and J. A. Marohn, J. Vac. Sci. Technol. B,22, pp. 909-915, 2004.

[123]. K. Y. Yasumura, T. D. Stowe, E. M. Chow, T. Pfafman, T. W. Kenny, B. C. Stipe, and D. Rugar, J. of Microelectromechanical Systems,9, pp. 117-25, 2000.

[124]. A. N. Cleland and M. L. Roukes, J. Appl. Phys.,92, pp. 2758-2769, 2002.

[125]. P. M. Morse and K. U. Ingard, Theoretical acoustics. Princeton, N.J: Princeton University Press, 1986.

[126]. W. Thomson, Proceedings of the Royal Society of London, 8, pp. 50-55, 1856

[127]. Meyer, G. &Amer, N.M.,Appl. Phys. Lett., 53(12), 1045-47,(1988).

[128]. Blanc, N., Brugger, J., Rooij, N.F.D. &Durig, U.;J Vac. Sci. Technol. B, 14(2), 901-05. (1996)

[129]. Erlandsson, R., McClelland, G.M., Mate, C.M. & Chiang, S.; J. Vac. Sci. Technol. A,6(2), 266-70. (1988)

[130]. Rugar D, Yannoni CS, Sidles JA. 1992. Nature 360:563–66

[131]. R. G. Beck, M. A. Eriksson, M. A. Topinka, R. M. Westervelt, K. D. Maranowski, and A. C. Gossard, Appl. Phys. Lett. 73, 1149 (1998).

[132]. R. G. Beck, M. A. Eriksson, R. M. Westervelt, K. L. Chapman, and A. C. Gossard, Appl. Phys. Lett. 68, 3763 (1996).

[133]. K. Fricke, J. Appl. Phys.70, 914 (1991).

[134]. J. M. Ziman, Electrons and Phonons Oxford University, Oxford (1960).

[135]. M. S. Suh, J. H. Choi, Y. Kuk, and J. Jung, Appl. Phys. Lett. 83, 386 (2003).

[136]. L. H. Chen, M. A. Topinka, B. J. LeRoy, R. M. Westervelt, K. D. Maranowski, and A. C. Gossard, Appl. Phys. Lett. 79, 1202 (2001).

[137]. G. Shekhawat, S. H. Tark, and V. P. Dravid, Science 311, 1592 (2006).

[138]. S. H. Tark, A. Srivastava, S. Chou, G. Shekhawat, and V. P. Dravid, Appl. Phys. Lett. 94, 104101 (2009).

[139]. J. Wang, W. G. Wu, Y. Huang, and Y. L. Hao, Appl. Phys. Lett. 95, 124101 (2009).

[140]. G. Tosolini, G. Villanueva, F. Perez-Murano, and J. Bausells, Microelectronic Engineering 87, 1245 (2010).

[141]. S. Mostafa, I. Lee, S. K. Islam, S. A. Eliza, G. Shekhawat, V. P. Dravid, and F. S. Tulip, IEEE Elec. Dev.Lett.32, 408 (2011).

[142]. T. Zimmermann, M. Neuburger, P. Benkart, F. J. Hernandez-Guillen, C. Pietzka, M. Kunze, I. Daumiller, A. Dadgar, A. Krost, and E. Kohn, IEEE Elec. Dev.Lett.27, 309 (2006).

[143]. M. Nonnenmacher, M. P. Oboyle, and H. K. Wickramasinghe, Appl. Phys. Lett. 58, 2921 (1991).

[144]. G. Koley, and M. G. Spencer, In Encyclopedia of Nanoscience and Nanotechnology, 327 (2004).

[145]. G. Koley, and M. G. Spencer, J. Appl. Phys.90, 337 (2001).

[146]. Z. L. Wang , J. Song , Science 2006 , 312 , 242 .

[147]. X. Wang , J. Song , J. Liu , Z. L. Wang , Science 2007 , 316 , 102 .

[148]. R. Yang , Y. Qin , L. Dai , Z. L. Wang , Nat. Nanotechnol. 2009 ,4 , 34.

[149]. R. Yang , Y. Qin , C. Li , G. Zhu , Z. L. Wang , Nano Lett. 2009 ,9 , 1201.

[150]. Y. F. Lin , J. Song , Y. Ding , S. Y. Lu , Z. L. Wang , Appl. Phys. Lett. 2008 ,92 , 022105.

[151]. C. T. Huang , J. H. Song , W. F. Lee , Y. Ding , Z. Y. Gao , Y. Hao , L. J. Chen , Z. L. Wang , J. Am. Chem. Soc. 2010 , 132 , 4766.

[152]. Chi-Te Huang , Jinhui Song , Chung-Min Tsai , Wei-Fan Lee , Der-Hsien Lien , ZhiyuanGao , YueHao , Lih-Juann Chen , and Zhong Lin Wang, Adv. Mater. 2010, XX, 1–6

[153]. Jungchul Lee a, KianoushNaeli, Hanif Hunter, John Berg, Tanya Wright, Christophe Courcimault, NisargaNaik, Mark Allen, Oliver Brand, Ari Glezer, William P. King, Sens. ActuatorsA,134 (2007) 128–139

[154]. I. Langmuir, J. Am. Chem. Soc. 38, 2221 (1916).

[155]. T. Sahm, A. Gurlo, N. Barsan, and U. Weimar, Sens. Actuators B,118, 78 (2006).

[156]. S. Cesaro-Tadic, G. Dernick, D. Juncker, G. Buurman, H. Kropshofer, B. Michel, C. Fattinger, and E. Delamarche, Lab on a Chip 4, 563 (2004).

[157]. Cui, Y., et al., Science (2001) 293, 1289

[158]. Patolsky, F., et al., Proc. Natl. Acad. Sci. USA (2004) 101, 14017

[159]. Stadler, K., et al., Nat. Rev. Microbiol. (2003) 1, 209

[160]. Atlas, R. M., Nat. Rev. Microbiol. (2003) 1, 70

[161]. Niiler, E., Nat. Biotechnol. (2002) 20, 21

[162]. N. Barsan and U. Weimar, J. Electroceramics, 7, 143 (2001).

[163]. G. Koley and M. G. Spencer, J. Appl. Phys. 90 (1), 337-344 (2001).

[164]. G. Koley, M. Qazi, L. Lakshmanan and T. Thundat, Appl. Phys. Lett.90 (17) (2007).

[165]. N. Sasaki and M. Tsukada, Jpn. J. Appl. Phys. 37 (5A), L533-L535 (1998).

[166]. M. Qazi and G. Koley, Sensors8 (11), 7144-7156 (2008).

[167]. M. Qazi, G. Koley, S. Park and T. Vogt, Appl. Phys. Lett.91 (4) (2007).

[168]. Panev, N., et al., Appl. Phys. Lett. (2003) 83

[169]. K. L. Ekinci, and M. L. Roukes, Rev. Sci. Instr.,76, 061101 (2005).

[170]. Y. T. Yang, C. Callegari, X. L. Feng, K. L. Ekinci, and M. L. Roukes, Nano Lett., 6, 583 (2006).

[171]. D. Rugar, R. Budakian, H. J. Mamin, and B. W. Chui, Nature, 430, 329 (2004).

[172]. K. C. Schwab, and M. L. Roukes, Phys. Today, July, 36 (2005).

[173]. X. L. Feng, C. J. White, A. Hajimiri, and M. L. Roukes, Nat. Nanotech. 3, 342 (2008).

[174]. M. L. Roukes, In Technical Digest 2004 IEEE International Electron Devices Meeting, San Francisco, CA, December 13-15, p 539 (2004).

[175]. X. L. Feng, R. He, P. Yang, and M. L. Roukes, Nano Lett.,7, 1953 (2007).

[176]. I. Mahboob, T. D. Veal, C. F. McConville, H. Lu and W. J. Schaff, Phys. Rev. Lett. 92, 036804 (2004).

[177]. S. Strite and H. Morkoc, J. Vac. Sci. Technol. B10, 1237 (1992).

[178]. http://www-opto.e-technik.uni-ulm.de/lehre/cs/index.html

[179]. F. Patolsky, B. P. Timko, G. Zheng, and C. M. Lieber, MRS BULLETIN, 32, 142 (2007).

[180]. Wilke, I.; Ascazubi, R.; Lu, H.; and Schaff W. J.; Appl. Phys. Lett.2009, 93, 221113

[181]. Jones, R. E.; Li, S. X.; Haller, E. E.; van Genuchten, H. C. M.;Yu, K. M.; Ager III, J. W.; Liliental-Weber, Z.; and Walukiewicz, W.; Lu, H.; and Schaff W. J.; Appl. Phys. Lett.2007, 90, 162103

[182]. Cai, Z.; Garzon, S.; Chandrashekhar, M. V. S.; Webb, R. A.; Koley, G.; J. Electron. Mater.008, 37, 585-592.

[183]. O. Ambacher, J. Phys. D: Appl. Phys., 31, 2653 (1998).

[184]. G. Koley, Ph. D. dissertation, Connell University, p.10, (2003).

[185]. O. Ambacher, J. Smart, J. R. Shealy, N. G. Weimann, K. Chu, M. Murphy, W. J. Schaff, L. F. Eastman, R. Dimitrov, L. Wittmer, M. Stutzmann, W. Rieger, and J. Hilsenbeck, J. Appl. Phys., 85, 3222 (1999).

[186]. V. Cimalla, M. Niebelschütz, G. Ecke, V. Lebedev, O. Ambacher, M. Himmerlich, S. Krischok, J. A. Schaefer, H. Lu, and W. J. Schaff, phys. stat. sol. (a) 203(1), 59–65 (2006)

[187]. I. Mahboob, T. D. Veal, L. F. J. Piper, C. F. McConville, Hai Lu, W. J. Schaff, J. Furthmu¨ller and F. Bechstedt, Phys. Rev. B69, 201307(R) (2004)

[188]. I. Mahboob, T. D. Veal, C. F. McConville, H. Lu and W. J. Schaff, Phys. Rev. Lett.92.036804

[189]. K. Jeganathan, V. Purushothaman, R. K. Debnath, R. Calarco, and H. Luth, Appl. Phys. Lett., 97, 093104(2010)

[190]. Nuria Lopez, Monica Garcia-Mota, and Jaime Gomez-Diaz, J. Phys. Chem. C 2008, 112, 247-252

[191]. F. Agulló-Rueda, E.E. Mendez, B. Bojarczuk, S. Guha, Solid State Comm., 115, 19-21, 2000

[192]. Staffan Westerberg, Chen Wang, Keng Chou, and Gabor A. Somorjai, J. Phys. Chem. B 2004, 108, 6374-6380

[193]. J Fogelberg, I Lundström and L-G Petersson, Phys. Scr., 1987, 35, 702

[194]. D.P. Sobczyk, A.M. de Jong, E.J.M. Hensen, and R.A. van Santen, J. of Catalysis219 (2003) 156–166

[195]. Nu´riaLo´pez, Mo´nicaGarcı´a-Mota, and Jaime Go´mez-Dı´az, J. Phys. Chem. C 2008, 112, 247-252

[196]. A. Franceschetti, S.J. Pennycook, S.T. Pantelides, Chem. Phys.Lett.374 (2003) 471–475

[197]. Chen J, Cheng G, Stern E, Reed M A and Avouris P, 2007 Nano Lett. 7 2276–80

[198]. Cheng G, Stern E, Turner-Evans D and Reed M A, 2005 Appl. Phys. Lett. 87 253103

[199]. Wilke I, Ascazubi R, Lu H and Schaff W J, 2009 Appl. Phys. Lett. 93 221113

[200]. Jones R E, Li S X, Haller E E, van Genuchten H C M, Yu K M, Ager J W III, Liliental-Weber Z, Walukiewicz W, Lu H and Schaff W J 2007,Appl. Phys. Lett. 90 162103

[201]. Thakur J S, Naik R, Naik V M, Haddad D, Auner G W, Lu H and SchaffW J, 2006 J. Appl. Phys. 99 023504

[202]. Huang Y, Duan X, Cui Y and Lieber C M 2002 Nano Lett. 2 101–4

[203]. Chang C Y, Chi G C, Wang W M, Chen L C, Chen K H, Ren F and Pearton S J 2006 J. Electron. Mater. 35 738–43

[204]. Richter T, L¨uth H, Schapers T, Meijers R, Jeganathan K, Hernandez S E, Calarco R and Marso M, 2009 Nanotechnol.20 405206

[205]. Werner F, Limbach F, Carsten M, Denker C, Malindretos J and Rizzi A, 2009 Nano Lett. 9 1567–71

[206]. Cai Z, Garzon S, ChandrashekharM V S, Webb R A and Koley G 2008 J. Electron. Mater. 37 585–92

[207]. Cha H, Wu H, ChandrashekharM V S, Choi Y C, Chae S, Koley G and Spencer M G 2006 Nanotechnol.,17 1264–71

[208]. Liu J, Cai Z and Koley G 2009 J. Appl. Phys.,106 124907

[209]. Dayeh S A, Susac D, Kavanagh K L, Yu E T and Wang D, 2008 Nano Lett. 8 3114–9

[210]. Mahboob I, Veal T D, Piper L F J, McConville C F, Lu H, Schaff W J, Furthmuller J and Bechstedt F, 2004 Phys. Rev. B 69 201307

[211]. Khanal D R andWu J, 2007 Nano Lett. 7 2778–83

[212]. Mahboob I, Veal T D, McConville C F, Lu H and SchaffW J, 2004 Phys. Rev. Lett. 92 036804

[213]. Colakerol L et al,2006 Phys. Rev. Lett. 97 237601

[214]. Petersen G, Hernandez S E, Calarco R, Demarina N andSchaepers T, 2009 Phys. Rev. B 80,125321

[215]. Aravind K, Su Y W, Ho I L, Wu C S, Chang-Liao K S, Su W F,Chen K H, Chen L C and Chen C D, 2009 Appl. Phys. Lett.95 092110

[216]. Hamaguchi C, 2001 Basic Semiconductor Physics (Berlin:Springer) pp 375–77

[217]. Kane B E, Pfeiffer L N, West K N and Harnett C K, 1993 Appl.Phys. Lett. 63 2132–4

[218]. Scheffler M, Nadj-Perge S, Kouwenhoven L P, Borgstrom M Tand Bakkers E P A M 2009,J. Appl. Phys. 106 124303

[219]. Ford A C, Ho J C, Chueh Y, Tseng Y, Fan Z, Guo J, Bokor Jand Javey A, 2009 Nano Lett. 9 360–5

[220]. K. L. Ekinci, and M. L. Roukes, Rev. Sci. Instr., 76, 061101 (2005).

[221]. Y. T. Yang, C. Callegari, X. L. Feng, K. L. Ekinci, and M. L. Roukes, Nano Lett., 6, 583 (2006).

[222]. D. Rugar, R. Budakian, H. J. Mamin, and B. W. Chui, Nature, 430, 329 (2004).

[223]. K. C. Schwab, and M. L. Roukes, Phys. Today, 36, July 2005.

[224]. X. L. Feng, C. J. White, A. Hajimiri, and M. L. Roukes, Nature Nanotech.3, 342 (2008).

[225]. M. L. Roukes, In Technical Digest 2004 IEEE International Electron Devices Meeting, San Francisco, CA, December 13-15, p 539 (2004).

[226]. Wu J, Walukiewicz W, Yu K M, Ager J W III, Haller E E, Lu H, Schaff W J, Saito Y and Nanishi Y, 2002 Appl. Phys.Lett. 80 3967–9

[227]. V. Rochus, D. J. Rixen and J. -C. Golinval, Nonlinear Analysis, pp. 1619-1633, 2005.

[228]. M. Gyimesi, I. Avdeev and D. Ostergaard, IEEE Trans. Mag., 2004.

[229]. D. H. Y. a. W. W. S.P. Timoshenko, Vibration Problems in Engineering, 4 ed., New York: Wiley, 1974, pp. 416-20.

[230]. J. Sader, Rev. Sci. Instrum., 4583, p. 66, 1995.

[231]. A. T. Hubbard, Encyclopedia of Surface and Colloid Science, 2nd ed.,1, P. Somasundaran, Ed., Boca Raton, FL: CRC Press, 2006.

[232]. K. S. T. C. E. P. T. K. T. S. a. R. D. Yasamura, J. Microelectromechanical Systems,9, no. 1, pp. 117-125, 2000.

[233]. K. I. S. K. Hiroshi Hosaka, Sens. Actuators,49, pp. 87-95, 1995.

[234]. R. a. R. M. Lifshitz, Physical Review B,61(8), pp. 5600-5609, 2000.

[235]. V. a. S. S. Srikar, J. of Microelectromechanical Systems,11 (5), pp. 499-504, 2002.

[236]. K. T. Weibin Zhang, Sens. Actuators,134 (2), pp. 594-599, 2007.

[237]. I. G. T. M. Andrews, Sens. Actuators,36 (1), pp. 79-87, 1993.

[238]. J. J. A. B. Willian H. Hayt, Engineering Electromagnetics, 7 ed., New York: McGraw-Hill, 2006, p. 157.

[239]. P. G. Datskos, N. V. Lavrik and S. Rajic, Rev. Sci. Instr.,75, 2004.

[240]. V. Cimalla, J. Pezoldt, and O. Ambacher, J. Phys. D,40, 6386 (2007).

[241]. G. Koley, "PhD Dissertation," In Electrical and Computer Engineering, Cornell University, Ithaca, NY (2003).

[242]. J. H. Edgar, Properties of Group III Nitrides, INSPEC, London (1994).

[243]. F. Bernardini, V. Fiorentini, and D. Vanderbilt, Phys. Rev. B 63, 193201 (2001).

[244]. F. Bernardini, V. Fiorentini, and D. Vanderbilt, Phys. Rev. B 56, 10024 (1997).

[245]. O. Ambacher, J. Smart, J. R. Shealy, N. G. Weimann, K. Chu, M. Murphy, W. J. Schaff, L. F. Eastman, R. Dimitrov, L. Wittmer, M. Stutzmann, W. Rieger, and J. Hilsenbeck, J. Appl. Phys.85, 3222 (1999).

[246]. S. C. Jain, M. Willander, J. Narayan, and R. Van Overstraeten, J. Appl. Phys.87, 965 (2000).

[247]. S. Vicknesh, S. Tripathy, V. K. X. Lin, L. S. Wang, and S. J. Chua, Appl. Phys. Lett. 90, 071906 (2007).

[248]. J. Lv, Z. C. Yang, G. Z. Yan, W. K. Lin, Y. Cai, B. S. Zhang, and K. J. Chen, IEEE Elec. Dev.Lett.30, 1045 (2009).

[249]. H. Amano, N. Sawaki, I. Akasaki, and Y. Toyoda, Appl. Phys. Lett. 48, 353 (1986).

[250]. I. Vurgaftman, J. R. Meyer, and L. R. Ram-Mohan, J. Appl. Phys.89, 5815 (2001).

[251]. S. Timoshenko, Strength Materials, Krieger, Malabar, FL, 1984.

[252]. Yang K, Li Z, Jing Y, Chen D and Ye T, 2009 4th IEEE Int. Conf. on Nano/Micro Engineered and Molecular System (NEMS ’09, Shenzhen, China) pp 59–62

[253]. Muhammad Qazi, "PhD Dissertation," In the Department of Electrical Engineering, University of South Carolina, Columbia

[254]. T. Thundat, G.Y. Chen, R.J. Warmack, D.P. Allison, E.A. Wachter, Anal. Chem. 67 (1995) 519–521.

[255]. G.Y. Chen, R.J.Warmack, T. Thundat, D.P. Allison, A. Huang, Rev. Sci. Instr. 65 (1994) 2532–2537.

[256]. R. Berger, C. Gerber, J.K. Gimzewski, E. Meyer, H.J. Guntherodt, Appl. Phys. Lett. 69 (1996) 40–42.

[257]. N. Abedinov, P. Grabiec, T. Gotszalk, T. Ivanov, J. Voigt, I.W. Rangelow, J. Vac. Sci. Technol. A19 (2001) 2884–2888.

[258]. S. Semancik, R. Cavicchi, Acct. Chem. Res.31 (1998) 279–287.

[259]. B.W. Chui, T.D. Stowe, Y.S. Ju, K.E. Goodson, T.W. Kenny, H.J. Mamin, B.D. Terris, R.P. Ried, J. Microelectromech. Syst.7 (1998) 69–78.

[260]. U. Drechsler, N. Burer, M. Despont, U. D¨urig, B. Gotsmann, F. Robin, P. Vettiger, Microelectr. Eng.67/68 (2003) 397–404.

[261]. F.T. Zhang, Z. Tang, J. Yu, R.C. Jin, Sens. ActuatorsA 126 (2006) 300–305.

[262]. D.-S. Lee, J.-S. Huh, D.-D. Lee, Sens. Actuators B93 (2003) 1–6.

[263]. D.N. Pagonis, G. Kaltsas, A.G. Nassiopoulou, J. Micromech. Microeng. 14 (2004) 793–797

[264]. P.E. Sheehan, L.J. Whitman,W.P. King, B.A. Nelson, Appl. Phys. Lett. 85 (2004) 1589–1591.

[265]. B.A. Nelson,W.P. King, A. Laracuente, P.E. Sheehan, L.J. Whitman, Appl. Phys. Lett. 88 (2006) 033104.

[266]. E.O. Sunden, T.L. Wright, J. Lee, S.A. Graham, W.P. King, Appl. Phys. Lett. 88 (2006) 033107.

[267]. W.P. King, S. Saxena, B.A. Nelson, B.L.Weeks, R. Pitchimani, Nano Lett. 6 (2006) 2145–2149.

[268]. P.E. Sheehan, L.J. Whitman,W.P. King, B.A. Nelson, Appl. Phys. Lett.85 (2004) 1589–1591.

[269]. S.L. Biswal, D. Raorane, A. Chaiken, A. Majumdar, J. Assoc. Lab. Auto. 11 (2006) 222–226.

[270]. L.A. Pinnaduwage, A. Gehl, D.L. Hedden, G. Muralidharan, T. Thundat,R.T. Lareau, T. Sulchek, L. Manning, B. Rogers, M. Jones, J.D. Adams, Nature425 (2003) 474.

[271]. T. R. Hart, R. L. Aggarwal, and B. Lax, Phys. Rev. B1, 638 (1970).

[272]. J. Menendez and M. Cardona, Phys. Rev. B29, 2051 (1984).

[273]. J. B. Cui, K. Amtmann, J. Ristein, and L. Ley, J. Appl. Phys. 83, 7929 (1998).

[274]. J. R. Shealy and G. W. Wicks, Appl. Phys. Lett. 50, 1173 (1987).

[275]. Ming S. Liu, Les A. Bursill, S. Prawer, K. W. Nugent, Y. Z. Tong et al, Appl. Phys. Lett. 74, 3125 (1999)

[276]. V. Cimalla, J. Pezoldt, and O. Ambacher, J. Phys. D. 40, 6386 (2007).

[277]. D. F. Wang, S. W. Feng, C. Lu, A. Motayed, M. Jah, S. N. Mohammad, K. A. Jones, and L. Salamanca-Riba, J. Appl. Phys.89, 6214 (2001).

[278]. Q. Z. Liu, and S. S. Lau, Solid-State Electronics 42, 677 (1998)

APPENDIX A

PROCESS FLOW FOR CANTILEVER FABRICATION

Step 1: MESA Isolation		
Step	***Description***	***Process Details***
1.1	Lithography	Photoresist: Microposit SC1827 Spin: 3000 rpm at 1000 rpm/sec for 30 secs (thickness: ~3 µm) Soft Bake: 115°C for 5 mins on hotplate Exposure: λ = 405 nm, UV density = 450 mJ/cm^2 Developer: MF 319 for 1 min 15 secs Hard Bake: 80°C for 5 mins on hotplate (before ICP etc)
1.2	AlGaN/GaN etch in ICP	Equipment: Plasma Therm ICP with Cl_2/BCl_3 Plasma Sample mount on 4" SiO_2/Si wafer with cool grease. GaN etch for 30 secs (Cl_2 = 32 sccm, BCl_3 = 8 sccm, Ar = 5 sccm, 5 mtorr, RF1 = 70 W, RF2 = 500W, DC=225 V. Etch rate is ~ 350 nm/min). ▪ Etch time depends upon etch rate, etching down AlGaN is enough, however further GaN etching needed to ensure total mesa isolation, in this case 40 sec etching was performed which confirms 230 nm etching

Step 2: Top Cantilever outline		
2.1	SiO_2 mask deposition	Equipment: Uniaxis Plasma Enhanced Chemical Vapor Deposition (PECVD) 1.25µm SiO_2 deposition (300 °C, SiH_4 = 400 sccm, N_2O = 900 sccm, 900 mtorr, RF = 25 W. Deposition rate is ~ 50 nm/min).

2.2	Lithography	Photoresist: Futurrex NR71-3000P Spin: 3000 rpm at 1000 rpm/sec for 40 secs (thickness: ~4 μm) Soft Bake: 150°C for 1 min on hotplate Exposure: λ = 365 nm, UV density = 180 mJ/cm^2, Image Reversal Bake: 100°C for 1 min on hotplate Developer: RD6 for 35~45 secs
2.3	SiO_2 etch in ICP	Equipment: Plasma Therm ICP with C_4F_8 Plasma Sample mount on 4" SiO_2/Si wafer with cool grease. SiO_2 etch for 7 mins (C_4F_8 = 15 sccm, CO_2 = 28 sccm, Ar = 5 sccm, 5 mtorr, RF1 = 40 W, RF2 = 800W, DC=158 V. Etch rate is ~ 200 nm/min). ▪ Etch time depends upon etch rate, 7'30" min should be sufficient to etch down 1.25μm SiO_2.
2.4	PR removal	Clean with acetone, methanol, and isopropanol, rinse with de-ionized (DI) water and dry with a nitrogen spray
2.5	GaN etch in ICP	Equipment: Plasma Therm ICP with Cl_2/BCl_3 Plasma Sample mount on 4" SiO_2/Si wafer with cool grease. GaN etch for 7 mins (Cl_2 = 32 sccm, BCl_3 = 8 sccm, Ar = 5 sccm, 5 mtorr, RF1 = 70 W, RF2 = 500W, DC=225 V. Etch rate is ~ 350 nm/min). ▪ Etch time depends upon etch rate, with GaN etch rate of 350 nm/min, it should take ~11'30" min to etch the remaining GaN
2.6	Removal of SiO_2	Removal of remaining SiO_2 with Buffered Oxide Etch (BOE) for 10 mins
Step 3: Ohmic contacts		
3.1	Lithography	*Same as step 2.1*
3.2	Metal depostion	Equipment: CVC E-beam metal evaporator Deposition of following metal stack at pressure below 2×10^{-6} torr Titanium (Ti) : 20 nm Aluminum (Al): 100 nm Titanium (Ti): 45 nm Gold (Au): 55nm
3.3	RTP	Equipment: Rapid Thermal Annealer (RTP) Annealing at 800°C for 60 secs in N_2
3.4	Metal liftoff	Metal liftoff in acetone with stirring, spraying by syringe
Step 4: Schottky contacts		
4.1	Lithography	*Same as step 2.1*
4.2	Metal deposition	Equipment: CVC E-beam metal evaporator Deposition of following metal stack at pressure below 2×10^{-6} torr Nickel (Ni) : 25 nm Gold (Au): 375 nm

4.3	Metal liftoff	*Same as step 3.4*
Step 5: Probe contact pads		
5.1	Lithography	*Same as step 2.1*
5.2	Metal deposition	Equipment: CVC E-beam metal evaporator Deposition of following metal stack at pressure below 2×10^{-6} torr Titanium (Ti): 20 nm Gold (Au): 200 nm
5.3	Metal liftoff	*Same as step 3.4*
Step 6: Through wafer Si etch from backside		
6.1	Thick SiO_2 mask deposition (backside)	Equipment: Uniaxis Plasma Enhanced Chemical Vapor Deposition (PECVD) 10 µm SiO_2 deposition (300 °C, SiH_4 = 400 sccm, N_2O = 900 sccm, 900 mtorr, RF = 25 W. Deposition rate is ~ 50 nm/min).
6.2	Lithography (backside)	Photoresist: Futurrex NR71-3000P Spin: 3000 rpm at 1000 rpm/sec for 40 secs (thickness: ~4 µm) Soft Bake: 150°C for 1 min on hotplate **Backside alignment** *Same as step 2.1*
6.3	SiO_2 wet etch (backside)	SiO_2 etch with Buffered Oxide Etch (BOE) for 25 mins
6.4	Through wafer Si etch (backside)	Equipment: STS ICP (Bosch Process) Sample mount on 4" SiO_2/Si wafer with cool grease. Carrier wafer should have at least 9 µm PECVD oxide. Thermally grown oxide can be of lesser thickness. Si etch for as many cycles as needed, typically 1200 cycles for 625 µm Si substrate. Etch cycle: 10 sec (SF_6 = 130 sccm, O_2 = 13 sccm, 94 mtorr, RF1 = 10 W, RF2 = 600W, Passivation cycle: 8 sec (C_4F_8 = 100 sccm, 94 mtorr, RF1 = 0 W, RF2 = 600W.

APPENDIX B

ELECTRON BEAM LITHOGRAPHY

1.1	Lithography	Photoresist layer 1: PMMA 495K Spin: 6000 rpm at for 40 secs Soft Bake: 180°C for 2 mins on hotplate Photoresist layer 2: PMMA 950K Spin: 6000 rpm at for 40 secs) Soft Bake: 180°C for 2 mins on hotplate Total PR thickness: 0.270 µm Exposure: Specimen/Collector Current = 20 pA to 1500 pA, Dose: 3.7 to 3.81 pC/ μm^2 Developer: MIBK: IPA 1:3 Ratio Temperature: 23°C Time: 40 Sec Rinse: IPA 30 sec, N_2 blow dry
1.2	SiO_2 Dry etch in ICP	Equipment: Plasma Therm ICP with C_4F_8 Plasma Sample mount on 4" SiO_2/Si wafer with cool grease. SiO_2 etch for 7 mins (C_4F_8 = 15 sccm, CO_2 = 28 sccm, Ar = 5 sccm, 5 mtorr, RF1 = 40 W, RF2 = 800W, DC=158 V. Etch rate is ~ 200 nm/min).
1.3	SiO_2 Wet etch 6:1 BOE	Removal of SiO_2 with Buffered Oxide Etch (BOE 6:1) The etch rate is ~2 nm/sec
1.4	Metal deposition	Equipment: E-beam metal evaporator Deposition of following metal stack at pressure below 2×10^{-6} torr Titanium (Ti): 20 nm Aluminium (Al): 50 nm Titanium (Ti): 20 nm Gold (Au): 50 nm